Tunneling under squeezing conditions : Effect of the excavation method

Manuel de La Fuente Mata

Tunneling under squeezing conditions: Effect of the excavation method

Thèse soumise pour l'obtention du grade de

Docteur de l'Université Paris Est

Ecole Doctorale Sciences, Ingénierie et Environnement (SIE)

Spécialité : *Géotechnique*

présentée le 19 Novembre 2018 à Champs-sur-Marne par

Manuel DE LA FUENTE MATA

Laboratoire Navier, Equipe Géotechnique CERMES

JURY

Amade POUYA	Ecole des Ponts ParisTech	Président du Jury
Georg ANAGNOSTOU	ETH Zürich	Rapporteur
Fréderic PELLET	Ecole des Mines ParisTech	Rapporteur
Marc PANET	Ecole des Ponts ParisTech	Examinateur
Daniel BILLAUX	ITASCA Consultants	Examinateur
Jean SULEM	Ecole des Ponts ParisTech	Directeur de thèse
Reza TAHERZADEH	TRACTEBEL Engineering	Co-encadrant de thèse
Didier SUBRIN	Centre d'Etudes des Tunnels	Co-encadrant de thèse
Michel LEVY	SETEC	Invité

Tunneling under squeezing conditions: Effect of the excavation method

Thèse soumise pour l'obtention du grade de

Docteur de l'Université Paris Est

Ecole Doctorale Sciences, Ingénierie et Environnement (SIE)

Spécialité : *Géotechnique*

présentée le 19 Novembre 2018 à Champs-sur-Marne par

Manuel DE LA FUENTE MATA

Laboratoire Navier, Equipe Géotechnique CERMES

To my parents and to Laura

REMERCIEMENTS

Ce travail est le fruit de collaborations humaines avec des nombreux chercheurs et ingénieurs qu'il me tient à cœur de remercier.

Je tiens à exprimer tout d'abord ma profonde gratitude envers mon directeur de thèse, M. **Jean SULEM**, Professeur à l'Ecole des Ponts, pour avoir assuré l'encadrement scientifique de mes travaux. Je le remercie pour le temps qu'il m'a accordé et surtout par sa gentillesse et ses idées brillantes.

Mes plus vifs remerciements vont ensuite à mon conseiller d'étude M. **Reza TAHERZADEH**, Directeur Adjoint de l'unité Transports & Infrastructures à TRACTEBEL ENGIE qui m'a fait partager sa grande expérience dans le domaine de la géotechnique de tunnels. Je le remercie également pour être à l'origine du sujet de recherche de ma thèse qui est très passionnant.

Je remercie chaleureusement mon conseiller d'étude M. **Didier SUBRIN**, Responsable du pôle Géologie, Géotechnique et Dimensionnement au Centre d'Études des Tunnels (CETU), pour tout le temps qu'il m'a consacré et pour sa vaste connaissance et expérience dans le monde des tunnels qu'il a su me transmettre.

Le succès de ce travail a été possible grâce au soutien de l'équipe de ITASCA Consultants SAS. Je remercie vivement M. **Daniel BILLAUX**, Président de ITASCA Consultant SAS, pour m'avoir accepté dans la formation Itasca Education Partnership (IEP) et M. **Huy TRAN MANH**, Ingénieur chez ITASCA Consultant SAS, pour m'avoir aidé à maîtriser le code du logiciel FLAC3D.

Je n'oublie pas d'adresser mes remerciements à la Société Française du Tunnel Routier du Fréjus (SFTRF) pour la mise à disposition des données d'auscultations effectuées dans le tunnel routier du Fréjus et sa galerie de sécurité.

J'exprime ma vive reconnaissance à M. **Georg ANAGNOSTOU**, Professeur à l'ETH de Zürich et à M. **Fréderic PELLET**, Professeur à l'Ecole des Mines de Paris, pour l'intérêt qu'ils ont bien voulu manifester à l'égard de ce travail, en acceptant de rapporter ce mémoire.

Ma reconnaissance va également à M. **Amade POUYA**, Professeur à l'Ecole des Ponts, pour m'avoir fait l'honneur d'accepter la présidence du jury de thèse.

Mes remerciements vont également à Messieurs **Marc PANET**, Professeur Honoraire à l'Ecole des Ponts, **Daniel BILLAUX**, Président de ITASCA Consultant SAS et **Michel LEVY**, Directeur à la SETEC, pour avoir accepté de faire partie de mon jury de thèse.

Cette thèse CIFRE a été réalisé dans le cadre de la collaboration entre TRACTEBEL ENGIE, le Centre d'Etudes des Tunnels (CETU) et l'équipe Géotechnique du laboratoire Navier de l'Ecole des Ponts (CERMES). Je les remercie pour m'avoir donné l'opportunité de réaliser ce travail.

J'aimerais de remercier mes collègues et amis à TRACTEBEL ENGIE et au CERMES pour leur accueil toujours sympathique et pour tous les bons moments que nous avons passés ensemble. En spécial je voudrais remercier M. **Xuan-Son NGUYEN,** Ingénieur chez TRACTEBEL ENGIE qui a participé dans l'obtention d'une grande partie des résultats de ce travail et M. **Gildas POTIN,** Directeur Technique chez TRACTEBEL ENGIE qui a encadré ma thèse du point de vue des démarches administratives.

Je terminerai en remerciant ma mère, mon père, ma copine Laura et toute ma famille pour son soutien et ses encouragements permanents.

ABSTRACT

During the excavation of deep tunnels, squeezing ground conditions are often encountered. The squeezing behavior of the ground is characterized by large time-dependent and usually anisotropic convergences that take place at the tunnel wall. The technique of excavation has a strong influence on the tunnel response when it is excavated under squeezing conditions. This phenomenon is illustrated throughout the case study of the Fréjus road tunnel excavated with conventional drill and blast methods and of its safety gallery excavated with a single shield tunneling boring machine. They exhibit a very interesting configuration of two tunnels excavated in parallel under the same geotechnical conditions but with different excavation techniques. Monitored geotechnical data from both tunnels are analyzed and compared. Numerical simulations of both tunnels have been carried out with Flac^{3D}. An anisotropic creep model which includes weakness planes of given orientation embedded in a visco-elasto-plastic matrix has been used for describing the behavior of the ground. A back-analysis of convergence measurements of the Fréjus road tunnel has been carried out. The behavior of the ground identified from the Fréjus road tunnel is extrapolated to predict the response of the Fréjus safety gallery in terms of the stress state in the lining. The influence of the technique of excavation on the time-dependent parameters of the ground is taken into account in the computations and its effects are discussed. It is shown that the long term ground deformations are significantly reduced with TBM excavation as compared to traditional blast and drill method.

Furthermore, the convergence-confinement methods are reviewed and their applicability is discussed when they are applied to full face circular tunnels excavated in rock masses with a stiff support system near the face. In this context, a set of empirical formula are proposed which allows to accurately predict the equilibrium state between the ground and the lining in circular tunnels excavated in full section. These formula are useful in the preliminary phase of tunnel design.

Keywords: tunnel, squeezing ground behavior, Fréjus tunnel, time-dependent behavior, numerical modeling, convergence-confinement method, tunnel boring machine

RESUME

L'excavation d'un tunnel profond dans des terrains poussants pose des difficultés particulières de conception et d'exécution. Ce type de terrain est caractérisé par des fortes convergences en paroi du tunnel de nature différée et souvent anisotrope. Le comportement d'un tunnel excavé en terrain poussant est très influencé par la technique d'excavation utilisée. Le cas d'étude du tunnel routier du Fréjus et de sa galerie de sécurité permet d'illustrer ce phénomène. Il s'agit de deux tunnels parallèles qui montrent une configuration très intéressante étant donné qu'ils traversent des conditions géotechniques similaires et qu'ils sont creusés avec des techniques d'excavation différentes : le tunnel routier a été creusé par méthode conventionnelle à l'explosif tandis que la galerie de sécurité a été creusée avec un tunnelier à bouclier simple. Les mesures d'auscultation réalisées pendant l'excavation des deux tunnels ont été analysées et comparées. Des modélisations numériques pour simuler la réponse des deux tunnels ont été développées avec le logiciel Flac^{3D}. Le comportement du terrain est simulé avec un modèle visco-elasto-plastique et anisotrope. L'anisotropie liée à la schistosité du terrain est introduite dans le modèle par la présence de plans de faiblesse d'orientation donnée (*ubiquitous joint model*) insérés dans une matrice rocheuse caractérisée par un comportement visco-elasto-plastique isotrope. Une rétro-analyse a été réalisée sur les mesures de convergence obtenues lors du creusement du tunnel routier du Fréjus. Le comportement du terrain identifié dans le tunnel routier est ensuite extrapolé pour prédire la réponse de la galerie de sécurité. L'objectif est de reproduire l'état des contraintes observé dans les voussoirs de la galerie de sécurité et d'extrapoler les sollicitations à long terme. L'influence que la technique d'excavation, en particulier sur le comportement différé du terrain a été prise en compte dans les simulations numériques. On a mis en évidence que les déformations différées du terrain sont réduites lorsque l'excavation est réalisée au tunnelier.

Par ailleurs, une synthèse critique de la méthode convergence-confinement et de ses variantes a été réalisée. Une discussion a été menée sur l'applicabilité des méthodes convergence-confinent quand elles sont utilisées pour le dimensionnement des tunnels circulaires excavés en section pleine avec l'installation d'un soutènement raide près du front d'excavation comme c'est le cas lors d'une excavation au tunnelier. Dans ce contexte, un ensemble de formules empiriques sont proposées. Elles permettent d'obtenir avec une bonne précision l'état d'équilibre entre le terrain et le soutènement et peuvent être utilisées dans la phase de pré-dimensionnement des ouvrages.

Mots-clés : tunnel, terrains poussants, tunnel du Fréjus, comportement différé, simulation numérique, méthode convergence-confinement, excavation au tunnelier

TABLE OF CONTENTS

LIST OF TABLES

LIST OF FIGURES

Chapter 1

Chapter 2

Chapter 5

Chapter 6

Chapter 7

Chapter 8

GENERAL INTRODUCTION

1. Motivation and scope

Nowadays the use of Tunnel Boring Machines (TBMs) in tunnel excavation is increasing. This trend is even observed in tunnels excavated under difficult conditions such as squeezing grounds. Tunneling with TBM under squeezing ground conditions is confronted to many challenges because of the large time-dependent and usually anisotropic ground convergences that take place. This type of behavior is observed in argillite, tuf, flysch, mudstone, gneiss and schist rock masses submitted to a high stress state.

Many tools have been developed for the study of tunnels under squeezing conditions. These tools are of different nature: analytical solutions, empirical solutions and numerical models. All of them are very useful but they need to be employed at the right stage of a tunnel design and taking into consideration their applicability limits.

In the present work, the squeezing ground phenomenon is illustrated through the case study of the Fréjus road tunnel and its safety gallery excavated under the Alps between France and Italy. They exhibit an interesting configuration of two parallel tunnels with a similar size excavated with different techniques under the same geological and geotechnical conditions. The Fréjus road tunnel was carried out in the seventies by drill and blast methods while its safety gallery was executed between 2009 and 2016 with a single shield Tunnel Boring Machine (TBM). During the excavation of the Fréjus road tunnel, the final lining was installed four months after the passage of the advancing face. It allowed carrying out a monitoring campaign where time-dependent convergence measurements were continuously retrieved along the tunnel. On the contrary, during the excavation of the safety gallery, the ground was immediately covered by the segmental lining installed right after the passage of the TBM. In consequence, the ground behavior can’t be properly studied. However, monitoring data was obtained from strain gauges embedded in the segmental lining of several sections in the safety gallery.

2. Knowledge gaps

In a preliminary stage of a tunnel design, analytical and empirical tools are preferred. One of the most extended calculation methods is the ConVergence-ConFinement (CV-CF) closed form solution where the rock-support interaction analysis is simplified by means of a two-dimensional plane-strain assumption. It has been commonly and successfully employed in conventional tunnel excavation with light support systems. However, if the installed support is very stiff as in the case of tunnels excavated with TBM, the results obtained with the CV-CF method may significantly

differ from those obtained with numerical 3D simulations. Some improvements of the CV-CF method as the so-called implicit methods deal with the strong interaction between the stiff support and the rock mass by modifying the Longitudinal Displacement Profile (LDP) of the ground. However, when the lining is very stiff, the Ground Reaction Curve (GRC) is also significantly modified. For this reason, the domain of applicability of the different CV-CF methods needs to be clarified for the case of full face circular tunnels with a stiff support system (tunnels excavated with a TBM or tunnels excavated with conventional methods where a stiff lining is installed near the tunnel face as the so-called "heavy" method).

In an advanced stage of the tunnel design, complex numerical simulations are often developed. However, the number of parameters in a complex numerical model is very important and many of them can't be properly evaluated. This is the case for the ground properties which generally exhibit a large variability within the same geological unit. Furthermore, the properties of the ground will be influenced by the technique of excavation and by the installed support/lining. In this context, a back-analysis of a tunnel can provide a very rich information of the global behavior of the ground and of the main mechanisms which govern the tunnel response. In the literature there exist several examples of back-analyses of tunnels carried out with the aim of studying the mechanical properties of the ground. However, the effect of the technique of excavation on the mechanical properties of the ground and consequently on the tunnel response is still poorly documented.

3. Aims of the study

Regarding the CV-CF methods, in the present study the aim is at obtaining their applicability domain when dealing with full face circular tunnels with a stiff support system. The CV-CF method is a very used tool which has been improved by different authors since it was proposed. For his reason, we aim at reviewing the existing CV-CF methods in order to clarify the way they may be applied.

In the present work, the Fréjus road tunnel and its safety gallery are in-depth back-analyzed as an extensive geotechnical monitoring has been carried out in both tunnels during their excavation. They represent an opportunity of comparing the response of the safety gallery excavated with a TBM and of the road tunnel excavated with conventional drill and blast methods. In order to account for the time-dependent and anisotropic response of the rock mass, the constitutive model proposed for the ground is visco-elasto-plastic and anisotropic. This model has been successfully applied by Tran-Manh et al. (2015a) in the simulation of the response of Saint-Martin-la-Porte access adit within the framework of Lyon-Turin railway project. In the present work the ground behavior is calibrated on convergence measurements retrieved from the Fréjus road tunnel. This behavior is extrapolated to the neighboring zones of the Fréjus safety gallery which show a similar behavior in

order to predict the response of the safety gallery. Throughout this case study, the question of the extrapolation of a model calibrated with a tunnel excavated in conventional methods in order to study the response of a tunnel excavated with TBM is addressed. Another objective of this work is to study the time-dependent response of a tunnel which depends on the mechanical properties of the surrounding rock mass. These properties are influenced by the excavation method and the installed support/lining. It is generally considered that when a tunnel is executed by conventional drill and blast methods, the damage induced to the surrounding rock is more significant than when the excavation is carried out with mechanized techniques. We aim at exploring this phenomenon and its consequences in terms of time-dependent of rock mass deformation and long term loading of the final support for the proposed case study.

4. Thesis structure

The present work is organized in four parts with each part divided in two chapters:

Part I is a general introduction of the state-of-the-art and englobes the first and the second chapters:

The first chapter summarizes the main issues of tunneling in squeezing ground using conventional or mechanized techniques as well as the influence of the installed support on the tunnel response. The different techniques used for data monitoring are described and their important role in the design and the control of the civil works is highlighted.

In the second chapter we summarize the main calculation tools used in the study of the ground-support/lining interaction in a tunnel. In early stages of the design of a tunnel, simplified methods such as the rock mass classification systems are employed. A review of the most commonly used rock classification systems can be found in the present work. Furthermore, the CV-CF closed form solution and its utility in a pre-design stage of a tunnel is recalled. Finally, in an advanced stage of the tunnel design, complex calculations are required. In consequence, numerical simulations are presented as an advantageous tool capable of reproducing complex interaction problems.

Part II studies the convergence-confinement methods and its limits. It englobes the third and the fourth chapters:

The third chapter discusses the applicability of the CV-CF methods to full face circular tunnels with a stiff support system excavated in rock masses. A detailed comparison of plane-strain closed form solutions and numerical results which take into account the 3D effects at the vicinity of the tunnel face is carried out.

In chapter four, a set of empirical formula are proposed. With this formula, the equilibrium state between the ground and the support in full face circular tunnels with a stiff support system can be accurately predicted. A large range of ground and support properties are covered.

Part III shows a general description of the Fréjus road tunnel and of its safety gallery and their monitoring data processing.

Chapter five within part III is a description of the Fréjus road tunnel and of its excavation technique. Convergence data monitored during the excavation are in-depth analyzed in this chapter. A robust fitting of the convergence data is carried out by means of the semi-empirical law of Sulem et al. (1987b) allowing the identifications of the zones of the tunnel showing a similar behavior.

Chapter six describes the main features of the Fréjus safety galley and of its excavation with a TBM. Monitoring data from an important survey campaign carried out in the gallery is presented (strain gauges embedded in the segmental lining, thrust force exerted by the TBM, etc., …). Monitoring data of the safety gallery is compared to monitoring data of the parallel road tunnel.

Part IV of this work concerns numerical modelling. Chapters seven and eight are included in this part:

In chapter seven, a visco-elasto-plastic constitutive model is proposed for the simulation of the Fréjus safety gallery. A back-analysis of the Fréjus road tunnel based on convergence measurements is carried out. The applicability limits of the constitutive model are also discussed.

The last chapter aims at predicting the response of the Fréjus safety gallery in terms of the stress state developed in the lining. Ground behavior identified from the study of the Fréjus road tunnel is extrapolated to the neighboring zones of the safety gallery in order to reproduce its response. The influence of the technique of excavation on the time-dependent parameters of the ground is taken into account.

Finally, the conclusion summarizes the main findings of this thesis and includes some suggestions for future research.

PART I: STATE-OF-THE-ART

CHAPTER 1 TUNNELING IN SQUEEZING GROUND

1.1 Introduction

The excavation of a tunnel faces tremendous difficulties when it is executed through weak and deformable grounds typically encountered within highly tectonized zones at great depth. This phenomenon is called ‘squeezing ground’ in which large time-dependent and anisotropic deformations occur.

A squeezing ground needs specific efforts to design adapted constructive measures and can lead to large adaptations of both the excavation method and the support system leading to an increase in the cost and the delay of the project. Furthermore, the issues arising from this behavior are also observed well after the completion of the civil works with an overloading of the support system.

When executed using conventional techniques, the excavation process can be modified and adjusted during the works according to the encountered ground conditions. A deformable support can be installed to withstand the large convergences to be tackled. On the contrary, although TBM excavation presents many advantages, the adaptation and the optimization of both the excavation and the lining are difficult to achieve as the tunnel geometry and support system are largely fixed before the tunnel excavation. Therefore, the lining can be overloaded and the large convergences can lead to the TBM jamming. The immediate installation of the lining gives a lack of information concerning the ground convergences and, as a consequence, it hinders the study of the ground behavior.

In the present chapter, a general description of the squeezing ground phenomenon can be found. Furthermore, some approaches for squeezing ground identification are presented. The different techniques of excavation in squeezing grounds and related issues are then discussed. Finally, monitoring data techniques are presented and their crucial role in tunnel design is highlighted.

1.2 Definition of squeezing ground

A definition of “squeezing ground” was given by Barla (1995): “Squeezing of rock is the time dependent large deformation which occurs around the tunnel and is essentially associated with creep caused by exceeding a limiting shear stress. Deformation may terminate during construction or continue over a long time period”.

There exist many examples of tunnels excavated under squeezing conditions: Fréjus road tunnel (Panet, 1996) between France and Italy, Lötschberg base tunnel under the Swiss Alps (Richard et

al. 2006), Sidi Mezghiche tunnel in Algeria or Strenger tunnel in Austria. The squeezing behavior of a tunnel can be described by the magnitude of the convergences, the extent of the yielding zone and the rate of deformation. It is influenced by the geological and geotechnical conditions, the rock mass strength, the *in-situ* state of stresses, the properties of the rock mass, the ground water flow and pore pressure, the technique of excavation and the support system. Squeezing conditions may vary over short distances because the rock and its properties are usually heterogeneous. It is advisable for squeezing rock conditions to excavate an exploration gallery in order to improve the understanding of geological and geomechanical conditions.

Empirically, a squeezing rock shows low resistance, high deformability and a softening behavior. It is generally encountered in ductile and altered rock complexes under high overburden. This type of behavior is encountered in claystone, tuf, flysch, mudstone, gneiss and schist massifs and is usually associated with specific mineralogy (micas, chlorite, serpentine, clayed minerals). The origin of the anisotropy usually observed may be the result of the combination of an anisotropic state of stresses and of the anisotropy in the structure of the material. If high stresses are combined with the presence of underground high-water pressures, the occurrence of squeezing behavior can be favored e.g. Terzaghi (1946), Gioda (1982), O'Rourke (1984), Jethwa (1996), Kovari (1998), Einstein (1989), Aydan (1996), Panet (1996).

From an engineering point of view, time-dependent ground behavior can have two origins and it is important to identify the differences between both phenomena: "squeezing" and "swelling". Gioda (1982) described the swelling behavior as a time-dependent volume increase of the geotechnical medium produced by absorption of water in the zone close to the excavation. It can be found in soils or rocks with a content of clayed minerals such as smectite and in rocks with a content of anhydrite.

Furthermore, squeezing has also to be distinguish from rock-burst phenomenon. Indeed, in brittle rocks under high stress concentration, a brutal decompression phenomenon can be observed in the walls of the tunnel which is known as "rock bursting".

1.3 Identification of squeezing behavior

The identification and quantification of squeezing conditions is of paramount importance before the execution of the works. The existing approaches are commonly of empirical or semi-empirical nature. One of the first tools for assessing the stability of a tunnel was proposed by Muir-Wood (1972) and was based on the competency factor (also called stability factor) which is the ratio between the uniaxial compression strength of the massif σ_{cm} and the initial stress state σ_0

$$Nc = \sigma_{cm}/\sigma_0 \tag{1.1}$$

The same parameter was later on used by Nakano (1979) to recognize the squeezing potential of some tunnels excavated in Japan in soft-rock.

The following paragraphs present some commonly used approaches.

1.3.1 Empirical approaches

This group of approaches is based on classification schemes which allow to identify potential squeezing problems in tunnels. Singh et al. (1992) studied the impact of the rock mass quality index Q (Barton et al, 1974) and the overburden *H* on the squeezing behavior of 39 case histories. They plotted a cut demarcation line in order to differentiate squeezing cases from non-squeezing ones, Fig. 1.1. Equation (1.2) gives the expression adopted for this division line.

$$H = 350\, Q^{1/3}\ [\text{m}] \tag{1.2}$$

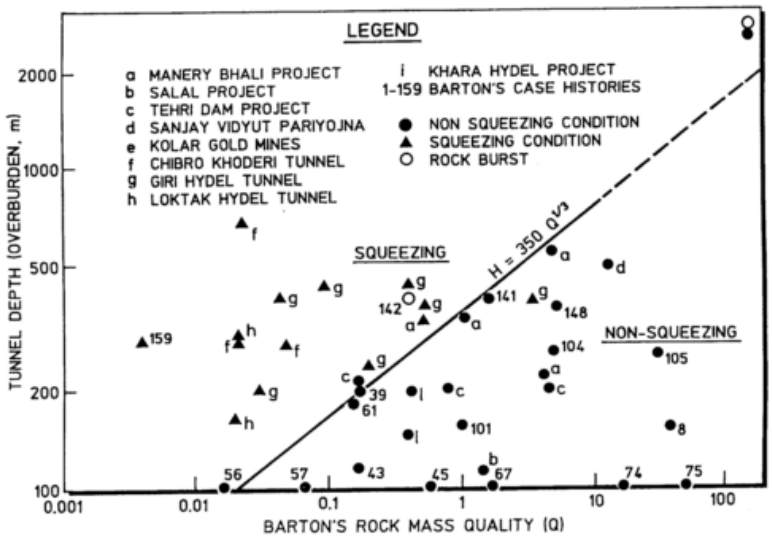

Fig. 1.1 Empirical approach for predicting squeezing conditions after Singh et al. (1992)

Based on the rock mass number N[1] defined as stress-free Q index (by assigning a value of 1 to parameter SFR the problem of obtaining an accurate value of SFR is avoided)

[1] The *rock mass number N* as defined here should not be confused the *stability number* also commonly noted *N* as used later in the thesis (see chapter 3)

$$N = (Q)_{SFR=1} \tag{1.3}$$

as well as on the tunnel depth H on the tunnel span or diameter B, Goel et al. (1995), proposed another expression

$$H = (275N^{0.33})B^{-1}\ [\text{m}] \tag{1.4}$$

In Figure 1.2, a line separates the squeezing and non-squeezing cases. Figure 1.2 also allows to predict a “rock bursting” phenomenon.

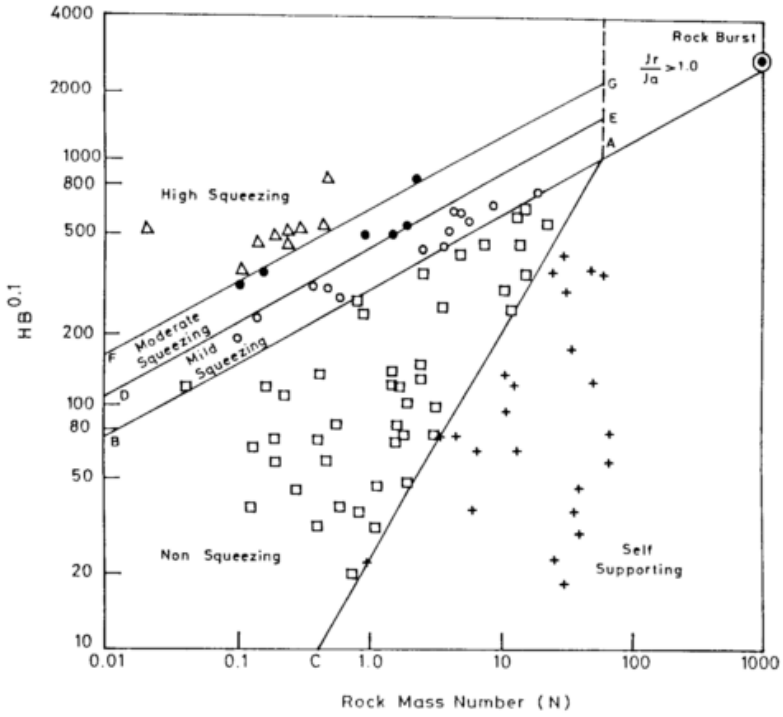

Fig. 1.2 Empirical prediction of squeezing conditions after Goel et al. (1995)

The method presented by Goel et al. (1995) is more detailed than the one presented by Singh et al., (1992) as not only the squeezing potential is identified but also the degree of squeezing can be estimated: mild squeezing, moderate squeezing and high squeezing. The degree of squeezing can be represented by tunnel convergences as described by Singh and Goel (1999):

- Mild squeezing (convergence 1-3% tunnel diameter)
- Moderate squeezing (convergence 3-5% tunnel diameter)
- High squeezing (convergence >5% tunnel diameter)

1.3.2 Semi-empirical approaches

Semi-empirical approaches aim not only at identifying the potential squeezing behavior of a ground but also at estimating the deformation around the tunnel and/or the required support pressure to withstand the radial pressure exerted by the rock.

The degree of squeezing is defined by Jethwa et al. (1984) based on the "stability factor" Nc. Based on the value of N_C different levels of squeezing potential can be considered, Fig.1.3:

- Nc < 0.4: highly squeezing
- 0.4<Nc < 0.8: moderately squeezing
- 0.8<Nc < 2.0: mildly squeezing
- 2.0<Nc: non squeezing

If an elasto-plastic behavior is considered for the ground and *Nc*>2.0 the ground will show an elastic behavior during the excavation. With this method, squeezing is considered as soon as there is plasticity.

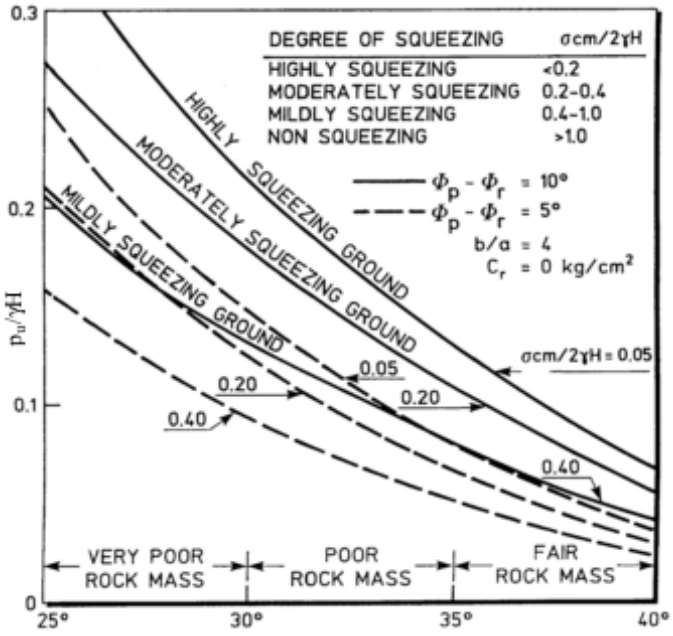

Fig. 1.3 Approach for predicting squeezing conditions after Jethwa et al. (1984)

Fig. 1.3 gives p_u/σ_0 (where p_u is the ultimate rock pressure on the tunnel lining defined as the radial rock pressure acting on the lining until the rate of tunnel-wall displacement becomes zero. This term is used in squeezing ground where creep deformations take place) versus the peak friction value of the rock ϕ_p, for different values of $\sigma_{cm}/2\sigma_0$ and a set of residual friction angles ϕ_r considering always a residual cohesion c_r equal to zero.

A similar approach is proposed by Aydan et al. (1993) but in this case the uniaxial compression strength of the massif σ_{cm} is replaced by the uniaxial compression strength of the intact rock σ_{ci} (σ_{cm} and σ_{ci} are considered to be the same with this approach which can lead to an overestimation of the uniaxial compression resistance) and compared to the overburden pressure γH, as shown in Fig. 1.4. Squeezing conditions will potentially appear if $\sigma_{ci}/\gamma H$<2. The concept of this method is based on the analogy between the hoop stress - hoop strain response at the tunnel wall and the stress-strain response of rock in uniaxial compression.

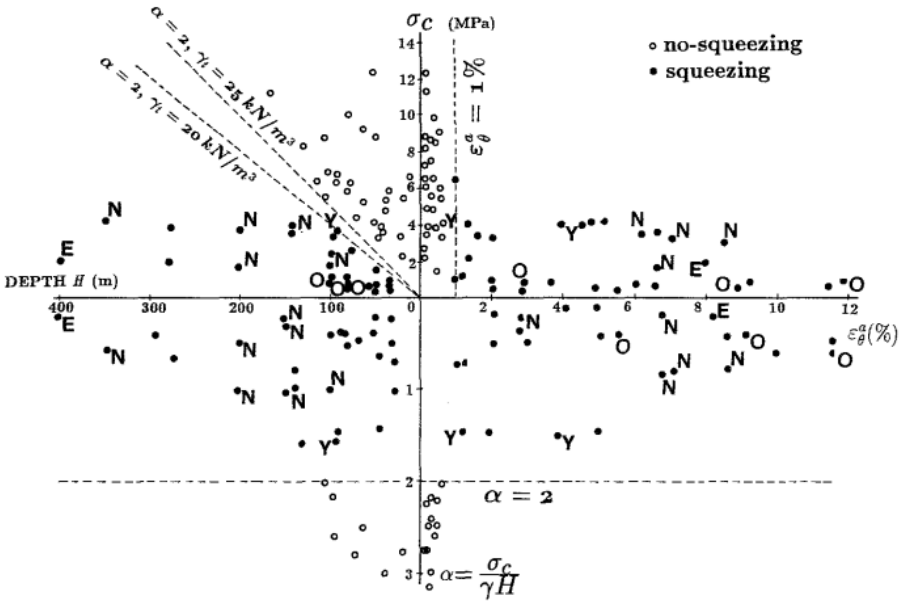

Fig. 1.4 Approach for predicting squeezing conditions (Aydan et al., 1993)

Aydan et al. (1996) proposed a method which allows for the prediction of five degrees of squeezing behavior based on the normalized deformation at the tunnel wall. This deformation is calculated as the ratio of the tangential deformation around the tunnel ε_θ^a (defined as the ratio of the radial displacement around the tunnel to the tunnel radius) to the limit elastic deformation ε_θ^e ($\varepsilon_\theta^e = \sigma_{ci}/2G$ where G is the elastic shear modulus):

- $\varepsilon_\theta^a/\varepsilon_\theta^e \leq 1$: non-squeezing
- $1 < \varepsilon_\theta^a/\varepsilon_\theta^e \leq \eta_p$: light-squeezing
- $\eta_p < \varepsilon_\theta^a/\varepsilon_\theta^e \leq \eta_s$: fair-squeezing
- $\eta_s < \varepsilon_\theta^a/\varepsilon_\theta^e \leq \eta_f$: heavy-squeezing
- $\eta_f < \varepsilon_\theta^a/\varepsilon_\theta^e$: very heavy-squeezing

where the levels of normalized deformation are given in function of the intact rock uniaxial strength: $\eta_p = 2{\sigma_{ci}}^{-0.17}$, $\eta_s = 3{\sigma_{ci}}^{-0.25}$, $\eta_f = 3{\sigma_{ci}}^{-0.32}$.

Hoek & Marinos (2000) have proposed a classification for the squeezing level based on the deformation around the tunnel ε_t (ratio of the radial displacement around the tunnel to the tunnel radius). This deformation can reach 10 % when the squeezing conditions are severe:

- $\varepsilon_t \leq 1$: few support problems
- $1 < \varepsilon_t \leq 2.5$: minor squeezing
- $2.5 < \varepsilon_t \leq 5$: severe squeezing
- $5 < \varepsilon_t \leq 10$: very severe squeezing
- $\varepsilon_t < 10$: extreme squeezing

Hoek (2001) proposed a closed-form solution for the estimation of ε_t based on the factors σ_{cm}/σ_0 and on p_u/σ_0

$$\varepsilon_t(\%) = 0.15\left(1 - \frac{p_u}{\sigma_0}\right)\frac{\sigma_{cm}}{\sigma_0}^{-\left(\frac{3p_u}{\sigma_0}+1\right)/\left(\frac{3.8p_u}{\sigma_0}+0.54\right)} \tag{1.5}$$

The approach of Hoek and Marinos (2000) covers a larger range of squeezing behavior in comparison to the approach of Aydan et al. (1993) as the extreme squeezing can also be identified. Both approaches are compared by Barla (2001) in Tab. 1.1. The two approaches consider different thresholds with different qualitative descriptions.

Tab. 1.1 Classification of squeezing behavior according to Hoek and Marinos (2000) compared with Aydan et al. (1993) classification (σ_{ci} is assumed to be 1 MPa)

	Aydan et al. (1993) ([4])		Hoek (2000)	
class no.	squeezing level	tunnel strain (%)	squeezing level	tunnel strain (%)
1	no-squeezing	$\varepsilon_\theta^a \leq 1$	few support problems	$\varepsilon_t \leq 1$
2	light-squeezing	$1 < \varepsilon_\theta^a \leq 2.0$	minor squeezing	$1 < \varepsilon_t \leq 2.5$
3	fair-squeezing	$2.0 < \varepsilon_\theta^a \leq 3.0$	severe squeezing	$2.5 < \varepsilon_t \leq 5.0$
4	heavy-squeezing	$3.0 < \varepsilon_\theta^a \leq 5.0$	very severe squeezing	$5.0 < \varepsilon_t \leq 10.0$
5	very heavy-squeezing	$\varepsilon_\theta^a \leq 5.0$	extreme squeezing	$\varepsilon_t > 10.0$

1.4 Excavation methods in squeezing conditions

The excavation method has an important influence on the squeezing behavior of the ground. It is important to adapt the excavation procedure to the local geological and *in-situ* stress conditions. The cost and the excavation delay will be very influenced by the technique of excavation.

We can basically classify the excavation methods in two categories: the conventional excavation methods carried out by successive excavation steps and the mechanized methods using a TBM.

1.4.1 Conventional excavation in squeezing conditions

When employing a conventional drill and blast excavation method, an hydraulic breaker or a roadheader machine, the lining design can be easily modified during the excavation. There exist different traditional excavation methods which are more or less adapted to the squeezing ground behavior:

- the side drift method: the cross section open in one stage is reduced by means of advanced concrete sides (Fig. 1.5). This technique can be applied in poor ground conditions (Fig. 1.6a).
- the top heading and benching down excavation: the top heading is excavated in a first stage and the benching down is excavated at a later stage (Fig. 1.6b).
- the full-face excavation method: the entire face of the tunnel is drilled and blasted in one round (Fig. 1.6c). In deformable ground conditions, the systematic reinforcement of the working head and of the ground ahead by means of fiber-glass elements is usually necessary (Barla, 2016).

Fig. 1.5 Side drift excavation (Prague subway)

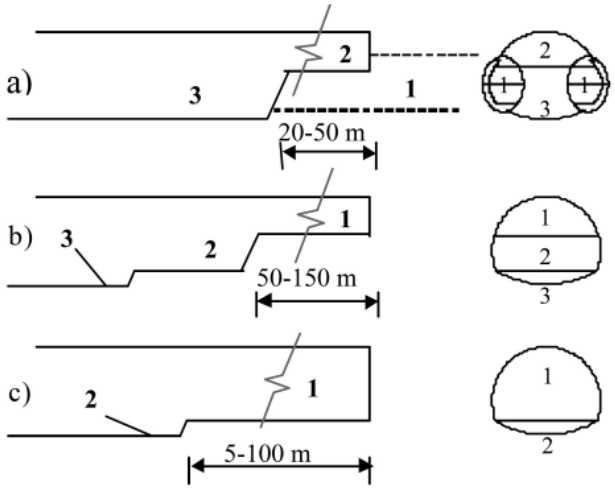

Fig. 1.6 Conventional excavation methods after Kovari (1998)

Different measures can be taken to stabilize the opening and the type of rock support which is used. It can consist on steel sets, fully grouted bolts, mesh or fiber reinforced shotcrete, etc. An active or a passive approach can be adopted when tunneling in squeezing rock conditions (Barla, 2001):

- Active approach (also called “heavy method” or “resistance principle”): the deformation of the rock is limited by means of a strong support/stabilization/lining system. However, with this technique the support can be overloaded. Pre-reinforcement and pre-treatment of the ground can be considered in order to limit the large convergences behind the working face.
- Passive approach (also called “light method” or “yielding principle”): with this technique, the deformations of the squeezing ground are absorbed by a yielding support which consists on shotcrete and sliding steel sets. After a certain controlled yielding of the support, its resistance is mobilized. An over-excavation of the tunnel is necessary to accommodate the ground deformations in order to obtain the desired section. The amount of over-excavation depends on previous auscultations and on the engineering judgment. The shotcrete lining can be divided into segments as shown in Figure 1.7. Compression longitudinal slots are introduced between the segments in order to prevent load built up in the same segmental lining which could lead to uncontrolled failure.

Furthermore, different support/lining systems can be employed within the same tunnel e.g. Dalgıç, (2002).

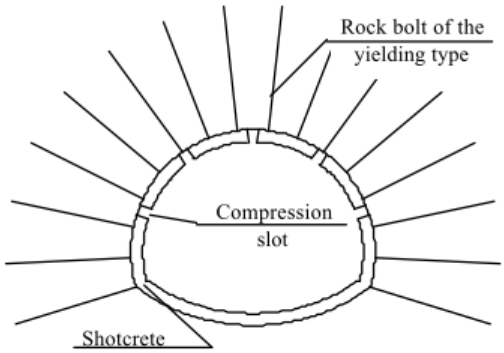

Fig. 1.7 Cross section of a tunnel with compression slots applied in squeezing rock conditions (redrawn from Schubert W. & Schubert P., 1993)

The case study of the Saint-Martin-La-Porte access adit (Fig. 1.8) done for the Lyon-Turin link project is an example of tunnel excavated in squeezing ground conditions using conventional techniques where the passive approach is applied. The un-stabilized deformations led to the development of an innovative "yield-control" support system carried out in different phases consisting on radial bolting, fiber-glass dowels, sliding steel ribs and highly deformable concrete elements. Finally, the installation of a concrete lining was carried out once the deformations were considered as stabilized.

Fig. 1.8 Squeezing phenomenon in a cross section of Saint-Martin-La-Porte access adit (Lyon-Turin Base Tunnel), after Bonini & Barla (2012)

The principles of two methods which are commonly employed in conventional excavation are described here:

The New Austrian tunneling method (NATM), is a method of modern tunnel design and construction. The method takes advantage of the inherent geological strength available in the

surrounding rock mass to stabilize the tunnel. It is based on monitoring the performance of underground construction during the excavation. The NATM is oftenly referred to as “design as you go” based on the convergences and the divergences in the lining and mapping of prevailing rock conditions. It is not a set of specific excavation and support techniques. The NATM has seven elements:

- The main component of tunnel support is the strength of the surrounding rock mass.
- Shotcrete protection. A thin layer of shotcrete is immediately applied after the face advance.
- Measurements and monitoring. The deformations of the excavation must be carefully monitored.
- Flexible support. Active rather than passive approach is used. The tunnel is strengthened by a flexible combination of rockbolts, wire mesh and steel ribs.
- Quick closing of the invert.
- Changes in support and construction method are possible, but only if the contractual system enables them.
- RMC, ranging from very hard to very soft determines the minimum support measures and avoids economic waste that comes from needlessly strong support measures.

The ADECO method was developed in the eighties in Italy by Professor Lunardi and has the following particularities (e.g. Lunardi et al., 1993, Vydrová 2015):

- It is a method of controlled deformation. The deformation response of the medium to the action of excavation must be principal question with which a tunnel designer is concerned. It indicates the triggering and position of an arch effect (level of stability reaches by the tunnel).
- The deformation response begins ahead of the face in the core and develops backwards from it along the cavity and that it is not only convergence, but consists of extrusion, preconference and convergence.
- The deformation response of the face advance system is directly connected to the deformation response of the cavity.
- It is possible to control deformation of the advance core and as a consequence the deformation of the cavity by acting on the rigidity of the core employing measures to protect and reinforce it.
- The application of the method requires the use of rigid linings as an absolutely essential condition.
- The passage from preconfinement to confinement occurs as gradually and as uniformly as possible.

1.4.2 Mechanized excavation in squeezing conditions

The need for excavating long and deep tunnels is continuously increasing. There exist many examples of deep tunnels excavated in the last years: the two base tunnels of the Alptransit Project in Switzerland (Kovári, 1995) or the Brenner Base Tunnel between Austria and Italy (Bergmeister, 2007). In order to reduce the construction time and the cost, the choice between multiple types of TBMs can be made. TBM excavate circular tunnels through a variety of soil and rock strata. They can work in almost any kind of material from hard rock to loose sand. The diameter of the cutter head can range from a meter in the case of a micro-TBM to almost 17.5 meters to date. They have the advantage of limiting the disturbed area around the opening. The main disadvantage of a TBM is its cost and the difficulty to transport it. Nevertheless, as modern tunnels become longer, the cost of TBM in comparison to the conventional methods become less. Figure 1.9 shows the most important parts of a hard rock shield TBM.

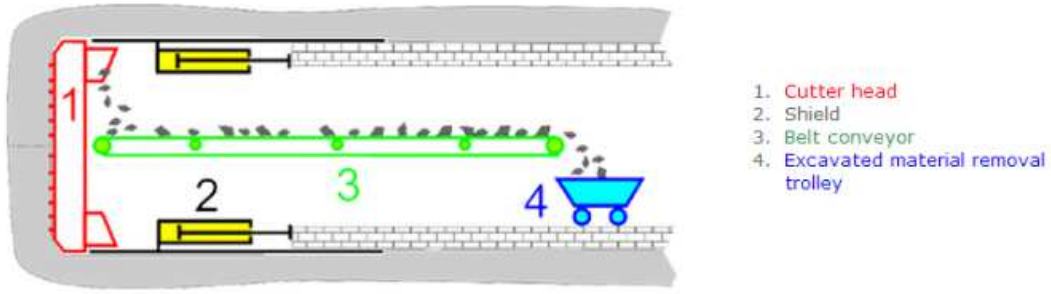

Fig. 1.9 Different parts of a hard rock shield TBM

Tab. 1.2 Characteristics of the different TBM types (Ramoni & Anagnostou, 2008)

Type of machine	Risk of shield jamming	Advance rate	Support system	Thrusting and torque system
Gripper TBMs	Low (short shield)	Low in poor ground	Grippers	Gripper forces are transmitted to the ground which must be able to provide a sufficient reaction to them
Single shield TBMs	Moderate (medium length shield)	High in poor ground	Longitudinal support	The TBM is jacked against the segmental lining
Double shield TBMs	High (long shield)	Very high in poor ground (simultaneous installation of the lining and excavation)	Longitudinal support	The TBM is jacked against the segmental lining

In hard rock, shield or open-type TBMs can be employed. The technique of excavation is by means of disc cutters mounted on the cutter head. The excavated rock is transferred through the existing openings in the cutter head. Then, by means of a conveyor belt, it runs through the machine until it is removed from the tunnel.

The different hard rock TBM models differ on the installed thrusting and support systems. Furthermore, they can dispose or not of a shield, Fig. 1.10. The machine types and their characteristics (Ramoni & Anagnostou, 2008) are summarized in Tab. 1.2.

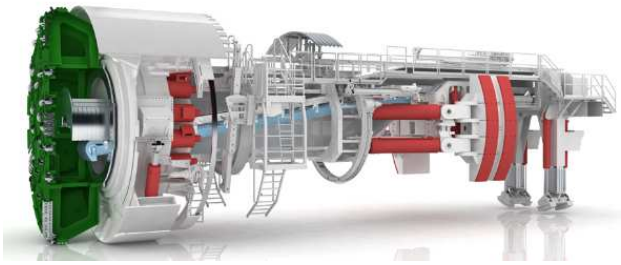

(a)

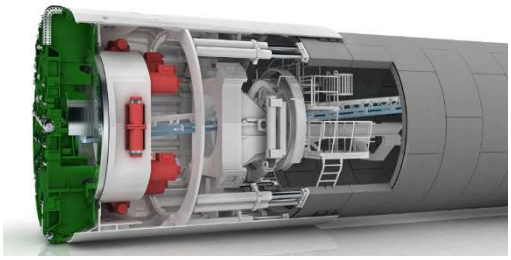

(b)

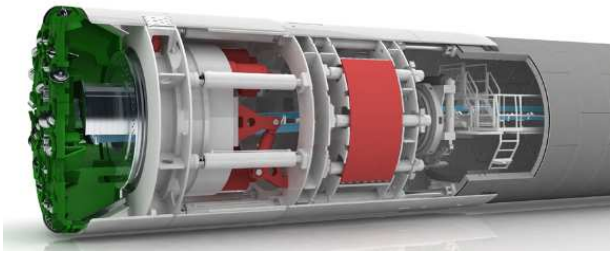

(c)

Fig. 1.10 Example of a gripper TBM **(a)**, of a single shielded TBM **(b)** and of a double shielded TBM **(c)** (Herrenknecht)

When a tunnel is excavated with a TBM in squeezing ground, many problems can occur. If heavily squeezing conditions are encountered the use of a TBM is not recommended as the shield may be trapped and the stiff support may be overloaded. TBM performance is the result of an interaction between the machine, the tunnel support and the ground (Ramoni & Anagnostou, 2008). Due to the fixed geometry and the limited flexibility of the TBM, the technique consisting in the excavation of a larger diameter gallery becomes more difficult to carry out than in conventional excavation. However, in the case of a very long stretch excavated through squeezing ground, there exist the possibility of selecting a larger boring diameter for all the tunnel. The overboring will reduce the exerted pressure on the shield and thus the frictional resistance during the excavation will be reduced but the overstressed area around the tunnel will be larger. The pre-treatement of the

ground can be also aimed in order to reduce ground deformability and it can be carried out by drainage, reinforcement or grouting.

Squeezing conditions may lead to: a cutter head sticking, a shield jamming causing the obstruction of the machine, the instability of the face and the difficulty to control the direction of the machine if the ground is soft and heterogeneous. Furthermore, the short and long-term overloading of the segmental lining is also a common issue. Barla et al. (2014) provide guidelines for TBM tunneling in squeezing conditions.

Even relatively small convergences up to 10-20 cm which would not be problematic in conventional tunneling, may lead to difficulties in mechanized tunneling (Ramoni & Anagnostou, 2011a). For Kovari (1986) when the convergence is more important than 5% of the diameter problems can arise. It is also observed that standstills of the TBM drive may be unfavorable in squeezing ground as the "time" factor plays a major role. For instance, in the 23.3 km long Yacambu-Quibor tunnel in Venezuela excavated under severe squeezing conditions the TBM got trapped when the work was suspended during technical and contractual discussions (Hoek & Guevara, 2009).

There exist a certain controversy concerning the most appropriate TBM types when dealing with squeezing conditions. The gripper TBM provides advantage of having a shorter shield and of being more flexible with respect to the tunnel support but the grippers used to take hold on the ground are not usually adapted to poor grounds. Single or double shield TBMs allow for a higher advance rate, however, the risk of shield jamming is more important than for a gripper TBM. Anyway, the choice of the TBM will depend on the specific geological conditions of the project and on the experience of the engineers.

For the design of the TBM and the support, the following parameters are investigated to evaluate the feasibility of a TBM drive in a squeezing ground (Ramoni & Anagnostou, 2011a), Fig. 1.11.

- Ground pressure p (acting upon the cutting head, the shield and the lining)
- Convergence of the tunnel wall u
- Extrusion rate of the core e
- Required thrust force F
- Required torque T
- Resulting reaction forces $R_{\mathrm{F,T}}$ between the lining and the TBM
- Rate of advance v
- Excavation standstills

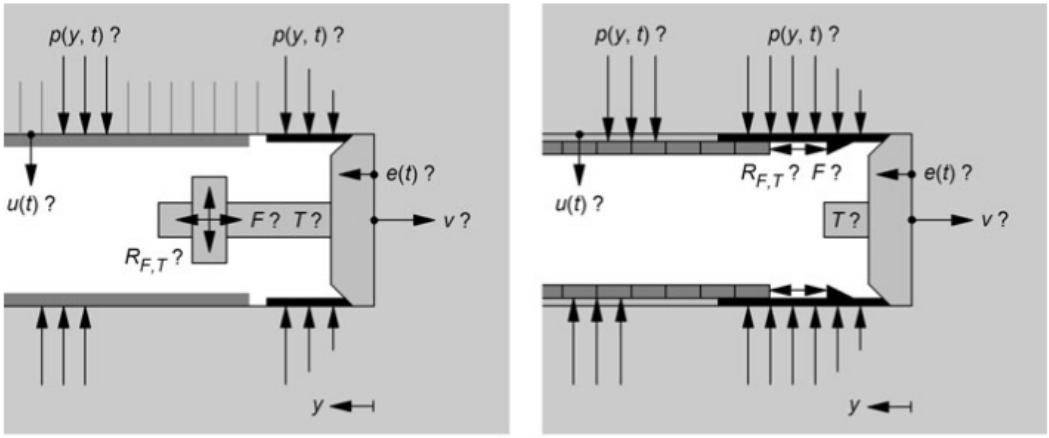

(a) **(b)**

Fig. 1.11 Critical parameters for a gripper TBM **(a)** and a single shielded TBM **(b)** after Ramoni & Anagnostou (2011a)

In the choice of the TBM the main objective is to maintain a high gross advance rate although it is difficult to achieve if the ground is of poor quality.

The installed thrust force, is also a fundamental characteristic in order to avoid TBM trapping (Ramoni & Anagnostou, 2006, 2010). The installed thrust force should be stronger than the friction exerted by the ground over the shield because if an entrapment takes place, it will be necessary to free the TBM by means of manual mining around the machine area or by installing auxiliary thrust cylinders. However, it should be noted that it may not be possible to utilize the full installed thrust force. Depending on the bearing capacity of the ground in the case of a gripper TBM or on the bearing capacity of the segmental lining in the case of a single or double shielded TBM, there could exist an upper limit.

In a TBM tunnel, there exist a gap between the installed lining and the ground. This gap is filled up with a backfilling material. This backfilling permits a better distribution of the loads applied to the lining extrados and thus a reduction of the bending moments which appear in the lining. The type, the location and the thickness of the backfilling are the parameters which play a very important role. It can consist on grouting injected via shield tail or a backfilling composed of pea gravel in the upper part (injection in the vault is generally difficult to achieve) and mortar in the bottom of the cross section injected via the segmental lining. An irregular backfilling of the segmental lining may reduce the trust capacity of a TBM. The reason stems from the fact that the longitudinal support system exerts a pressure against the segmental lining. If the gap is not properly filled up with the backfilling material the segmental lining could be laterally displaced by the exerted pressure. Ramoni et al. (2011b) have studied the effect of backfilling in the loading of the segmental lining of tunnels excavated in squeezing ground.

Ramoni & Anagnostou (2010) have presented a detailed research work based on a parametric study over the required thrust force for overcoming friction. They have observed, that the stiffer the lining, the lower the required force will be. This is the result of the arching effect of the liner in the longitudinal direction reducing shield loading. Furthermore, they could conclude that the shorter the shield and the longer the radial gap, the lower the required thrust force would be.

Ramoni & Anagnostou (2011a) have highlighted how a conicity in the shield reduces the pressure exerted by the ground over the lining and the shield. Figure 1.12, shows an example of the ground pressure p acting upon the shield and the lining for different geometrical configurations. The ground at the excavation boundary experiences several unloading and reloading cycles.

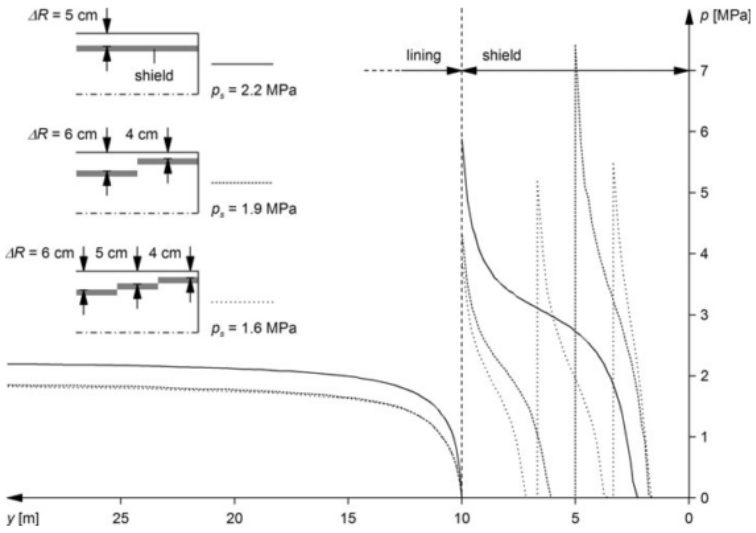

Fig. 1.12 Ground pressure p acting upon the shield and the lining for three different shield geometries after Ramoni & Anagnostou (2011a)

1.5 Monitoring of a tunnel excavation

It is mandatory to carry out an appropriate monitoring of the tunnel response. Along with calculations and observation, monitoring is essential in tunnel design.

Observation and monitoring conducted during tunnel excavation are intended to achieve the next objectives (Barla, 2001):

- evaluation of the stability of the tunnel and of the face
- extrapolation of the observed behavior to sections yet to be excavated
- providing factual documentation of tunnel performance as a function of rock conditions and the adopted construction methods
- providing valuable data for interpretation and back-analysis in order to clarify design assumptions and improve models of behavior for rock mass and rock-structure interaction

Monitoring of a tunnel depends on the excavation technique.

1.5.1 Monitoring of the convergences in a tunnel excavated with conventional techniques

Convergence measurements on the tunnel wall

Generally, when tunneling with conventional methods there exist a reasonable time for the observation of ground/support convergences. Convergence measurements represent the most common data retrieved during the excavation of a tunnel. Convergences measurements are generally relative as they are often carried out by means of tape extensometers. The length variation of a tape extensometer is equal to the length variation of the distance between two points. This technique is generally employed in galleries of a small section. When the tunnel section is large, the employed monitoring tool is generally a remote theodolite station, the measured displacements in this case should be absolute with an outside reference known at each measurement data.

Monitoring of the convergences on the tunnel wall during the excavation allows for a progressive optimization of the installed support.

Sulem (1994) described that the convergence of a tunnel is due to the combination of two effects:

- The effect of the face advance
- The time-dependent behavior of the rock mass

The semi-empirical law proposed by Sulem et al. (1987b), (Equation 1.6) permits to distinguish these two effects and is commonly used in the analysis of convergence data.

$$C(x,t) = C_{\infty x}\left[1 - \left(\frac{X}{x+X}\right)^2\right]\left\{1 + m\left[1 - \left(\frac{T}{t+T}\right)^n\right]\right\} \tag{1.6}$$

where $C_{\infty x}$ represents the instantaneous convergence obtained in the case of an infinite rate of face advance (no time-dependent effect), X is a parameter related to the distance of influence of the face, T is a parameter related to time-dependent properties of the system (rock mass– support), m is a parameter which represents the relationship between the long term total convergence and the instantaneous convergence and n is a form-factor which is often taken equal to 0.3.

By fitting convergence data with this law the total long-term convergence $C_{\infty x}(1 + m)$ can be obtained.

A new fitting procedure based on the works by Sulem (1983) and Sulem et al. (1987b) has been proposed by Vu et al. (2013). It allows for an analysis of the convergence anisotropy and a forecast of its evolution with time. This fitting procedure was tested with convergence data retrieved from

Saint Martin-la-Porte access adit (Lyon-Turin Base Tunnel) (Tran-Manh et al, 2015a) and in the galleries of the Meuse/Haute-Marne Underground Research Laboratory of Andra (Guayacán-Carillo et al, 2016). A geometrical treatment of the convergences has been carried out. The existence of main deformation axes has been observed. The initial circular shape of the gallery evolves into an elliptical shape with the front advancing and the time. The convergence law from Sulem (1983) and Sulem et al. (1987b) is independently applied to each axe of the ellipse.

Convergence measurements around the excavation

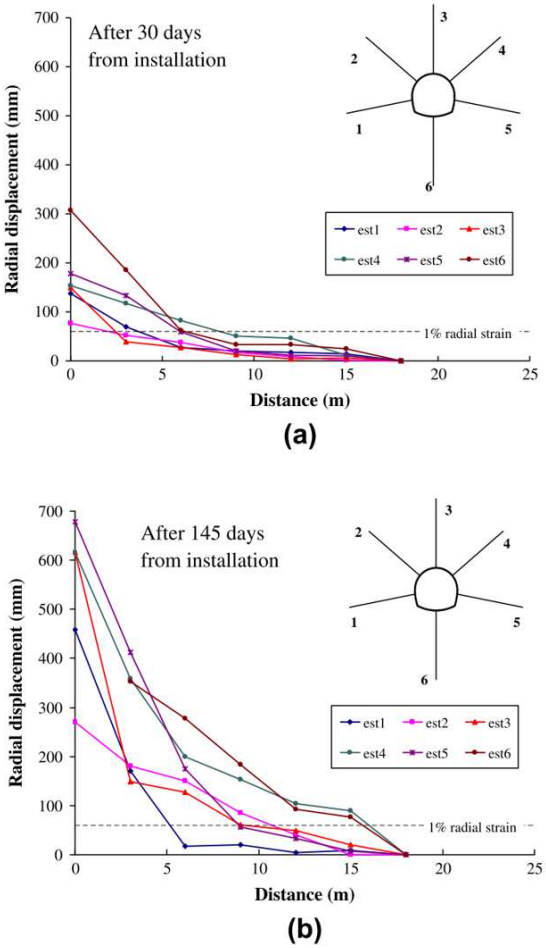

Fig. 1.13 Radial displacements from multi-point borehole extensometers installed at chainage 1330 m in Saint-Martin-la-Porte acces adit after **(a)** 30 and **(b)** 145 days from installation after Bonini & Barla (2012)

When a tunnel is excavated, there appears a decompressed area around the excavation. This area is studied by means of extensometers. They determine the relative displacements between points in a borehole in the direction of the borehole axis. Multiple boreholes extensometers are installed oriented in different directions around the tunnel showing is many cases an anisotropic behavior of the rock mass, Fig. 1.13.

Extrusion measurements of the core

The ground core which is ahead of the face loses its axial confinement as the tunnel face approaches, Fig. 1.14. The extrusion of the core is affected by ground quality, the initial stress state and the construction method (Cantieni et al., 2011).

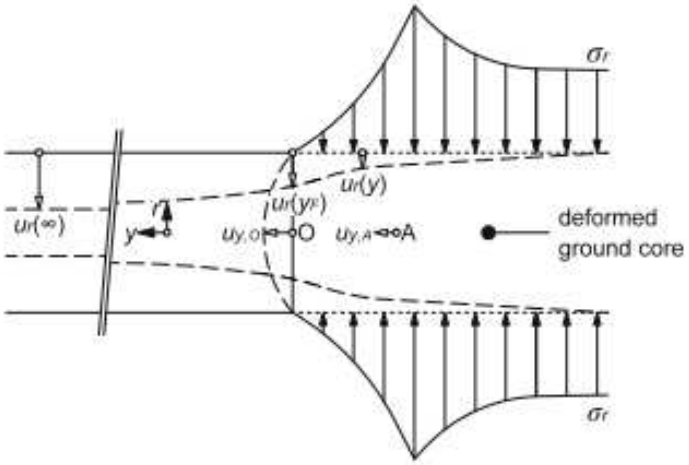

Fig. 1.14 Schematic mechanism of core extrusion (Cantieni et al., 2011)

The axial deformations of the ground ahead of the face are monitored usually by means of sliding micrometers (Kovari et al., 1979). The resolution of the strain distribution along a line of micrometers is generally of around 1 m. However, it is a time-consuming measuring procedure, which interferes with the excavation of the tunnel face (Steiner & Yeatman, 2009). Extrusion measurements of the core are very useful with the ADECO method. Certain modern technologies such as optical fiber extensometers allow for a real time automatic acquisition.

1.5.2 Monitoring of the convergences in a tunnel excavated with a TBM

Convergence measurements of the ground

The convergences of the ground can be retrieved by means of hydraulic jacks which measure the gap existing between the shield of the TBM and the ground. This technique is carried out through the shield tail of the TBM, as seen in Fig. 1.15. It provides information on the convergence of the ground as the measured gap represents the difference between the initial gap and the convergence of the ground. However, it is not easy to obtain reliable information with this technique as the initial gap is difficult to evaluate due to the complex geometry of the TBM (overcutting, eccentricity, shield conicity). Furthermore, hydraulic jacks measurements can be disrupted by rock blocks which are detached from the tunnel wall.

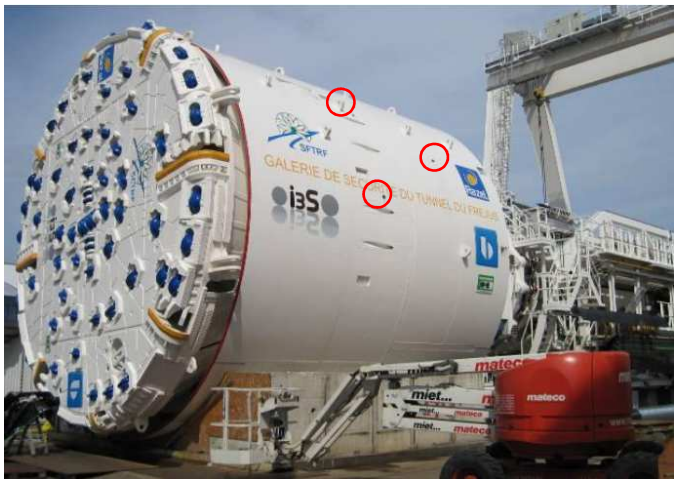

Fig. 1.15 Image of the TBM used for the excavation of the Fréjus safety gallery. The red circles indicate the position of the hydraulic jacks which measure the gap between the ground and the TBM

1.5.3 Monitoring of the stress state in tunnel support

Monitoring and interpretation of stresses in tunnel support happens to be a challenging task nowadays. It provides information of the support behavior during the excavation and/or the service life of the structure. It can also be an alarm in case of malfunctioning of tunnel support (Barla & Rossi, 1983).

The stress state observed in the lining can be obtained from strain measurements in the support elements (shotcrete and concrete linings, steel ribs, dowels or anchors, etc.). It is carried out by means of strain gages attached to steel members or embedded within shotcrete or concrete. Generally, segmental lining is considered to be linear elastic and in consequence stress state can be obtained from strain measurements by multiplying them by the Young's Modulus of the concrete or the steel. There exists another method which consists in measuring the pressure exerted by the ground over the support by means of pressure captors placed at the outer face of the support. These techniques can provide a time-dependent evolution of the stress state in the lining.

Flat-jack tests may be employed in order to obtain a punctual measurement of the stress state of tunnel lining. A flat-jack is a "thin envelope-like bladder with inlet and outlet ports which may be pressurized with hydraulic oil" (ASTM, 1991), Fig.1.16. Firstly, a slot needs to be created in the lining which provokes a stress relief and a deformation of the thickness of the slot. The flat-jack is inserted into the slot and the pressure inside it is progressively increased until the slot recovers its original thickness. The cancellation pressure obtained by this procedure corresponds to the stress acting in the lining (Barla & Rossi, 1983).

Fig. 1.16 Image of a flat-jack test

All these data allow for the study of the ground-support interaction.

1.6 Conclusion

Squeezing ground is encountered in deep geological formations and can cause many difficulties during the excavation of a tunnel. The response of the tunnel depends on the technique of excavation and also on the installed support. In conventional tunneling a soft temporary support can be adapted to the ground convergences. On the contrary, when a mechanized excavation is carried out the tunnel geometry is almost fixed from the beginning and so the technique of excavation cannot be adapted to the convergences which take place. The main issues that can be encountered in mechanized excavation are the TBM jamming, the cutter-head sticking and the overstress of the lining.

The TBM advance with the problematic of the shield jamming has been a topic of study during the last decade. It is essential to highlight the importance of identifying the required thrust force and the torque demand in order to choose an appropriate TBM. The time-dependent loading of the installed lining could lead to an overstress state in the short-term or even in the long-term after a few decades. The reason stems from the fact that a stiff support is installed near the tunnel face and in consequence a large part of the convergences are directly applied to the lining. Note that this is also the case in tunnels excavated with conventional techniques where a “heavy approach” is adopted.

Monitoring is a very important tool for the design and the control of the civil works. Monitoring data allow for an very good understanding of the tunnel response and are essential for the fitting of the constitutive models parameters, their validation and improvement during and well after the tunnel excavation.

CHAPTER 2 DESIGN METHODS

2.1 Introducción

The process of a tunnel design is based on the study of the interaction of the ground-support/lining. In early stages the available geotechnical data are often limited. At that point, simplified preliminary design methods such as the rock mass classification systems and the convergence-confinement methods are commonly used. However, as the project progresses, the tunnel design is likely to experiment significative adjustments. When more data are available, more detailed calculations become possible and numerical simulations represent then an essential tool for the tunnel design capable of reproducing complex interaction problems.

In the present chapter, the main calculation tools used in the study of the ground-support/lining interaction in a tunnel are summarized with an emphasis on their applicability under squeezing ground conditions.

2.2 Rock mass classification systems

Rock mass classification is the process of placing a rock mass into groups or classes on defined relationships (Bieniawski, 1989). They allow to determine the quality of the rock mass in an empirical way in order to predict its behavior. Rock mass classification systems are frequently used in rock engineering and design. However, according to Bieniawski (1989) they are not suitable for an elaborated and final design as they are estimative. The principal parameters employed in these classifications are summarized below:

- Strength of the intact rock material
- Fracture density and mechanical behavior of the discontinuities
- Stress state
- Hydrogeological conditions

Although they are most commonly used for obtaining the mechanical parameters of the rock by means of some empirical correlations, some of the systems provide information about the amount and the type of temporary support in a tunnel excavation depending on the rock mass quality. “In practice, rock mass classification systems have provided a valuable systematic design aid on many engineering projects especially on underground constructions, tunneling and mining projects” Hoek (2007).

Classification systems employed in tunneling design can be considered as qualitative such as the Geological Strength Index (GSI) or quantitative such as the *Q*-system, and the Rock Mass Rating (RMR) system.

Rock Tunneling Quality Index Q-system

The Q-system was developed for Scandinavian hard rocks at Norwegian Geotechnical Institute (NGI) between 1971 and 1974 (Barton et al.1974). It is worldwide employed in several domains. Two revisions of the method have been carried out in order to adapt it to new excavation techniques. The first revision took place in 1993 mainly based on examples from Norwegian underground excavations (Grimstand and Barton, 1993). The second revision in 2002 took into account excavation examples from Norway, Switzerland and India (Grimstad et al. 2002). Unlike Bieniawski method the geometry of the cavern is considered in the Q-system and the uniaxial compression strength is not considered.

The Q-value gives a description of the rock mass stability in jointed massifs when an underground opening is executed. High values of Q show a good stability and low value indicate poor stability. Q-value can be calculated based on 6 parameters:

$$Q = \frac{RQD}{J_n}\frac{J_r}{J_a}\frac{J_w}{SFR} \tag{2.1}$$

The six parameters are:

RQD = Rock Quality Designation

J_n = Joint set number

J_r = Joint roughness number

J_a = Joint alteration number

J_w= Joint water reduction factor

SFR = Stress reduction Factor (adjusting parameter)

The following chart allows for the definition of the needed support for the opening depending on Q-value, the excavation span or height and the purpose of the excavation taken into account by the ESR ratio low for high security structures (for example in nuclear power stations) and high for low security ones (for example in mines), Fig 2.1 and 2.2.

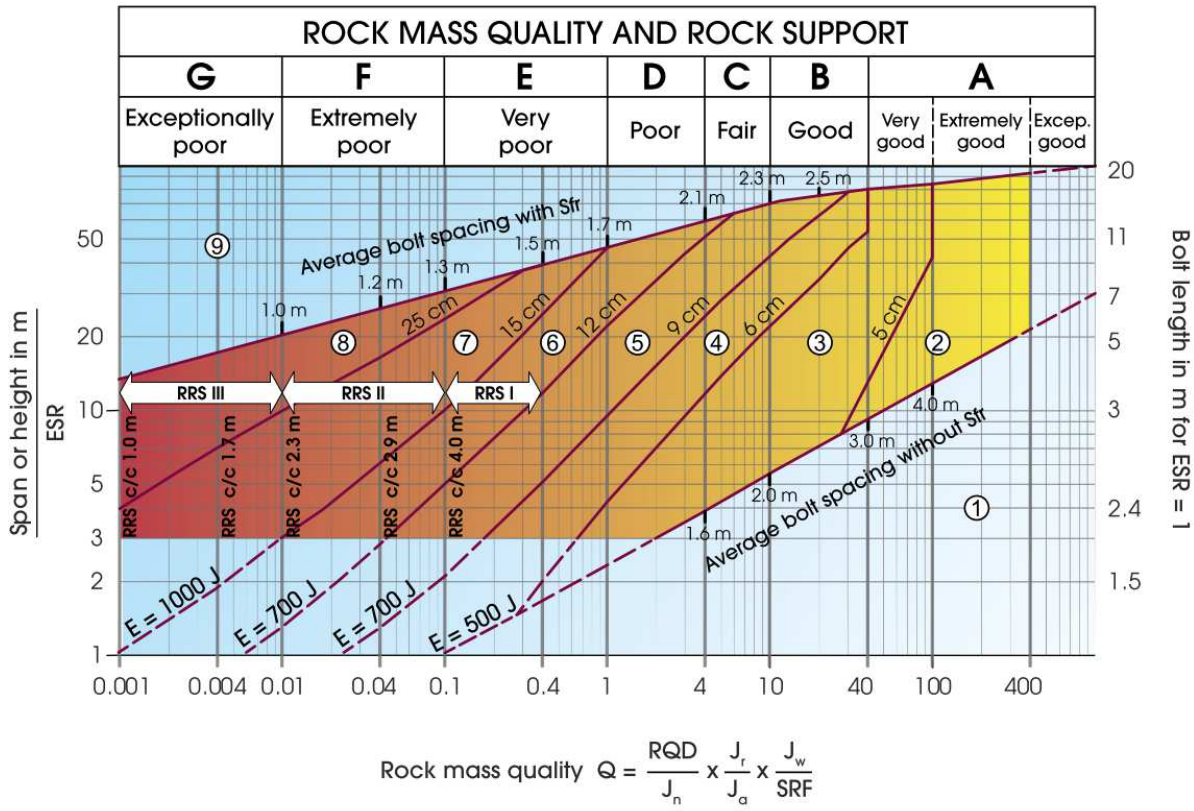

Fig. 2.1 Barton chart for the support design (NGI, 2015)

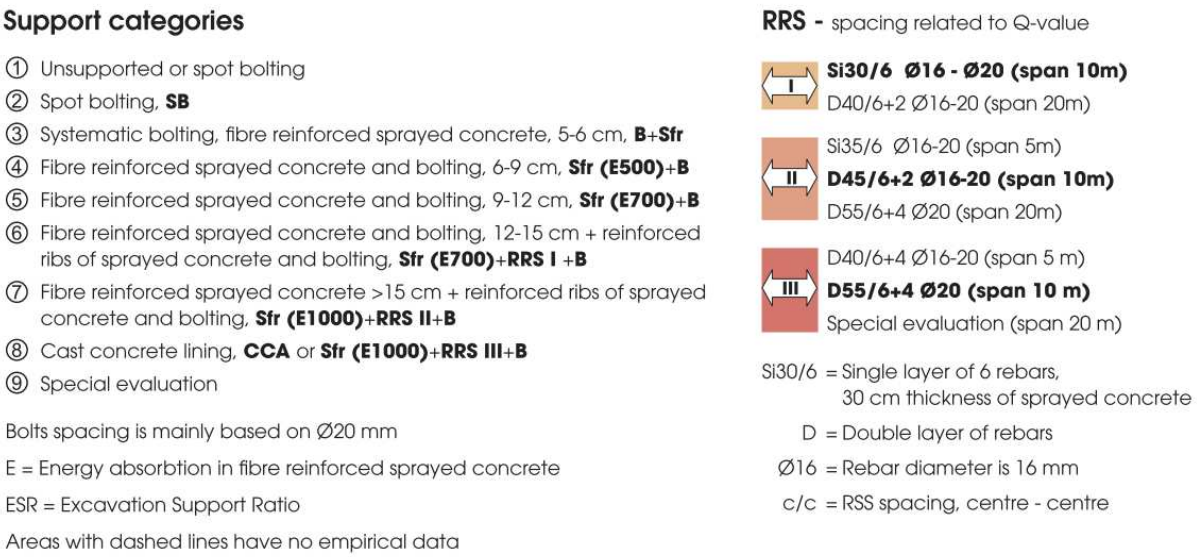

Fig. 2.2 Description of the types of support (NGI, 2015)

Rock Mass Rating (RMR)

Rock Mass Rating (RMR) was developed for hard rocks in South Africa by Bieniawski (1973). Only a few basic parameters relating to the geometry and mechanical conditions of the rock mass are used, Tab. 2.1 (a):

- Uniaxial compressive strength if the intact rock (A1)
- Rock Quality Designation (RQD) defined as the percentage of intact core pieces longer than 100 mm in the total length of a core diameter of 54.7 mm, Fig. 2.3 (A2)

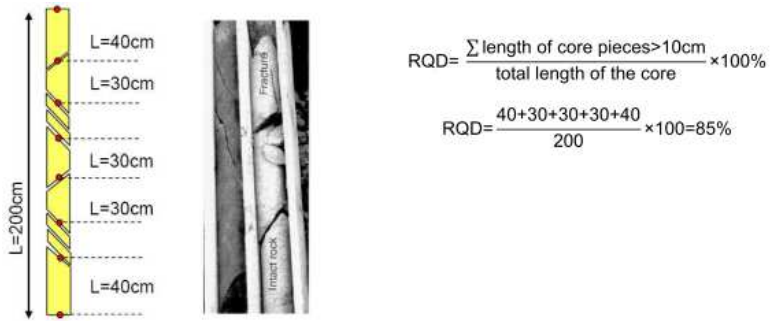

Fig. 2.3 Procedure for measurement and calculation of RQD after Deere (1988)

- Discontinuity spacing (A3)
- Condition of discontinuity surfaces (A4)
- Groundwater conditions (A5)

This system provides guidelines for the choice of rock support in tunnels as shown in Table 2.2.

$$RMR = A1 + A2 + A3 + A4 + A5 + B \tag{2.2}$$

where B is a correction parameter which depends on joints orientations with respect to the tunnel axis.

Tab. 2.1 Rock Mass Classification RMR system ratings (Bieniawski, 1989)

(a) Five basic rock mass classification parameters and their ratings

	Parameter		Range of Vaules					
1	Strength of intact rock material	Point load strength index (MPa)	>10	4–10	2–4	1–2	for this low range uniaxial compressive strength is preferred	
		Uniaxial Compressive Strength (MPa)	>250	100–250	50–100	25–50	5–25	1–5 <1
		Rating	15	12	7	4	2	1 0
2	Drill Core Quality RQD (%)		90–100	75–90	50–75	25–50	<25	
	Rating		20	17	13	8	3	
3	Joint Spacing (m)		>2	0.6-2	0.2–0.6	0.06–0.2	<0.06	
	Rating		20	15	10	8	5	
4	Condition of Joints		Not continuous, very rough surfaces, unweathered, no separation	Slightly weathered surfaces, slightly weathered, separation < 1 mm	Slightly rough surfaces, highly weathered, separation < 1 mm	Continuous, slickensided surfaces, or gouge < 5mm thick, or separation 1–5 mm	Continuous joints, soft gouge > 5mm thick, or separation > 5 mm	
	Rating		30	25	20	10	0	
5	Groundwater	Inflow per 10 m tunnel length (1/min)	none	<10	10–25	25–125	>125	
		Joint water pressure / major in situ stress	0	0–0.1	0.1–0.2	0.2–0.5	>0.5	
		General conditions	dry	damp	wet	dripping	flowing	
	Rating		15	10	7	4	0	

(b) Guidelines for classification of discontinuity conditions

Parameter	Ratings				
Discontinuity length (persistence)	<1 m	1–3 m	3–10 m	10–20 m	>20 m
	6	4	2	1	0
Separation (aperture)	None	<0.1 mm	0.1–1.0 mm	1–5 mm	>5 mm
	6	5	4	1	0
Roughness	Very rough	Rough	Slightly rough	Smooth	Slickensided
	6	5	3	1	0
Infilling (gouge)	Hard filling			Soft filling	
	None	<5 mm	>5 mm	<5 mm	>5 mm
	6	4	2	2	0
Weathering	Unweathered	Slightly weathered	Moderately weathered	Highly weathered	Decomposed
	6	5	3	1	0

(c) Effects of joint orientation in tunneling

Strike perpendicular to tunnel axis				Strike parallel to tunnel axis		Dip 0° – 20°
Drive with dip		Drive against dip				
Dip 45° – 90°	Dip 20° – 45°	Dip 45° – 90°	Dip 20° – 45°	Dip 45° – 90°	Dip 20° – 45°	Irrespective of strike
Very favorable	favorable	fair	unfavorable	Very unfavorable	fair	fair

(d) Rating adjustment for joint orientations

Strike and dip orientation of joints		Very favorable	favorable	fair	unfavorable	Very unfavorable
Ratings	Tunnels	0	-2	-5	-10	-12
	Foundations	0	-2	-7	-15	-25
	Slopes	0	-5	-25	-50	-60

Tab. 2.2 Guidelines for excavation and support of 10 m span horseshoe shaped rock tunnels constructed using drill and blast method at depth < 900 m, in accordance with the RMR system (Bieniawski, 1989)

Rock mass class	Excavation	Rock bolts (20 mm diameter, fully grouted)	Shotcrete	Steel sets
I- Very good rock RMR: 81–100	Full face, 3 m advance	Generally, no support required except spot bolting		
II- Good rock RMR: 61–80	Full face, 1–1.5 m advance complete support 20 m from the face.	Locally, bolts in crown 3m long, spaced 2.5 m with occasional wire mesh	50 mm in crown where required	None
III- fair rock RMR: 41–60	Top heading and bench 1.5–3 m advance in top heading. Commence support after each blast. Complete support 10 m from the face.	Systematic bolts 4 m long, spaced 1.5–2 m in crown and walls with wire mesh in the crown.	50–100 mm in crown and 30 mm in sides	None
IV- Poor rock RMR: 21–40	Top heading and bench 1.0–1.5 m advance in top heading Install support currently with excavation, 10 m from the face.	Systematic bolts 4–5 m long, spaced 1–1.5 m in crown and wall with wire mesh	100–150 mm in crown and 100 mm in sides	Light to medium ribs spaced 1.5 m where required.
V- Very poor rock RMR: <20	Multiple drifts 0.5–1.5 m advance in top heading. Install support currently with excavation. Shotcrete as soon as possible after blasting.	Systematic bolts 5–6 m long, spaced 1–1.5 m in crown and walls with wire mesh, Bolt invert	150–200 m in the crown, 150 mm in sides, and 50 mm on the face.	Medium to heavy ribs spaced 0.75 m with steel lagging and forepoling if required. Close invert.

Geological Strength Index (GSI)

The GSI was introduced by Hoek (1994). The objective of this system is to facilitate the determination of the properties of the rock mass for both hard and weak rock masses. It is based on the relationship between rock mass conditions and rock discontinuity surface conditions. Since its original form, it has been modified by some authors. One of the most employed graphics in order to obtain an average GSI of the rock mass is the one proposed by Hoek et al. (1998), as seen in Fig. 2.4.

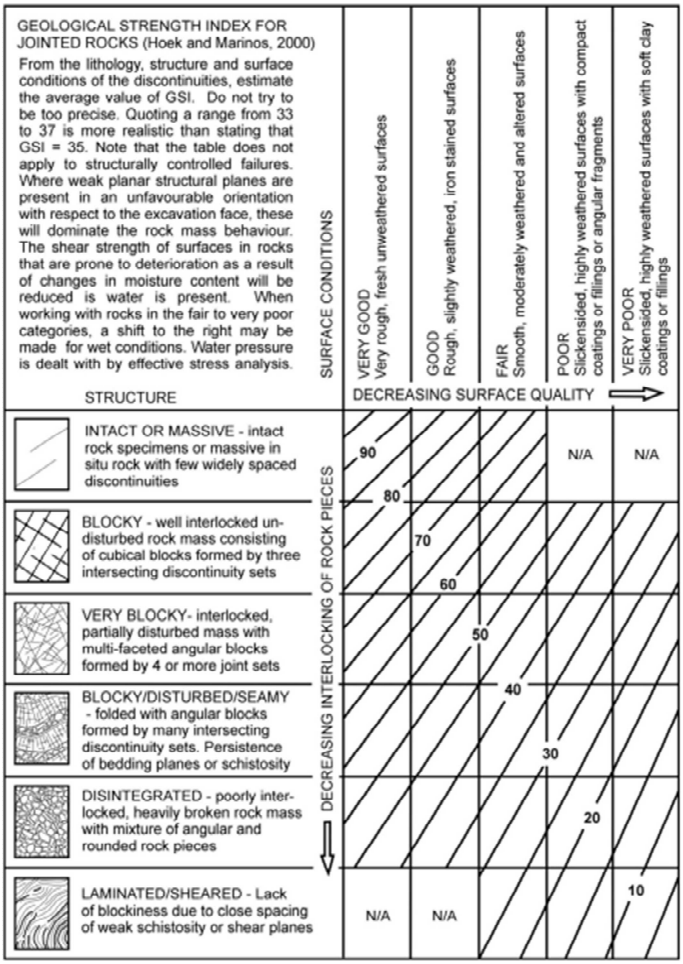

Fig. 2.4 Modified graphic for estimating the Geological Strength Index (Hoek et al., 1998)

It is commonly used for instance to estimate Young's modulus E_m of a poor rock mass with (σ_{ci} < 100 MPa) defined as Hoek et al. (2002):

$$E_m = \left(1 - \frac{D}{2}\right)\sqrt{\frac{\sigma_{ci}}{100}}\,10^{(GSI-10)/40} \tag{2.3}$$

The rock mass modulus is expressed in GPa. D is a disturbance factor which ranges from 0 to 1. σ_{ci} is the uniaxial compression strength of the intact rock. This method is however limited as it assumes that the rock mass is isotropic.

The generalized Hoek-Brown failure criterion proposed by Hoek et al. (2002) is closely connected to the GSI index. The generalize Hoek-Brown model is an evolution of the Hoek-Brown model by Hoek & Brown (1980) who introduced their failure criterion with the aim of providing input data for the analyses required for the design of underground excavations in hard rock. The criterion started from the properties of intact rock and then introduced factors to reduce these properties on the basis of the characteristics of joints in a rock mass (Hoek et al., 2002).

Tunnel behavior and support applied to weak rocks masses

The design of tunnels in weak rock masses is a major challenge nowadays. The complexity of this materials involves that they cannot be easily classified following the commonly used characterization schemes. When weak rocks are submitted to a high stress state a squeezing behavior can be triggered. Marinos et al. 2011 defined a special GSI chart for the heterogeneous rock masses such as flysch. Based on the types of rocks defined on this chart, Marinos (2014) gave specific suggestions for the theory of temporary support in tunnel excavation through each flysh type (Fig. 2.5). The study was carried out by evaluating data from the design and construction of 12 tunnels driven in flysch in Northern Greece some of which were excavated under squeezing ground conditions. Types of flysch VI to XI are more prone to develop squeezing conditions. Under severe squeezing, the application of yielding systems is the recommended solution.

ROCKMASS TYPE	STRUCTURE	TEMPORARY SUPPORT RECOMMENDATIONS
Type I. Undisturbed, with thick to medium thickness sandstone beds with sporadic thin films of siltstone.		• Excavation step: ≥3.0m • Installation of split-set bolts (e.g. Swellex) to support the unstable wedges (Sparse installation is not recommended due to the large dimensions of typical transportation tunnels)
Type II. Undisturbed massive siltstone with sporadic thin interlayers of sandstones.		• Excavation step: 2-3m • Bolts installation to support the unstable wedges and control the deformation in case of high overburden • Light steel sets in case of weathered rockmass, depending on excavation depth
Type III. Moderately disturbed sandstones with thin of siltstone interlayers.		• Excavation step: 1.5-2m • Installation of split-set bolts (e.g. Swellex type) for the support of unstable wedges • Light steel sets in case of loose structure
Type IV. Moderetaly disturbed rock mass with sandstone and siltstone similar amounts.		• Excavation step: 1.5-2m • Systematic bolt installation to support the unstable wedges, prevent the rockmass loosening and control the deformation in case of high overburden • Spiles and light steel sets in case of loose structure and weathered rockmass to avoid local chimney type failures
Type V. Moderately disturbed siltstones with thin sandstone interlayers.		• Excavation step: 1.5-2m • Systematic bolt installation to support the unstable wedges, prevent rockmass loosening and control the deformation under high overburden • Light steel sets to increase the rigidity and strength of the support shell • Spiles in case of loose and weathered structures to avoid chimney type failures • Face retaining measures: Depending on excavation depth (fibreglass nails)
Type VI. Moderately disturbed siltstones with sparse sandstone interlayers.	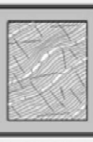	• Excavation step: 1.5-2m • Dense bolt pattern to control the deformation and prevent rockmass loosening • Steel sets to increase the rigidity and strength of the support shell • Spiles to stabilise loose and weathered structures and avoid chimney type failures • Face retaining measures: Depending on excavation depth (fibreglass nails) • Depending on bedding orientation, anisotropic stress induced deformations may be observed
Type VII. Strongly disturbed, folded rock mass that retains its structure, with sandstone and siltstone in similar extent.		• Excavation step: 1.5-2m • Dense bolt pattern to control of deformation and rockmass loosening prevention • Steel sets to increase the rigidity and strength of the support shell • Face retaining measures: Depending on excavation depth (fibreglass nails or/and forepolling)
Type VIII. Strongly disturbed, folded rock mass with siltstones and sandstone interlayers. The structure is retained and deformation – shearing is not strong.		• Excavation step usually small: 1-1.5m • Dense bolt pattern to control the deformation • Steel sets to increase the rigidity and strength of the support shell • Face retaining measures: Depending on excavation depth (fibreglass nails or/and forepolling) • Permanent and probably temporary invert to improve the shell rigidity.
Type IX. Disintegrated rockmass that can be found in wide zones of faults or/and of high weathering.		• Excavation step usually small (~1m) • Face buttress • Dense pattern of self-drilling anchors. Grouting to locally increase the rockmass cohesion • Steel sets to increase the rigidity and strength of the support shell • Spiles to presupport tunnel roof and prevent the development of chimney type failure • Alternatively in case of completely cohesionless rockmass grouting around tunnel section is proposed (e.g. through perforated forepolles)
Type X. Tectonically deformed intensively folded/faulted siltstone or clay shale with broken and deformed sandstone layers forming an almost chaotic structure.		• Small excavation step (~1m) • Dense bolt pattern to control the deformation • Steel sets in order to increase the rigidity and strength of the support shell • Face retaining measures: Depending on excavation depth (fibreglass nails or/and forepolling) • Permanent and temporary invert to improve the shell rigidity
Type XI. Tectonically strongly sheared siltstone or clayey shale forming a chaotic structure with pockets of clay.		• Small excavation step (~1m) • Dense bolt pattern and steel sets to increase the rigidity and strength of the support shell • Face retaining measures: Depending on excavation depth (fibreglass nails or/and forepolling) • Permanent and temporary invert to improve the shell rigidity • In case of very high overburden (>100-150m) the construction of a flexible support system using yielding elements may be required.

Remarks:

- The excavation is referred to Top heading and Bench method. Full face excavation in weak rockmasses imposes strong face retaining measures and small distance between temporary support and final lining.
- Shotcrete is not referred in the recommendations due to its wide application. More specifically, when shotcrete is used to avoid rockmass loosening and to ensure the personnel safety, its thickness is generally small and it is determined according to experience and evaluation of the magnitude of possible wedge failure. In stress induced phenomena due to the combination of weak rockmass and high excavation depth or/and swelling phenomena, shotcrete should be analysed as a structural element and the requisite thickness and reinforcement is determined through numerical analyses.
- The excavation step will be determined according to: (a) the anticipated size of wedges in the case of competent undisturbed rockmasses (b) the size of the wedges and the structure loosening prevention, in the case of disturbed rockmasses with no deformation problems (c) the prevention of structure loosening and decrease of deformation, in the case of weak rock masses where significant deformation is anticipated. However, the installation of spiles allows the increase of the excavation step.
- Drainage holes are proposed in case of permeable sandstone beds and relief holes in case of trapped, low permeable, groundwater zones under the water table.
- Special support requirements should be considered in case of swelling rockmasses (e.g. possible in type VI, VIII, X, XI).

Fig. 2.5 General directions for the immediate support measures for every flysch type (Marinos et al., 2011)

2.3 Convergence-confinement (CV-CF) method

The ConVergence-ConFinement (CV-CF) method is a basic and largely used tool for the preliminary design of underground support structures. Based on the analysis of stresses and strains around a circular tunnel, it provides an insight into the interaction between the support and the ground by means of a plane-strain model of the tunnel excavation. This technique is based on three different curves which are combined in order to calculate the equilibrium state between the support and the ground. These curves are the Longitudinal Displacement Profile (LDP), the Ground Reaction Curve (GRC) and the Support Confining Curve (SCC).

The CV-CF method has been originally developed for full face circular tunnels excavated in a homogeneous ground in isotropic stress conditions where the gravity effects can be disregarded (e.g. AFTES, 2002). The mechanical behavior of the rock is considered as instantaneous. The combination of GRC, LDP and SCC allows to obtain the equilibrium state as will be explained in the subsequent sections.

The 3D problem is simplified by means of a 2D plane-strain assumption where the tunnel excavation is simulated by a progressive reduction of a 'fictitious' internal support pressure p_f applied at the tunnel wall

$$p_f = (1 - \lambda)\sigma_0 \tag{2.4}$$

where σ_0 is the initial stress state which is here assumed isotropic and λ is the deconfining rate.

The idea of employing a deconfining rate λ in order to simulate the support effect of the face advance was introduced by Panet and Guellec (1974). It takes the value of 0 at the initial state and grows until reaching the value of 1 when the tunnel is completely excavated.

2.3.1 Ground reaction curve (GRC)

The GRC is the relationship between the progressive reduction of the fictitious pressure and the radial displacement of the tunnel boundary $u(x)$. Equation 2.5 gives the expression of the GRC for a linear elastic ground.

$$u(x) = \lambda(x)u(\infty)_{el} \tag{2.5}$$

where $u(\infty)_{el}$ is the radial displacement at the tunnel wall for an elastic tunnel far away from the tunnel face and is expressed as

$$u(\infty)_{el} = \frac{\sigma_0 R}{2G} \tag{2.6}$$

where R is the radius of the tunnel and G is the elastic shear modulus.

The expression of the GRC for an elastoplastic ground when a Mohr-Coulomb yield criterium is adopted can also be expressed in terms of λ (Panet, 1995)

$$u(\lambda) = R\frac{(1+\nu)}{E}\left(C_1 + C_2\left(\frac{R}{R_{pl}}\right)^{K_p-1} + C_3\left(\frac{R}{R_{pl}}\right)^{\beta+1}\right) \tag{2.7}$$

$$C_1 = -(1-2\nu)(\sigma_0 + H) \tag{2.8}$$

$$C_2 = \left(\frac{(1-\nu)\left(1+\beta K_p\right)}{K_p+\beta} - \nu\right)\frac{2(\sigma_0+H)}{K_p+1} \tag{2.9}$$

$$C_3 = 2(1-\nu)\frac{(K_p-1)(\sigma_0+H)}{K_p+\beta} \tag{2.10}$$

$$R_{pl} = \left[\frac{2(\sigma_0+H)}{K_p+1}\frac{R^{K_p-1}}{(1-\lambda)\sigma_0+H}\right]^{\frac{1}{K_p-1}} \tag{2.11}$$

$$H = \frac{c}{tan\phi} \tag{2.12}$$

$$\beta = \frac{1+sin\psi}{1-sin\psi} \tag{2.13}$$

$$K_p = \frac{1+sin\phi}{1-sin\phi} \tag{2.14}$$

where R_{pl} is the ultimate plastic radius, ϕ is the friction angle, ψ is the dilatancy angle, c is the cohesion, E is the Young's modulus, ν is the Poisson's ratio, β is the dilatancy parameter and K_p is the friction parameter.

2.3.2 Support Confining Curve (SCC)

The SCC describes the mechanical response of the support/lining. For an elastic support, assuming axial symmetry of the applied loads and of the support geometry, the relationship between the radial displacement of the wall at the outer face of the support ($\bar{u}(x) - \bar{u}(d)$) and the radial inward pressure exerted by the ground p_s acting upon the support is given by

$$\frac{\bar{u}(x) - \bar{u}(d)}{R} = \frac{p_s}{k_{sn}} \tag{2.15}$$

where $\bar{u}(x)$ is the radial displacement at the tunnel wall which depends on the distance to the advancing face x for a supported opening, d is the distance of support/lining installation and k_{sn} is the elastic normal stiffness of the support. For a sprayed concrete of thickness e, the stiffness is obtained from the thin shell theory, (equation 2.16).

$$k_{sn} = \frac{E_l}{1 - {\nu_l}^2}\frac{e}{R} \tag{2.16}$$

where E_l and ν_l are the Young's modulus and the Poisson's ratio of the sprayed concrete respectively.

However, thin shells theory can only be applied when $e < R/20$ (Flügge 1960). De Labriolle (2017) has shown that adopting a thin shell approach for a thick support, induces important errors. For TBM tunneling, the lining thickness is generally of the order of $R/10$. Therefore, resorting to the thick shell theory the normal stiffness of a thick lining K_{sn} is given by:

$$K_{sn} = \frac{2G_l\left(R_o^2 - R_i^2\right)}{(1 - 2\upsilon_l)R_o^2 + R_i^2} \tag{2.17}$$

where G_l is the shear modulus of the concrete lining, R_o and R_i are the outer and the inner radius of the lining respectively.

In the lining, the maximal hoop stress σ_{max} takes place at the inner face.

$$\sigma_{max} = \frac{2p_s R_o^2}{(R_o^2 - R_i^2)} \tag{2.18}$$

The equilibrium is obtained at the intersection of the GRC and the SCC as shown in Fig. 2.6. However, this result depends on the evaluation of the radial displacement of the support tunnel wall $\bar{u}(d)$ (obtained from the LDP).

2.3.3 Longitudinal Displacement Profile (LDP)

The closed-form expression of the GRC for an unsupported tunnel can be established for various constitutive models. The SCC can be calculated for most of the existing supports. However, the LDP, which relates the displacement around the tunnel and the distance to the advancing face, is commonly expressed by using empirical formulas derived from the results of axisymmetric numerical simulations. Depending on the underlying assumptions for the LDP (which determines the value of $\bar{u}(d)$), we can distinguish between various CV-CF approaches.

2.3.3.1 The Classical CV-CF approach

Within the classical approach (Fig. 2.6), the GRC and the LDP are considered to be intrinsic curves of the ground and they are assumed to be independent from the support behavior. As a consequence, the radial displacement of the supported tunnel wall $\bar{u}(d)$ is equal to the radial displacement of the unsupported tunnel wall at the instant of the support installation $u(d)$.

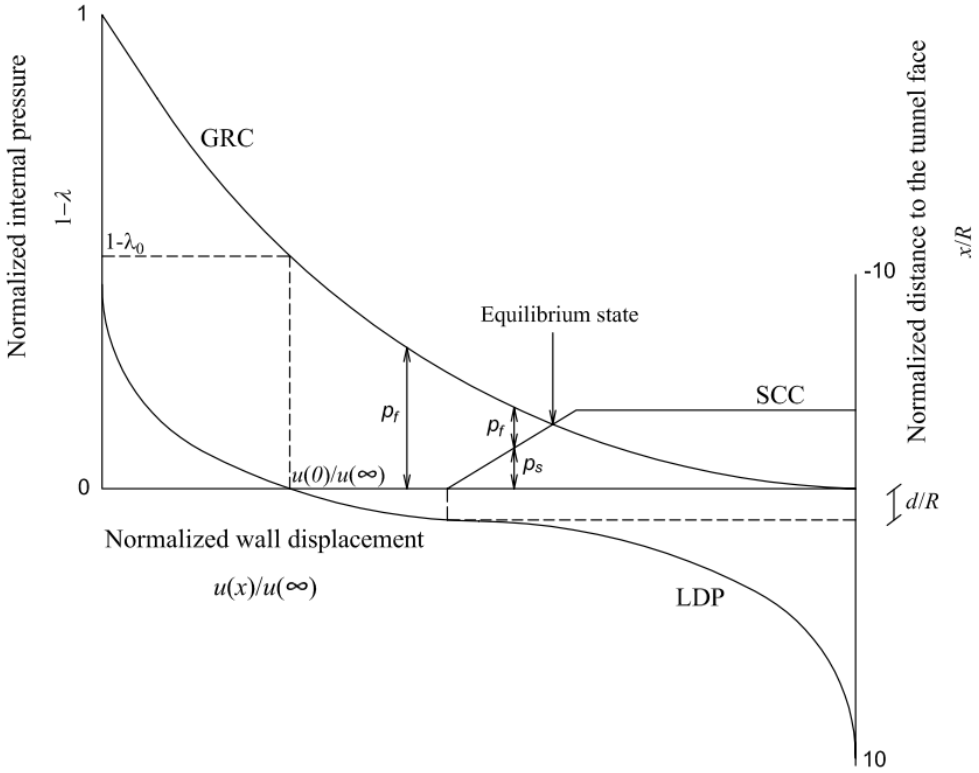

Fig. 2.6 Schematic representation of the curves employed in the CV-CF method

The LDP of an unsupported tunnel excavated in an elastic ground can be written as follows:

$$u(x) = a(x)\, u_{el}(\infty) \tag{2.19}$$

where x is the distance to the tunnel face, $a(x)$ is a dimensionless shape function

$$a(x) = \frac{u(x)}{u_{el}(\infty)} \tag{2.20}$$

A commonly used expression which describes the shape function is given by Panet (1995) as obtained by fitting the results obtained from axisymmetric numerical computations

$$a_1(x) = \alpha_0 + (1 - \alpha_0)\left(1 - \left[\frac{mR}{mR + x}\right]^2\right) \tag{2.21}$$

Typical values of the parameters are α_0= 0.25 and m = 0.75 or α_0= 0.27 and m = 0.84.

Corbetta et al. (1991) have proposed a different expression for the shape function:

$$a_2(x) = 0.29 + 0.71\left(1 - e^{(-1.5(\frac{x}{R})^{0.7})}\right) \tag{2.22}$$

Both expressions $a_1(x)$ and $a_2(x)$ lead to very similar LDP for an elastic ground.

The first empirical expression for the shape function for an elastoplastic ground was proposed by Panet and Guénot (1983)

$$b(x) = 1 - \left[\frac{0.84R_{pl}}{0.84R_{pl} + x}\right]^2 \tag{2.23}$$

which leads to the following expression for the LDP:

$$u(x) = u(0) + \left(1 - \left[\frac{0.84R_{pl}}{0.84R_{pl} + x}\right]^2\right)\left(u(\infty) - u(0)\right) \tag{2.24}$$

where $u(0)$ is the radial displacement at the tunnel wall at the face.

These authors also proposed a graphical approach which enables to obtain the deconfining parameter λ depending on the so-called stability number N (Equation 2.25) and on the distance to the tunnel face x.

$$N = \frac{2\sigma_0}{\sigma_c} \tag{2.25}$$

where σ_c is the uniaxial compression strength.

The formulation for the elastic ground behavior can be extended to an elastoplastic ground by using the Self Similarity Principle (SSP) as introduced by Corbetta et al. (1991). The principle of the method is to apply a homothetic transformation to the LDP of a tunnel excavated in an elastic $(.)_{el}$ ground in order to get the one for an elastoplastic $(.)_{pl}$ ground. The homothetic ratio χ is given by:

$$\chi = \frac{u(\infty)_{pl}}{u(\infty)_{el}} \tag{2.26}$$

From equations 2.21 (or 2.22) the LDP based on the SSP takes the following form:

$$u(x) = \chi a\left(\frac{x}{\chi}\right)\frac{\sigma_0 R}{2G} \tag{2.27}$$

For commonly encountered ground conditions ($N \leq 5$), the obtained LDP gives acceptable results.

A more robust formulation for the LDP was proposed by Vlachopoulous and Diederichs (2009). They consider that the LDP is a function of tunnel radius and the extent on the ultimate plastic radius. According to these authors, the proposed expression is appropriate for modelling large convergences when $N > 5$.

$$\begin{cases} u(0)^* = \dfrac{u(0)}{u(\infty)} = \dfrac{1}{3}e^{-0.15{R_{pl}}^*} & for\ x^* = \dfrac{x}{R} = 0\ (at\ the\ face) \\ u(x) = u(\infty)u_0^* e^{x^*} & for\ x^* = \dfrac{x}{R} \leq\ 0\ (ahead\ of\ the\ face) \\ u(x) = u(\infty)\left(1 - (1 - u_0^*)e^{\frac{-3x^*}{2{R_{pl}}^*}}\right) & for\ x^* = \dfrac{x}{R} >\ 0\ (in\ the\ tunnel) \end{cases} \tag{2.28}$$

where ${R_{pl}}^*$ is the normalized plastic radius (${R_{pl}}^* = \frac{R_{pl}}{R}$) , $x^*$is the normalized distance to the face and $u(0)^*$ is the normalized radial displacement around the tunnel boundary at the tunnel face for an unsupported opening.

Assuming that $\bar{u}(d)$is equal to $u(d)$ can induce significant errors when a stiff lining is installed quite close to the face, as in single shield TBM tunneling where a lining is placed after the TBM passage. In order to account for the ground-lining interaction, some authors have proposed to enhance the classical CV-CF method by resorting to the so-called implicit methods. In these methods, the effect of the support stiffness is taken into account in the evaluation of $\bar{u}(d)$.

2.3.3.2 The "new implicit CV-CF approach" of Bernaud & Rousset

Bernaud and Rousset (1992, 1994) have proposed the "new implicit CV-CF approach". This method modifies the shape of the LDP of a supported tunnel by applying a transformation to the x-axis. This transformation is a mathematical affinity which consists in squeezing the axis with a ratio which depends on the support stiffness. The new shape function $b^s(x)$ for the LDP can be obtained from the shape function of the unsupported LDP $b(x)$ (equation 2.24) as:

$$b^s(x) = b(\alpha x) \text{ with } \alpha = \alpha({k_{sn}}^*) \tag{2.29}$$

Assuming an elastic behavior of the ground, Bernaud and Rousset (1992) have proposed an empirical expression for $\alpha({k_{sn}}^*)$ by fitting axisymmetric finite element computations.

$$\alpha({k_{sn}}^*) = 1 + 0.635{k_{sn}}^* - 0.0293{k_{sn}}^{*2} + 0.781.10^{-3}{k_{sn}}^{*3} - 0.64.10^{-5}{k_{sn}}^{*4} \tag{2.30}$$

In the case of a Mohr-Coulomb elasto-plastic behavior, the proposed expression for $\alpha({k_{sn}}^*)$ is

$$\alpha({k_{sn}}^*) = 0.76583 + 1.029{k_{sn}}^* - 0.15454{k_{sn}}^{*2} + 0.02144{k_{sn}}^{*3} - 0.001293{k_{sn}}^{*4} + 0.035\phi \text{ (with } \phi \text{ expressed in degrees)} \tag{2.31}$$

These expressions are valid for ${k_{sn}}^* \leq 7.2$ where ${k_{sn}}^*$ is the normalized stiffness of the support:

$${k_{sn}}^* = \frac{k_{sn}}{E} \tag{2.32}$$

The implicit relationship between $\bar{u}(d)$and the ground displacement around a supported opening at the equilibrium state $\bar{u}(\infty)$ is given by:

$$\bar{u}(d) = u(0) + b^s(d)\big(\bar{u}(\infty) - u(0)\big) \tag{2.33}$$

Bernaud and Rousset (1992) proposed the following empirical expression for the calculation of the convergence at the tunnel face $u(0)$ if the behavior of the ground is elastic:

$$u(0) = 0.27\frac{\sigma_0 R}{2G} \tag{2.34}$$

whereas if the ground is elastoplastic, $u(0)$ will depend on the stability number *N*:

$$u(0) = R(0.17153 + 0.12747N - 0.027275N^2)\sqrt{3}\frac{c}{E}exp^{\left[\frac{\sigma_0}{2/\sqrt{3}c}-1\right]} \tag{2.35}$$

According to the authors, the "new implicit method" can be applied if $N \leq 5$.

2.3.3.3 The implicit CV-CF approach of Guo & Minh

The implicit method of Nguyen-Minh and Guo (1996) is more commonly used. These authors have proposed a general relationship between $\bar{u}(d)$ and $\bar{u}(\infty)$. In this method, a reduction factor which implicitly depends upon $\bar{u}(\infty)$ is applied to the radial displacement of the tunnel wall $u(d)$ at the instant of installation of the lining in order to obtain $\bar{u}(d)$

$$\bar{u}(d) = \Phi\left(\frac{\bar{u}(\infty)}{u(\infty)}\right)u(d) \tag{2.36}$$

and

$$\Phi(t) = 0.55 + 0.45t - 0.42(1-t)^3 \tag{2.37}$$

According to the authors, this method can be applied if $N \leq 5$ for any value of the support stiffness.

The application of the different methods is summarized in Tab 2.3.

Tab. 2.3 Summary for the application of the CV-CF methods

Method	$\bar{u}(d)$ (from equations)	**Equilibrium state** (by solving the system of equations)
Classical (elastic ground)	2.19	2.6 and 2.15
Classical (elasto-plastic ground)	2.24, 2.27 or 2.28	2.7 and 2.15
Bernaud & Rousset (elastic ground)	2.33	2.6, 2.15 and 2.33
Bernaud & Rousset (elasto-plastic ground)	2.33	2.7, 2.15 and 2.33
Guo & Minh (elastic ground)	2.36	2.6, 2.15 and 2.36
Guo & Minh (elasto-plastic ground)	2.36	2.7, 2.15 and 2.36

2.3.3.4 Limitations of the CV-CF method

Limitations of the CV-CF method have been discussed (e.g.Einstein and Branco, 1991) and extension have been proposed for shallow tunnels, non-circular cross sections, reinforced rocks, (e.g Gonzalez-Nicieza et al., 2008; Oreste, 2009; Wong et al., 2006; Tran et al., 2015b) and to account for time-dependent effects (Sulem et al., 1987a) or seepage forces (Lee et al., 2007).

The development of the CV-CF method is based on the assumption that an intrinsic GRC effectively exists. However, when a stiff lining is placed immediately near the advancing face, the GRC is affected by the presence of the lining (Cantieni and Anagnostou, 2009). Tunneling is indeed an inherently three-dimensional (3D) mechanical problem and as a consequence, the spatial effects that take place in the vicinity of the tunnel face are not properly simulated with a two-dimensional (2D) plane-strain model. Therefore, the calculated state of equilibrium differs between 2D and 3D analyses. This discrepancy is even stronger when large deformations take place (Cantieni and Anagnostou, 2009). Many other practical limitations of the 2D analysis have been highlighted. Schürch and Anagnostou (2012) have discussed the applicability limits of the closed-form GRC solution for a circular tunnel excavated in an isotropic ground when the rotational symmetry of the problem in terms of stress state and section shape is violated. Vlachopoulous and Diederichs (2014) have shown that for tunnels with sequenced support installation steps or non-isotropic stresses, 3D analyses are necessary.

2.4 Numerical simulations of ground-support interaction

The complexity of a tunnel excavation usually makes necessary the implementation of numerical simulations based on the Finite Element or Finite Difference Methods. These simulations allow for:

- Complex geometries
- Consideration of the support-ground interaction
- Complex behavior of the ground
- Consideration of work phasing

A three-dimensional simulation can accurately describe the complexity of a tunnel excavation. Two techniques can be employed to model the tunnel excavation when using 3D simulations:

- Step-by-step method (Hanafy and Emery, 1980)
- One-step method (Corbetta et al., 1991)

On the first hand, in the step-by-step method, the grid needs to integrate since its creation all the regions in which the stiffness will change. The tunnel excavation is modeled by the annulation of assigning zero stiffness to the elements placed in the excavated area. The length of the excavated area in each step is called the step-round-length s. The simulation of the lining installation is reproduced by imposing a constitutive law and certain properties in the correspondent grid elements.

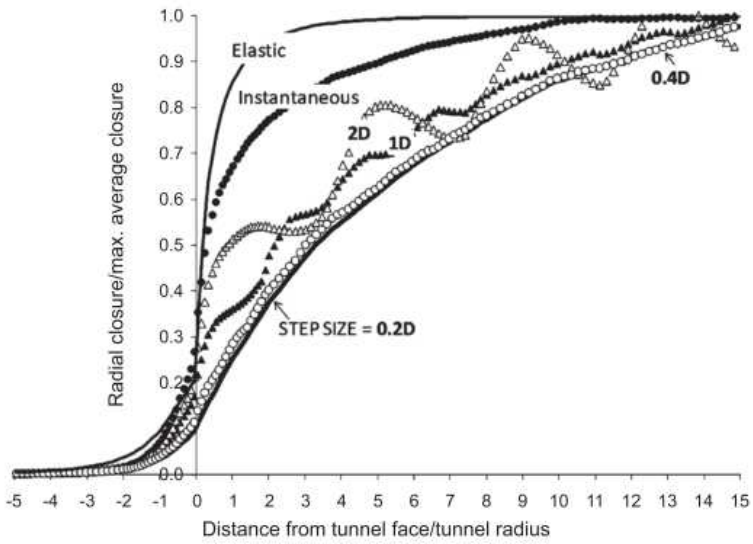

Fig. 2.7 Influence of the step size on the LDP. Instantaneous excavation and elastic excavations are shown for comparison, after Vlachopoulos & Diederichs (2009)

When choosing a step-by-step approach, it is of paramount importance to simulate the actual excavation step size. If tunneling is a continuous process such as for certain TBM tunnels, an appropriate step size must be chosen. Some authors like Vlachopoulos & Diederichs, (2009) have studied the influence of s in the simulations (Fig. 2.7). They have concluded that a step size smaller than $0.4D$ (where D represents the tunnel diameter) is enough to simulate a continuos excavation.

On the other hand, the one-step method can be employed in the study of tunnels excavated in a homogenous ground with constant advance rate, stress state, section, overburden and excavation technique. Time-integration is transformed into space integration. The one-step method corresponds, to the limiting case of a step-by-step model with zero round-length (Cantieni & Anagnostou, 2009). Within the framework of tunnel simulation the one-step method has been used by several authors e.g. Corbetta et al. (1991), Nguyen-Minh & Guo (1996) , Ramoni & Anagnostou (2011b), Maiolino (2006).

However, 3D computations might be disadvantageous in terms of cost and time of calculation. For this reason, under certain conditions the use of two-dimensional calculations can be considered as they are faster and cheaper. The most commonly used two-dimensional calculations in tunneling simulation are:

- Axisymmetric calculation. If the tunnel is excavated under isotropic conditions the axial symmetry of the problem allows for the use of a 2D axisymmetric model, Fig. 2.8.
- Plane-strain approaches, Fig. 2.9

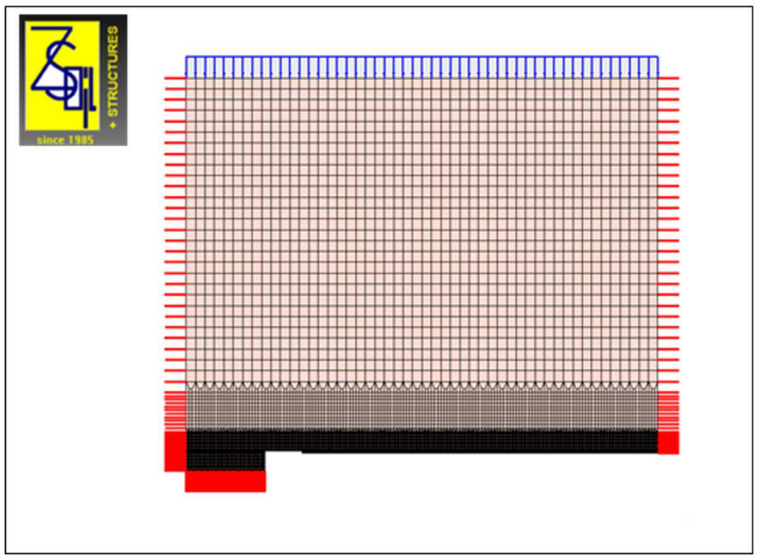

Fig. 2.8 Example of an axisymmetric model of a deep tunnel (ZSoil 2014 software)

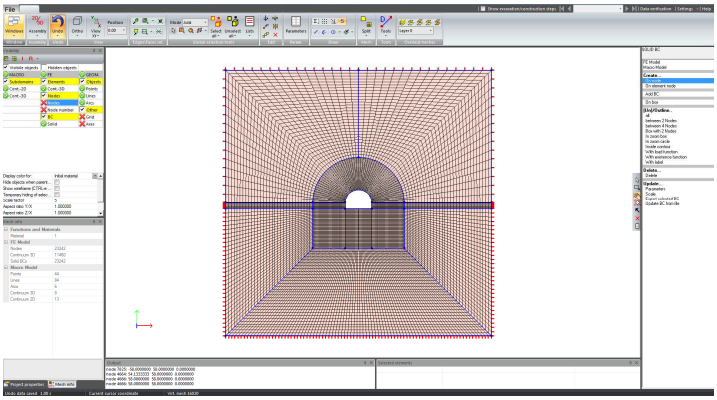

Fig. 2.9 Example of a plane-strain model of a deep tunnel with a horse shoe section (ZSoil 2014 software)

Plane-strain approaches usually employ the CV-CF concepts. The effect of an advancing face can be considered throughout two different techniques:

- The first one is the so called fictive pressure technique. A pressure which is applied on the tunnel wall and which is progressively diminished.
- The second one is known as the softening technique and consists on the progressive reduction until zero (excavated opening far away from the advancing face) of the ground stiffness which is placed in the excavated area.

2.4.1 Numerical simulations of ground-support interaction for conventional excavation

In squeezing ground, the time-dependent and often anisotropic convergences of the tunnel wall lead the engineers to progressively adapt the flexible support composed of elements such as shotcrete, rockbolts or steel ribs. This complex interaction between ground and support can be accurately addressed by means of numerical methods.

Barla et al. (2011) carried out a detailed back-analysis of the support response in Saint-Martin-La-Porte access adit using an axisymmetric model based on available performance monitoring data. Two constitutive models, Stress Hardening Elastoviscoplastic (SHELVIP) model and Three Stages Creep (3SC) model which were specifically developed to describe the rock mass squeezing behavior were presented. Both models are based on a viscoplastic potential and a viscoplastic flow rule and the magnitude of the viscoplastic strains depend on the deviatoric stress component.

More recently, Tran-Manh (2014) employed the “ubiquitous joints” model in FLAC^{3D} in order to reproduce the response of the yield-control support in the saint-Martin-la-Porte acces adit by simulating the highly deformable concrete elements, Figure 2.10. The “ubiquitous joints” model consists in a set of joints of a given orientation which pass through any point in the rock mass. When the yield criterion is reached (Coulomb criterion with tension cut-off) the joints are activated.

With this approach the anisotropic behavior observed in the Saint-Martin-la-Porte acces adit is well reproduced in the numerical computations.

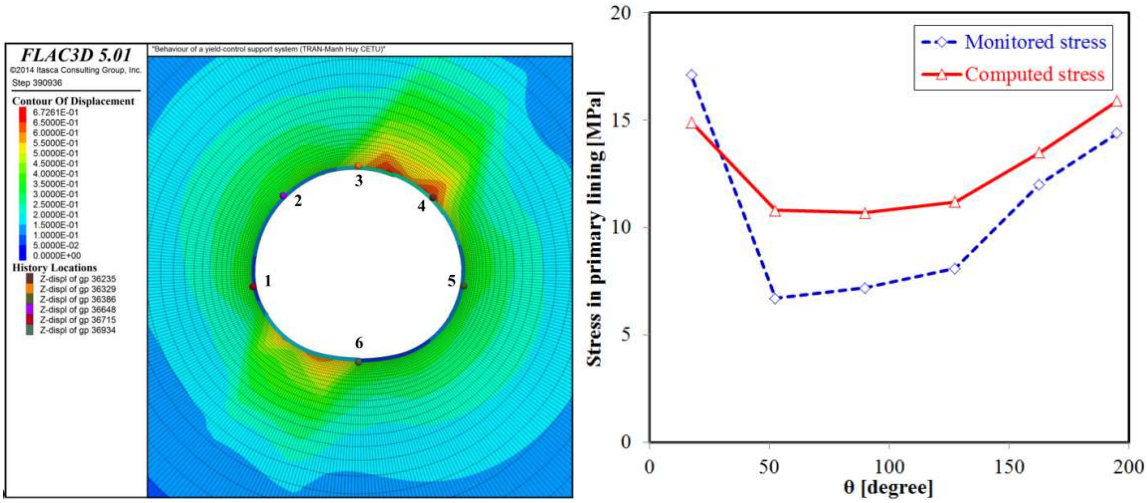

(a) **(b)**

Fig. 2.10 Displacements around the tunnel after the support installation **(a)** and average stress state in the sprayed concrete layer **(b)** after Tran-Manh (2014)

The study carried out by Sharifzadeh et al. (2013) deals with the issue of ground-support interaction in weak rock by using the Burger-creep visco-plastic (CVISC) constitutive model for simulating the ground behavior in the case study of Shibli twin tunnels in Iran. The CVISC model considers an elasto-plastic volumetric behavior and a visco-elasto-plastic deviatoric behavior driven by a Burgers visco-elastic element and a plasticity element. They performed a long term stability analysis of the lining and they concluded that after 55 years the compressive strengths of concrete cannot withstand the forces exerted by the ground. However, CVISC model which contains a Maxwell visco-elastic element leads to a constant rate of the convergences of the ground. Therefore, this model yields to increasing stresses in the lining with time and collapse in the long-term.

2.4.2 Numerical simulations of ground-lining-TBM interaction for mechanized excavation

A first group of simulations has been carried out considering an instantaneous response of the ground. The complex interaction between the rock mass, the tunnel machine, its system components and the tunnel support during tunnel excavation was studied by Zhao et al. (2012). Two simulations are developed: one simulation of an excavation with a double shield universal TBM working in conventional gripper mode in a brittle ground behavior (case study of the Brenner tunnel) and one simulation of an excavation of a double shield universal TBM working in single shield mode in a Mohr-Coulomb highly deformable ground (case study of the Lyon-Turin base Tunnel), Fig. 2.11.

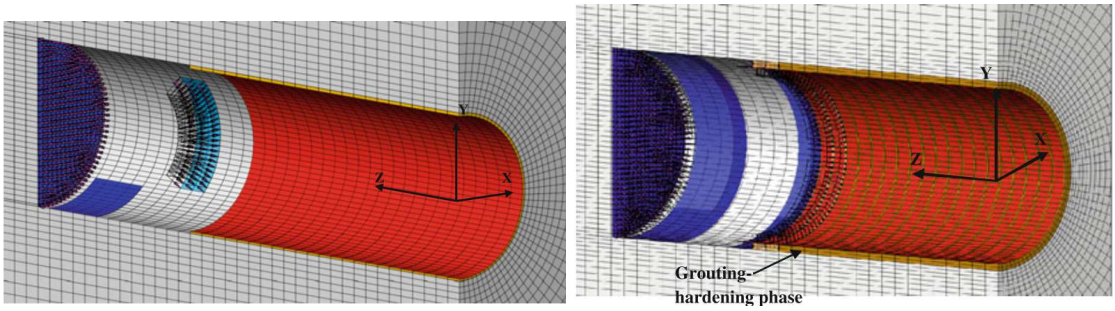

(a) **(b)**

Fig. 2.11 3D model of a double shielded universal TBM excavation **(a)** working in gripper mode in hard rock and **(b)** working in single shielded mode in weak rock (Zhao et al., 2012)

The results show that the 3D numerical simulations are highly effective in reproducing both the rock mass response and its interaction with the TBM components (Zhao et al., 2012). Fig. 2.12 shows the results of the ground-TBM/lining interaction of the simulation of the Lyon-Turin Base Tunnel. Fig 2.12a depicts the results in terms of the LDP on both the shields and the lining (at the invert as well as at the crown). The annular gap due to the over-excavation (sum of the overcut and the over-boring) and the conicity of the machine are considered in the simulation by means of special interface elements between the shield and the ground. The annular gap is smaller at the shield invert than at the shield crown. In consequence the closure of the gap takes place before at the shield invert than at the shield crown in the front shield as well as in the rear shield. Contact pressure is depicted in Fig 2.12b showing a greater pressure at the shield invert with respect to the crown value in accordance with the LDPs. Due to the conical shape of the shield the contact stress between the ground and the rear shield is initially zero.

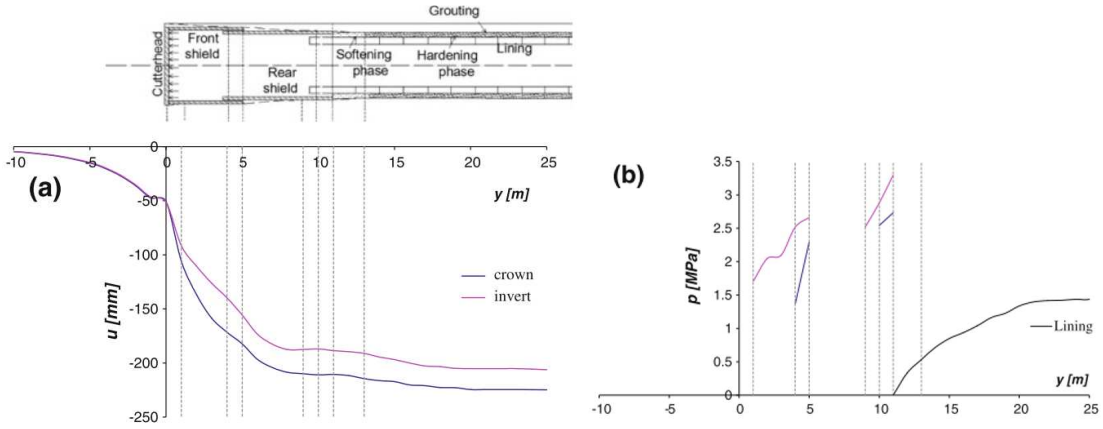

Fig. 2.12 Lyon-Turin Base Tunnel : results for the complete model, crown and invert: **(a)** longitudinal displacement profile and **(b)** contact pressure on the shield and on the lining (Zhao et al., 2012)

Zhao et al., (2015) carried out a 3D simulation of the Headrace Tunnel for the Kishanganga Hydroelectric Project in India using a non-linear criterion for simulating the squeezing ground

conditions of the ground. The results from the 3D simulation are compared with an axisymmetric simulation and with the CV-CF close-form solution. This work highlights the advantages of a 3D simulation against the other design approaches to model some important features (backfilling simulation, stepwise conicity of the shield or in-situ stress state). Hasanpour (2014) and Hasanpour et al. (2014) carried out a complex 3D large-strain simulations for evaluating the feasibility of utilizing double shield TBMs in long deep tunnels by assuming a non-linear criterion for he ground behavior. A non-uniform annular gap was considered in the simulations. For the given conditions, it is observed that higher contact forces are developed between the ground and the rear shield than between the ground and the front shield. The probability of shield entrapment in potentially squeezing ground can be evaluated with this model.

A second group of simulations considers the time-dependency of the ground in order to simulate its behavior. Hasanpour et al. (2015) used the CVISC model available in FLAC^{3D} in order to represent the rheological characteristics of the ground considering an isotropic stress state and address the question of the effect of the advance rate on the risk of entrapment of the machine and on the ground pressure exerted on the lining. They simulate the excavation with a double-shield TBM with the injection of the backfilling grouted via shield tail, Fig 2.13. Their results show that the effect of the advance rate on the ground load applied on the shields has a more important impact in the rear shield as compared to the front shield, Fig. 2.14. The front shield is loaded up to 8.5 MN at the crown when the advance rate is of 3 m/day as compared to 6.6 MN for an advance rate of 24 m/day, thus a difference of 1.9 MN. For the rear shield the difference is of 4 MN. Consequently, the entrapment of a shield TBM can occur in squeezing ground conditions during the machine arrests or when lower advance rates are adopted.

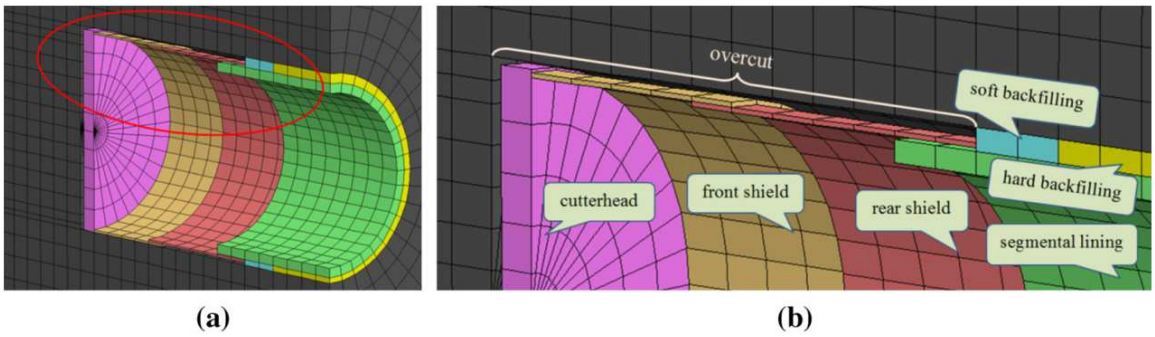

Fig. 2.13 Numerical model for the simulation of tunneling with a double shielded TBM: **(a)** complete model and **(b)** description of the model (Hasanpour et al., 2014)

Hasanpour et al. (2015) have also studied the effect of the advance rate on the ground pressure applied on the lining immediately behind the machine. They conclude that the advance rate is of prime importance. Fig. 2.15, shows the pressure applied to the lining for those rings located right

behind the shield. It can be observed that for the advance rate of 24 m/day, the last set of segmental rings installed experiences a pressure of about 2.5 MPa less than when the advance rate is 3 m/day. The efficiency of the backfilling in the homogenization of the ground pressure transferred to the ring is also assessed (Fig. 2.15a).

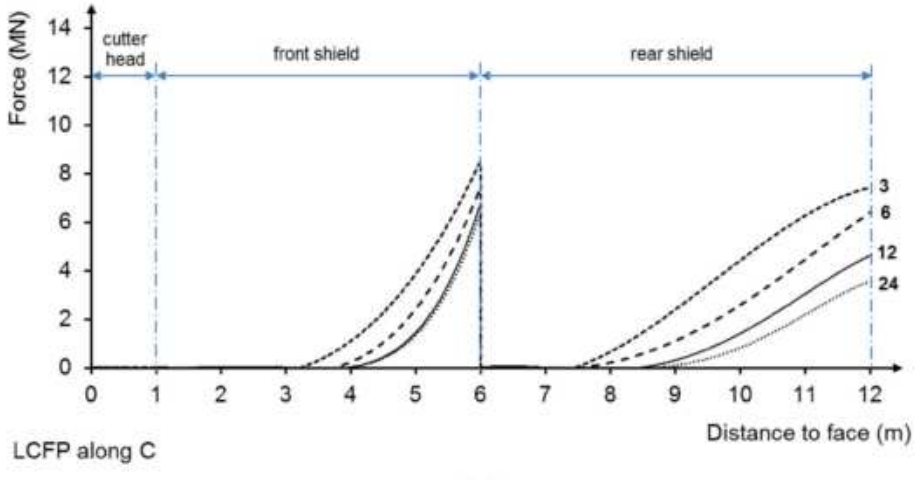

Fig. 2.14 Longitudinal contact force profile (LCFP) for different advance rates (3, 6, 12, and 24 m/day) at the tunnel crown over the front shield and the rear shield (Hasanpour et al., 2015)

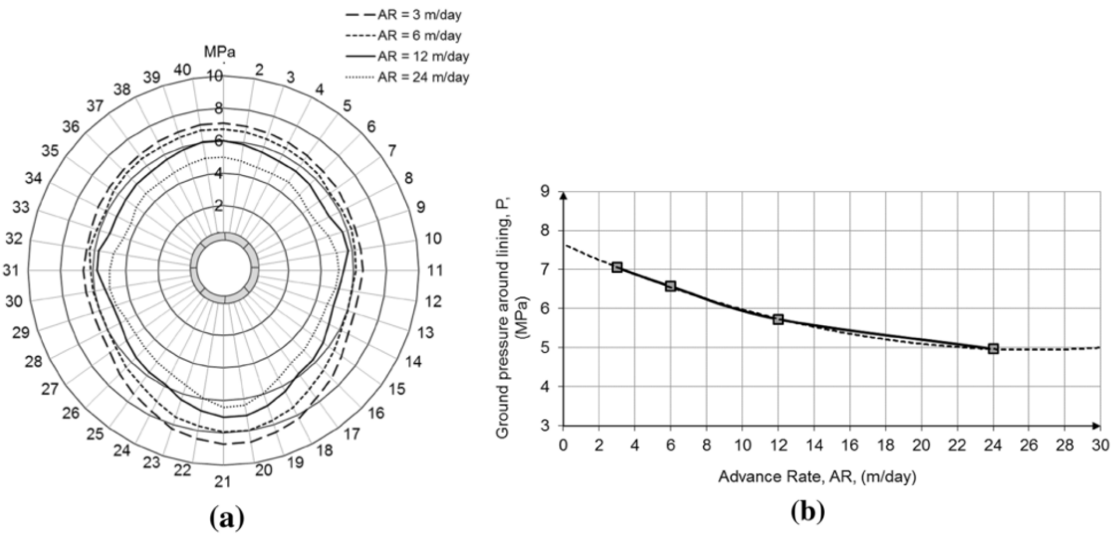

Fig. 2.15 Ground pressure around the lining: **(a)** distribution on the ring segment and **(b)** average ground pressure on the last set of segment rings versus TBM daily advance rate (Hasanpour et al., 2015)

2.5 Conclusion

Design methods for tunneling in squeezing ground combine empirical tools, analytical models and advanced numerical simulations. There exist several empirical tools such as the rock classification systems which are useful in the first stages of the design in order to estimate the required support. The analytical 2D models based on the convergence-confining methods represent a simple and powerful tool. Various extensions of the classical CV-CF methods exist which permit to take into account the effect of a stiff support installed close to the face through the so-called *implicit* methods. However, these analytical models reach their limit when the sequence of excavation is complex and when the ground behavior exhibits an anisotropic and time-dependent behavior. The 3D state of stress at the vicinity of the tunnel face is not properly simulated with a 2D plane-strain approach and in consequence the equilibrium state between the ground and the lining is not always well reproduced. The advance rate of the excavation plays an important role on the risks of TBM jamming and on the ground pressure acting on the lining. Therefore, advanced numerical simulations are necessary and more and more used for complex configurations, in order to correctly capture the behavior of the ground and its interaction with the installed support/lining.

PART II: PRELIMINARY DESIGN METHODS

CHAPTER 3 APPLICABILITY OF THE CONVERGENCE-CONFINEMENT METHOD TO FULL-FACE EXCAVATION OF CIRCULAR TUNNELS WITH STIFF SUPPORT SYSTEM

The CV-CF method is widely used in conventional tunneling at a preliminary stage of the design. In this method, the rock-support interaction analysis is simplified by means of a two-dimensional plane-strain assumption. However, when the ground exhibits large deformation and/or when the support is very stiff and installed close to the tunnel face, the results obtained with the CV-CF method may significantly differ from those obtained using 3D numerical computations. The strong interaction taking place between the stiff lining and the rock mass is not considered in the most common use of the CV-CF method. Some improvements of the CV-CF method as the so-called implicit methods have been developed in order to better account for this interaction.

In this chapter, the applicability of the CV-CF methods is discussed for full face excavation tunneling with a stiff support installed near the face as it is the case when a single shielded Tunnel Boring Machine (TBM) is used. An in-depth comparison between plane-strain closed form solutions and numerical results which properly accounts for the 3D effects at the vicinity of the tunnel face is carried out. The range of application of the different approaches of the CV-CF method is discussed.

3.1 Introduction

The present chapter deals with the design of circular tunnels with stiff support system focusing on the typical example of tunnels excavated with a single shield TBM in rock masses. This topic was already addressed by Ramoni et al. (2011) for tunnels excavated in squeezing conditions with a single shield TBM. These authors have provided a series of design charts for the estimation of the maximal load exerted on the segmental linings considering the effect of the TBM characteristics (stiffness, conicity, backfilling). In the present study, the applicability of the different approaches of the CV-CF method is discussed considering a large range of ground properties and various excavation methods. Finally, some empirical relationships are proposed for use within preliminary design of tunnels excavated with single shield TBM.

3.2 Applicability of the CV-CF methods

Conventional tunnel excavation may be undertaken using different support methods: the so-called ‘heavy method’ makes use of a stiff primary lining whereas the ‘light method’ makes use of a deformable support system, which may even be allowed to yield so as to tackle difficult ground

conditions such as within high overburden and squeezing rock behavior. In those cases, when the support accompanies the ground deformations, the GRC is not significantly modified and the CV-CF method is appropriate. On the contrary, when a stiff support is installed close to the face, the modification of the GRC cannot be disregarded and, as emphasized by Barla (2016), the 'heavy method' may somehow become impractical since very high ground pressures are expected.

The present study focuses on tunneling using single shield TBM with a stiff lining installed just at the rear of the shield tail. Even if the lining is not installed very close to the face as in the 'heavy method' its stiffness may induce a modification of the GRC, depending on the ground conditions. In the Appendix A , the study is extended to tunnels excavated with a double shield TBM.

The results obtained with the various CV-CF approaches as recalled in the previous sections are compared with those obtained with a 3D numerical model which permits to simulate the effect of the advancing tunnel face. A sensitivity analysis is performed in order to compare the performance of the different CV-CF approaches. The choice of the values for the mechanical parameters of the ground and of the lining is carried out in an attempt to cover the large range of situations encountered within single shield TBM. A circular tunnel of diameter D and excavated in a homogeneous ground is considered with isotropic initial stress state. A Mohr-Coulomb elasto-plastic model is used for the constitutive behavior of the ground and a linear elastic model is assumed for the lining.

3.2.1 Numerical 3D reference model

The axial symmetry of the problem allows for the use of a simple axisymmetric model. The numerical analysis is performed by using FLAC^{3D}, (ITASCA, 2011) (Fig. 3.1). In FLAD^{3D}, the mesh is composed of 26500 hexahedral elements. Close to the tunnel walls where the stress gradients are high, zones with a size smaller than $0.03D$ x $0.03D$ are generated. The size of the elements in those areas has been chosen after carrying out a sensitivity analysis. The lining is discretized into six hexahedral zones along its thickness. The tunnel excavation is modelled by incrementally removing the ground material and installing the support at a given distance from the tunnel face.

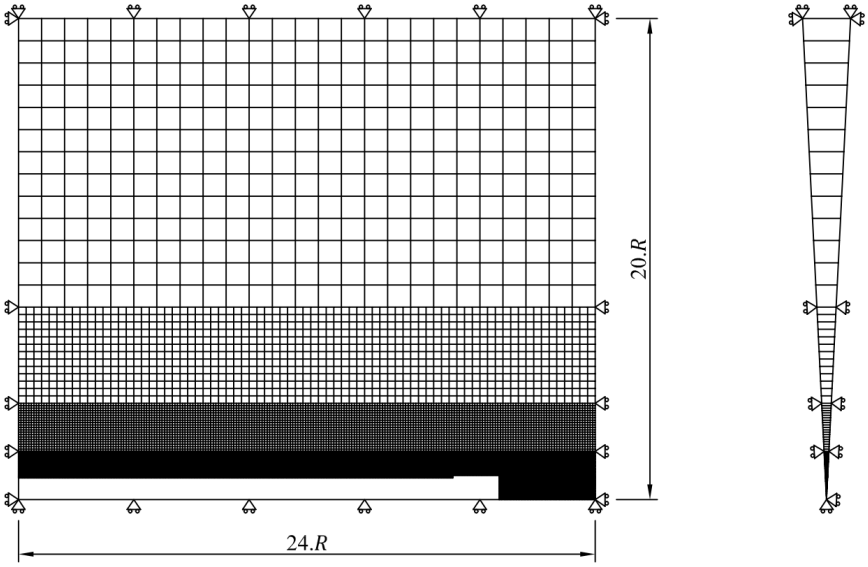

Fig. 3.1 Grid geometry. Axisymmetric model

The sequential excavation is governed by two parameters, the step round length s and the unsupported span x_f, Fig. 3.2. The step round length needs to be small enough in order to simulate a continuous excavation. Vlachopoulos and Diederichs (2009) have shown that a step of excavation below $0.4D$ is sufficient to simulate the continuous excavation of an unsupported tunnel. In the present work, the chosen value for s is $0.08D$. The distance of support installation d can be expressed as:

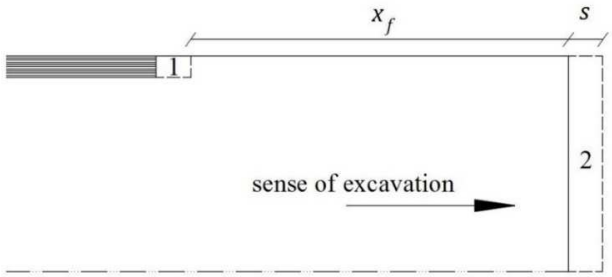

Fig. 3.2 Sequence of calculation in the step-by-step method. 1. Installation of the lining. 2. Excavation and calculation

$$d = x_f + \frac{s}{2} \tag{3.1}$$

3.2.2 Plane-strain reference model

The studied plane-strain methods are summarized in Tab. 3.1. The Classical method and the implicit method of Nguyen-Minh & Guo are studied in combination with the expressions of the LDP of

Panet (1995) and Vlachopulous and Diererichs (2009). The comparison with the method of Bernaud and Rousset is also carried out.

Tab. 3.1 Plane-strain approach: Combination of different LDP curves for various CV-CF methods for the comparison with 3D numerical results

Classical CV-CF Method - LDP Panet (1995)
Classical CV-CF Method - LDP Vlachopoulos and Diederichs (V & D) (2009)
Guo and Minh Method (G & M) - LDP Panet (1995)
Guo and Minh Method (G & M) - LDP Vlachopoulos and Diederichs (V & D) (2009)
Bernaud and Rousset Method (B & R) (1992) – LDP Panet and Guénot (P & G) (1983)

3.2.3 Sensitivity analysis

Dimensionless variables and parameters are used in order to perform a sensitivity analysis. They are noted with the superscript (.)*.

$$\sigma_{max}{}^{*} = \frac{\sigma_{max}}{\sigma_0} \tag{3.2}$$

$$\bar{u}(\infty)^{*} = \frac{\bar{u}(\infty)\ 2G}{\sigma_0 R} \tag{3.3}$$

$$d^{*} = \frac{d}{2R} \tag{3.4}$$

$$R^{*} = \frac{R}{e} \tag{3.5}$$

$$E^{*} = \frac{E}{E_l} \tag{3.6}$$

The validation of the normalization is shown in Fig 3.3, Fig. 3.4 and Fig. 3.5. The equilibrium points obtained in the various numerical simulations fall into a single curve once the normalization is applied. The range of ground and lining properties is summarized in Tab. 3.2.

Tab. 3.2 Range of values for the parameters

Parameter	Values
υ	0.25
υ_l	0.2
d^*	1
R^*	10, 12.5 and 15
E^*	0.05, 0.25, 0.5, 0.75 and 1
ϕ	20°, 25°, 30° and 35°
ψ	0°, ϕ/3 and ϕ
N	1, 2 and 5

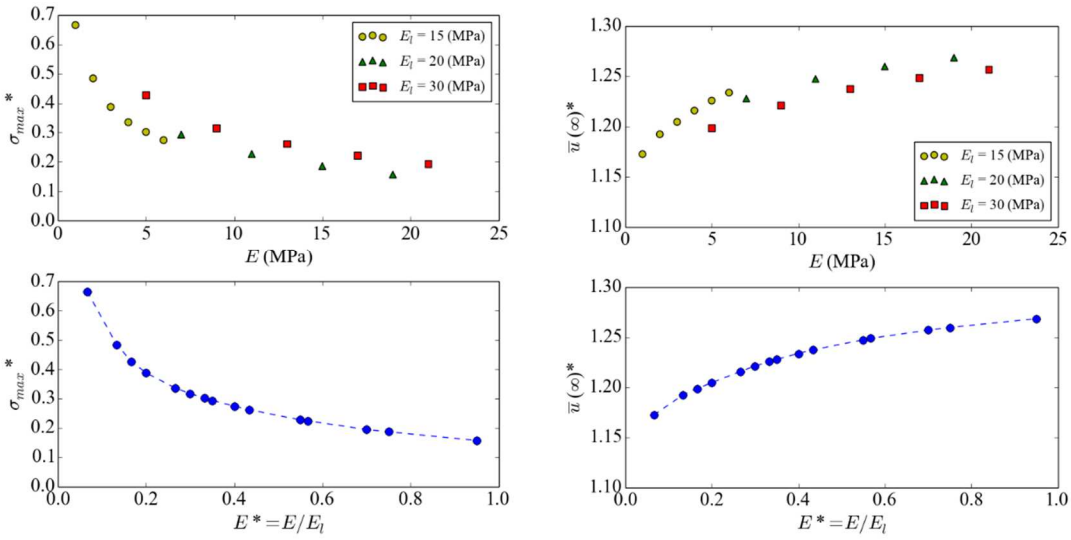

Fig. 3.3 Results of the numerical calculations regarding the normalization. $\sigma_{max}{}^*$and $\bar{u}(\infty)^*$ as a function of E^*

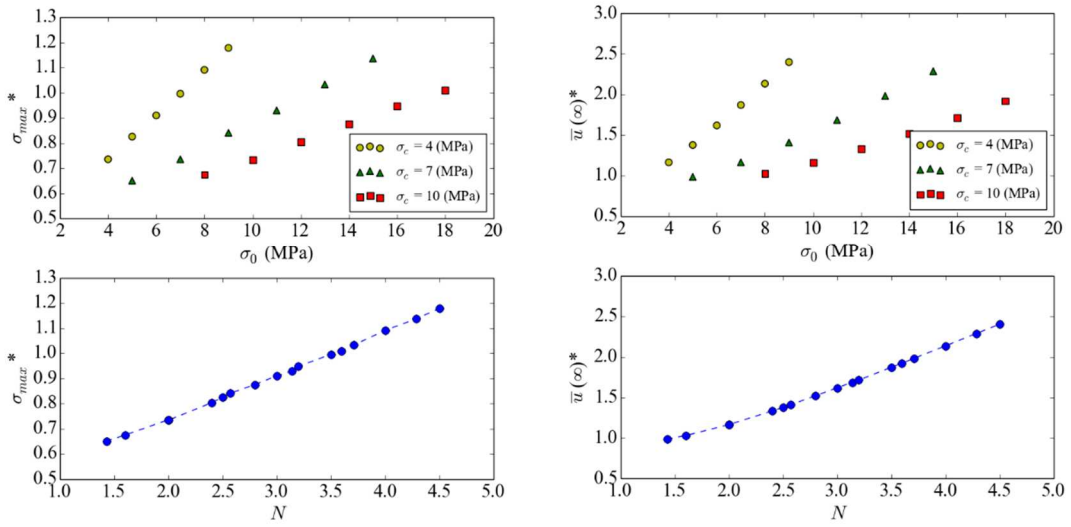

Fig. 3.4 Results of the numerical calculations regarding the normalization. $\sigma_{max}{}^*$ and $\bar{u}(\infty)^*$as a function of N

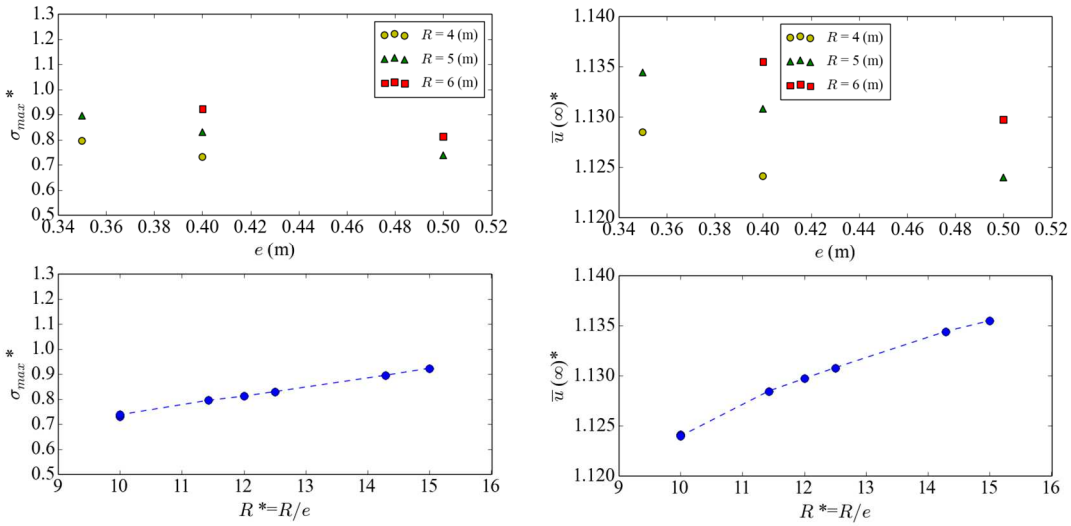

Fig. 3.5 Results of the numerical calculations regarding the normalization. $\sigma_{max}{}^{*}$ and $\bar{u}(\infty)^{*}$ as a function of R^{*}

The Poisson's ratio of the ground is kept constant and equal to $\upsilon = 0.25$. The Poisson's ratio of the lining is also kept constant and equal to $\upsilon_l = 0.2$. Within single shield TBM excavation, the first contact between the ground and the lining takes place between one and two diameters after the advancing face. A trade-off was carried out in order to reduce the number of calculations by fixing the value of the parameter d^{*} to 1. This assumption is on the safe side for the evaluation of the stresses in the lining.

In practice, the most common thickness for a segmental lining is 0.4 m and the radius length generally varies between 4 and 6 m for current metro, railway or road tunnels. It leads us to the choice R^{*} = 10, 12.5 and 15. To cover the range of relative stiffness between ground and lining, the study is carried out for E^{*} = 0.05, 0.25, 0.5, 0.75 and 1. The chosen values for the friction angle ϕ are 20°, 25°, 30° and 35°. We have assumed three different dilatancy angle ranging from zero dilatancy to associate plasticity depending on the friction angle: ψ = 0°, $\phi/3$ and ϕ. Finally, the calculations are performed for some representative values of N: 1, 2 and 5.

3.2.4 Results and discussion

The equilibrium states obtained from 540 axisymmetric simulations resulting from the combination of the different parameters are compared with the CV-CF approaches considered herein. In order to provide a large sensitivity analysis, parameters N and E^{*} have been varied independently. Note that, in practice, the ratio E/σ_c varies between 200 and 1000. Nevertheless, for values of N between 1 and 5, realistic values of E^{*} are covered in the proposed study.

In the present study, the maximal hoop stress obtained from the axisymmetric numerical models is compared with the one obtained from the plane-strain closed-form solutions. Fig. 3.6, Fig. 3.7 and Fig. 3.8 show the comparison between the CV-CF approaches and the results of the axisymmetric simulations in terms of $\sigma_{max}{}^{*}$ for a representative set of values. The total set of results for $\sigma_{max}{}^{*}$ is given in Appendix B.

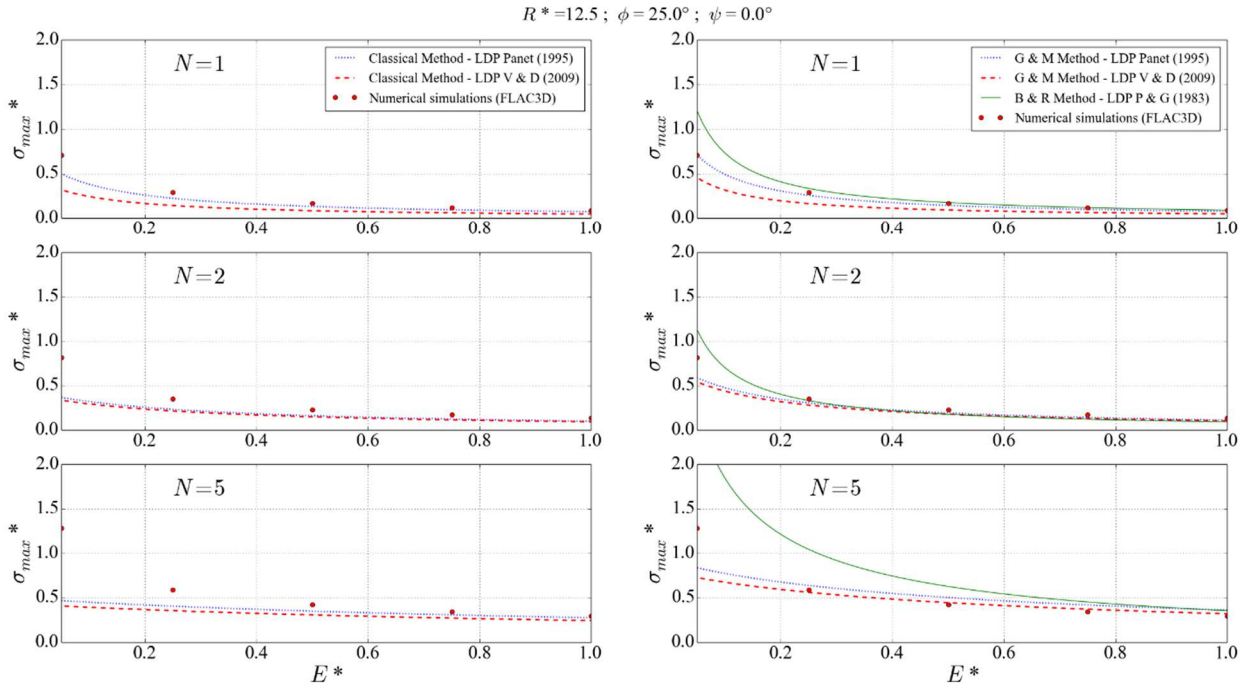

Fig. 3.6 Comparison of $\sigma_{max}{}^{*}$ between the different approaches when R^{*}=12.5 and ϕ=25° for incompressible plasticity (ψ = 0). Classical methods on the left column and implicit methods on the right column

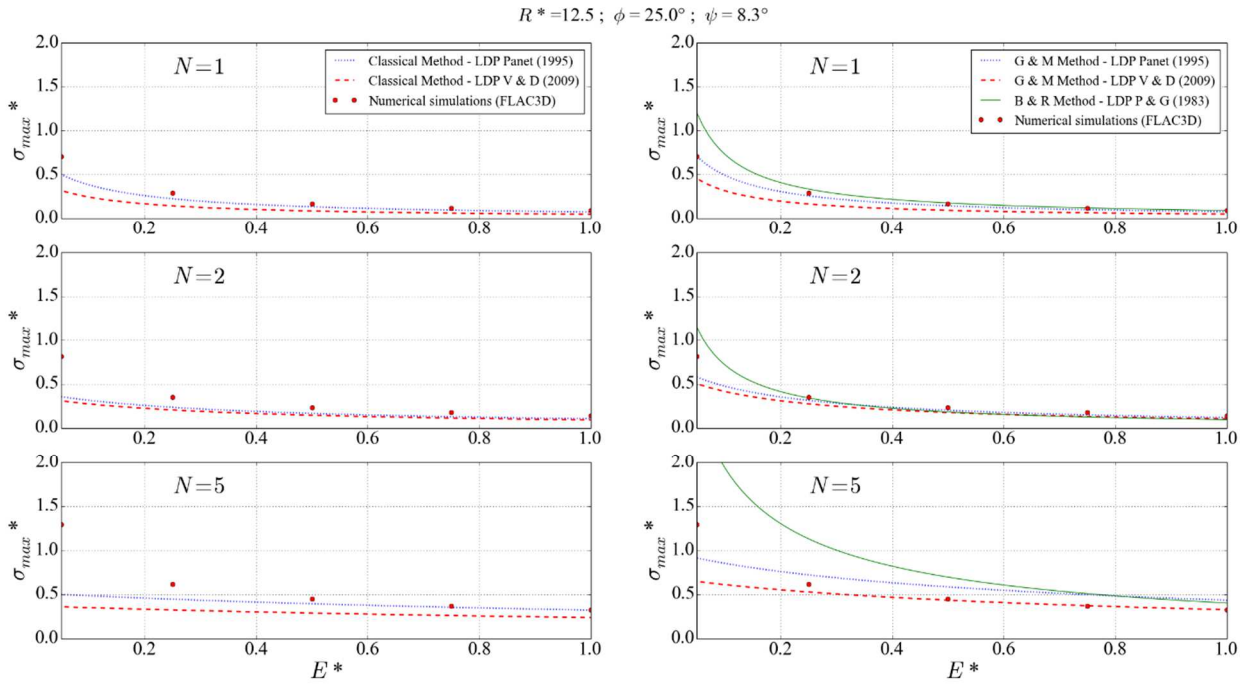

Fig. 3.7 Comparison of $\sigma_{max}{}^{*}$ between the different approaches when R^{*}=12.5 and ϕ=25° for non-associate plasticity (ψ = ϕ/3). Classical methods on the left column and implicit methods on the right

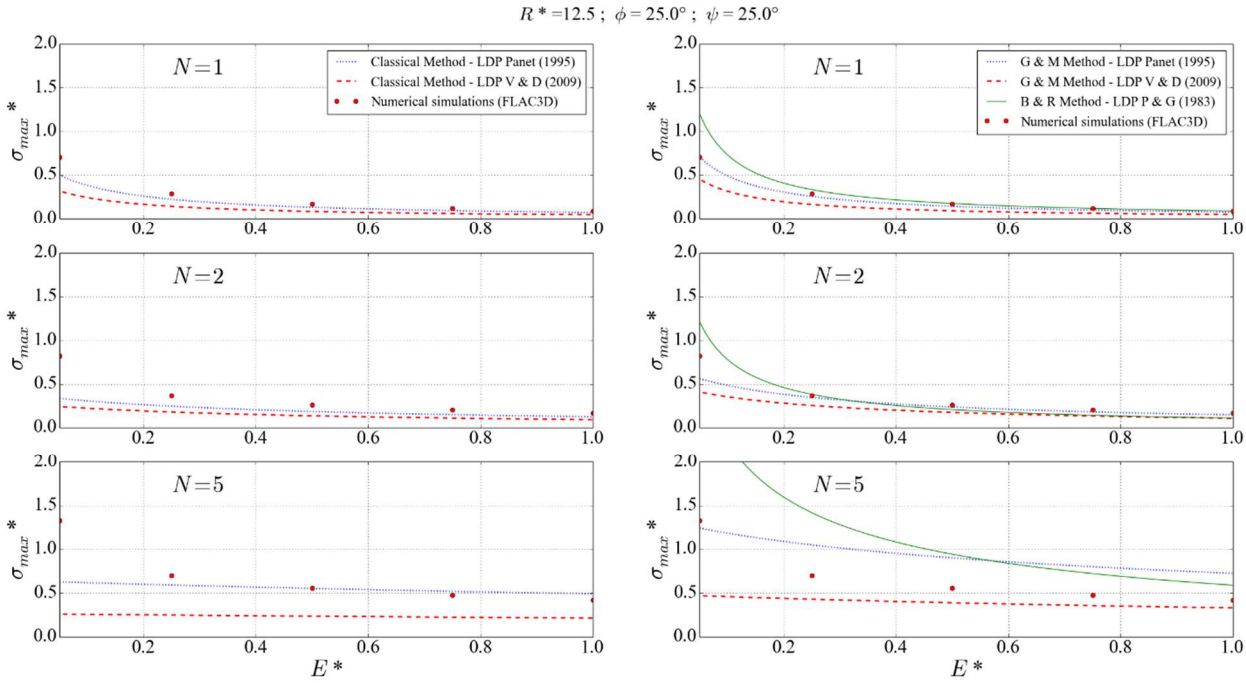

Fig. 3.8 Comparison of $\sigma_{max}{}^{*}$ between the different approaches when R^{*}=12.5 and ϕ=25° for associate plasticity (ψ = ϕ). Classical methods on the left column and implicit methods on the right column

It can be inferred that the classical approach in combination with any LDP tends to underestimate the stress state in the lining. When a value of N varying from 1 to 5 is adopted, a good agreement

between the numerical simulations and the implicit method of Nguyen-Minh & Guo combined with any LDP is observed. The implicit method of Bernaud and Rousset shows also similar results. However, when the ground is rather soft ($E^* < 0.25$), due attention should be paid even though values assigned to E^* fall within the applicability domain given by the authors. In this case, the implicit methods cannot be accurately applied as the GRC is significantly modified and the implicit methods do not take this modification into account. Finally, errors tend to increase with increasing dilatancy angle.

Regarding $\bar{u}(\infty)^*$ a good agreement is observed between the numerical simulations and the solution of Nguyen-Minh & Guo when it is combined with the LDP of Panet if N varies from 1 to 5, Fig 3.9. However, for associate plasticity and N = 5 Nguyen-Minh & Guo method combined with the LDP of Panet underestimates $\bar{u}(\infty)^*$, Fig. 3.10 This is also the case for the implicit method of Bernaud and Rousset. The solution of Nguyen-Minh & Guo combined with the LDP of Vlachopoulos & Diederichs provides a good result for any value of N and E^* and gives the best estimate of $\bar{u}(\infty)^*$, (Fig. 3.9 and Fig. 3.10). Note that errors tend to increase with increasing dilatancy angle. The total set of results for $\bar{u}(\infty)^*$ can be found in Appendix C.

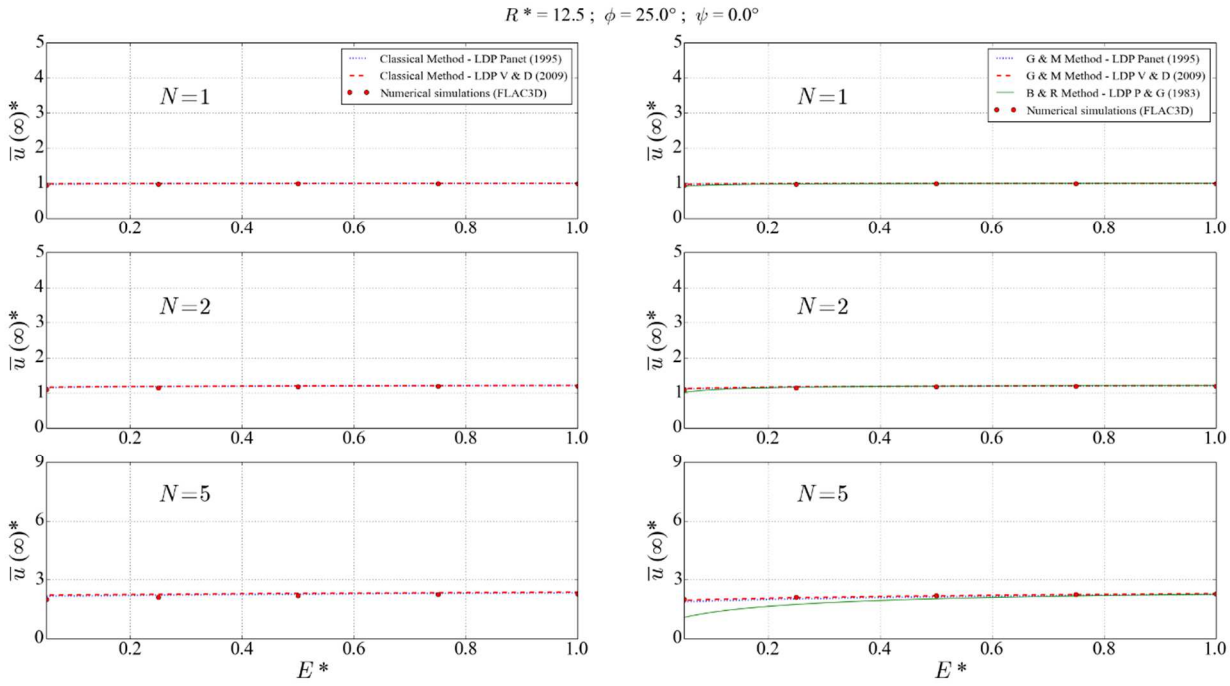

Fig. 3.9 Comparison of $\bar{u}(\infty)^*$ between the different approaches when R^*=12.5 and ϕ=25° for incompressible plasticity (ψ = 0). Classical methods on the left column and implicit methods on the right column

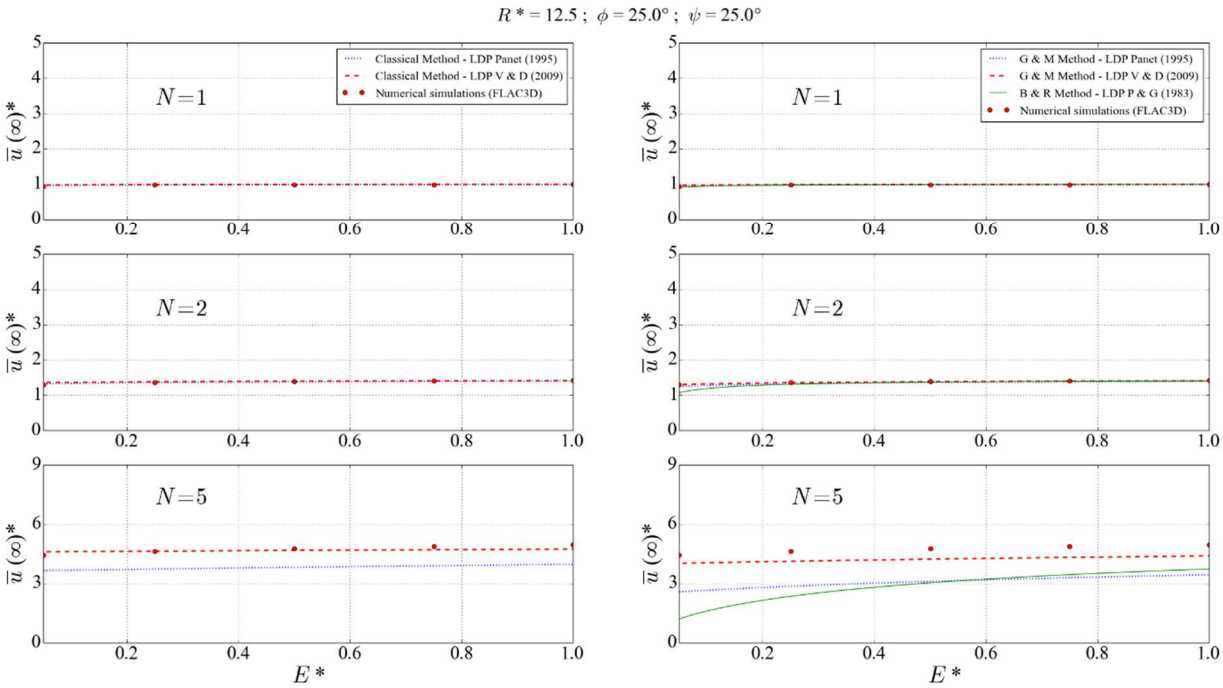

Fig. 3.10 Comparison of $\bar{u}(\infty)^*$ between the different approaches when R^*=12.5 and ϕ=25° for associate plasticity (ψ = ϕ). Classical methods on the left column and implicit methods on the right column

The effect of the dilatancy of the ground is further highlighted by considering an unlined tunnel. The difference between the axisymmetric numerical computations $(.)_{axy}$ and the plane-strain analytical results $(.)_{ps}$ are plotted in Fig.3.11 in terms of $((u(\infty)^*{}_{axi} - u(\infty)^*{}_{ps})/u(\infty)^*{}_{ps})$. When the flow rule is strongly non-associated (values of ψ between 0 and ϕ/3), which is a case commonly encountered in practice, both approaches give very similar results for the final radial displacement. However, when assuming an associated flow rule, the discrepancy between the results is amplified for higher values of N and can reach 20 % (Fig 3.11). Fig 3.12 shows that even for N=5, the results are only slightly affected by the friction angle which confirms that the dilatancy angle is the controlling parameter.

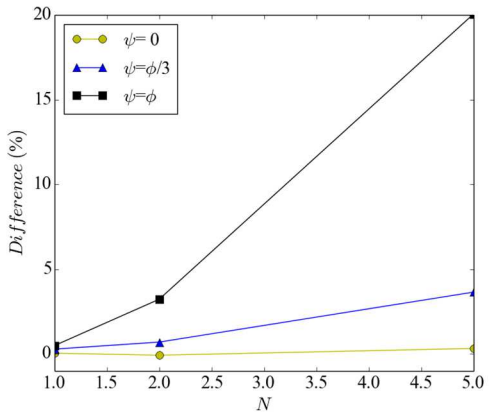

Fig. 3.11 Effect of N on the difference between the numerical simulation and the plane strain assumption (ϕ = 35° and υ = 0.25)

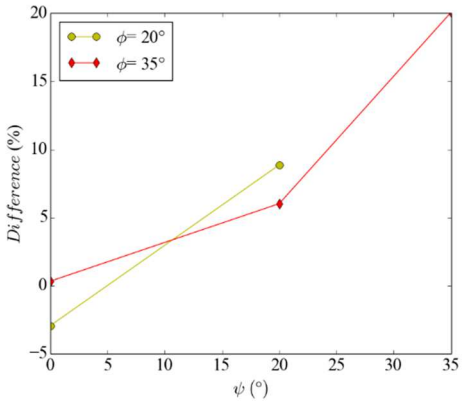

Fig. 3.12 Effect of the friction angle ϕ on the difference between the numerical simulation and the plane strain closed form solution for the radial displacement at the tunnel wall (N = 5 and υ = 0.25)

3.3 Conclusion

Due attention should be paid when applying the CV-CF methods in a pre-design stage of a circular tunnel excavated in full section with a stiff support/lining system. In this work, we have compared different CV-CF methods which are based on plane-strain assumptions with a numerical model which captures the spatial effects at the vicinity of the tunnel face.

It was shown that for reliable evaluation of the stress state at equilibrium in the lining, implicit methods (Nguyen-Minh & Guo or Bernaud & Rousset) should be used and can be combined with any LDP expression (Panet, Corbetta or Vlachopoulos & Diederichs) for values of the stability number N ranging from 1 to 5 and relatively hard rock mass ($E^* > 0.25$). The evaluation of the radial convergence of the ground is good with any CV-CF approach.

The influence of the ground dilatancy on the displacement around the tunnel is also highlighted for an unlined tunnel. It is shown that for low values of the dilatancy angle, the discrepancy between the 2D closed-form solution and the 3D numerical computations is small but tends to increase with increasing dilatancy angle.

CHAPTER 4 EMPIRICAL FORMULAS FOR THE DESIGN IN THE CASE OF SINGLE SHIELD TBM

4.1 Introduction

As an application of the previous chapter and making use of the large sensitivity analysis performed in the numerical study, some simple empirical formula which can be used in preliminary design of tunnels excavated with a single shield TBM are proposed in this chapter.

4.2 Fitting procedure

The same numerical data base used for the study of the applicability of the convergence-confinement method to tunnels excavated with single shield TBM in chapter 3 has been used herein. It consists of 540 axisymmetric simulations which cover a large range of ground and lining properties (Tab. 3.2 in chapter 3).

In order to obtain empirical formula for the design of tunnels excavated with single shielded TBM, JMP statistical software has been used (Nguyen, 2018). With JMP it is necessary to propose a linear combination of expressions based on the mechanical parameters of the problem (f (R^*, E^*, ϕ, ψ, N), $g(\ldots)$, $h(\ldots)$, …)

$$A f + B g + C h + \ldots \tag{4.1}$$

in order to obtain an expression of the equilibrium state of the tunnel excavation ($\sigma_{max}{}^*$, $\bar{u}(\infty)^*$). The software assigns values to the coefficients (A, B, C, …) of the linear combination to obtain the best fit of the formula with regards to our data base.

4.3 Expression for the maximal hoop stress in the lining at the equilibrium state ($\sigma_{max}{}^*$)

For practical applications, a set of empirical expressions is proposed to give accurate predictions of $\sigma_{max}{}^*$ within a large range of rock and support conditions. In order to cover the whole range of considered parameters, three different expressions are provided. The choice of the appropriate expression for each configuration is based on the value of a dimensionless parameter F which depends on the mechanical parameters and is given in equation 4.2 in which the friction and dilatancy angles ϕ and ψ are expressed in degrees.

$$F = 0.922 + 0.0224R^* + N\left(\frac{3.88}{\phi} + 9.66 * 10^{-4} * (\psi + 1) - 0.063\right) + 0.365\frac{E^*}{N} - 0.76\, log_{10}(100E^*) \quad (4.2)$$

For F <0.4, $\sigma_{max}{}^*$ is given by equation 4.3.

$$\sigma_{max}{}^* = 0.42 + 0.004\phi + R^*\left(0.0082 - 0.0096\frac{E^*}{N}\right) - N\left(0.123 + \frac{1}{\phi}\left(0.0685N + \frac{64.57}{\phi} - 7.79\right) - 0.000174(\psi + 1)\right) + E^*\left(0.0027\frac{1}{E^{*3}} + 0.1954\frac{1}{N} + \frac{(\psi + 1)}{\phi}\left(-\frac{0.1}{N} + 0.0916\right)\right) - 0.3455\log_{10}(100E^*) \quad (4.3)$$

Figure 4.1 shows the graphical result of the regression if F <0.4, for $\sigma_{max}{}^*$ carried out with JMP.

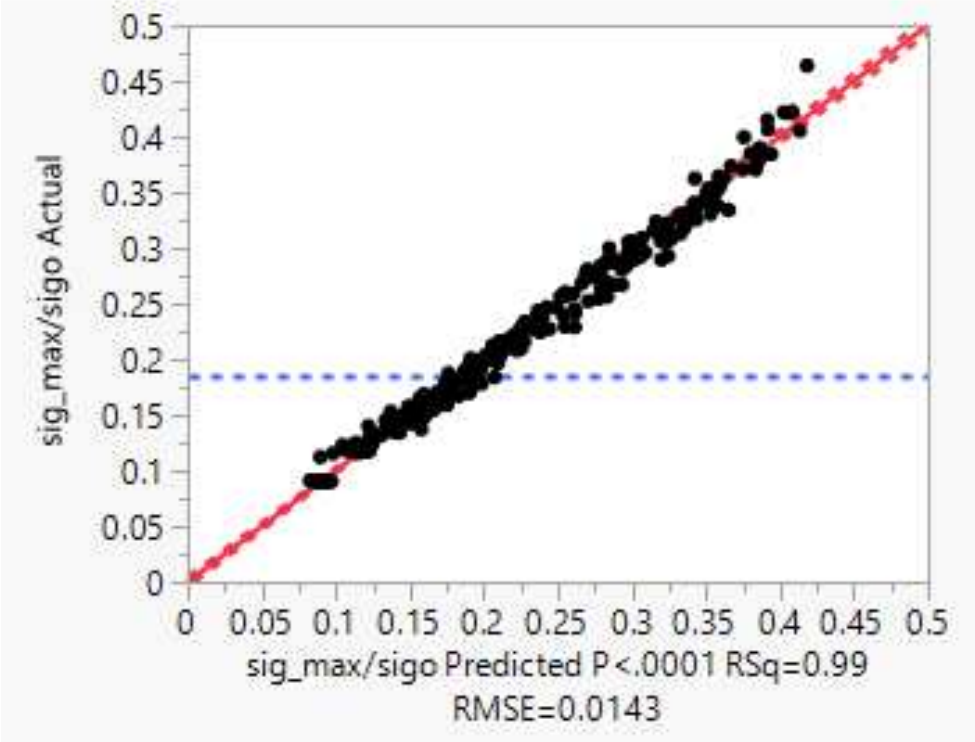

Fig. 4.1 Graphical result of the regression if F < 0.4, for $\sigma_{max}{}^*$ carried out with JMP (regression coefficient R^2 of 0.99)

For $0.4 \leq F < 0.8$, ${\sigma_{max}}^*$ is given by equation 4.4:

$$
\begin{aligned}
{\sigma_{max}}^* = {} & 1.1149 + 0.0227R^* + \psi(0.0038 - 0.0001\psi) + 0.04\frac{1}{(\psi+1)^2} \\
& - N\left(0.0879 + \frac{0.00826}{E^*} - 0.000148\frac{N}{E^{*2}} + 0.158\frac{N}{\phi} + \frac{41.785}{\phi^2} + \frac{4.06}{E^*.\phi^2}\right. \\
& \left. - 0.000463(\psi+1) - \frac{8.3}{\phi}\right) \\
& + E^*\left(-\frac{0.253}{N.\phi} + \frac{0.244}{\phi}\right)(\psi+1) \\
& - 0.96\log_{10}(100E^*)
\end{aligned}
\tag{4.4}
$$

Figure 4.2 shows the graphical result of the regression for $0.4 \leq F < 0.8$, for ${\sigma_{max}}^*$ carried out with JMP.

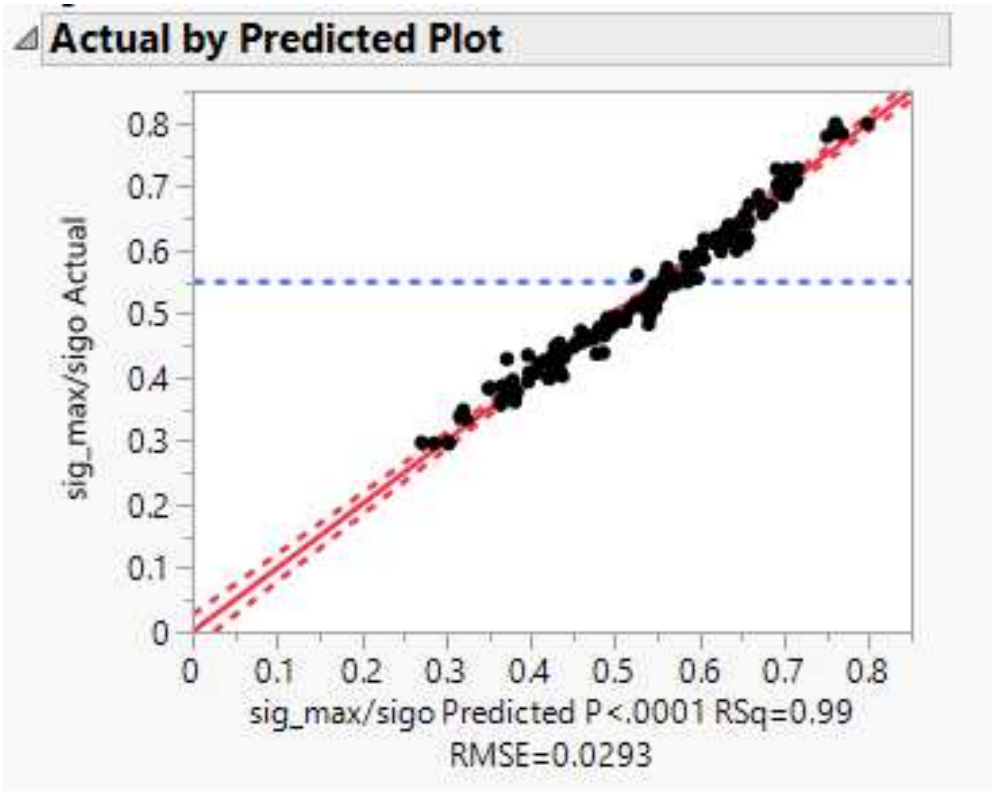

Fig. 4.2 Graphical result of the regression if $0.4 \leq F < 0.8$, for ${\sigma_{max}}^*$ carried out with JMP (regression coefficient R^2 of 0.99)

Finally, if $F \geq 0.8$,

$$\begin{aligned}\sigma_{max}{}^{*} = {} & 0.9617 - 0.0143\phi + 0.0458R^{*} - 194.85\frac{1}{\phi^2} + 0.0647\frac{1}{(\psi+1)^2} \\ & + N\left(-0.06\frac{N}{\phi} + \frac{69.55}{\phi^2} - 0.0000357(\psi+1)^2 + 0.00192(\psi+1) + \frac{0.095}{E^{*}.\phi} - \frac{1.303}{E^{*}.\phi^2}\right) \\ & + E^{*}\left(-0.202E^{*} + 0.000267\frac{1}{E^{*3}} + 0.478\frac{(\psi+1)}{\phi}\right) \\ & - 0.675\,log_{10}(100E^{*})\end{aligned} \tag{4.5}$$

Figure 4.3 shows the graphical result of the regression for $F \geq 0.8$ carried out with JMP.

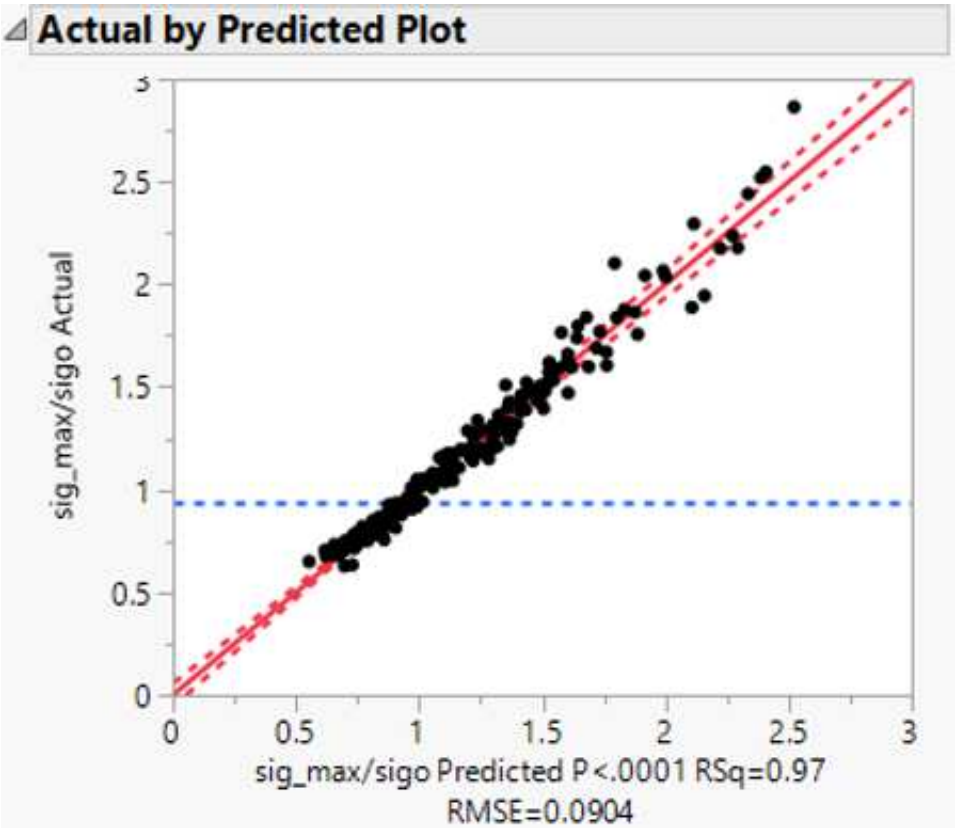

Fig. 4.3 Graphical result of the regression if $F \geq 0.8$ for $\sigma_{max}{}^{*}$carried out with JMP (regression coefficient R^2 of 0.97)

Fig. 4.4, Fig. 4.5 and Fig. 4.6 show the comparison between the empirical formula and the results of the numerical simulations in terms of $\sigma_{max}{}^{*}$ for a representative set of values. The fit is very good. The total set of results is given in Appendix B.

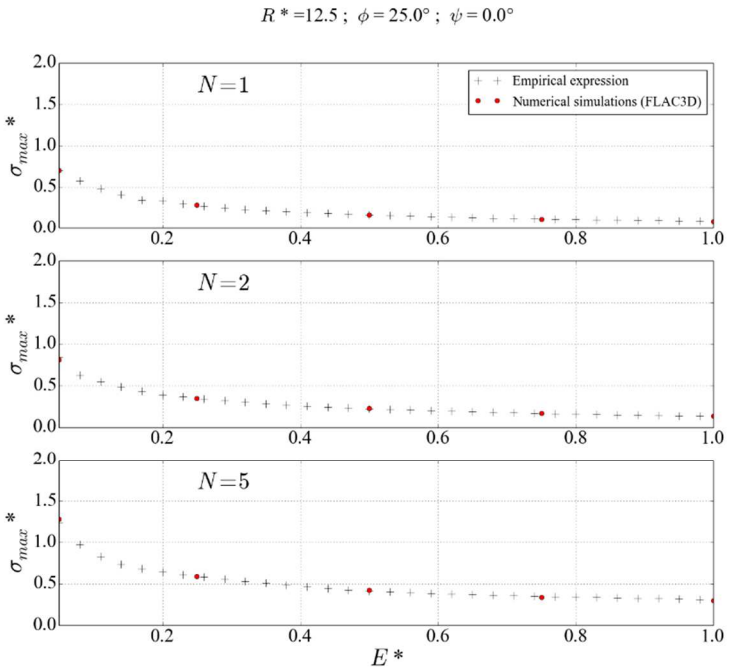

Fig. 4.4 Comparison of $\sigma_{max}{}^{*}$ between the numerical simulations and the empirical formula when R^{*}=12.5 and ϕ=25° for incompressible plasticity (ψ = 0)

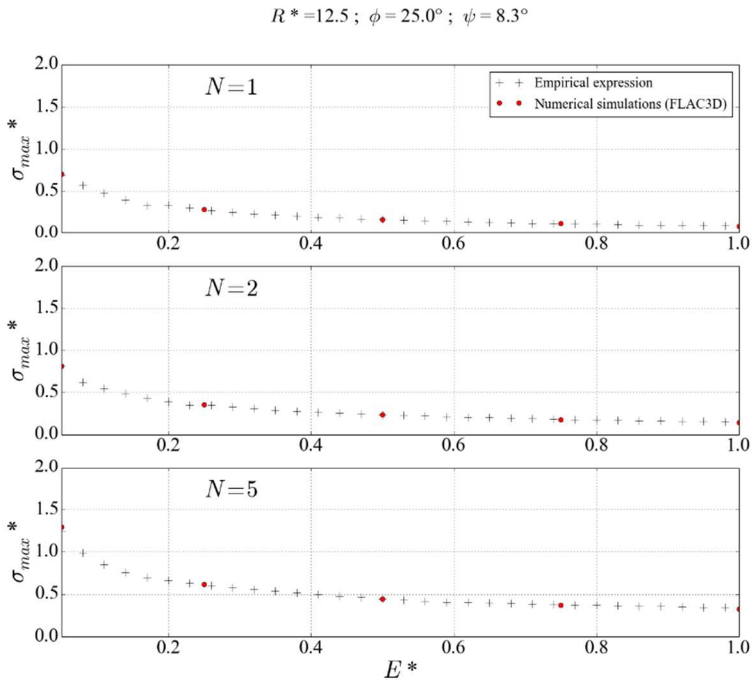

Fig. 4.5 Comparison of $\sigma_{max}{}^{*}$ between the numerical simulations and the empirical formula when R^{*}=12.5 and ϕ=25° for non-associate plasticity (ψ = ϕ/3)

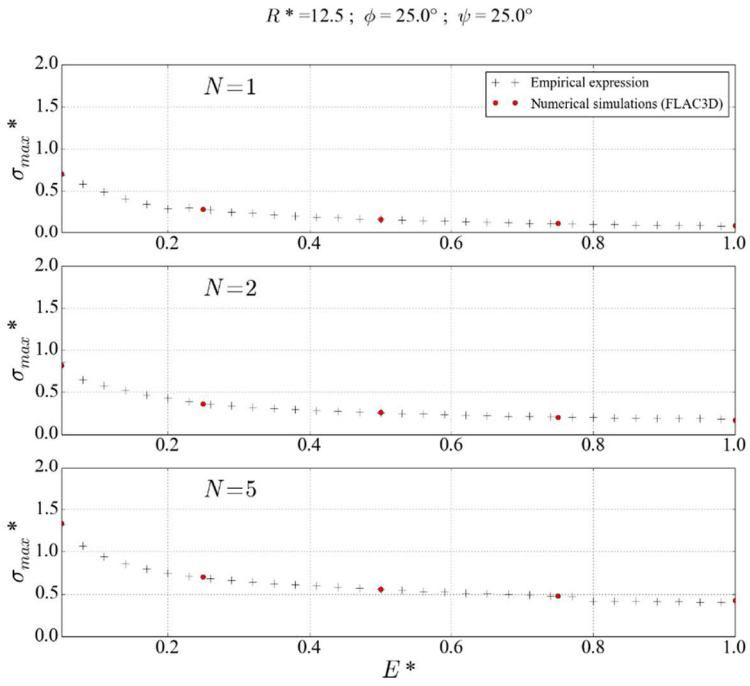

Fig. 4.6 Comparison of $\sigma_{max}{}^{*}$ between the numerical simulations and the empirical formula when R^{*}=12.5 and ϕ=25° for associate plasticity (ψ = ϕ)

4.4 Expression for the radial displacement at the tunnel wall at the equilibrium state ($\bar{u}(\infty)^{*}$)

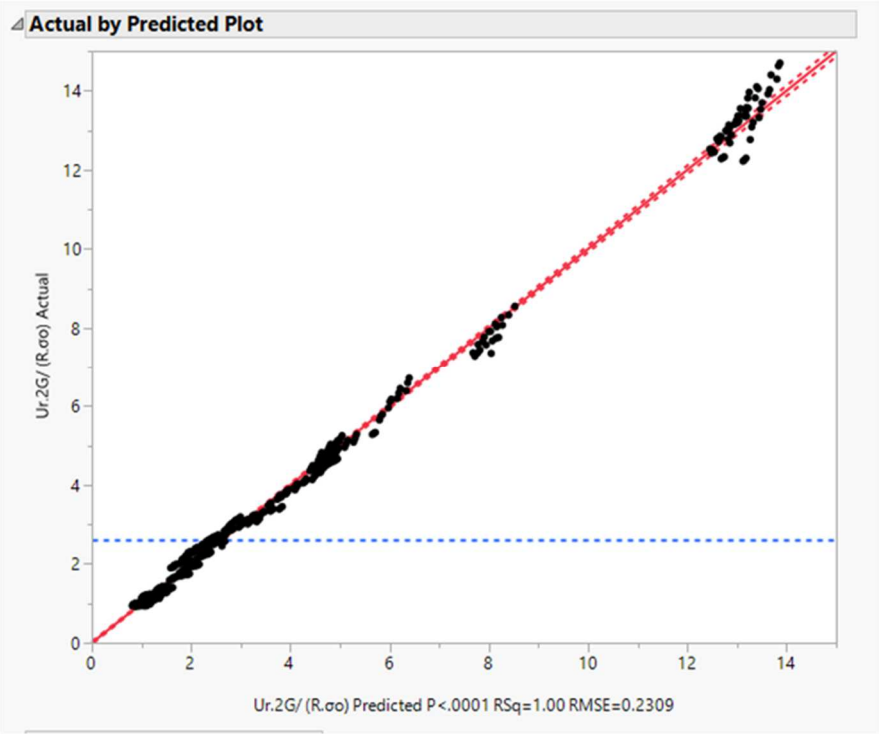

Fig. 4.7 Graphical result of the regression for $\bar{u}(\infty)^{*}$ carried out with JMP (regression coefficient R^2 of 0.99)

Following the same procedure, a unique expression is proposed for $\bar{u}(\infty)^*$:

$$\bar{u}(\infty)^* = 1.6244 + 0.012R^* + \phi\left(1.3.10^{-5}\phi^2 - \frac{0.027}{N}\right) + N.\left(0.0178E^* + 0.01855(\psi+1) + \frac{0.543}{\psi+1} - 0.017\phi + \frac{5}{\phi} - \frac{21.99}{\phi(\psi+1)} + \frac{4.076N}{\phi(\psi+1)} - \frac{0.24N^2}{\phi(\psi+1)}\right) + \frac{(\psi+1)}{\phi}(-0.0146N^3 + 0.323N^2 - 0.99N) \quad (4.6)$$

Figure 4.7 shows the graphical result of the regression for $\bar{u}(\infty)^*$ carried out with JMP.

Regarding $\bar{u}(\infty)^*$ a very good agreement is also observed between the numerical simulations and the empirical formula (Fig. 4.8 and 4.9). The total set of results is given in Appendix C.

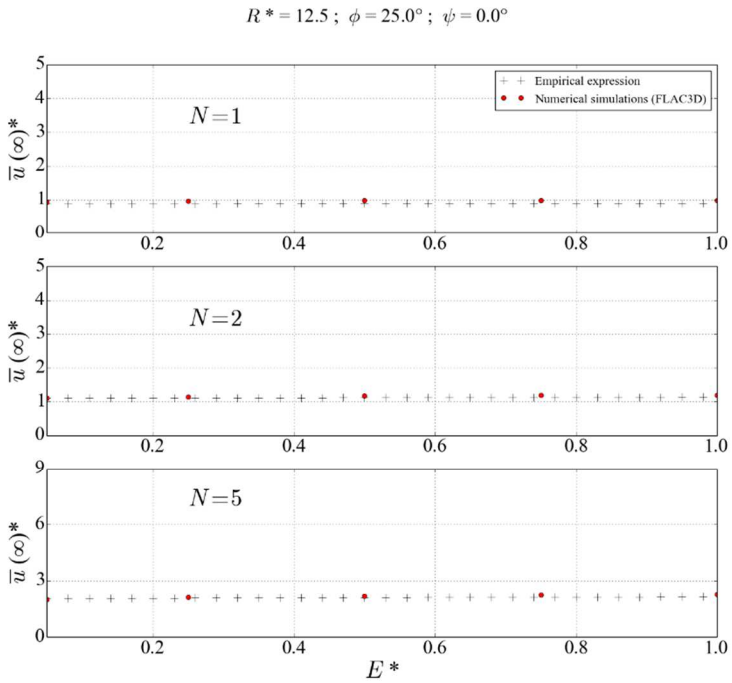

Fig. 4.8 Comparison of $\bar{u}(\infty)^*$ between the numerical simulations and the empirical formula when R^*=12.5 and ϕ=25° for incompressible plasticity (ψ = 0)

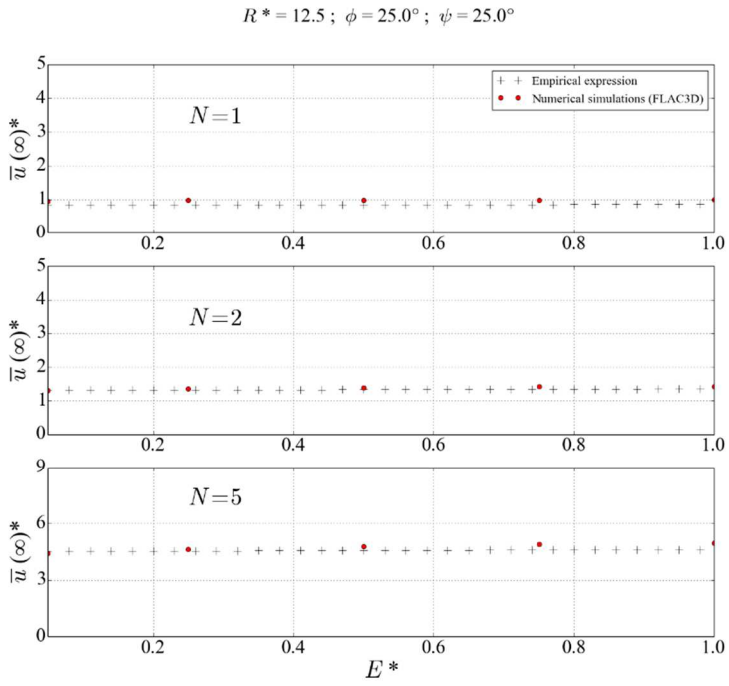

Fig. 4.9 Comparison of $\bar{u}(\infty)^*$ between the numerical simulations and the empirical formula when R^*=12.5 and ϕ=25° for associate plasticity (ψ = ϕ)

4.5 Validation of the empirical formulation

As it can be observed in Tab. 4.1, by using the proposed formulation, the point of equilibrium for arbitrary combinations of the parameters within the studied range of values can be obtained with acceptable accuracy.

Tab. 4.1 Validation of the empirical formulation

d^*	R^*	E^*	N	ϕ(°)	ψ(°)	F	$\sigma_{max}{}^*$ (FLAC3D)	$\sigma_{max}{}^*$ (Empirical formulation)	Error (%)	$\bar{u}(\infty)^*$ (FLAC 3D)	$\bar{u}(\infty)^*$ (Empirical formulation)	Error (%)
1	10	0.05	2	20	6.7	0.90	0.736	0.712	-3.3	1.165	1.325	13.7
1	10	0.05	2.5	20	6.7	0.97	0.826	0.813	-1.5	1.378	1.463	6.2
1	10	0.05	3	20	6.7	1.04	0.910	0.913	0.4	1.619	1.632	0.8
1	10	0.05	3.5	20	6.7	1.10	0.996	1.012	1.6	1.871	1.833	-2.0
1	10	0.05	4	20	6.7	1.17	1.091	1.109	1.7	2.134	2.066	-3.2
1	10	0.05	4.5	20	6.7	1.24	1.178	1.204	2.2	2.400	2.326	-3.1
1	10	0.05	1.4	20	6.7	0.83	0.651	0.594	-8.7	0.985	1.186	20.4
1	10	0.05	2	20	6.7	0.90	0.736	0.712	-3.3	1.165	1.325	13.7
1	10	0.05	2.6	20	6.7	0.98	0.841	0.828	-1.6	1.409	1.485	5.4
1	10	0.05	3.1	20	6.7	1.06	0.930	0.942	1.3	1.686	1.686	0.0
1	10	0.05	3.7	20	6.7	1.13	1.033	1.054	2.0	1.983	1.929	-2.7
1	10	0.05	4.3	20	6.7	1.21	1.136	1.163	2.4	2.288	2.211	-3.3
1	10	0.05	1.6	20	6.7	0.85	0.675	0.630	-6.7	1.029	1.228	19.3
1	10	0.05	2	20	6.7	0.90	0.734	0.712	-3.0	1.165	1.325	13.7
1	10	0.05	2.4	20	6.7	0.95	0.804	0.793	-1.3	1.333	1.433	7.5
1	10	0.05	2.8	20	6.7	1.01	0.876	0.874	-0.3	1.520	1.560	2.7
1	10	0.05	3.2	20	6.7	1.06	0.948	0.953	0.6	1.713	1.708	-0.3
1	10	0.05	3.6	20	6.7	1.12	1.009	1.031	2.2	1.921	1.877	-2.3
1	10	0.13	2	20	6.7	0.59	0.484	0.467	-3.4	1.192	1.328	11.4

1	10	0.20	2	20	6.7	0.47	0.387	0.375	-3.2	1.205	1.330	10.4
1	10	0.27	2	20	6.7	0.39	0.335	0.344	2.6	1.216	1.332	9.6
1	10	0.33	2	20	6.7	0.33	0.302	0.301	-0.2	1.226	1.335	8.9
1	10	0.40	2	20	6.7	0.28	0.274	0.271	-1.1	1.234	1.337	8.4
1	10	0.35	2	20	6.7	0.31	0.293	0.293	-0.2	1.228	1.335	8.8
1	10	0.55	2	20	6.7	0.20	0.227	0.225	-0.8	1.247	1.343	7.6
1	10	0.75	2	20	6.7	0.13	0.186	0.187	0.6	1.260	1.350	7.1
1	10	0.95	2	20	6.7	0.09	0.157	0.163	4.2	1.268	1.357	7.0
1	10	0.17	2	20	6.7	0.52	0.427	0.419	-1.8	1.199	1.329	10.9
1	10	0.30	2	20	6.7	0.35	0.316	0.321	1.4	1.221	1.334	9.2
1	10	0.43	2	20	6.7	0.26	0.262	0.258	-1.2	1.237	1.338	8.2
1	10	0.57	2	20	6.7	0.19	0.223	0.221	-1.1	1.249	1.343	7.6
1	10	0.70	2	20	6.7	0.15	0.194	0.195	0.5	1.257	1.348	7.2
1	11.43	0.05	2	20	6.7	0.93	0.795	0.777	-2.2	1.128	1.342	18.9
1	14.29	0.05	2	20	6.7	1.00	0.830	0.908	9.5	1.134	1.376	21.3
1	12	0.05	2	20	6.7	0.95	0.812	0.804	-1.0	1.130	1.349	19.4

4.6 Conclusion

A set of empirical formula have been proposed that can easily provide reliable predictions of the equilibrium state in tunnels excavated with a single shield TBM for a large range of ground and lining properties. The predicted displacements can be obtained with an accuracy of about 20% and the stresses in the lining with an accuracy of 10%.

Part III: CASE STUDY (THE FREJUS ROAD TUNNEL AND ITS SAFETY GALLERY)

CHAPTER 5 THE FRÉJUS ROAD TUNNEL

In this chapter, the Fréjus road tunnel is studied as an example of tunnel excavated in squeezing ground showing a time-dependent and anisotropic behavior. The general and geological contexts as well as the excavation method are first presented. Monitoring and data processing are then thoroughly presented so as to serve as a reference for the simulations in chapter 7.

5.1 Project introduction and general context

The Fréjus road tunnel was excavated by conventional drill and blast method in the seventies and came into service on July, 12th 1980. A new path between North-West Europe and the Mediterranean was opened. The tunnel links Modane (France) and Bardonnechia (Italy) under the ridge between the pic of Fréjus (3019 m) and the pic of Grand-Vallon in the Alps, following an average North-South direction. The design and construction of the tunnel were on behalf of a two-state company named *Société française du tunnel routier du Fréjus* (SFTRF) for the French part and *Società italiana per il Traforo Autostradale del Frejus* (SITAF) for the Italian part. The geological and geotechnical context is described in the papers of Beau et al. (1980) and Lévy et al. (1981) (see also Sulem (2013)).

The tunnel is 12.87 km long and 11.6 m wide between the sidewalls with a two-lane classical horse shoe section. The overburden along most of the layout is over 1000 m (with a maximum of 1800 m). The Italian tunnel portal is at an altitude of 1297 m whereas the French tunnel portal is at an altitude of 1228 m. The tunnel slopes down 0.54% from Italy towards France. There exist two ventilation shafts placed at 1/3 and 2/3 of the tunnel and six ventilation plants.

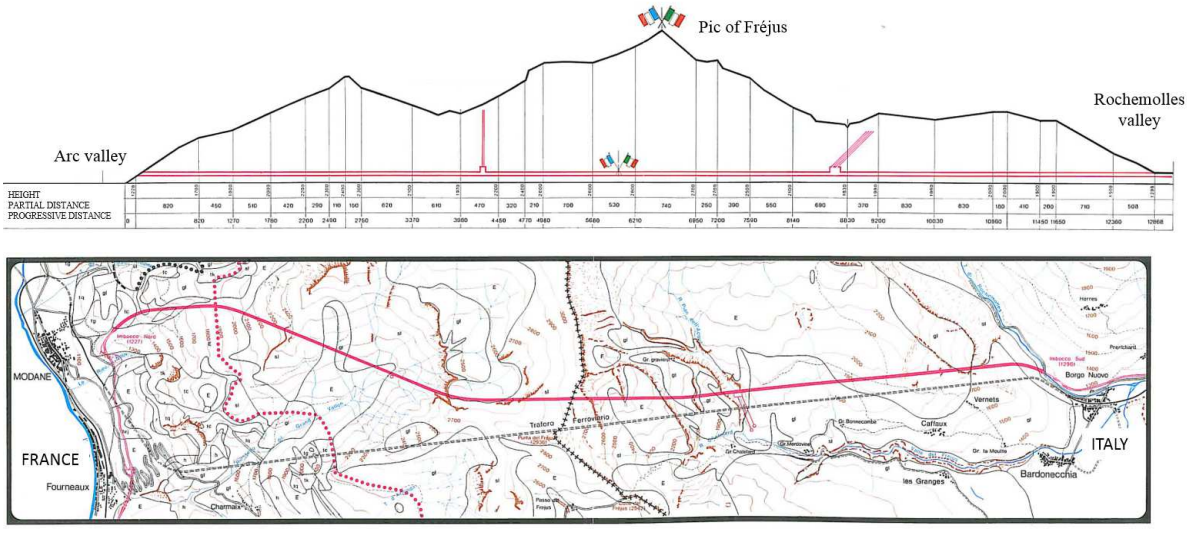

Fig. 5.1 Track alignment in red (bottom) and longitudinal profile (top) of the road tunnel after SITAF (1982) [the railway tunnel is shown by the discontinuous grey line]

The average advancing rate was 5.6 m/day. Fig. 5.1 Shows the longitudinal profile and the track alignment of the tunnel.

5.2 Geological context

The road tunnel goes through a ground where three main tecto-stratigraphic alpine units can be identified:

- The Briançonnaise unit (chainage 0 to chainage 1710): from the French portal, this zone is characterized by the succession of different aged facies: quartzite (early Triassic), quartzitic schists (Permian-Triassic) and fractured black calcareous schists (middle Triassic). The quartzitic schists have a foliated to massive texture showing a pale green color and enter in contact with the black calcareous schists between chainage 1448 and chainage 1480. The black calcareous schists are highly fractured and localized buckling had to be tackled.
- Gypsum unit: This formation separates the Briançonnaise area and the Piémontaise unit. At the origins, evaporitique rocks (Triassic) were injected during the formations of The Alps between the main tectostratigraphic unities acting as a “tectonic lubricant”. This lithotype appears also in the French tunnel portal. It is a highly tectonized unit.
- The Piémontaise unit (from chainage 1720): This area represents the largest stretch of the tunnel (Fig. 5.2) and is characterized by a sequence of well foliated calcareous schists (lustrous schists). The calcschists result from a light metamorphism of marls and limy marls with the formation of phyllitous minerals (Panet, 1996).

Tab. 5.1 Average mineralogy in the Piémontaise unit

Calcite	65 %
Quartz	15 %
Muscovite and Chlorite	10 %
(Albite, Pyrite, Zoïsite, Epidote and Graphite)	-
Phyllites	-

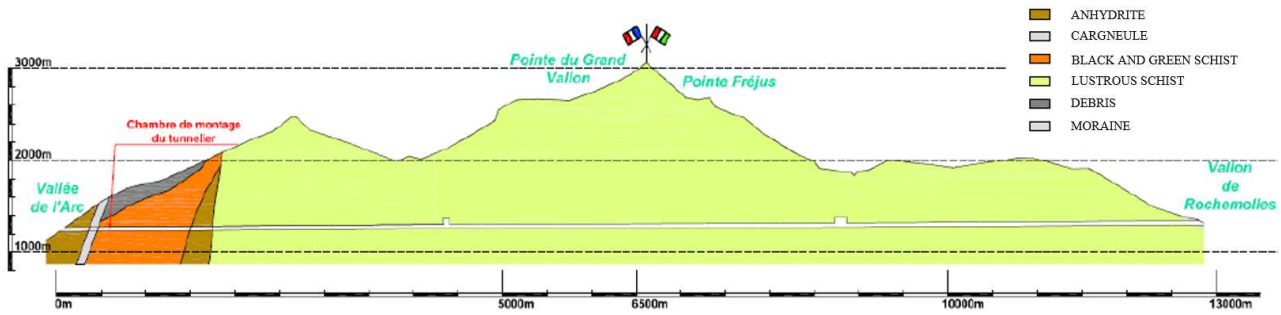

Fig. 5.2 Geological profile of the alignment

In the peculiar Piémontaise unit, the schistosity is oriented parallel to the tunnel axis with an average dip angle of 45°. The average mineralogy in the Piémontaise unit is shown in Tab. 5.1. Four families of discontinuities were identified during the excavation (Fig. 5.3):

- Regional schistosity. Dip angle varying from 25° to 70° towards the West. (25°-70°/N270°-N315°).
- Joints following the direction East-West. Dip angle 45° towards the North (joints perpendicular to the tunnel axis, 45°/N360°).
- Shear fractures following the direction East-West. Dip angle 45° towards the South (45°/N180°)
- Joints which are sub-parallel to the tunnel axe (North-South) and characterized by sub-vertical plans slightly inclined towards the East (50°-70°/N90°).
- The water amount is very low and well localized.

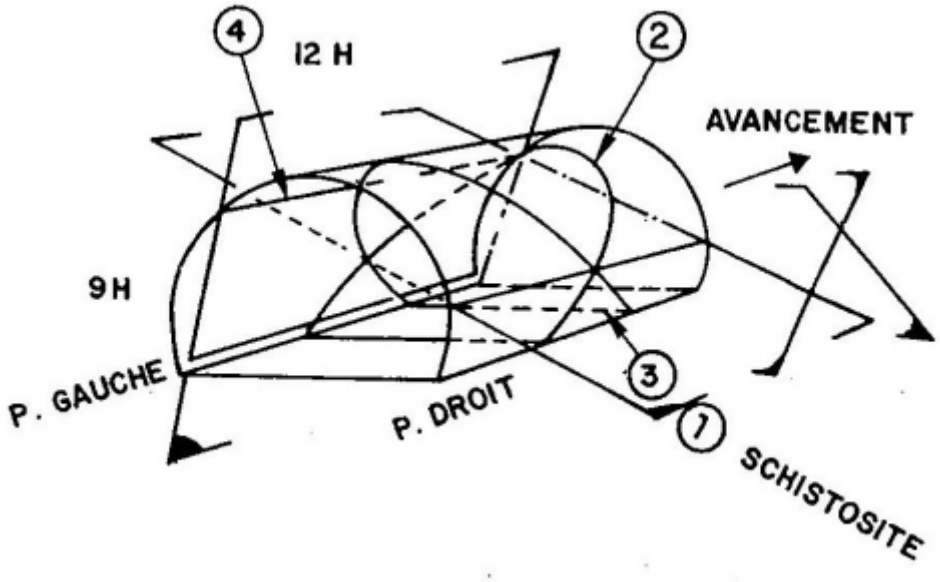

Fig. 5.3 Main families of discontinuities in the Fréjus road tunnel after Beau et al. (1980)

5.3 Excavation and support techniques

The works were carried out over a total length of 12,500 m according to the following steps (Levy et al., 1981):

- Excavation (horse shoe section with installation of rockbolts and a wire grid)
- Execution of the invert (execution at 300 to 400 m from the tunnel face)
- Concreting operations of the final lining (execution at 600 m from the tunnel face)
- Execution of the ventilation ducts (execution at 750 m from the tunnel face)
- Injections and execution of the final tasks (1 100 to 1 250 m from the tunnel face)

The full-cross section was excavated in one step by drilling and blasting. The average length of the excavation step was between 3.50 and 4.50 m (Panet, 1996).

A soft support was installed before the final lining. The tunnel was supported with radial rockbolts before the final lining was installed at a distance of 600 m from the face of excavation. It consisted of an average amount of 21 punctually anchored rockbolts per linear meter of 4.65 m of length. Rockbolts have a diameter of 20 mm and a strength of 450 MPa (Fig. 5.4). A wire grid (10 cm x 10 cm Φ 5 mm) was also installed to avoid rock debris falling down (Fig. 5.5).

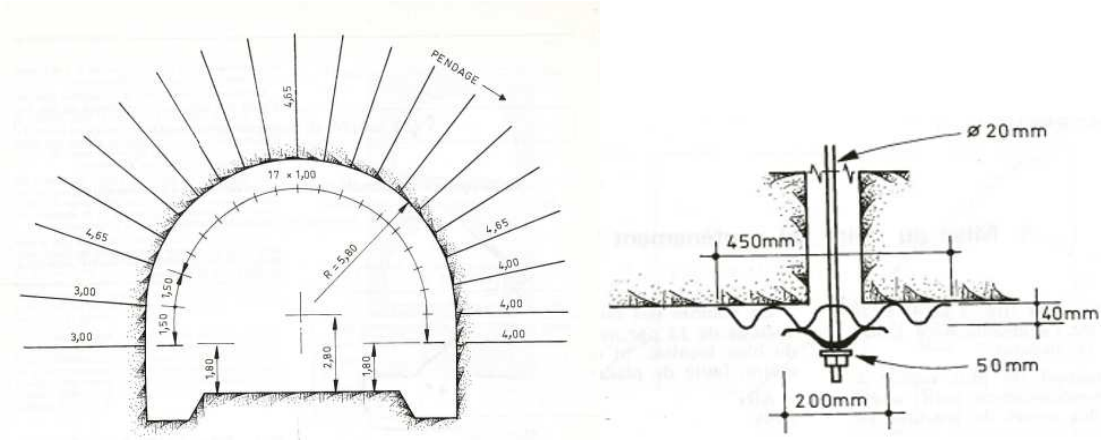

(a) **(b)**

Fig. 5.4 Cross section with the boltsing pattern **(a)** and longitudinal-section of the bolts **(b)** after Levy et al., (1981)

Fig. 5.5 Front face of the Fréjus road tunnel showing the support composed of rockbolts and a wire grid. Presence of schistosity planes at the tunnel face after SITAF (1982)

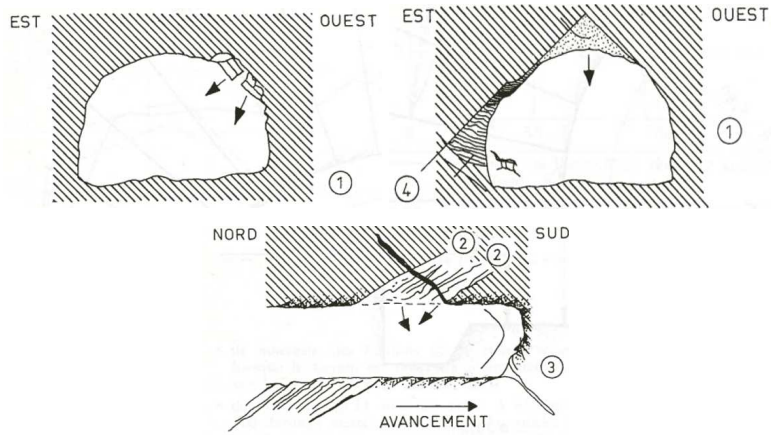

(a) **(b)** **(c)**

Fig. 5.6 Some instabilities related to the massif discontinuities after Levy et al., (1981)

A buckling phenomenon of the schistosity planes is observed at the West part of the vault where schistosity planes are tangent to the tunnel wall (Fig. 5.6 (a)). The presence of several families of discontinuities can favor the formation of isolated blocks which can fall down during the excavation (Fig. 5.6 (b) and (c)).

The execution of the final lining was carried out at an average distance of 600 m from the tunnel face.

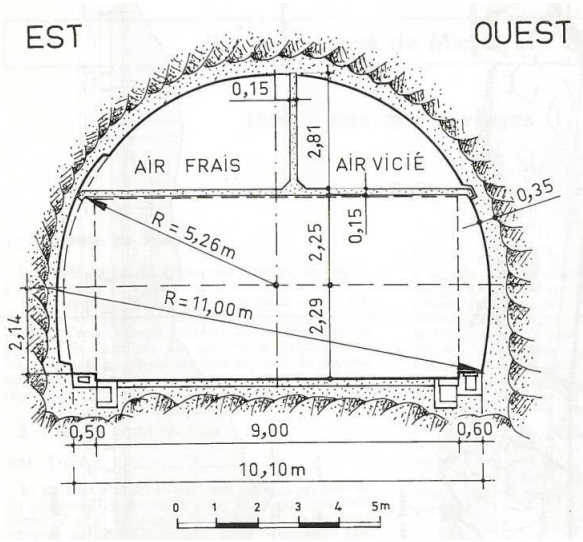

Fig. 5.7 Typical cross section of Fréjus tunnel once the final lining is completed after Levy et al., (1981)

5.4 Monitoring data and data processing

Convergence measurements were monitored in 127 sections along the tunnel. Convergences are the variations of distance between two opposite points of the tunnel wall. Monitored sections are spaced 30 m apart in average. Measurements are carried out by using invar type alloy wire until the

installation of the final lining which occurred around 107 days after the face excavation of the section. At that moment the average rate of convergence is 0.2 mm/day.

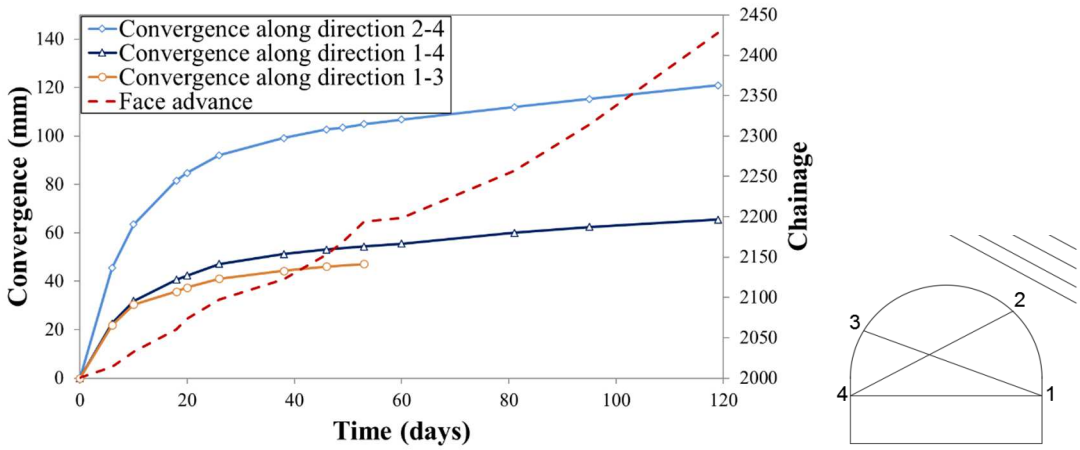

Fig. 5.8 Convergence curves and schematic position of the targets in section 13 (chainage 1998)

Fig. 5.8 shows a typical convergence curve. The largest convergence generally occurs along the direction defined by targets 2 and 4 which is quasi perpendicular to the schistosity planes. This large convergence is attributed to the buckling of the schistosity planes. Convergence along direction defined by targets 1 and 4 is parallel to the tunnel invert. In some of the sections, convergence along direction 1-3 was also monitored. However, convergence data following this direction have been recorded over a shorter period of time. Fig. 5.9, Fig. 5.10 and Fig. 5.11 show convergence data along the different directions between chainage 1872 and 2772 corresponding to zone A as defined later in Fig 5.14.

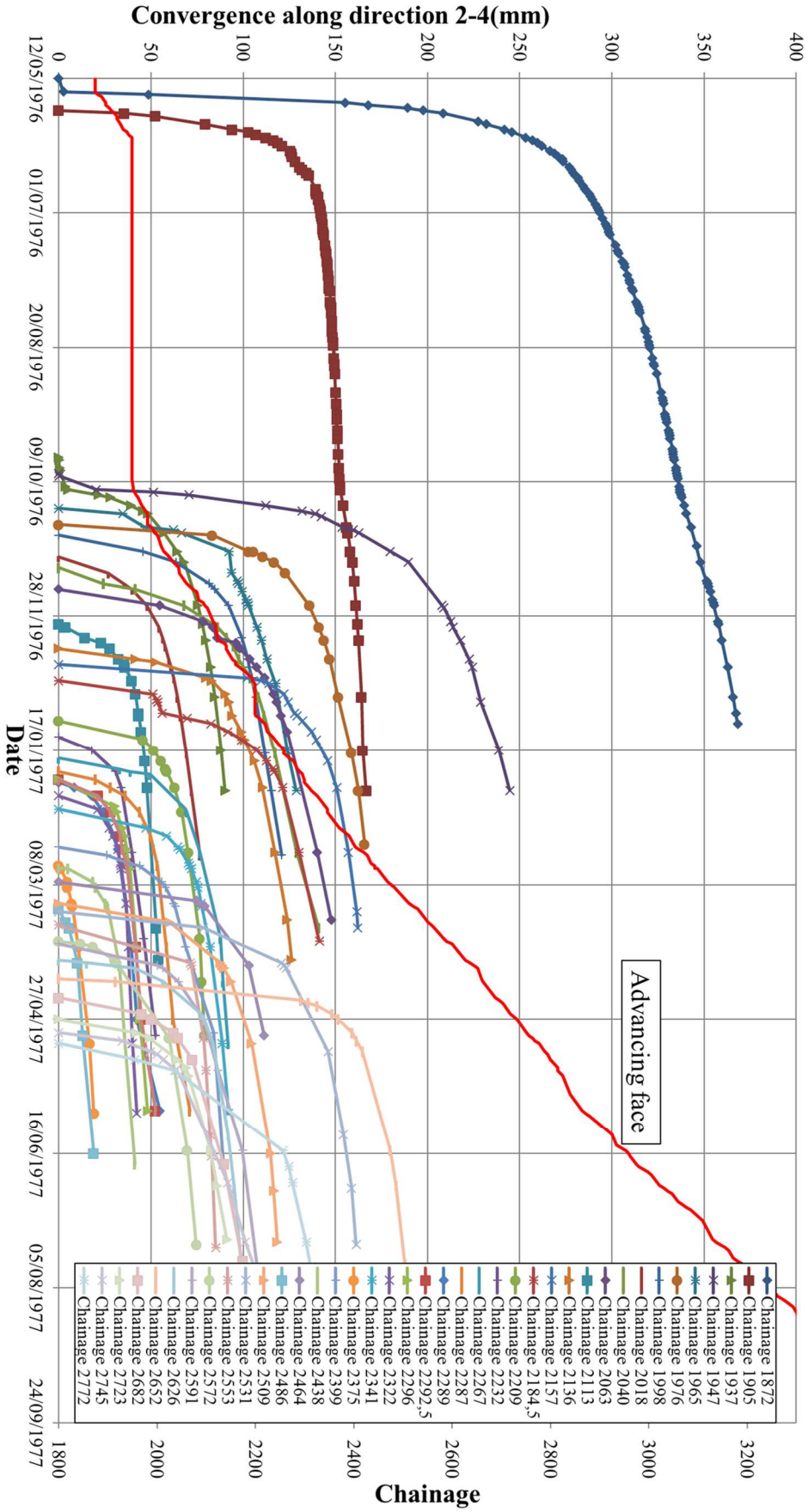

Fig. 5.9 Convergences along direction 2-4 between chainage 1872 and 2772

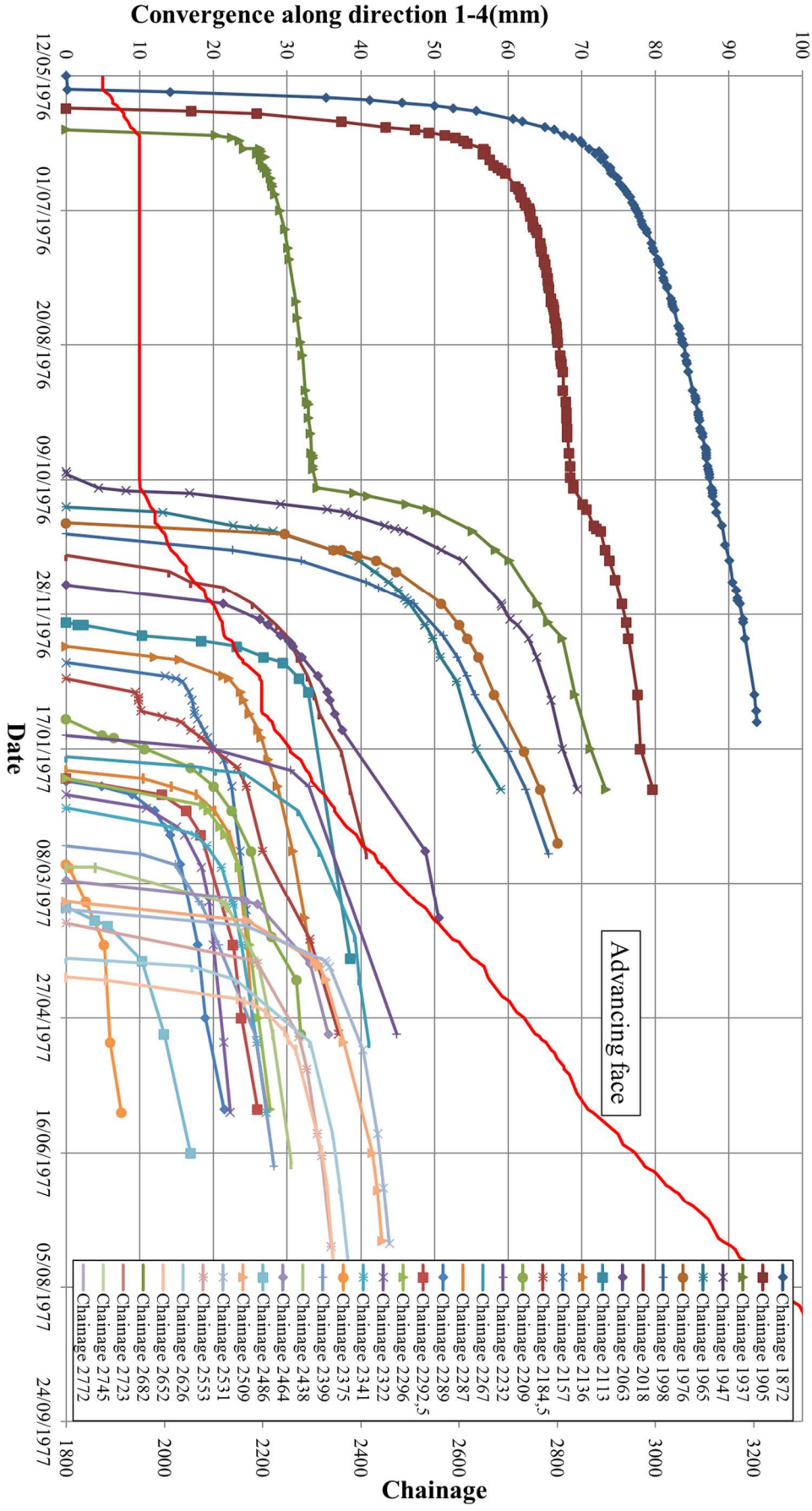

Fig. 5.10 Convergences along direction 1-4 between chainage 1872 and 2772

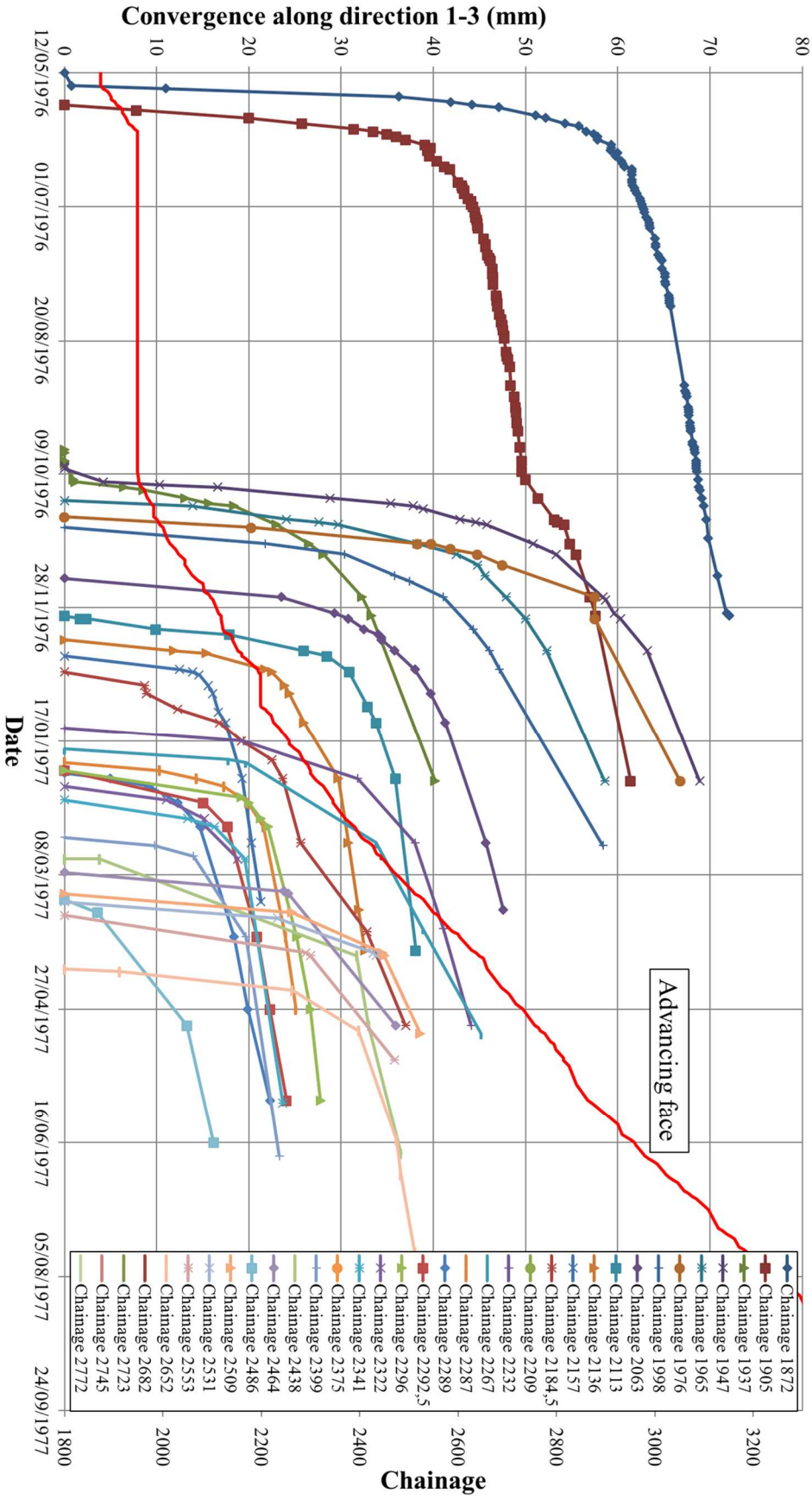

Fig. 5.11 Convergences along direction 1-3 between chainage 1872 and 2772

Convergence data show the differed behavior of the ground and the influence of the advancing face. Section in chainage 1905 illustrates the time-dependent behavior of the ground. This section is affected by two standstills: the first one takes place at chainage 1949 and lasts 127 days and the second one takes place at chainage 2198.5 and lasts 12 days. We can observe how the ground keeps on converging even though the face is not advancing. The convergences which take place during the standstills are only associated to the differed behavior of the ground. Furthermore, we can observe an acceleration of the convergences of section in chainage 1905 when a resumption of the excavation takes place after the standstill in chainage 1949. This indicates that the distance of influence of the advancing face is larger than 44 m because the convergence at chainage 1905 are still slightly influenced.

The semi-empirical law proposed by Sulem et al. (1987b), (equation 5.1) has been used in the analysis of convergence data of the road tunnel (De la Fuente et al., 2017).

$$C(x,t) = C_{\infty x}\left[1 - \left(\frac{X}{x+X}\right)^2\right]\left\{1 + m\left[1 - \left(\frac{T}{t+T}\right)^n\right]\right\} \tag{5.1}$$

where $C_{\infty x}$ represents the instantaneous convergence obtained in the case of an infinite rate of face advance (no time-dependent effect), X is a parameter related to the distance of influence of the face, T is a parameter related to the time-dependent properties of the system (rock mass – support), m is a parameter which represents the relationship between the long term total convergence and the instantaneous convergence and n is a form-factor which is often taken equal to 0.3. By fitting the convergence data, it is possible to distinguish the total long-term convergence $C_{\infty x}(1 + m)$ from the instantaneous convergence $C_{\infty x}$ which takes place in each section. In convergence data fitting it is important to account for the "lost convergence" ΔC which is the convergence which takes place between the face excavation and the beginning of convergence monitoring (at a distance from the face x_0 and at a time elapsed from the face excavation t_0):

$$\Delta C(x,t) = C(x,t) - C(x_0,t_0) \tag{5.2}$$

The study shows that parameters X, m and n can be considered the same for the fitting of almost all of the sections in the tunnel (X = 10.5 m, m = 4.5 and n = 0.3). Parameters T and $C_{\infty x}$ are fit for every single section and direction. A very good approximation of convergence data is obtained as shown in the examples in Figure 5.12.

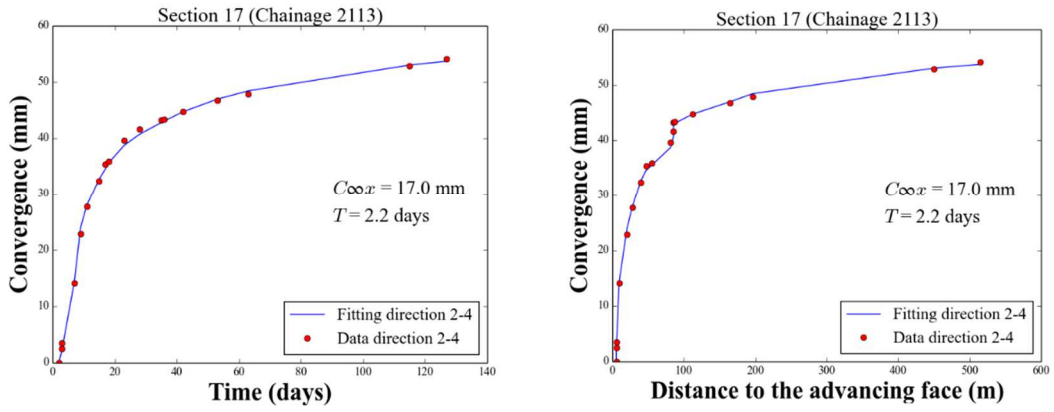

(a)

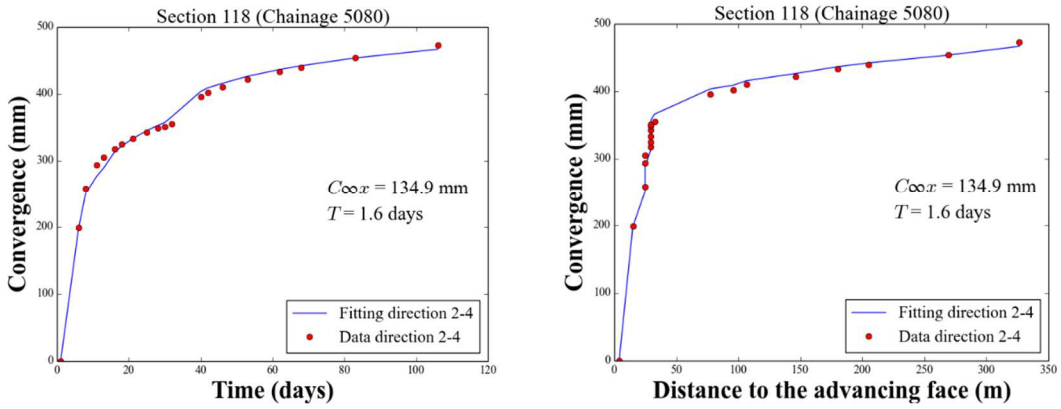

(b)

Fig. 5.12 Convergence evolution along direction 2-4 and fit with the empirical convergence law of from Sulem et al. (1987b) for section 17 at chainage 2113 **(a)** and section 118 at chainage 5080 **(b)**. On the left in function of time and on the right in function of the distance to the advancing face

The fitting results of most of the sections along the road tunnel are shown in Tab. 5.2. The results of some of the sections are not shown in Tab. 5.2 as they are studied separately (Tab. 5.3). The reason stems from the “special” behavior that they exhibit.

Tab. 5.2 Results of the fit of sections along the alignment, symbol (*) indicates that monitoring data is lacking or non-reliable

Chainage (section nb.)	**Direction 2-4**				**Direction 1-4**				**Homogeneous zone**
	T (days)	$C_{\infty x}$ (mm)	C_{lost} (mm)	$C_{\infty x}(1+m)$ (mm)	T (days)	$C_{\infty x}$ (mm)	C_{lost} (mm)	$C_{\infty x}(1+m)$ (mm)	
1814 (3)	*	*	*	*	3.8	87.0	14.5	478.6	Degraded area
1825 (4)	*	*	*	*	5.3	54.1	62.4	297.7	Degraded area
1838 (5)	*	*	*	*	2.9	22.2	3.7	122.1	Degraded area
1850 (6)	*	*	*	*	3.3	25.9	41.4	142.4	Degraded area
1872 (7)	3.8	101.1	63.0	555.9	3.4	26.2	16.9	144.0	Degraded area
1905 (8)	0.7	40.7	24.1	224.0	0.7	18.2	10.9	100.2	A
1965 (11)	2.4	46.0	59.6	252.9	2.7	20.7	26.1	113.9	A
1976 (12)	1.1	58.4	93.4	321.2	2.7	23.3	29.4	128.0	A
1998 (13)	3.9	35.3	18.1	194.0	6.6	20.4	9.5	112.1	A
2018 (14)	5.1	27.1	25.5	148.8	6.0	14.8	13.4	81.1	A
2063 (16)	3.4	52.5	62.1	288.7	2.1	13.6	14.7	75.0	A
2113 (17)	2.2	17.0	17.4	93.7	*	*	*	*	A
2136 (18)	2.0	41.0	46.2	225.3	1.6	10.7	12.8	58.6	A
2157 (19)	0.5	46.1	50.8	253.7	1.6	7.2	5.6	39.5	A
2184.5 (20)	4.2	48.4	41.3	266.2	9.4	11.3	7.8	62.1	A
2209 (21)	1.6	22.6	17.3	124.5	*	*	*	*	A
2267 (23)	3.3	26.1	10.3	143.7	1.9	11.0	5.0	60.6	A
2287 (24)	2.6	18.2	10.1	100.0	0.7	7.0	5.6	38.4	A
2289 (25)	1.7	19.0	36.5	104.3	0.7	8.9	20.9	49.1	A
2292.5 (26)	2.3	14.6	14.1	80.3	1.1	7.6	9.0	41.8	A
2296 (28)	1.8	14.1	12.7	77.8	0.9	8.1	9.1	44.6	A
2322 (29)	1.3	12.0	10.3	66.0	1.2	6.3	5.7	34.9	A
2341 (30)	1.1	30.3	41.3	166.7	1.1	8.9	12.1	48.9	A
2399 (32)	2.5	26.4	24.8	145.4	*	*	*	*	A
2438 (33)	1.9	12.5	13.3	68.8	1.1	9.7	12.1	53.4	A
2509 (36)	2.1	36.7	35.3	201.9	1.1	13.1	15.2	71.8	A
2531 (37)	2.2	45.3	26.5	249.1	1.0	11.8	8.5	65.1	A
2572 (39)	2.8	26.6	32.8	146.2	*	*	*	*	A
2626 (41)	1.1	29.8	31.7	164.0	0.9	11.6	13.1	63.8	A
2682 (43)	3.3	34.1	33.7	187.5	0.8	10.9	16.4	60.0	A
2723 (44)	1.6	30.9	37.6	169.8	0.4	11.3	20.0	62.1	A
2745 (45)	4.8	37.4	32.1	205.5	0.9	8.0	11.0	44.2	A
2927 (50)	1.8	13.7	20.4	75.2	*	*	*	*	B
2969 (52)	1.2	6.7	12.0	36.6	0.8	4.1	8.3	22.7	B
3019 (53)	1.3	9.7	10.3	53.4	*	*	*	*	B
3040 (54)	1.1	5.9	6.9	32.3	*	*	*	*	B
3070 (55)	1.3	8.5	8.9	46.6	2.5	4.7	4.2	25.8	B
3132 (57)	1.0	14.3	15.7	78.7	0.5	4.9	6.6	26.7	B
3211 (60)	1.7	22.6	23.7	124.3	0.4	5.6	8.6	30.6	B
3275 (62)	0.4	12.5	11.8	68.5	0.4	6.2	5.8	34.1	B
3479 (68)	0.7	11.1	10.7	61.2	0.3	4.9	6.3	26.8	B
3506 (69)	2.3	6.6	2.8	36.3	2.6	4.3	1.8	23.5	B
3570 (71)	3.3	5.3	4.5	29.4	6.1	4.4	3.3	24.4	B
3602 (72)	1.3	9.0	6.8	49.4	0.6	4.5	4.3	24.9	B
3632 (73)	0.5	33.5	29.9	184.2	0.5	6.8	6.0	37.1	C
3732 (76)	0.5	12.5	12.7	68.8	0.2	2.9	3.9	16.2	C
3762 (77)	1.4	15.6	9.1	85.7	0.5	6.6	5.2	36.1	C
3791 (78)	1.0	37.6	32.9	206.9	0.2	8.2	11.1	45.2	C
3829 (79)	3.5	16.0	8.4	88.2	0.6	8.6	7.4	47.2	C
3865 (80)	4.7	14.2	7.0	78.3	*	*	*	*	C
3904 (81)	1.6	6.7	5.1	36.7	*	*	*	*	C
3936 (82)	1.7	14.1	10.6	77.3	1.0	6.8	6.0	37.2	C
3970 (83)	3.9	15.3	10.1	84.1	0.4	2.8	3.6	15.7	C
4074 (86)	1.8	17.1	14.4	93.9	*	*	*	*	C
4155 (89)	0.9	37.2	27.1	204.5	*	*	*	*	C
4226 (91)	3.9	35.7	20.3	196.3	2.3	14.1	9.0	77.6	C
4263 (92)	1.0	41.3	41.8	227.1	1.7	19.4	16.6	106.9	C

4317 (94)	0.3	23.4	26.6	128.7	1.7	10.8	7.5	59.2	C
4353 (95)	1.7	26.2	19.7	144.3	3.0	12.8	8.4	70.7	C
4382 (96)	1.6	35.0	22.0	192.3	1.6	14.7	9.3	80.6	C
4408 (97)	3.3	30.1	19.2	165.6	1.6	22.0	16.9	120.9	C
4443 (98)	2.0	55.4	40.2	304.5	2.2	20.2	14.2	111.3	D
4468 (99)	1.4	56.6	32.8	311.5	1.4	15.6	9.0	85.6	D
4495 (100)	1.5	25.6	12.4	140.7	1.8	15.5	7.1	85.1	D
4530 (101)	0.6	76.9	66.6	423.0	1.3	17.7	11.8	97.1	D
4561.5 (102)	1.2	59.8	30.5	329.1	1.6	22.6	11.5	124.1	D
4625.5 (104)	0.9	48.9	36.5	268.9	0.7	23.8	19.6	131.1	D
4648.5 (105)	4.1	39.0	17.4	214.5	2.3	27.2	13.8	149.5	D
4681 (106)	1.3	56.4	38.2	310.1	2.1	30.7	18.2	169.1	D
4709.5 (107)	0.7	75.5	62.3	415.3	0.7	18.3	14.6	100.4	D
4747 (108)	1.4	43.2	19.9	237.3	1.4	19.9	9.9	109.7	D
4773 (109)	2.8	25.9	15.9	142.6	*	*	*	*	D
4815 (110)	1.4	30.0	17.5	165.2	1.0	16.2	10.4	89.1	D
4846 (111)	0.6	57.9	63.3	318.3	*	*	*	*	D
4894 (112)	4.9	52.0	22.5	286.0	4.2	42.0	18.6	230.9	D
4937 (113)	3.2	94.4	72.8	519.1	1.7	26.1	23.3	143.3	D
4974 (114)	4.0	152.0	109.4	835.9	3.1	58.5	45.2	321.9	D
5008 (115)	2.3	115.9	66.6	637.3	5.8	40.2	19.2	221.0	D
5080 (118)	1.6	134.9	103.9	741.8	*	*	*	*	D
5130 (120)	2.2	48.9	47.4	269.2	2.6	43.1	40.0	237.2	D
5163 (121)	2.1	86.4	61.5	475.0	*	*	*	*	D
5235 (123)	3.1	111.8	45.0	615.0	4.1	80.5	30.4	442.5	D
5279 (124)	1.6	73.8	57.9	405.8	6.7	69.0	36.5	379.3	D

We can observe that T which controls the convergence rate which varies between 0.5 and 5 days along direction 2-4 (Fig. 5.13).

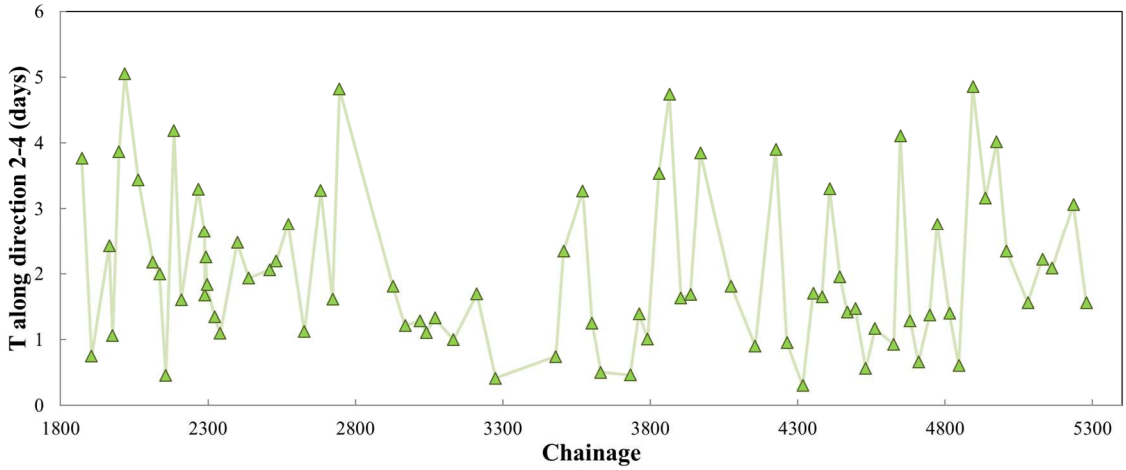

Fig. 5.13 Evolution of T along direction 2-4 along the road tunnel after De la Fuente et al., (2017)

However, some "homogeneous" zones corresponding to similar values of the instantaneous convergence along direction 2-4 have been identified, (Fig 5.14).

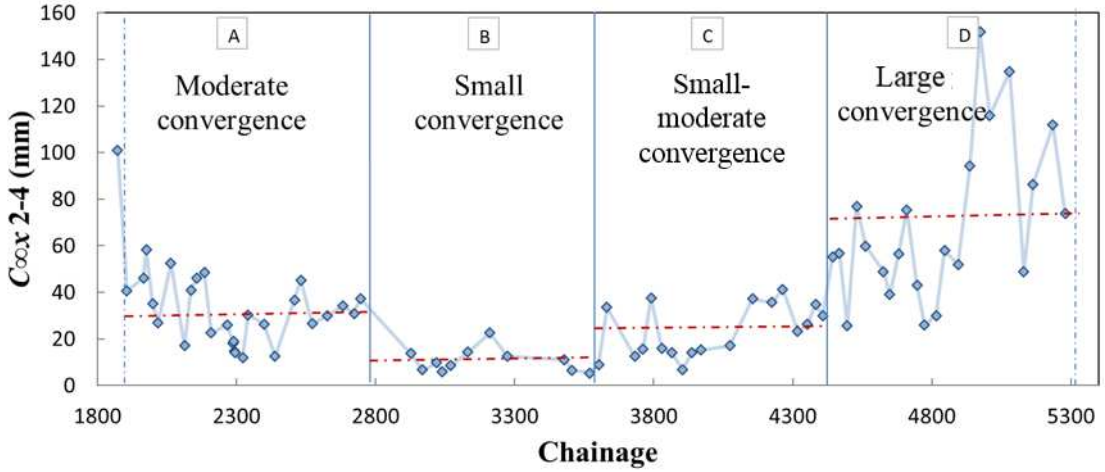

Fig. 5.14 Evolution of $C_{\infty x}$ along direction 2-4 along the road tunnel. The red dotted lines represent the average convergence value for each zone. After De la Fuente et al., (2017)

Fig. 5.15 shows the convergence along 1-4 for sections in the road tunnel. The identified "homogeneous zones" are included in the graph.

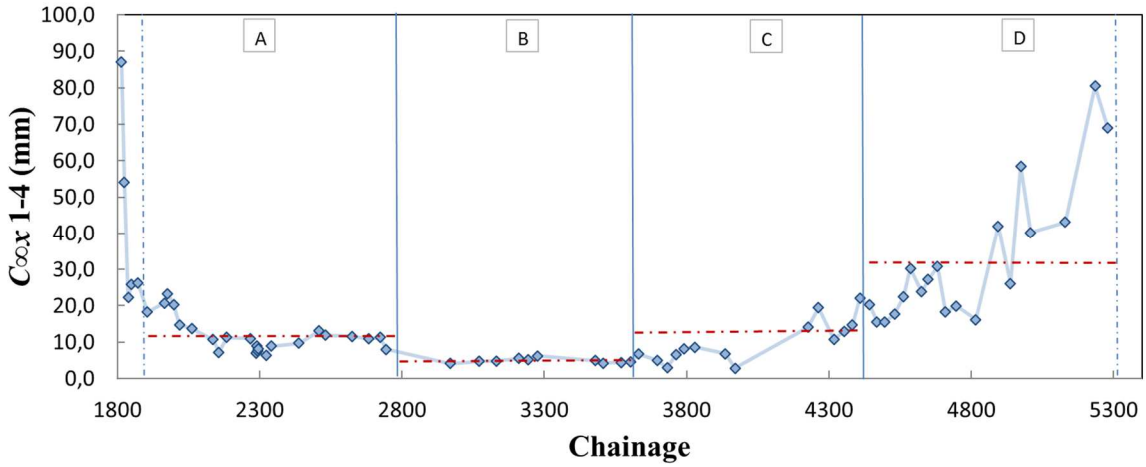

Fig. 5. 15 Evolution of $C_{\infty x}$ along direction 1-4 along the road tunnel. The red dotted lines represent the average convergence value for each zone

A significantly degraded area is identified in sections from chainage 1814 to chainage 1872 as the instantaneous convergences are significantly larger than in the rest of the alignment.

As it has been highlighted by Lunardi (1980) the largest convergences are not necessarily related to the largest overburden (Fig. 5.16). For instance, overburden in zone C is smaller than in zone B and however, convergences in zone B show a smaller amplitude. The magnitude of the convergences is not only influenced by the overburden but also by the existing sets of fractures and by the portion content of phyllosilicates (muscovite and chlorite) and graphite in the rock mass. These minerals favor the formation of schistosity planes during the metamorphism of the rock.

When the schistosity planes are well formed and are favorably oriented buckling phenomenon can be easily triggered during the excavation of the tunnel.

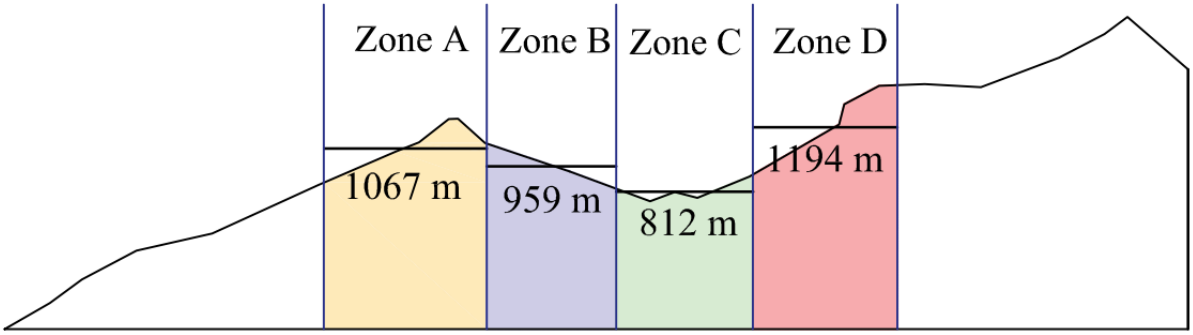

Fig. 5.16 Topographic profile for the French part along the road tunnel with the previously identified "homogeneous zones". The average overburden for each "homogeneous zones" is indicated

Figure 5.17 shows the anisotropy ratio between the instantaneous convergence along direction 2-4 and the instantaneous convergence along direction 1-4 : $\beta = C_{\infty x\,2-4}/C_{\infty x\,1-4}$ for each section along the road tunnel. The "homogeneous zones" cannot be characterized by the anisotropy ratio as this parameter varies significantly along the tunnel.

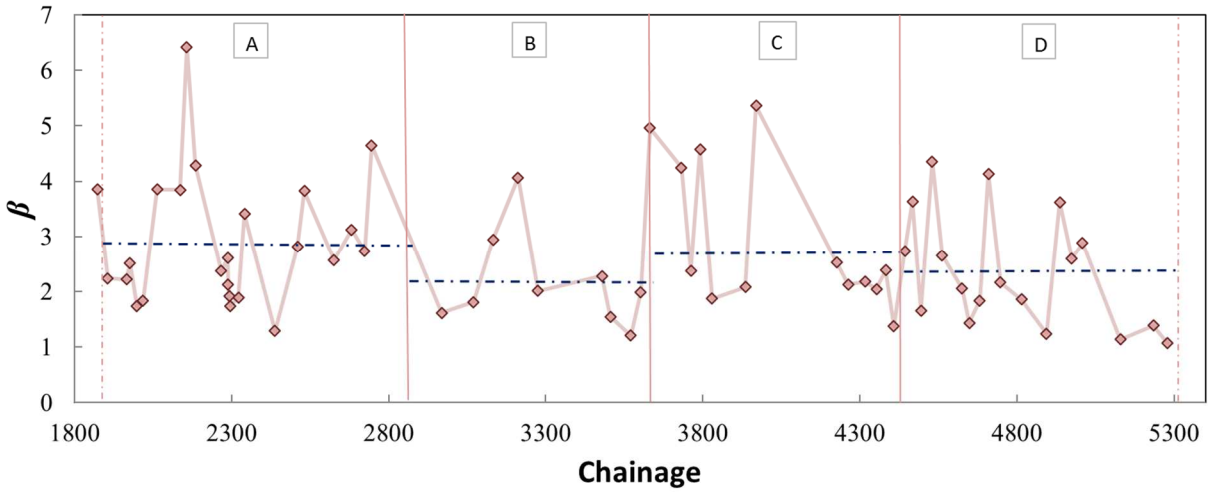

Fig. 5.17 Evolution of β along the road tunnel after De la Fuente et al., (2017)

The "special" sections are fitted by assigning values for parameter T along direction 2-4 bigger than 5 or smaller than 0.5. However, the section showing the most different response is 119 at chainage 5103.5 where a different value of X is necessary for an accurate fit (X = 30 m), Fig. 5.18. The reason of the existence of sections with a behavior that differs from the average one is not clear as we do not have more detailed geological and geotechnical data.

Tab. 5.3 Results of the fit of "special" sections along the alignment, symbol (*) indicates that monitoring data is lacking or non-reliable

Chainage (section nb.)	**Direction 2-4**				**Direction 1-4**				**"Homogeneous" zone**
	T (days)	$C_{\infty x}$ (mm)	C_{lost} (mm)	$C_{\infty x}(1+m)$ (mm)	T (days)	$C_{\infty x}$ (mm)	C_{lost} (mm)	$C_{\infty x}(1+m)$ (mm)	
2040 (15)	**10.3**	47.2	27.1	259.8	*	*	*	*	A
2591 (40)	**8.9**	32.5	6.2	178.8	*	*	*	*	A
2652 (42)	**0.1**	81.4	213.2	447.6	0.4	14.9	34.1	82.0	A
2772 (46)	**6.5**	52.9	44.7	291.1	2.4	5.9	44.7	32.3	A
3243 (61)	**0.2**	5.8	10.6	31.7	0.3	5.2	8.7	28.6	B
3536 (70)	**0.1**	5.8	9.4	31.9	*	*	*	*	B
3667 (74)	**0.1**	36.6	57.7	201.3	0.2	5.9	7.8	32.2	C
3696 (75)	**0.3**	27.7	37.4	152.3	1.4	5.0	4.3	27.6	C
4006 (84)	**9.3**	24.9	12.4	136.7	*	*	*	*	C
4105 (87)	**56.4**	25.3	13.5	139.1	*	*	*	*	C
4290 (93)	**10.4**	34.1	15.1	187.3	*	*	*	*	C
4586.5 (103)	**0.4**	102.4	97.0	563.0	1.9	30.2	18.3	166.3	D
5103.5 (119)	**29.6**	107.6	10.5	591.9	36.2	52.7	5.1	289.7	D
5205 (122)	**9.8**	152.8	15.3	840.2	13.4	54.3	5.3	298.7	D

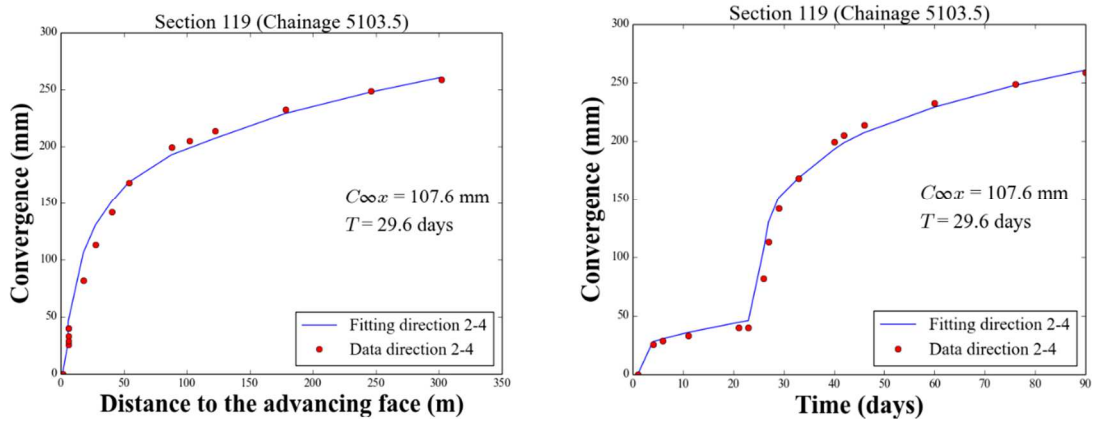

Fig. 5.18 Convergence evolution along direction 2-4 and fit with the law of de Sulem et al. (1987b) for section 119 at chainage 5103.5

5.5 Conclusion

Within a first analysis, a robust fitting of the convergence data of Fréjus road tunnel by means of the semi-empirical convergence law from Sulem et al. (1987b) has been carried out. This fitting allows for a good representation of the ground measurements and for the identification of some "homogeneous" zones in terms of convergence (similar value of the instantaneous convergence $C_{\infty x}$ along direction 2-4). However we have observed that the rate of convergence is heterogeneous along the tunnel with values of T ranging from 0.5 to 5 days without actual correlation to the magnitude of the convergences of the sections.

CHAPTER 6 THE FRÉJUS SAFETY GALLERY

In this chapter, a study of the Fréjus safety gallery is carried out. It is an example of a tunnel which was excavated with TBM under squeezing conditions. Time-dependent and anisotropic loading of the lining has been observed in this tunnel.

6.1 Project introduction and general context

Since the fire which took place in the Mont-blanc tunnel in 1999, a new safety regulation for tunnels was established. In order to be in accordance with it, the SFTRF and the SITAF decided to excavate a safety gallery which runs parallel to the existing road tunnel at a 50 m average distance between the axes of both tunnels. It was excavated between 2009 and 2016 and it is 9.5 m wide and 13 km long. As for the road tunnel, the safety gallery slopes down 0.54% from France towards Italy and the average overburden is of 1000 m (with a maximun of 1800 m). The safety gallery is connected with the road tunnel by means of 34 inter-tubes each 400 m apart. Among them, the existence of 5 by-pass allows the emergency team to access the road tunnel by vehicle from the safety gallery or *vice-versa*. Ten technical stations as well as two ventilation plants were also installed (Fig. 6.1) to complete the existing system.

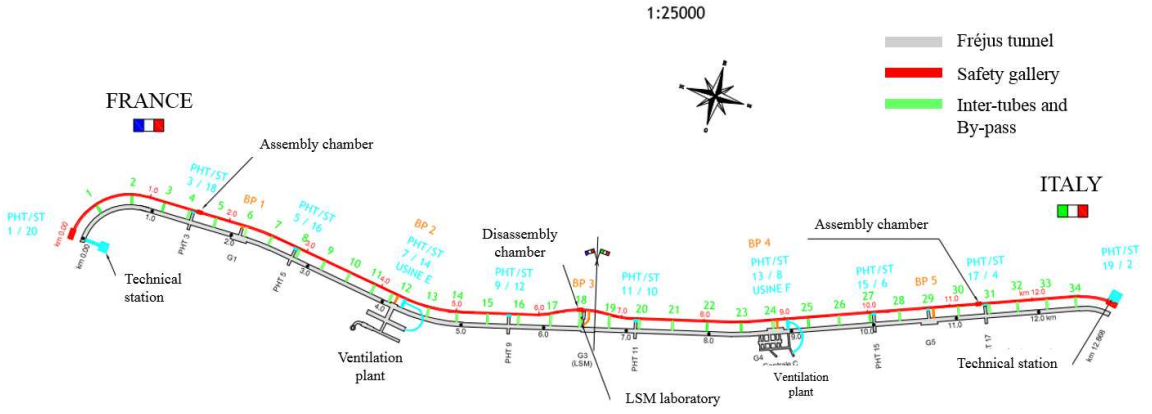

Fig. 6.1 Plan view scheme of Fréjus road tunnel and its safety gallery

The first 650 meters from the French portal were excavated by conventional drill and blast methods. The rest of the safety gallery was excavated with a single shield TBM. The TBM was firstly used to excavate the 6.5 km of the French part of the tunnel. Then it was used to excavate the tunnel through the Italian part thanks to an adaptation of the contractual dispositions. The TBM excavation allows for:

- A regular circular section which favors a homogeneous stress distribution in the segmental lining.
- Higher advancing rates compared to excavation with conventional techniques (12.9 m/day in average in the particular case of the safety gallery).
- An expected minor damage of the rock mass in comparison with the conventional drill and blast excavation that will be evidenced through the present work.

The geological context of the safety gallery is similar to that of the road tunnel, except that the gypsum unit was not encountered during the excavation of the safety gallery.

6.2 Mechanized TBM excavation technique

The choice of the TBM as well as the design of the lining was much determined by the squeezing behavior of the ground.

6.2.1 Characteristics of the TBM

The double shield TBM was rejected as a risk of shield jamming was identified. The chosen machine was a hard rock single shield TBM with longitudinal support (Fig. 6.2).

Fig. 6.2 TBM used in the excavation of the safety gallery after Vinnac (2012)

The total length of the TBM is 172 m. The shield measures 11.2 m. 24 hydraulic jacks are employed in the longitudinal support (Fig. 6.3). The maximal thrust force exerted by the hydraulic jacks is around 75.300 kN in service conditions. In an emergency situation the thrust force could reach 100.400 kN. The maximal torque that can be applied in case of emergency is 25.700 kN.m in order to release the TBM in case of no performance of the cutter head.

Fig. 6.3 Image of the hydraulic jacks of the TBM after Vinnac (2012)

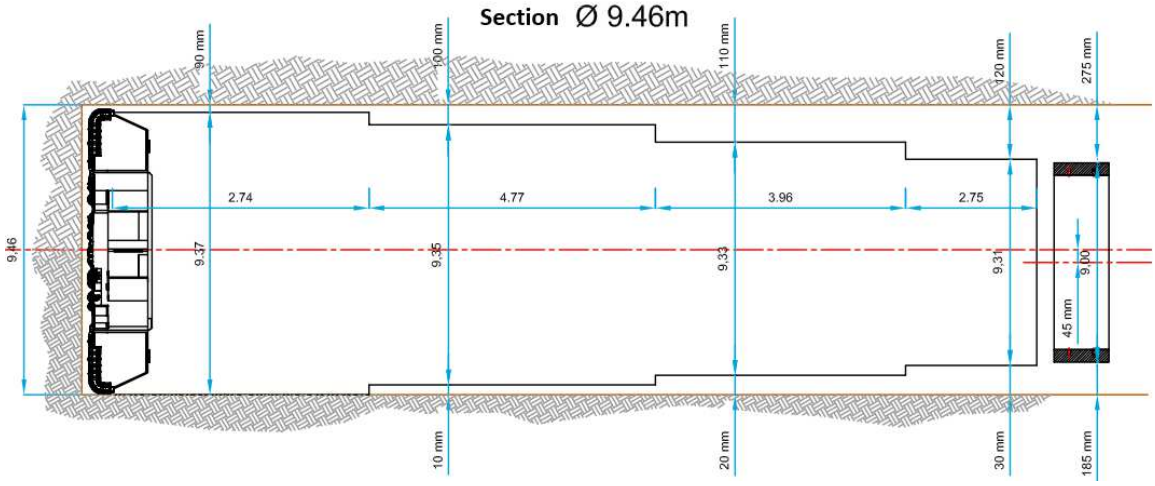

(a)

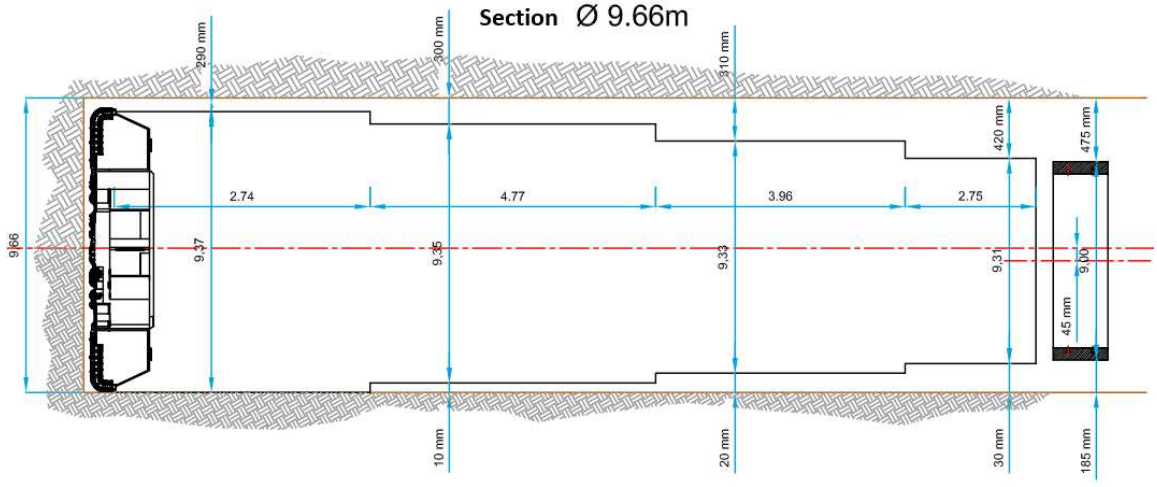

(b)

Fig. 6.4 Schemes of the TBM geometry in function of the nominal overcutting **(a)** and the large size overcutting **(b)**

The nominal shield diameter is 9.37 m and exhibits a conicity of 60mm which is used to absorb the convergences. The cutting head of 9.46 m of diameter disposes of a nominal overcutting of 90 mm at the crown. However, the overcutting can be increased to medium size (190 mm) and to large size (290 mm) (Fig. 6.4). The excavation began with the nominal overcutting. The medium size overcutting was activated around chainage 1635. At chainage 2929 the nominal overcutting is activated again. Before facing up the second area of strong convergences [see section 5.4 in chapter 5], the medium size overcutting was activated once again at chainage 4346.

6.2.2 Characteristics of the installed lining

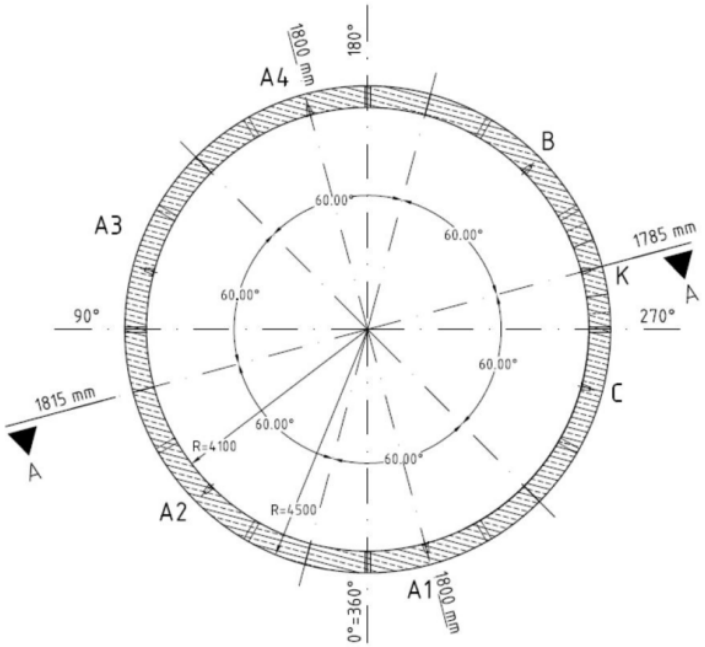

Fig. 6.5 Geometric characteristics of a ring of the lining installed in the safety gallery

The lining is composed of concrete rings made of precast segmental lining 40 cm in thickness. The average length of a ring is 1.80 m and it has an inner diameter of 8.20 m. The concrete of the segmental lining is class C45/55 (EuroCode 2). A universal ring constituted of 6+1 segmental linings has been used (4 standard segments, two counter keys and one key segment), Fig. 6.5. Two contiguous rings are relatively rotated of a demi-segment (Fig. 6.6). The segmental lining can be classified in three categories depending on the quantity of steel used to reinforce the lining (Type T1: 80 kg/m^3, Type T2: 125 kg/m^3, Type T3: 285 kg/m^3). T1 type segmental lining was used until chainage 1525. T3 type segmental lining was used between chainage 1526 and chainage 2953, between chainage 2987 and chainage 3021 and between chainage 3919 and chainage 4605. T2 type segmental lining was used in the rest of the alignment.

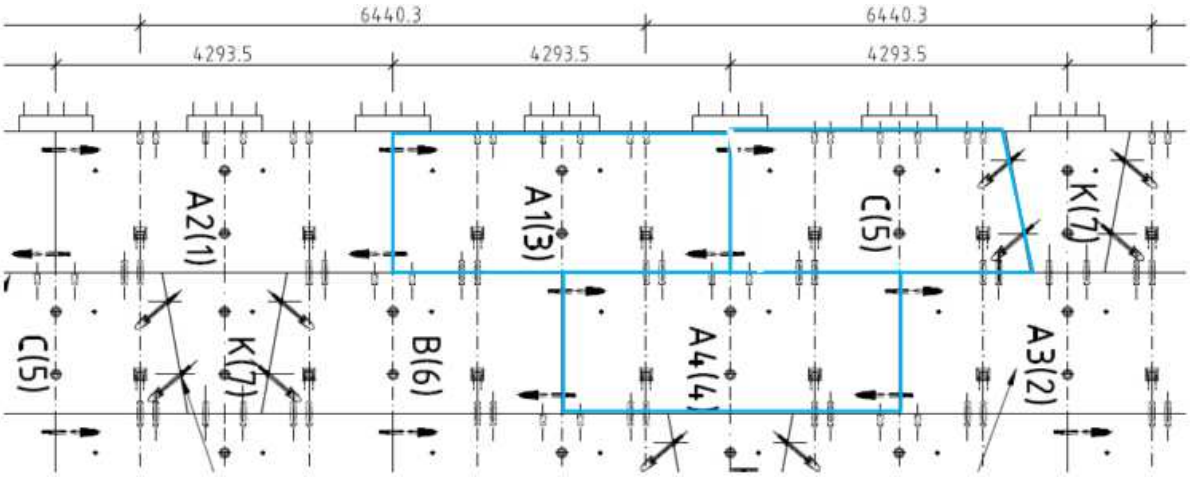

Fig. 6.6 Relative rotation of a demi-segment between two contiguous concrete rings after Vinnac (2012)

6.2.3 Backfilling technique of the annular gap

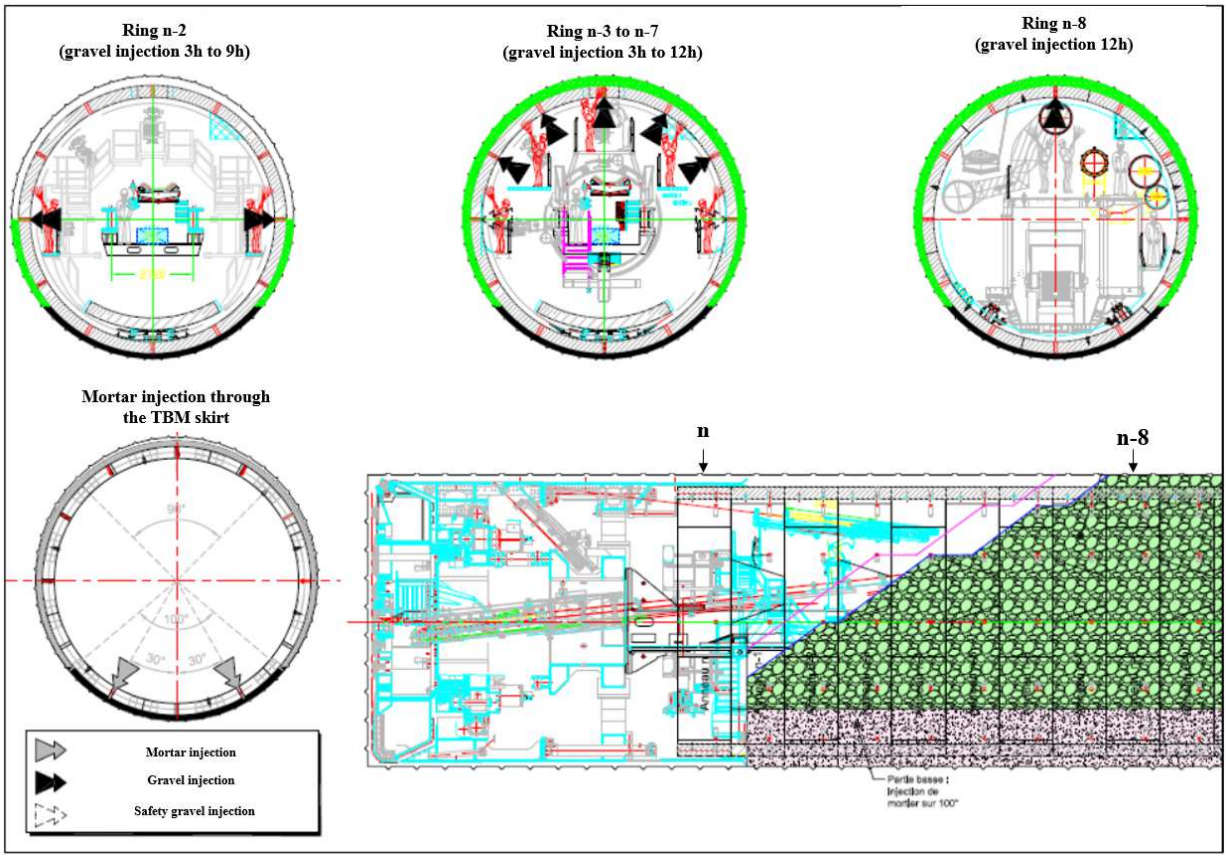

Fig. 6.7 Backfilling technique of the annular gap (after Vinnac 2012)

After the excavation process and the concrete ring installation, the annular gap existing between the lining and the ground needs to be filled. In the safety gallery, it was filled with mortar and gravel. To carry out this task a first lay of mortar C3/5 (Eurocode 2) was injected trough the shield before the installation of the concrete ring in the lower part on a 100° wide zone. This task was followed

by the gradual injection of the gravel through the segmental lining from the contact with the mortar to the vault. The onsite observations concluded that the gap is completely filled around the installation of ring n-7 (Fig. 6.7). To improve the backfilling technique and to remedy to some injection problems encountered in the vault a new method consisting on a mortar-gravel-mortar disposition ('sandwich technique') was proposed and executed from chainage 1763. The injection of the upper 60° with mortar improves the backfilling process.

6.3 Monitoring data and data processing in the safety gallery

During the excavation of the safety gallery, an important survey campaign was carried out. These measurements have three objectives:

- the collection of information to improve the excavation technique and/or the lining design during the excavation of the gallery,
- the prevention of risks that might be encountered during tunnel execution,
- the creation of a useful data base in order to back analyze the tunnel behavior.

6.2.4 Measurement of the annular gap between ground and TBM shield

In the TBM there exists 10 hydraulic jacks used to measure the existing gap between the shield and the ground G_m (Fig. 6.8). These data show the convergence of the tunnel wall along the TBM shield. A single measurement with all the jacks is carried out just after a new ring installation. In consequence G_m is measured as a function of chainage.

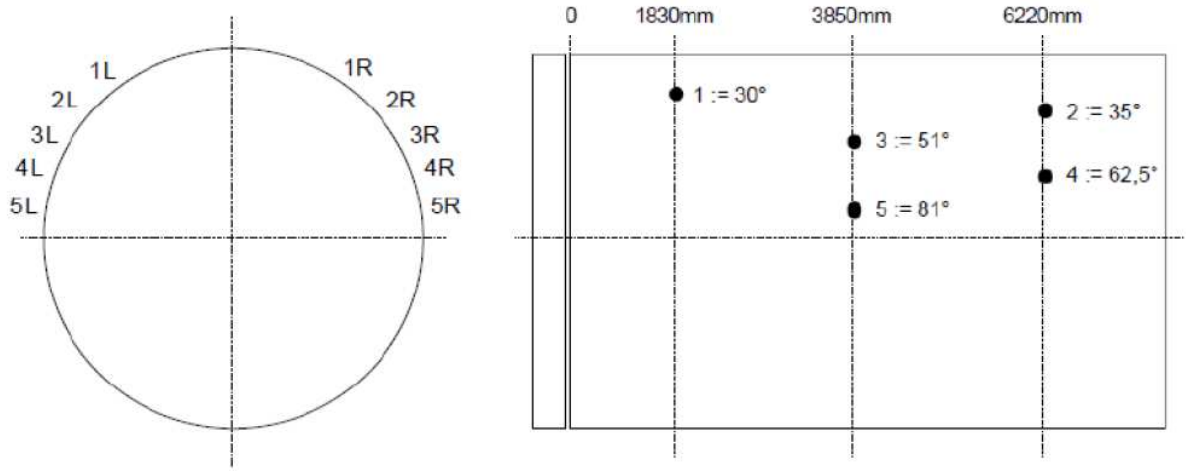

Fig. 6.8 Frontal and lateral schematic views of the TBM shield with the placed jacks (after Vinnac 2012)

For processing this convergence data we have firstly considered the geometry of the TBM in order to calculate the theoretical initial gap G_0 in function of chainage. Shield diameter is not

constant because of its conicity. Furthermore, the overcutting varies along the gallery and in consequence the initial gap varies too. Moreover, there is an eccentricity of the TBM with respect to the excavated opening. Ground convergence C_n for a given hydraulic jack n can be calculated as:

$$C_n = G_0 - G_m \tag{4.1}$$

Based on convergence data it is easy to calculate the slope of the tunnel wall between two hydraulic jacks along the TBM shield at a certain chainage (Fig. 6.9). The stronger the slope the stronger the convergences shown by the ground.

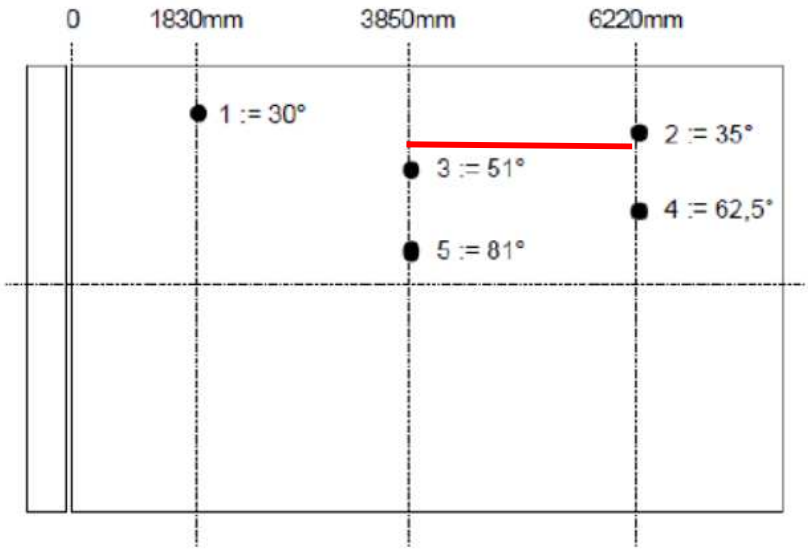

Fig. 6.9 Slope of the tunnel wall can be calculated between two hydraulic jacks

Slope between hydraulic jacks 3 and 2 on the right side of the TBM can be calculated as:

$$slope = \frac{C_3 - C_2}{6.22 - 3.85} \text{ (mm/m)} \tag{4.2}$$

It is worth to notice that this direction which is tangent to the schistosity planes leads to the largest convergence.

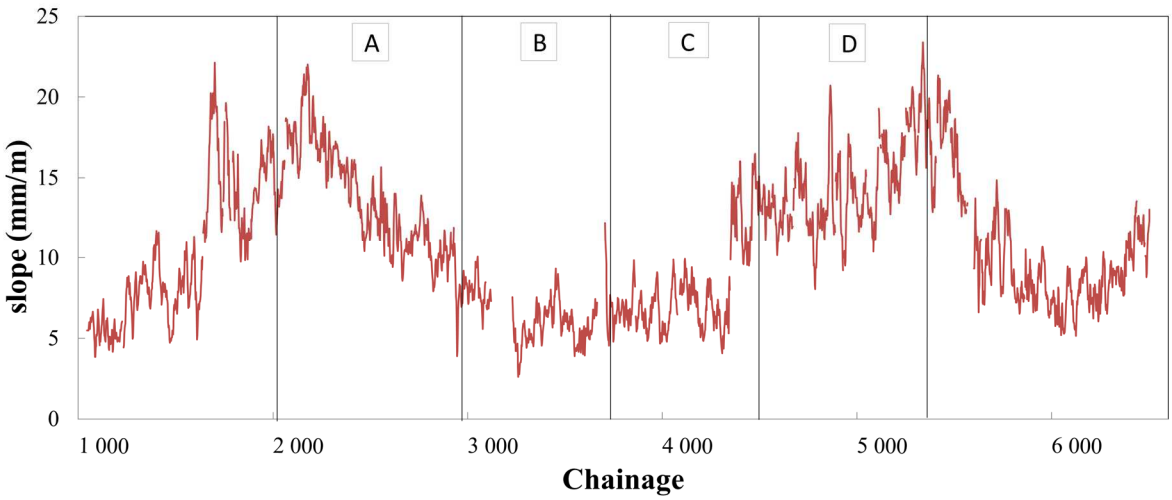

Fig. 6.10 Slope of the tunnel wall between hydraulic jacks 2 and 3. The "homogeneous" zones identified in the road tunnel are indicated in the graph.

Fig. 6.10 shows the slope of the tunnel wall between hydraulic jacks 2 and 3. The "homogeneous" zones identified in the road tunnel are indicated in the graph considering that $Chainage_{gallery} = Chainage_{tunnel} + 78$. There is a good agreement between the zones in the road tunnel showing the strongest convergences (A and D) and the strongest slopes measured by the hydraulic jacks in the gallery.

6.2.5 Stress state in the lining

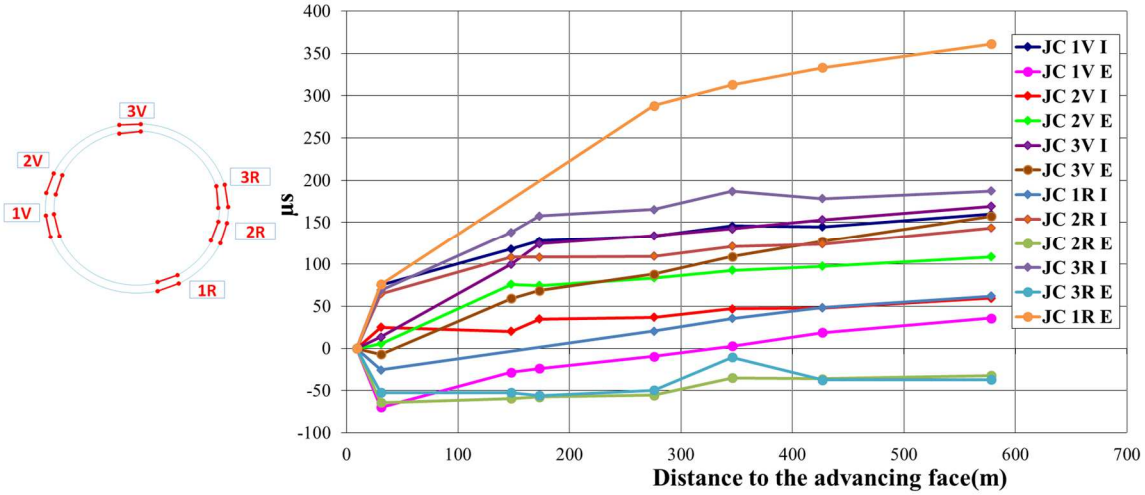

Fig. 6.11 Distribution of the strain gauges in the ring 1821, Chainage 3917 (raw data)

Monitoring data is obtained from strain gauges embedded in the segmental lining of 49 sections (Fig. 6.11) representing the most reliable source of information in the gallery. Six pairs of strain gauges were embedded in the segmental lining. Each pair can more or less represent the behavior

of the extrados and intrados fibers of the segmental lining. It should be noted that many interruptions are observed in the retrieved strain data.

The stress state in the lining can be obtained from strain gauges if concrete behavior is considered elastic and homogeneous. However, cracking induces that the lining is no longer elastic and that the modulus should be reduced to take into account damage.

Fig. 6.12 shows some of the results of the data processing of the safety gallery (De la Fuente et al 2017). The maximal compression stress retrieved from the lining is plotted and compared with the lateral friction exerted by the ground over the TBM (calculated as the difference between the total trust force exerted by the TBM and the trust force at the cutting head) and some values of RQD retrieved from the gallery. Fig. 6.12 also shows the previously identified "homogeneous" zones which are overlaid onto the safety gallery data. Monitoring data from both tunnels are in accordance. The areas of the road tunnel which exhibit larger convergence correspond to the zones of the gallery whit the higher stress level.

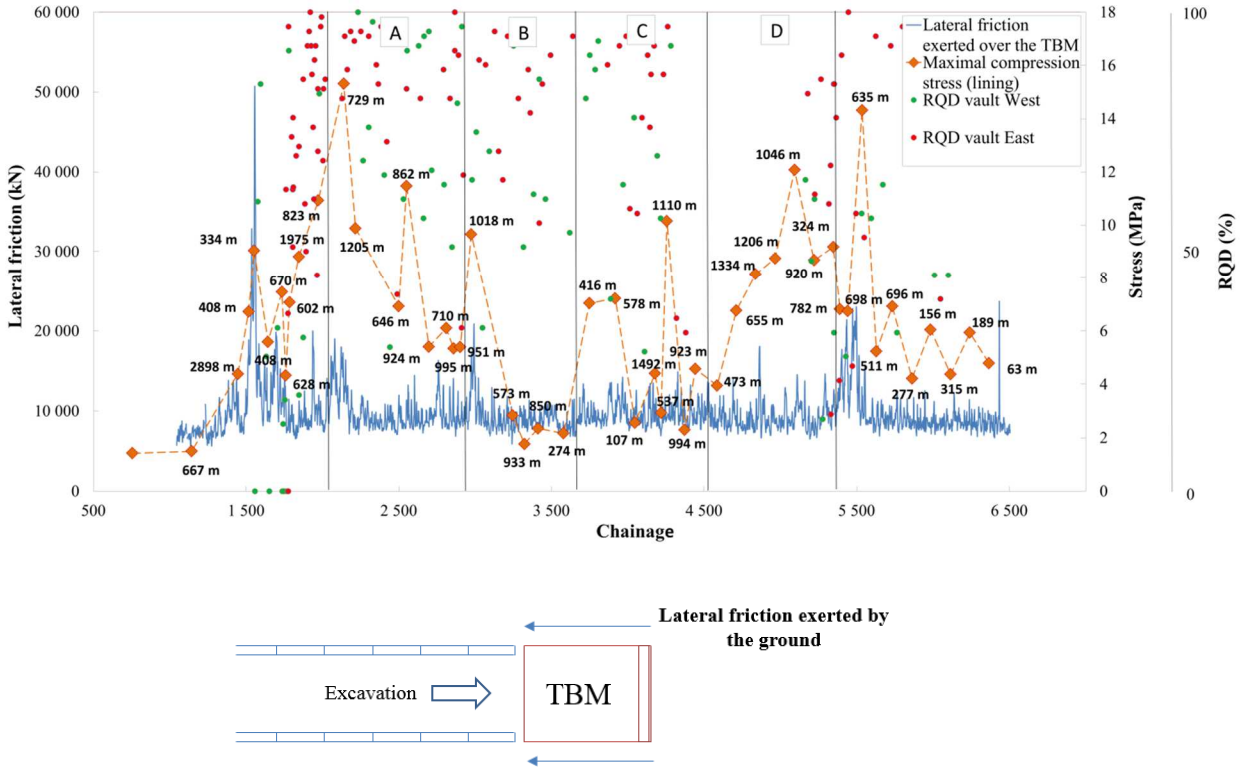

Fig. 6.12 Lateral friction exerted by the ground over the TBM tail shield, maximal compression stress measured in the lining (the distance to the excavation face at which the stress has been retrieved can be found next to each point representing the stress state) and RQD values of the ground retrieved from the East or the West side of the vault during the excavation, as a function of chainage in the gallery De la Fuente et al. (2017)

We can observe that in the areas where lateral friction exerted by the ground over the TBM is higher, the values of the RQD are lower than the average of 70 %. This can mainly be observed around chainage 1550 which corresponds to a very fractured rock. However, the RQD index is only representative of the degree of fracture and cannot describe the quality of the rock medium. Around chainage 1550 the highly fractured zone can also be identified with the increasing lateral friction over the TBM. The maximum friction which is observed around chainage 6430 is the result of the resumption of the excavation after a standstill of 126 days.

6.2.6 Convergence/divergence measurements inside the lining

Convergence/divergence measurements of the tunnel lining can be retrieved with a remote theodolite station. However, the presence of the TBM during the excavation can lead to a lack of visibility of the targets. In order to solve this problem, a system called RCMS (Ring Convergence Measurement System) was used in the safety gallery. It allows for a continuous monitoring of the convergences/divergences inside the lining as the presence of the backup train does not disturb the presence of the inclinometers. The variations of distance between two points are shown. This technique is based on a system of inclination measurements obtained by a set of inclinometers located in the segmental lining (Fig. 6.13). As the coordinates of the inclinometers are input data, the inclination measurements can be easily transformed into the relative displacements between the inclinometers. (Fig. 6.14). However, the measured relative displacements can be very small (of the order of few mm) and comparable to the uncertainty of measurements themselves.

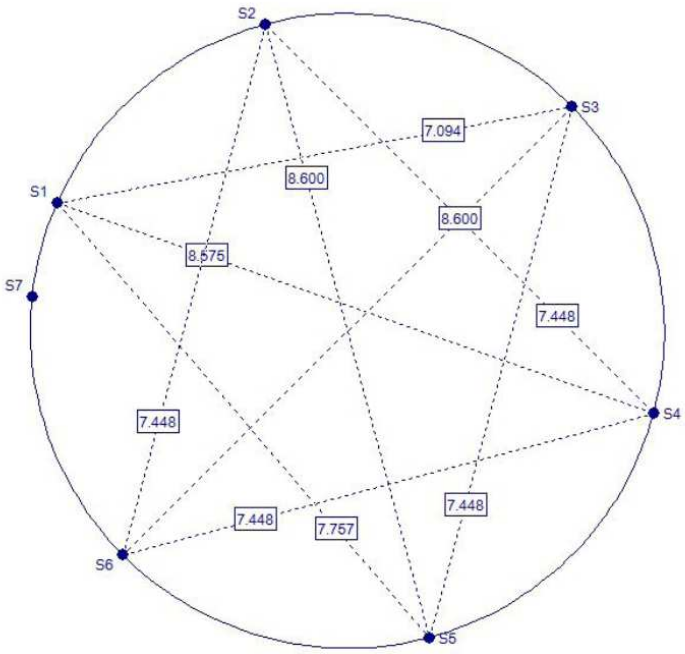

Fig.6. 13 Example of the strings' position in a ring

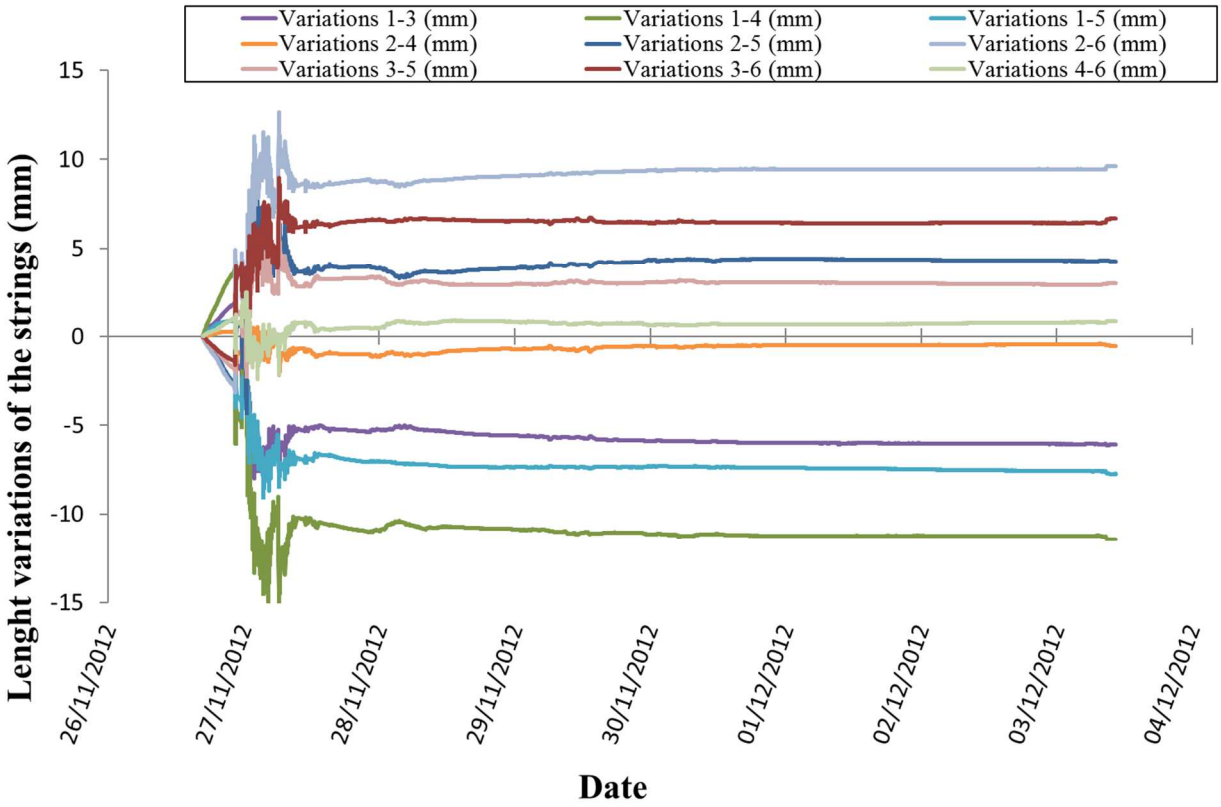

Fig. 6.14 Example of the RCMS monitoring raw data. Ring 2764 (chainage 5614.8)

6.2.7 Cracks observation

A cracking phenomenon has taken place all over the safety gallery. It is caused by buckling of schistosity planes. The homogeneity of the dip angle along the gallery induces a similar cracking disposition in all the rings. Cracks are generally developed on the right side of the vault at the wall. However, they are also commonly observed on the left side of the invert (Fig. 6.15).

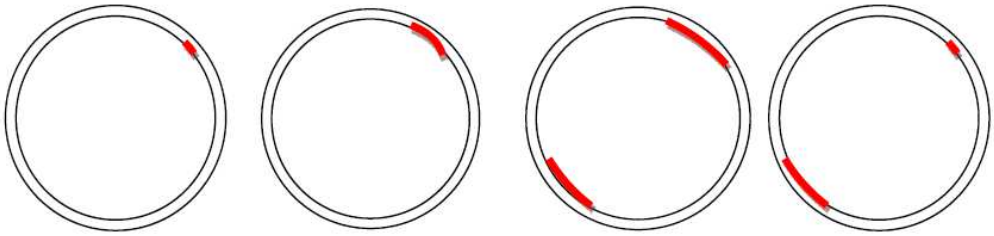

Fig. 6.15 Characteristic cracking location in the rings (oriented in the sense of excavation towards Italy) after Vinnac (2012)

A crack survey campaign was carried out by the company (Fig. 6.16). Vinnac (2012) studied the cracking degree of each ring along the alignment. In the present work crack data was processed following Vinnac (2012) approach. However, the right side of the ring is studied separately from the left side (Fig. 6.16).

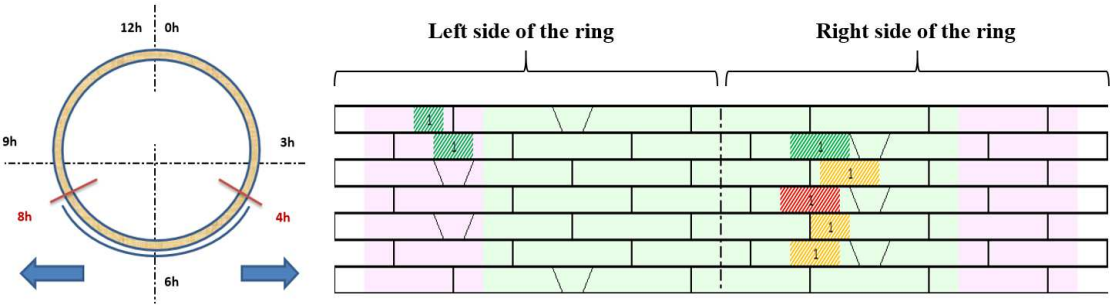

Fig. 6.16 Example of cracking data from the survey campaign

A quotation system has been adopted in order to attribute a cracking index from 10 to 100 to each ring (Tab. 6.1). It gives an idea of the cracking degree on each side of the ring. The thickness of the cracks, the number of cracks and the cracking state of the neighboring rings is studied for each particular ring.

Tab. 6.1 Quotation system used to assess the cracking degree of each ring Vinnac (2012)

		Microcracks ≤ 1/10 mm			Visible cracks > 1/10 mm and ≤ 3/10 mm			Very visible cracks > 3/10 mm and ≤ 1 mm			Very visible cracks > 1 mm		
		< 5 cracks	5 to 20 cracks	> 20 cracks	< 5 cracks	5 to 20 cracks	> 20 cracks	< 5 cracks	5 to 20 cracks	> 20 cracks	< 5 cracks	5 to 20 cracks	> 20 cracks
Isolated cracked ring (surrounded by non-cracked rings)	Crack in a single sector	10	12	14	18	22	24	30	32	34	36	38	40
	Crack in several sectors	15	18	21	27	33	36	45	48	51	54	57	60
Non- isolated cracked ring (in contact with cracked rings)	Crack in a single sector	20	24	28	36	44	48	60	64	68	72	76	80
	Crack in several sectors	25	30	35	45	55	60	75	80	85	90	95	100

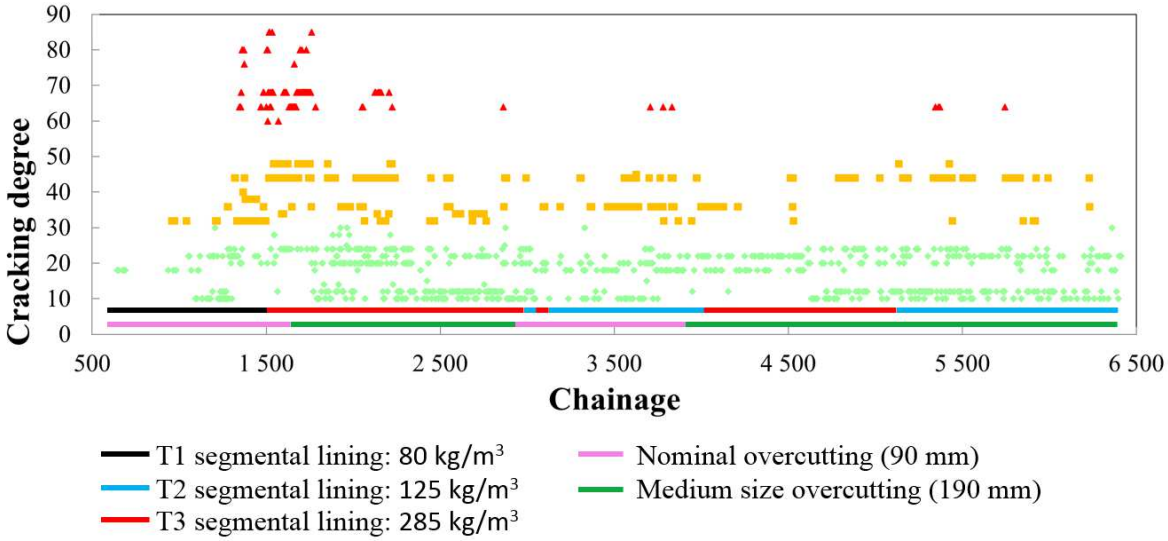

Fig. 6.17 Cracking degree on the right side of the lining in function of chainage. The lining type as well as the overcut size have been added.

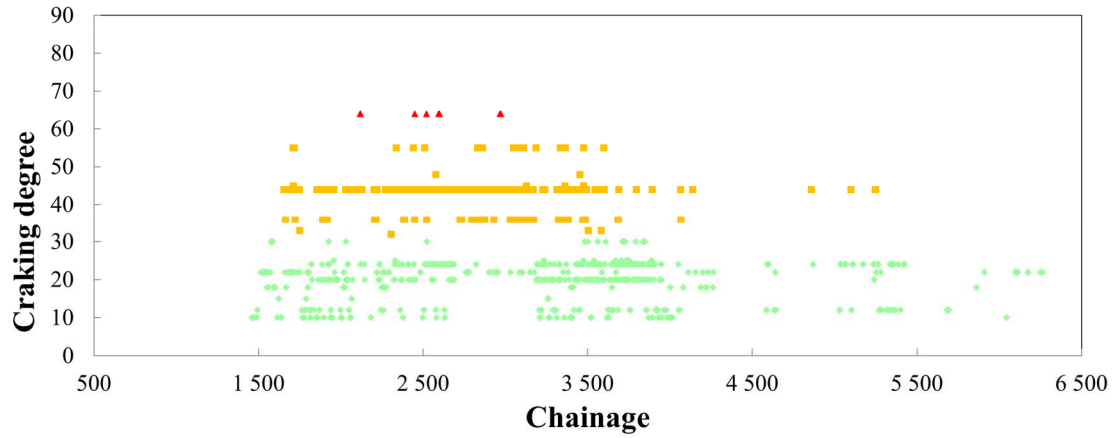

Fig.6.18 Cracking degree on the left side of the lining in function of chainage

The results of the cracking analysis are shown in Fig. 6.17 and 6.18. From cracking data, we can identify once again a very fractured area around chainage 1550 with a remarkable increase of the cracking degree. The activation of the medium size overcutting along with a continuous advance rate and the installation of T3 type segmental lining are very effective measures to reduce the cracking degree (Vinnac, 2012).

6.4 Conclusion

The Fréjus safety gallery is shown as an example of a tunnel excavated with TBM under squeezing conditions. A single shield TBM has been used for the excavation of the tunnel.

During the excavation of the safety gallery, an important survey campaign was carried out and the following data has been collected: convergence data at the inner face of the concrete ring, convergence data of the ground measured with hydraulic jacks through the TBM shield, monitoring data obtained from strain gauges embedded in the segmental lining of 49 sections which can provide information on the state of stress in the lining, cracks observations and other information obtained during the excavation such as the thrust force exerted by the TBM. The most reliable data seem to be the one which are retrieved from strain gauges. A cracking phenomenon caused by the buckling of the schistosity planes is continuously observed along the alignment.

A good agreement is observed between the behavior of the road tunnel and the behavior of the gallery. The zones of the road tunnel which show larger convergences are parallel to the zones of the gallery where the measured stress state in the lining is higher.

PART IV: NUMERICAL SIMULATIONS

CHAPTER 7 BACK-ANALYSIS OF THE FRÉJUS ROAD TUNNEL

7.1 Introduction

Large time-dependent and usually anisotropic displacements are observed from the measured convergence data of the Fréjus road tunnel. The time-dependent behavior of tunnels has been addressed in the last decades by using various numerical tools. Numerical simulations of the anisotropic response of tunnels have been carried out in various studies within the framework of elastoplasticity. However, the coupled anisotropic and time-dependent behavior of the ground has been less studied so far.

The present study focuses on the back-analysis of convergence measurements monitored in the Fréjus road tunnel. Convergence data is retrieved from the road tunnel over a period of four months before the installation of the final lining. A visco-elasto-plastic and anisotropic constitutive numerical model is proposed and calibrated on field data. This model considers one family of weakness planes embedded in an isotropic viscoelastic rock matrix. The anisotropic and time-dependent behavior of the ground observed in this tunnel can be accurately simulated with the selected constitutive model. The computations are performed using the numerical code FLAC3D which is commonly used for geotechnical applications.

A numerical back-analysis of the short-term convergences of the Fréjus road tunnel has been carried out. Furthermore, a numerical prediction of the long-term interaction between the ground and the lining of the Fréjus road tunnel is developed in the present chapter.

7.2 Finite difference technique used in the simulation of the Fréjus road tunnel

FLAC^{3D} (Fast Lagrangian Analysis of Continua) is a three dimensional numerical software which is based on the explicit finite differences theory.

The method of resolution of the considered non-linear problem is characterized in FLAC^{3D} by the following features (ITASCA, 2011):

- finite difference approach: First-order space and time derivatives of a variable are approximated by finite differences, assuming linear variations of the variable over finite space and time intervals, respectively.
- discrete-model approach: The continuous medium is replaced by a discrete equivalent-one in which all forces involved (applied and interactive) are concentrated at the nodes of a three-dimensional mesh used in the medium representation. The mesh is composed of

parallelepipedic or prismatic shape elements (containing 8 or 6 nodes respectively) divided into 3 or 5 tetrahedrals (Fig. 7.1).

- dynamic-solution approach: The inertia terms in the equations of motion are used as numerical means to reach the equilibrium state of the system under consideration.

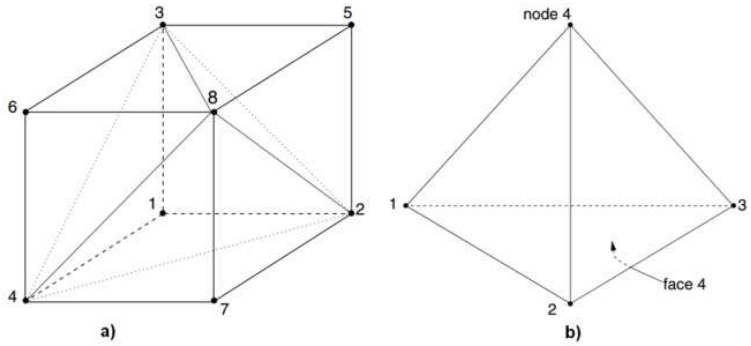

Fig. 7.1 Parallelepipedic shape elements **(a)** and tetrahedral **(b)**

7.3 Anisotropic time-dependent constitutive model

In the numerical simulations of the Fréjus road tunnel, the assumed constitutive behavior for the ground is visco-elasto-plastic and anisotropic. This constitutive model has been successfully employed by Tran-Manh et al. (2015a) to reproduce the response of Saint-Martin-La-Porte acces adit within the framework of Lyon-Turin railway project. This model considers one family of weakness planes embedded in an isotropic rock matrix. It combines the CVISC model which describes the behavior of the rock matrix and the ubiquitous joints model which introduces the anisotropy resulting from the presence of weakness planes (Fig. 7.2).

CVISC model considers an elasto-plastic volumetric behavior and a visco-elasto-plastic deviatoric behavior driven by a Burgers visco-elastic element and a plasticity element. The model can describe both instantaneous and delayed deviatoric strains (Boidy et al., 2002). This model is implemented in FLAC^{3D} and has been previously used in many numerical simulations (e.g. Barla et al. 2007, 2008, 2010, 2011, Pellet 2009, Sharifzadeh et al. 2013, Hasanpour et al. 2015).

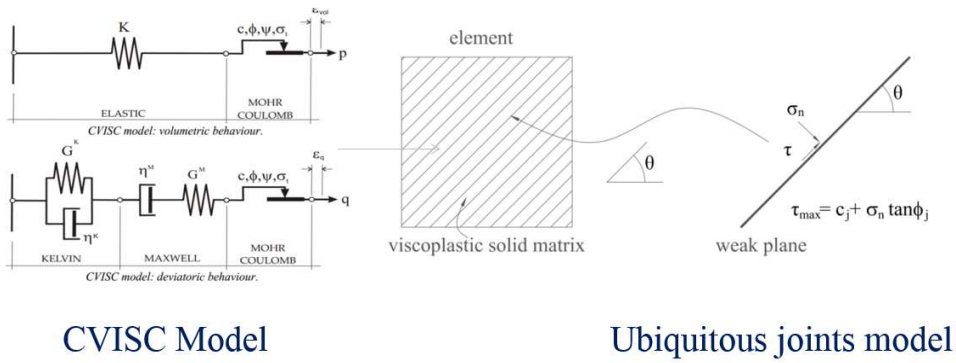

Fig. 7.2 Ubiquitous joint model embedded in a visco-elasto-plastic matrix

The presence of discontinuities such as schistosity planes is taken into account by means of the "ubiquitous joints model". It consists in a set of joints of a given orientation which pass through any point in the rock mass. These joints are activated if the yield criterion is reached (Coulomb criterion with tension cut-off). The ubiquitous joint approach permits to model a jointed rock-mass (Kazakidis and Diederichs, 1993). This model has been largely used in the simulation of underground excavations (Cartney 1977, Li et al. 2003, Plana et al. 2004, Russo et al. 2009, Wang & Huang 2009, 2013).

This constitutive model is characterized by 13 constitutive parameters. The mechanical behavior of the solid matrix is described by 9 parameters (elastic bulk modulus K, Kelvin shear modulus G_K, Kelvin dynamic viscosity η_K, elastic shear modulus G_M, Maxwell dynamic viscosity η_M, cohesion c, friction angle ϕ, dilation angle ψ , and tension limit σ_t). The behavior of the weak planes is described by 4 parameters (joint cohesion c_j, joint friction angle ϕ_j, joint dilation angle ψ_j and joint tension limit σ_{tj}). Two additional geometric parameters describe the orientation of the weak-plane (dip angle and dip direction of weakness plane).

The incremental numerical algorithm computes new stress from strain increments. This algorithm can be described in three steps (Tran-Manh et al., 2015a):

- Computation of a new trial stress state in the solid. Elastic or viscolastic increments are assumed;
- The new trial stress state is evaluated for the failure in the solid matrix (global failure) and plastic corrections are made if necessary;
- Local stress state is analyzed on the weak-plane (local failure) and stress corrections are applied if local failure takes place.

7.4 Identification of the envelope of the convergences in the Fréjus road tunnel

As shown in chapter 5, some "homogeneous" zones in terms of the amplitude of the convergences have been identified (De la Fuente et al., 2017). The present chapter aims at reproducing the behavior observed in the "homogeneous" zone A. Along this area of the tunnel, a moderate buckling phenomenon was observed during construction. The parameters ($T, X, C_{\infty x}, m, n$) have been obtained for each section from the fitting of the convergence data with the convergence law proposed by Sulem et al., (1987b).

With this values of parameters ($T, X, C_{\infty x}, m, n$), convergence curves are plotted again in Fig. 7.3 (De la Fuente et al., 2018) assuming a constant face advance rate of 5.6 m/day for all the sections. Therefore, the various convergence curves can be better compared as the effects of the

arrests of the face advance are removed. In doing so, it is assumed that the parameters of the convergence law do not depend on the advancing rate of excavation. Furthermore, all the curves are plotted considering that the first measurement is retrieved at a distance of 4.5 m from the tunnel face which corresponds more or less to the average length of one step of excavation. This means that the installation of the monitoring targets is assumed to be done 0.8 days after the opening of the section.

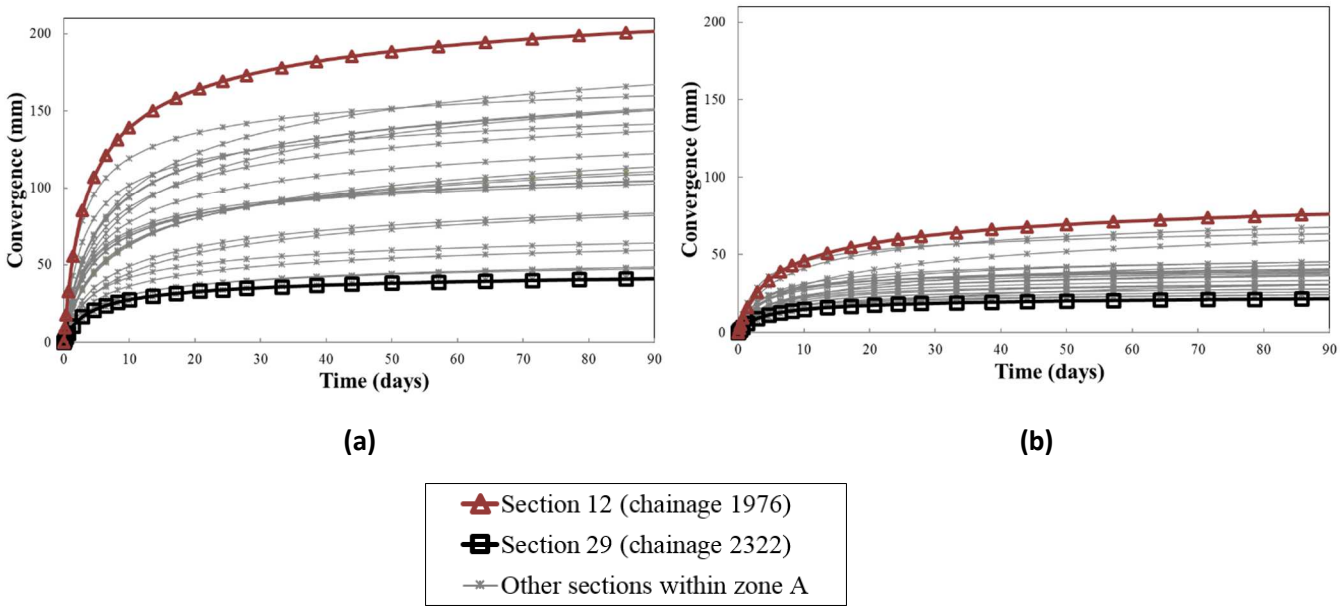

Fig. 7.3 Convergence curves in the "homogeneous zone A" along direction 2-4 **(a)** and along direction 1-4 **(b)**

Within "zone A", section 12 (chainage 1976) exhibits the largest convergence, whereas section 29 (chainage 2322) exhibits the smallest one.

7.5 Short-term numerical simulations of the Fréjus road tunnel

A 3D numerical simulation is carried out with FLAC^{3D} in order to simulate the behavior of the Fréjus road tunnel. Fig. 7.4 and 7.5 show the geometry of the model. The model is large enough in order to simulate the excavation and minimize boundary effects. Far field boundaries are placed at a distance of 28 radii (considering the vault radius) and the length of the model in the axial direction is 90 m. Mesh is discretized into small elements of 0.45 m (< 1/10 *R*). The *in-situ* stress state is initially imposed everywhere in the domain (average depth of 1067 m and average specific weight of the ground of 27 kN/m^3). Gravity effects are disregarded. The step of excavation is 4.5 m and an advancing rate of 5.6 m/day is imposed in the computations in accordance with the average values observed during the excavation of the tunnel. The coordinates of the targets in the simulations are the average coordinates of all the targets along the tunnel (Fig. 7.5).

In order to guarantee a quasi-static mechanical equilibrium, it is necessary to choose a small enough time step (Billaux and Cundall, 1993). The maximum creep time step Δt_{max}^{cr} is here estimated as the ratio of the material viscosity to the shear modulus $\Delta t_{max}^{cr} \leq \min\left(\frac{\eta_K}{G_K}, \frac{\eta_M}{G_M}\right)$ (ITASCA, 2011).

The dip direction of the schistosity planes is parallel to the tunnel axis and its dip angle is fixed to 45°. The support composed of 20 rockbolts/m is simulated by introducing cable structural elements which are punctually anchored to the tunnel wall and to the ground. Each cable can yield in tension but cannot resist a bending moment. The length of the rockbolts is 4.65 m with a diameter of 20 mm and a strength limit of 450 MPa.

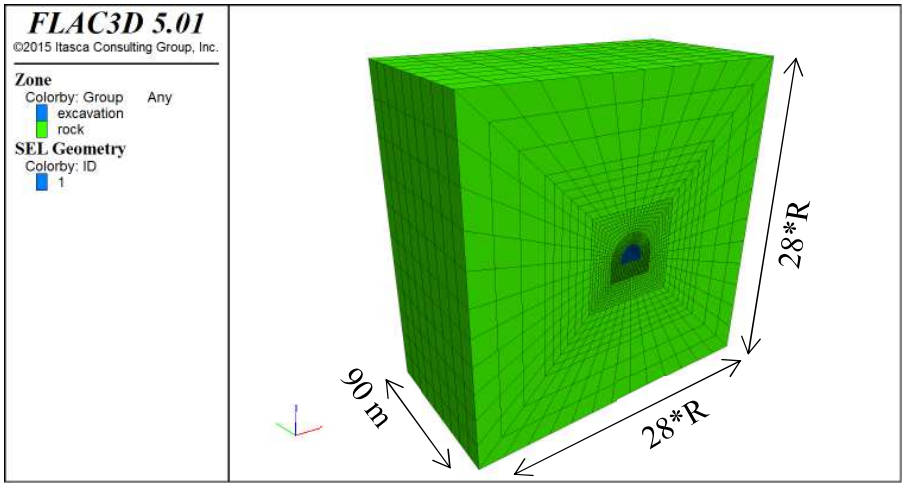

(a)

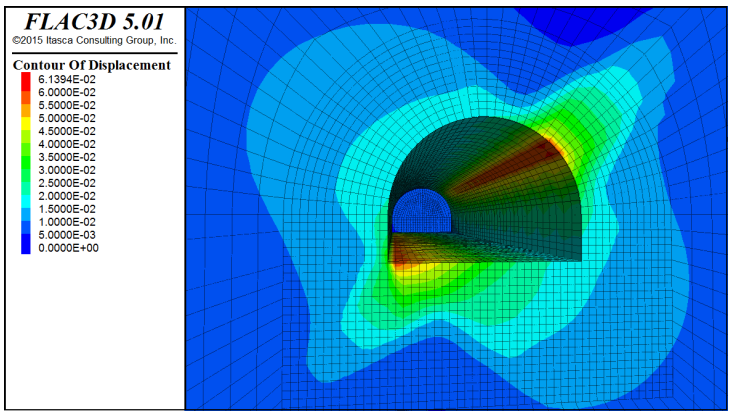

(b)

Fig. 7.4 Geometry of the model **(a)**. Detail of the displacements around the tunnel during its excavation for section 12 (chainage 1976) **(b)**. R is the radius of the vault of the excavated tunnel (5.8 m)

Sections showing the largest convergence and the smallest convergence are back-analyzed by using the above constitutive model, Fig. 7.6 and 7.7. A horizontal pressure coefficient K_0 of 1.4 has been assumed. The values of the mechanical parameters of the joints are identical in both cases (c_j = 0,15 MPa, ϕ_j = 20 °, ψ_j = 5 ° and σ_{tj} =0.01 MPa). The values of some of the parameters of the rock matrix are assumed the same in both sections (E = 40 GPa, ϕ = 40°, ψ = 15 °,$\sigma_t = \sigma_c$ /10 and υ = 0.3). The four other parameters of the matrix differ from one section to another, Fig. 7.6 and Fig. 7.7. The largest values $(.)_{max}$ of parameters c, η_K, G_M and η_M are assigned to the smallest convergence (section 29) and vice versa. The in situ observed behavior is accurately reproduced with the model.

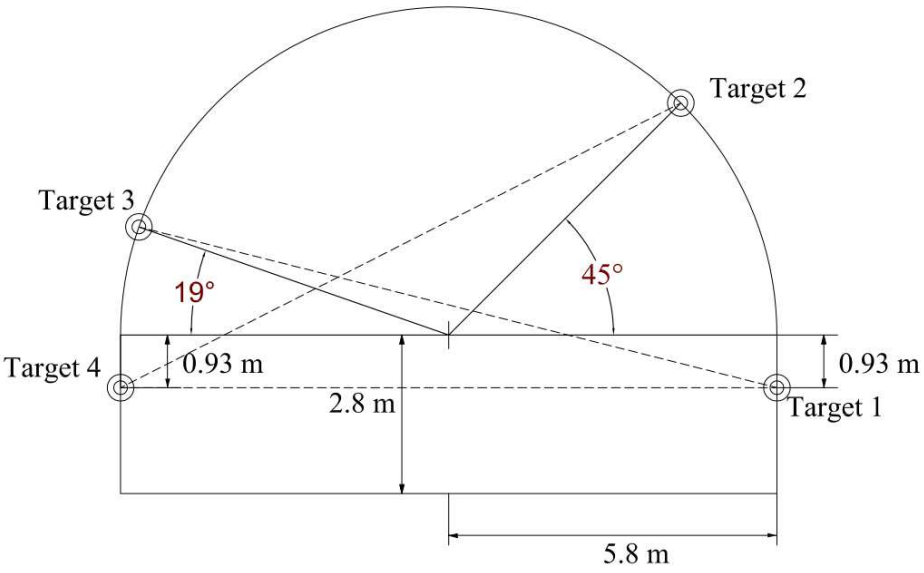

Fig. 7.5 Geometry of the tunnel and average position of the targets considered in the simulations

Section 12 (chainage 1976)

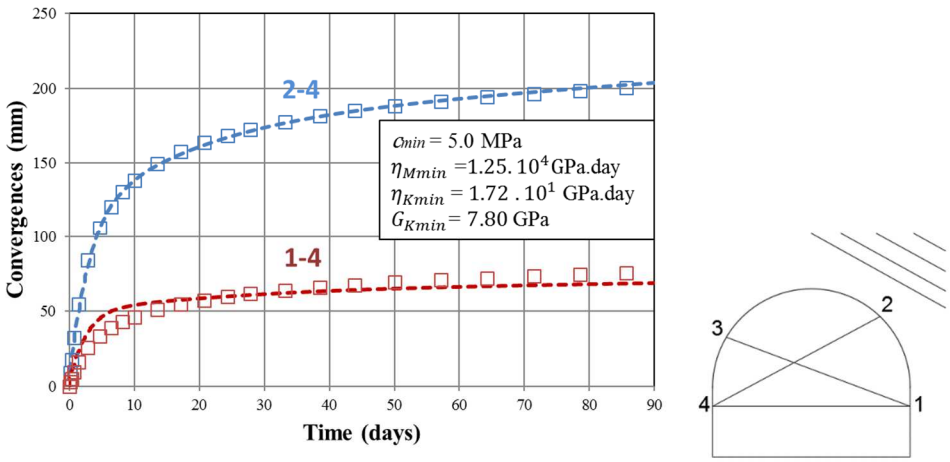

Fig. 7.6 Back analysis of convergence data of section 12 (chainage 1976) (largest convergence) and schematic average position of the targets (right) in the section

Section 29 (chainage 2322)

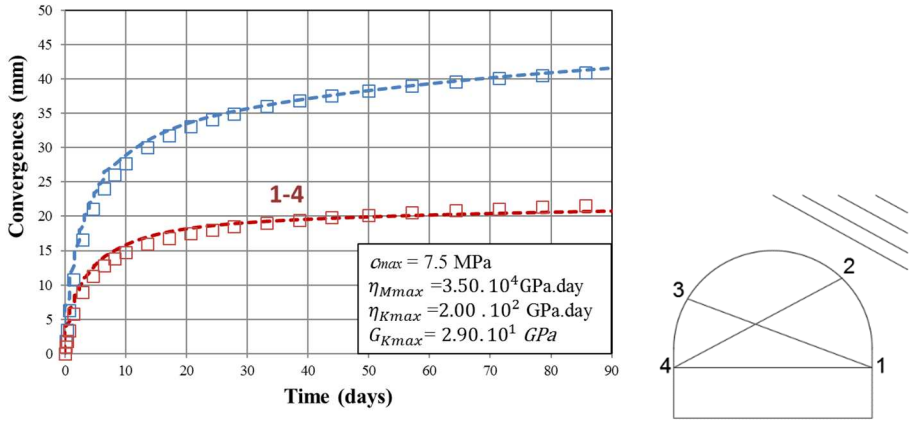

Fig. 7.7 Back analysis of convergence data of section 29 (chainage 2322) (smallest convergence) and schematic average distribution of the targets (right) in the section

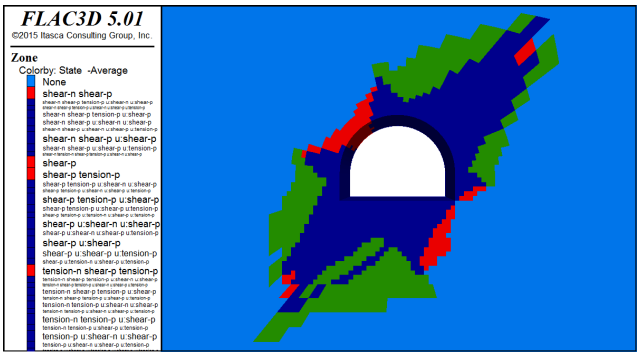

(a)

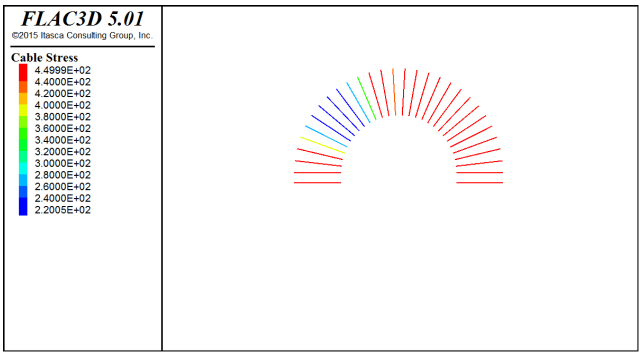

(b)

Fig. 7.8 Section 12 (chainage 1976) (largest convergence): Plastic area (red zones are the areas where the matrix is in plastic state, green zones are the areas where joints are in plastic state and blue zones are the areas where matrix and joints are in plastic state at the same time) **(a).** Stress state in the rockbolts (rockbolts drawn in red have reached the elastic limit)

The developed plastic zones around the tunnel and the rockbolts stress state 90 days after the excavation of the tunnel are shown in Fig. 7.8 for section 12 and Fig. 7.9. for section 29.

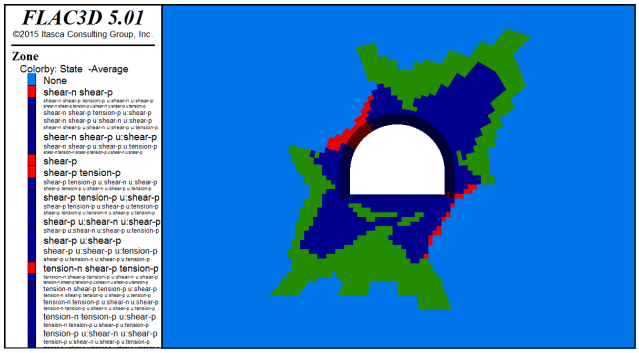

(a)

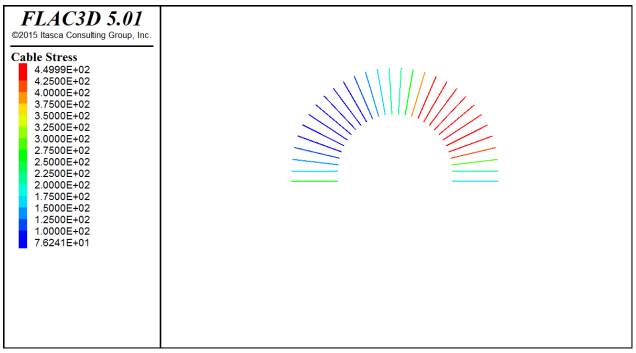

(b)

Fig. 7.9 Section 29 (chainage 2322) (smallest convergence): Plastic area (red zones are the areas where the matrix is in plastic state, green zones are the areas where joints are in plastic state and blue zones are the areas where matrix and joints are in plastic state at the same time) **(a)**. Stress state in the rockbolts (rockbolts drawn in red have reached the elastic limit) **(b)**

Sections within zone A can be simulated by fitting the cohesion of the joints *cj* and a variability parameter α with values between 0 and 1, which can be seen as a variable describing the degree of damage of the ground, taking as reference values 0 for section 19 giving the smallest convergence and 1 for section 12 giving the largest one. This parameter permits to simply evaluate the time-dependent parameters of the matrix and the matrix cohesion for all sections in zone A (Equation 7.1). The variability parameter α is evaluated for each section by fitting the convergence measured along direction 1-4. As this direction is sub-parallel to the weakness planes, it is assumed that the convergence measurements along 1-4 are representative of the matrix behavior. Once parameter α is evaluated, *cj* is fitted from the convergence measurements along direction 2-4. The stronger the convergence along 2-4, the stronger the anisotropy of the section and the lower the value of *cj*. The other parameters remain the same for all the sections.

$$
\begin{aligned}
c &= c_{min}\ \alpha + (1-\alpha)\ c_{max} \\
G_k &= G_{k_{min}}\alpha + (1-\alpha)\ G_{k_{max}} \\
\eta_k &= \eta_{k_{min}}\alpha + (1-\alpha)\ \eta_{k_{max}} \\
\eta_M &= \eta_{M_{min}}\alpha + (1-\alpha)\ \eta_{M_{max}}
\end{aligned}
\qquad (7.1)
$$

The comparison between computed and measured convergences along directions 2-4 and 1-4 for the various sections in zone A is shown in Fig. 7.10. The agreement of the numerical results with the observed field measurements over a period of 90 days is very good. A quasi-constant convergence rate is reached after four or five months because of the presence of a Maxwell viscous element η_M in the rheological model. α and c_j take different values for each section. Some of the sections which exhibit very strong anisotropy of the convergences are simulated by assuming then cohesionless ($c_j = 0$). Within the studied range of values assigned to the parameters of the constitutive model, sections showing an anisotropy ratio ($\beta = C_{\infty x\,2-4}/C_{\infty x\,1-4}$) larger than 4 cannot be properly simulated (sections 19, 20 and 45). The values of α and c_j for each section are reported in Table 7.1.

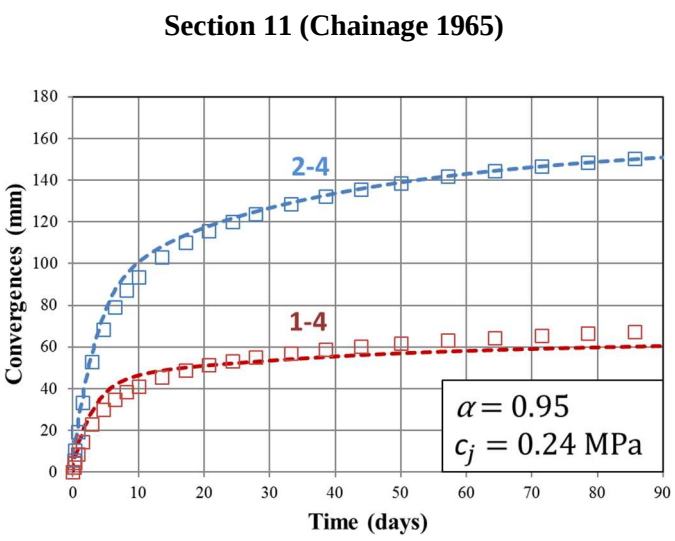

Fig. 7.10 Back analysis of convergence data of sections within zone A (from chainage 1905 to chainage 2723)

Section 23 (Chainage 2267)

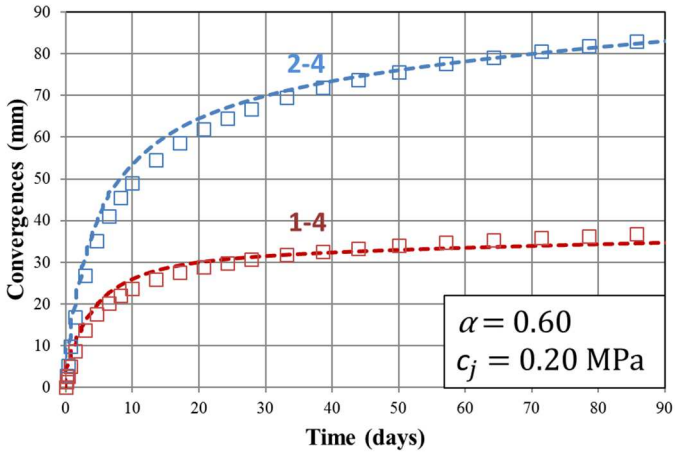

Section 24 (Chainage 2287)

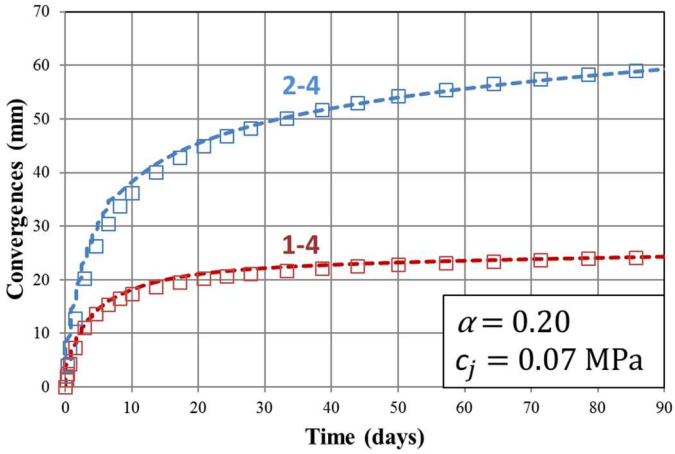

Section 33 (Chainage 2438)

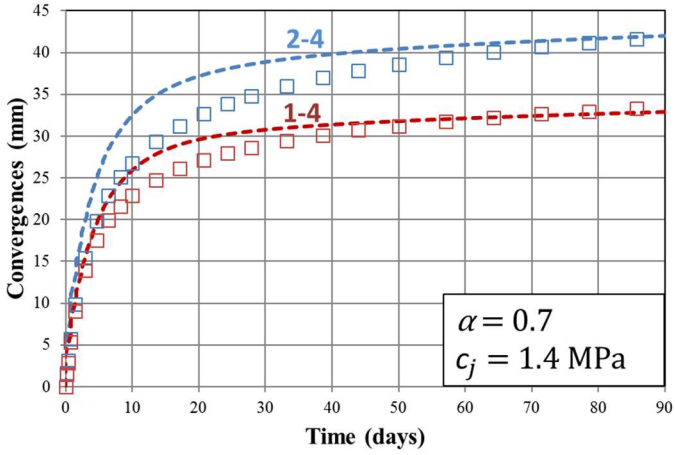

Fig. 7.10 Back analysis of convergence data of sections within zone A (from chainage 1905 to chainage 2723)

The fit for the rest of the sections within zone A can be found in Appendix D.

Tab. 7.1 Fitted values of α and c_j for each section within zone A

Section	Chainage	α	c_j	$C_{\infty x\ 1-4}$	β
8	1905	0.97	0.28	18.2	2.24
11	1965	0.95	0.24	20.72	2,22
12	**1976**	**1.00**	**0.15**	**23.28**	**2,51**
13	1998	0.85	0.30	20.38	1,73
14	2018	0.70	0.33	14.75	1,83
16	2063	0.75	0.00	13.64	3,85
18	2136	0.60	0.00	10.66	3,84
19	2157	**Anisotropy ratio > 4**		7.18	**6.42**
20	2184,5	**Anisotropy ratio > 4**		11.28	**4.29**
23	2267	0.60	0.20	11.01	2,37
24	2287	0.20	0.07	6.98	2,60
25	2289	0.50	0.28	8.93	2,12
26	2292,5	0.30	0.35	7.60	1,92
28	2296	0.45	0.52	8.11	1,74
29	**2322**	**0.00**	**0.15**	**6.34**	**1,89**
30	2341	0.45	0.00	8.88	3,41
33	2438	0.70	1.40	9.72	1,29
36	2509	0.77	0.15	13.05	2,81
37	2531	0.70	0.00	11.84	3,83
41	2626	0.70	0.15	11.60	2,57
43	2682	0.65	0.09	10.91	3,12
44	2723	0.70	0.15	11.30	2,73
45	2745	**Anisotropy ratio> 4**		8.03	**4.65**

A linear correlation can be found between the variability parameter α (fitted along direction 1-4) and a parameter ξ defined in equation 7.2. ξ is a function of the instantaneous convergence evaluated in the semi-empirical convergence law along direction 1-4 ($C_{\infty x\ 1-4}$) (see chapter 5) (Fig. 7.11). $C_{\infty x\ 1-4\ min}$ is the instantaneous convergence along direction 1-4 for section 29 (showing the smallest convergences) and $C_{\infty x\ 1-4\ max}$ is the instantaneous convergence along direction 1-4 for section 12 (showing the largest convergences).

$$\xi = \left(\frac{C_{\infty x\,1-4} - C_{\infty x\,1-4\,min}}{C_{\infty x\,1-4\,max} - C_{\infty x\,1-4\,min}}\right)^{\frac{1}{3}} \quad (7.2)$$

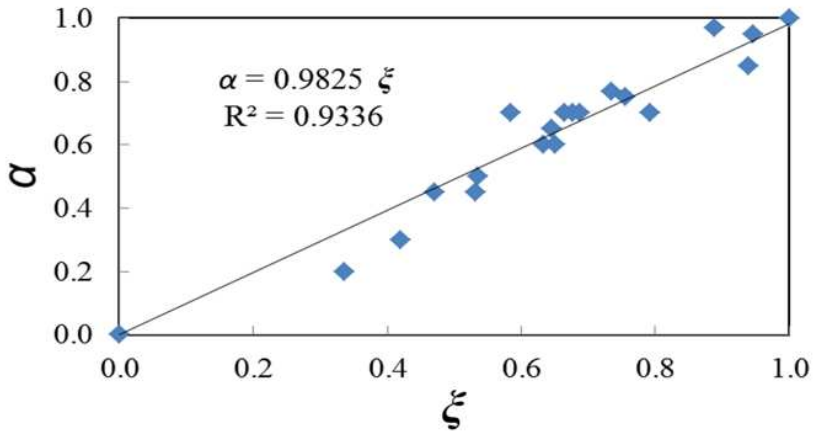

Fig. 7.11 Linear correlation between α and ξ

7.6 Long-term numerical simulations of the Fréjus road tunnel

We have shown above that the proposed constitutive model is able to correctly reproduce the field data. It is always a challenging question to assess the performance of a model that has been calibrated on data recorded during few months for predicting the very long term behavior of a structure. It is however, an interesting problem to test the predictive capacity of the model. Therefore, a numerical prediction of the average long-term behavior (40 years) of the Fréjus road tunnel has been carried out. We first identify a typical section (section 23 in chainage 2267) showing an average response within zone A. The values of the mechanical parameters which govern section 23 short-term behavior are: α = 0.6 and c_j = 0.2 MPa. With this set of parameters, we extrapolate the long-term convergences of section 23 at 40 years, assuming that the final support is not installed and by using the empirical convergence law fitted in the previous chapter (X = 10.5 m, m = 4.5, $n = 0.3$, $C_{\infty x\,2-4}$ = 26.1 mm, $C_{\infty x\,1-4}$ = 11.0 mm, T_{2-4} = 3.3 days, T_{1-4} = 1.9 days), Fig. 7.12. Finally, we perform a numerical analysis of section 23, using the proposed constitutive model and without the final support (Fig 7.12). It was obtained that with the chosen constitutive model, it is not possible to find a single set of parameters able to reproduce short-term convergences and mid and long-term convergences at the same time. This is due to the linear Maxwell element in the rheological model which leads to constant deformation rate in the long term and therefore cannot reproduce the decreasing convergence rate of the empirical convergence law. For this reason, in an attempt to keep the model as simple as possible, two sets of parameters are used in the same numerical simulation. The first set of parameters (α = 0.65 and c_j = 0.2 MPa) is used to fit short-term convergences. The short-term convergences are considered to be the ones that occur before

the installation of the final concrete lining (107 days after the excavation of the section). The blue vertical line shown in Fig. 7.12 (a) separates the short-term convergences from the mid and long-term convergences. A second set of parameters is used to reproduce the long-term convergences. Only two parameters of the second set are modified as compared to the first one: η_M is multiplied by 23 and G_k is multiplied by 12, (Fig. 7.12).

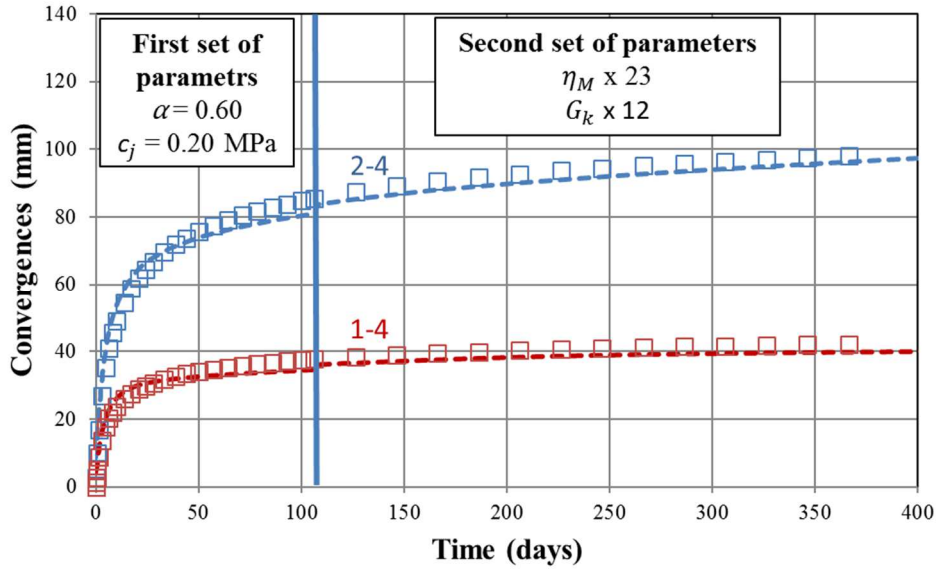

(a)

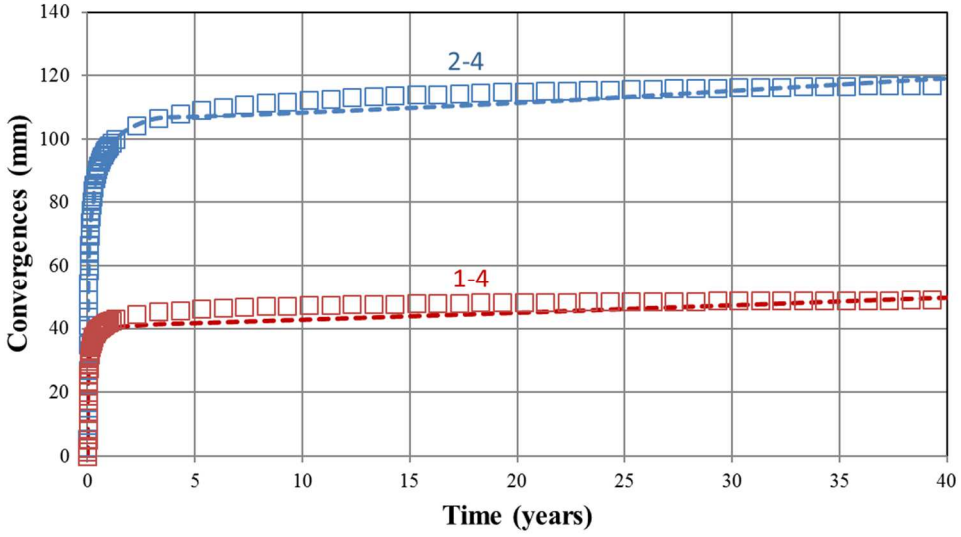

(b)

Fig. 7.12 Medium-term **(a)** and long-term **(b)** back analysis of convergence data of section 23 within zone A (chainage 2267)

Finally, we use the identified parameters of the model for the simulation of the Fréjus road tunnel with the installation of the final lining system in order to study the long-term ground/lining interaction, Fig. 7.13. The installation of the final lining is carried out in two steps: installation of

the invert at 350 m from the excavation face and installation of the final lining at 600 m from the excavation face (107 days after the excavation of the section). In consequence, the activation of the second set of parameters coincides with the installation of the final lining. With this approach, the effect of the installation of the final lining on the ground behavior is explicitly taken into account (the final lining exerts a pressure on the rock mass that can lead to the progressive closure of the existing joints of the ground which will therefore affect the time-dependent behavior of the rock mass). A long-term Young's modulus for the concrete of 11 GPa is used in the numerical simulations.

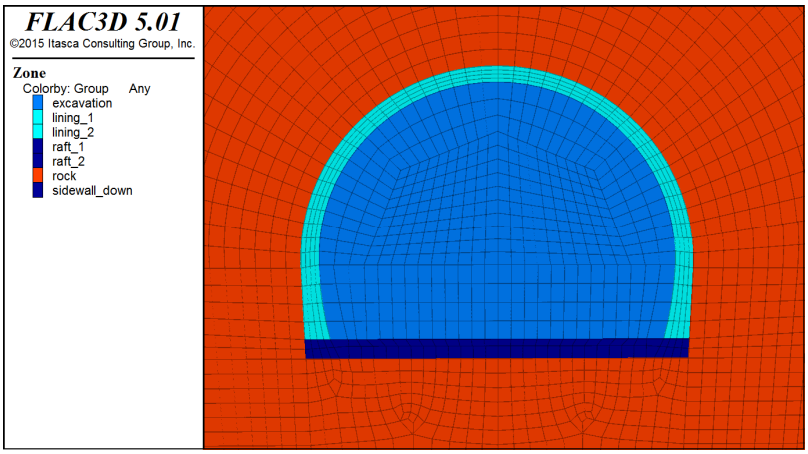

Fig. 7.13 Geometry of the model: the Fréjus road tunnel and its final lining

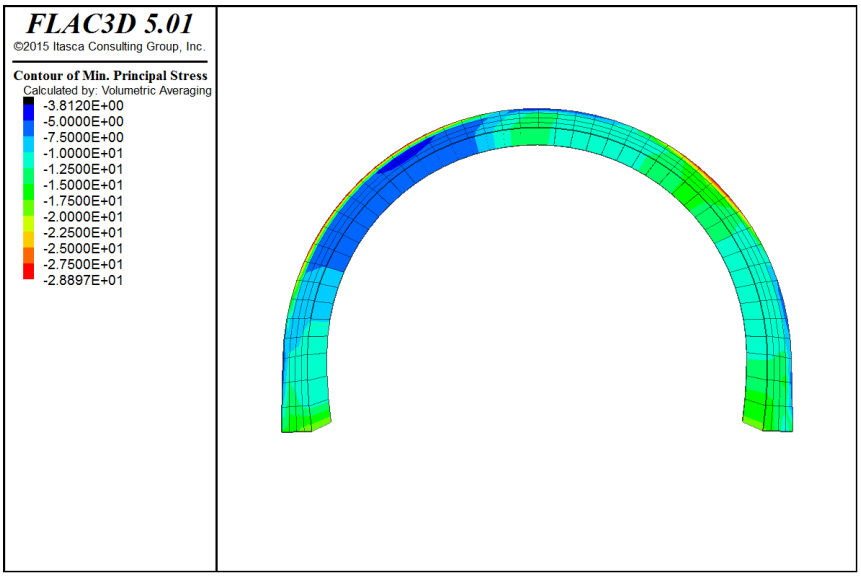

Fig. 7.14 Plot of the computed maximal principal stress in the vault of the road tunnel after 40 years

Fig 7.14 shows the computed maximal (in absolute value) principal stress in the vault of the road tunnel after 40 years. The highest value takes place in the East side of the vault where strongest

convergence occurs. The highest stress reaches 15 MPa after 40 years (Fig. 7.15). This value is slightly smaller than the admitted uniaxial compression strength of a C35/45 concrete estimated at 17 MPa. Measurements of stresses in the lining have been carried out in the road tunnel with a flat-jack test (between chainages 1800 and 2200) in recent years. In the East side of the vault values ranging from 5 to 32 MPa (with an average of 16 MPa) have been retrieved. These data are thus in accordance with the numerical predictions. From the numerical simulations, we obtain a constant convergence rate of 0.25 mm/year in the lining. The *in-situ* monitoring convergence rates of the lining range from 0.15 to 0.3 mm/year (data retrieved between chainages 1800 and 2200 from year 1980 to year 1997). The computed results and the in situ data are thus in an acceptable accordance.

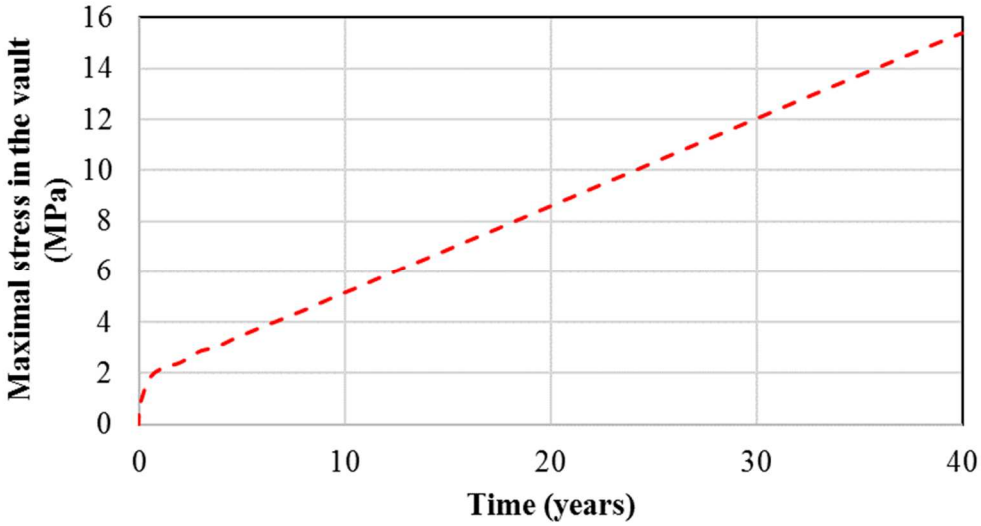

Fig. 7.15 Highest computed stress in the vault as a function of time

7.7 Conclusion

A numerical back-analysis of the convergence measurements of the Fréjus road tunnel has been carried out in order to calibrate a constitutive model able to reproduce the instantaneous and the time-dependent behavior of the rock mass in one of the most complex areas of the tunnel. The computed sections showing the smallest and the largest convergence successfully fit short-term convergences. The response of these extreme sections represents the envelope of convergences in the studied area. The obtained set of geotechnical parameters is realistic and is in accordance with the literature. The rest of the sections in the studied area are fitted by adjusting only two parameters: the joints cohesion which is related to the anisotropy of the section and a variability parameter which is representative of the magnitude of the convergences of the matrix which fall within the identified envelope of convergences.

A linear relationship between the variability parameter and a parameter which is a function of the instantaneous convergence along direction defined by targets 1 and 4 is proposed.

Furthermore, a numerical prediction of the long-term interaction between the ground and the lining of the Fréjus road tunnel has been carried out. This study is based on the hypothesis that the extrapolation of the convergence law of Sulem et al. (1987) allows for the prediction of the long term convergences of the ground integrating the rock bolting and the sprayed concrete support. These convergences are back-analyzed with the numerical model. Two different sets of parameters are necessary to fit short-term convergences and long-term convergences within the same numerical simulation. The behavior of the ground identified from the unlined tunnel is applied to simulate the lined tunnel in order to predict the long-term ground/lining interaction. Reasonable predictions of the stress state and of the convergence rate in the lining after 40 years are obtained with this approach.

CHAPTER 8 PREDICTION OF THE RESPONSE OF THE FRÉJUS SAFETY GALLERY

8.1 Introduction

In chapter 7 a calibration of a visco-elasto-plastic anisotropic model has been carried out based on convergence data recorded in the road tunnel. On the basis of the numerical study of the Fréjus road tunnel, an attempt to predict the response of the Fréjus safety gallery is presented in this chapter. The ground behavior identified from the study of the Fréjus road tunnel is extrapolated to the parallel zones of the safety gallery excavated in the same geological formation. The objective is to evaluate the stress state in the segmental lining of the gallery during excavation and to discuss also the long term predictions.

An interesting question concerns the effect of the excavation method on the ground properties. Drill and blast methods can significantly damage the rock mass whereas TBM excavation reduces the disturbance of the ground. Therefore, the long term ground properties might be affected by the excavation method. It has also been observed in several well documented cases that the deformations observed during the construction of a second parallel tube are smaller than in the first tube although the geology and the construction method of the second tube were the same as in the first tube like for example in the Simplon tunnel (Steiner 1996). This was attributed to the drainage and consolidation effects triggered by the excavation of the first tube. Even when the two tubes are far enough to preclude any mutual interaction, different responses can be observed in relation with the strong heterogeneity and local variability of the properties in squeezing grounds (Mezger et al., 2013).

Furthermore, a study of the effect of the backfilling used in the safety gallery on the stresses developed in the lining is carried out.

8.2 Interpretation of stress data retrieved from the segmental lining

Monitoring data from pairs of strain gauges embedded in the segmental lining of the safety gallery is first analyzed. The stress state in the lining can be obtained from strain data by assuming an elastic behavior of the concrete. A Young's modulus of 20 GPa is considered for the concrete.

The segmental lining is submitted to a loading which is the result of the combination of two mechanisms that take place during the excavation of the tunnel:

- Instantaneous buckling: Schistosity planes that are tangent to the tunnel wall tend to buckle during the excavation. This buckling mechanism takes place projecting rock blocks that are detached from the tunnel wall and impact the TBM and the installed

lining. Within the first meters after the TBM passage (9 m to 20 m from the tunnel face), the annular gap is not completely filled up with the backfilling material. As in consequence, the segmental lining is not protected and the detached rock blocks impact the lining favoring the emergence of cracks in the concrete.

- Time-dependent convergence of the ground: The time-dependent behavior of the ground results in a time-dependent loading of the lining during and well after the tunnel excavation.

These two mechanisms are generally combined and difficult to separate. However, in the present work, an attempt to identify the main mechanisms acting in each monitored section is carried out. From the stress data, the instantaneous buckling effect is identified and separated from the effect of a time-dependent response of the ground.

Fig 8.1 shows stress data in function of time in ring 1257 (chainage 2902). Measurements resulting from instantaneous buckling can be identified in those pairs of gauges (one at the intrados and one at the extrados) showing an opposite behavior (one gauge is compressed while the other one exhibits tensile stresses). In Fig. 8.1a, dotted lines represent stress measurements from those pairs of gauges embedded in a segmental lining which is affected by the impact of instantaneous buckling.

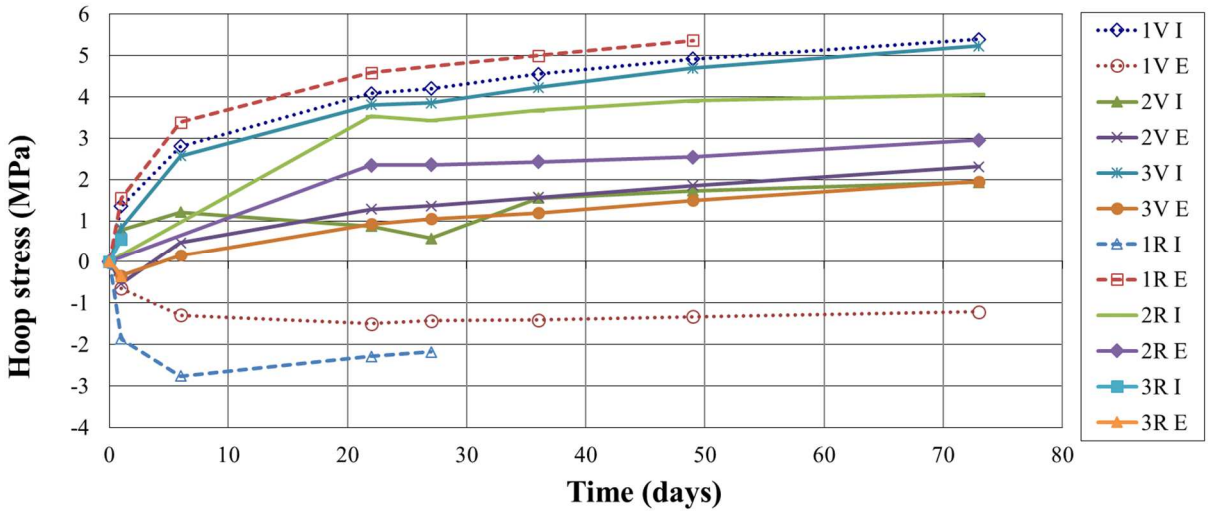

(a)

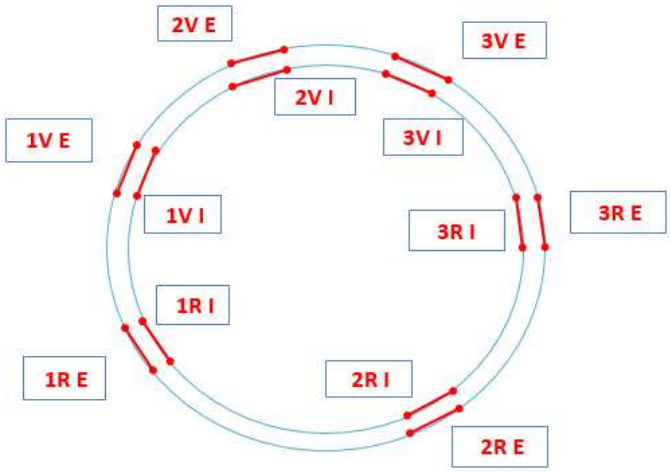

(b)

Fig. 8.1 Evolution of the stress state in function of time in ring 1257 (chainage 2902) **(a)** schematic representation of the position of the strain gauges within the concrete ring **(b)**

In Fig 8.2, the stress measurements recorded by the other sensors and mainly controlled by the time-dependent convergence of the ground are plotted.

Some tensile stresses are nevertheless observed on data plotted in Fig 8.2. They may be due to the efforts induced by the longitudinal support of the TBM which is jacked against the segmental lining in order to advance. Within the first meters after the TBM passage, the annular gap is not completely filled up with the backfilling material and as a consequence the longitudinal support of the machine may induce important tensile efforts in the segmental lining.

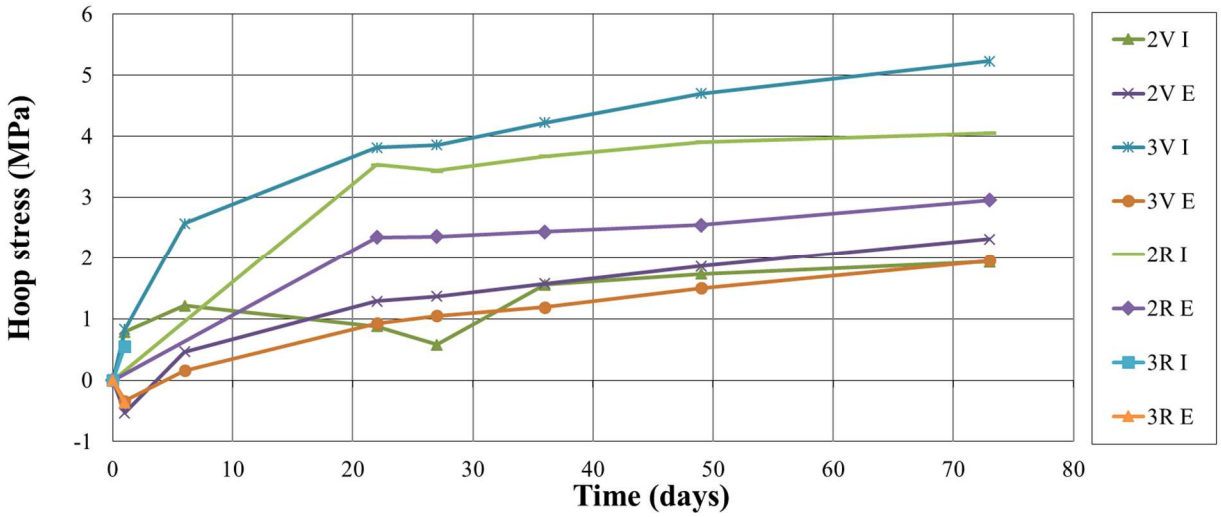

Fig. 8.2 Evolution of the stress state related to the time-dependent convergence of the ground as a function of time (ring 1257 at chainage 2902)

8.3 Numerical prediction of the safety gallery response

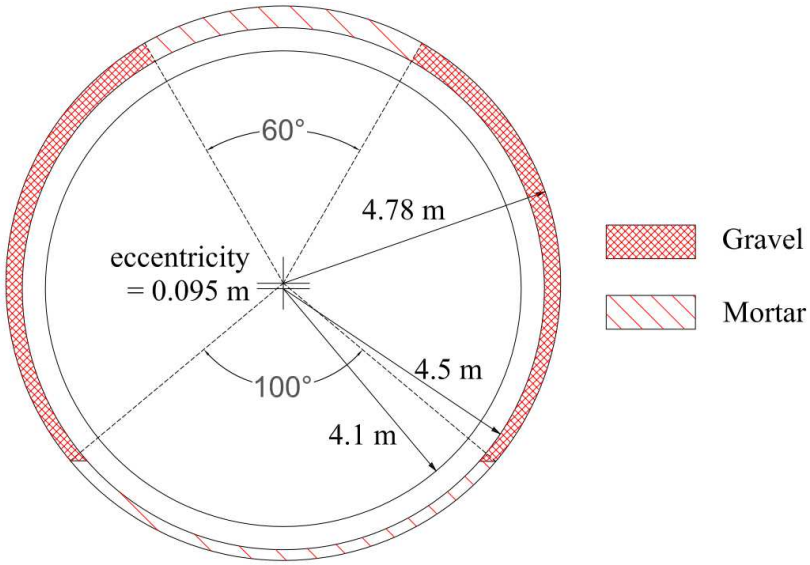

Fig. 8.3 Scheme of the geometry of the lining and the backfilling in the safety gallery

A 3D numerical simulation has been carried out with FLAC^{3D} in order to simulate the behavior of the Fréjus safety gallery. Fig. 8.3 and 8.4 show the geometry of the numerical model. Far field boundaries are placed at a distance of 36 radii (considering an outer radius of the gallery *R* of 4.5 m) in order to minimize boundary effects. The length of the model is 90 m. An average value of 190 mm is assumed for the overcutting and an eccentricity of the lining (0.095 m) with respect to the TBM cutting head is considered. The size of the elements at the tunnel wall is of 0.6 m. The *in-situ* stress state is initially imposed everywhere in the domain (average depth of 1067 m and average specific weight of the ground of 27 kN/m^3). Gravity effects are disregarded. The step of excavation is 1.8 m which corresponds to the transversal length of a segmental lining. An advancing rate of 12.9 m/day is considered in accordance with the average advancing rate observed during the excavation of the safety gallery. A small enough time step is chosen in order to guarantee quasi-static mechanical equilibrium (Billaux & Cundall, 1993).

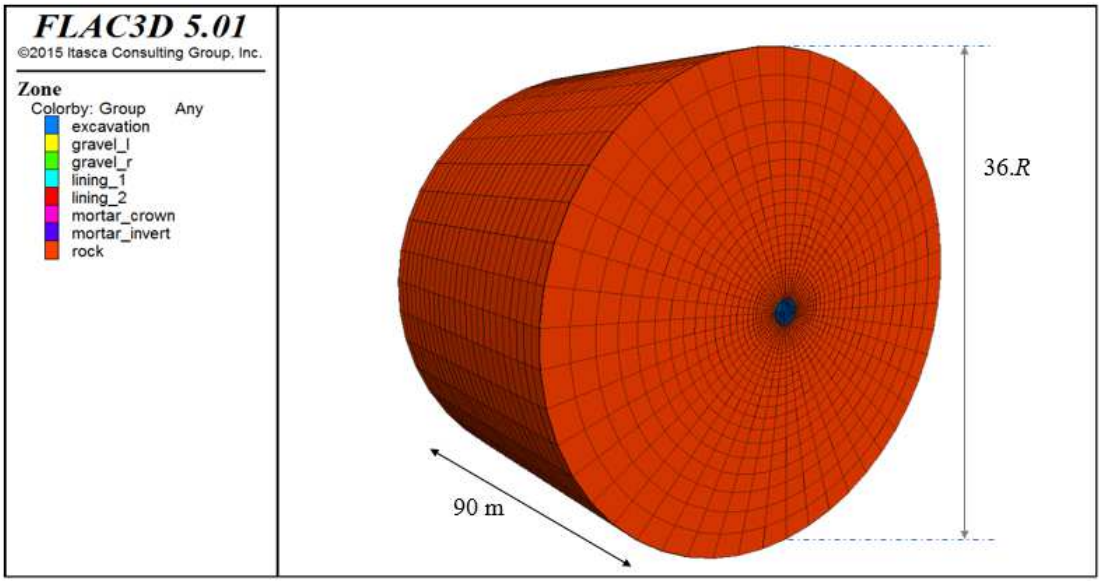

Fig. 8.4 Geometry of the numerical model of the safety gallery

Buckling phenomena are not considered in the present study. The unsupported spam is taken equal to 19.8 m. It is assumed that the annular gap is completely filled up with the backfilling material only at this distance of 19.8 m. A "sandwich" type backfilling composed of gravel and mortar is considered in the simulations. The gravel and the mortar are assumed to have an elastic response with a Young's modulus of 100 and 500 MPa respectively. The installed elastic lining has a thickness of 40 cm and its Young's modulus is 20 GPa.

The ground behavior identified from the study of the road tunnel is extrapolated for the simulation of the safety gallery. From preliminary computations, it was obtained that assuming the same values for the constitutive parameters as those calibrated on the road tunnel leads to an overestimation of the stresses in the lining. As the lining is placed at a distance of more than two diameters to the tunnel face, its response is mainly controlled by the time-dependent behavior of the rock mass. Therefore, the instantaneous constitutive parameters are kept the same in both tunnels and the time-dependent parameters (η_M, η_k, G_k) are adjusted and multiplied by a factor F. This is attributed to the fact that, when tunneling with a TBM, the ground is less damaged than when tunneling by drilling and blasting and as a consequence time-dependent convergence is expected to be lower. It is found that the Fréjus safety gallery response can be correctly reproduced by taking a value of F equal to 15.

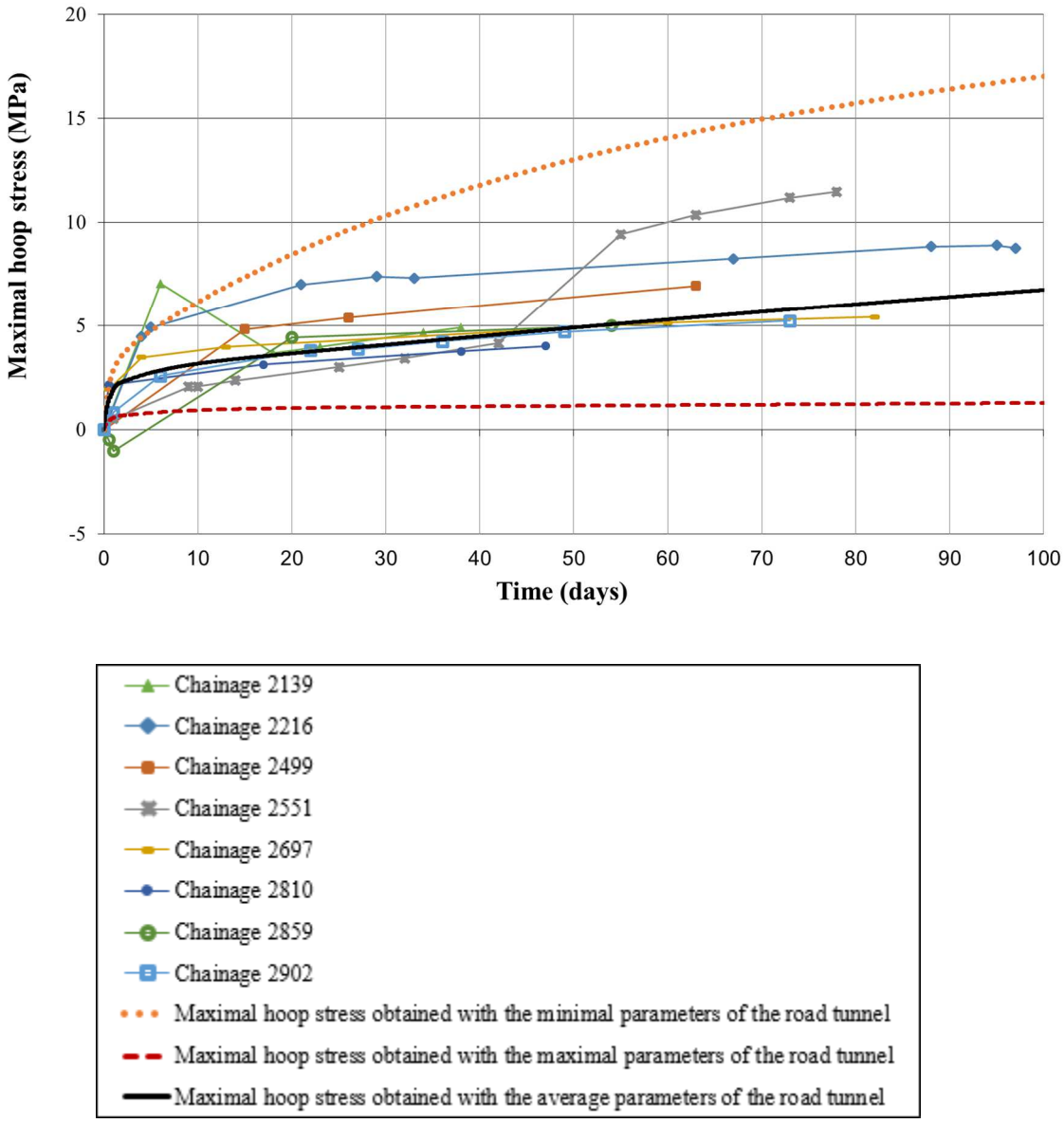

Fig. 8.5 Predicted envelope of maximal hoop stress in the safety gallery and retrieved maximal hoop stress from sections within zone A

Fig. 8.5 shows the envelope of the predicted maximal hoop stresses (dotted lines) in the lining. This maximal stress state corresponds to the zone of stress concentration in the lining (Fig. 8.7). These computations are performed by taking the constitutive parameters calibrated on the sections of the road tunnel which exhibits the highest and the lowest convergence. We can observe that the maximal hoop stresses (resulting only from the time-dependent behavior of the ground) retrieved from the different sections of the safety gallery in zone A fall within the predicted envelope. The average maximal hoop stress obtained with the model parameters describing the average behavior of the road tunnel (α = 0.6 and c_f = 0.2 MPa) is also plotted in Fig. 8.5 (black thick solid line).

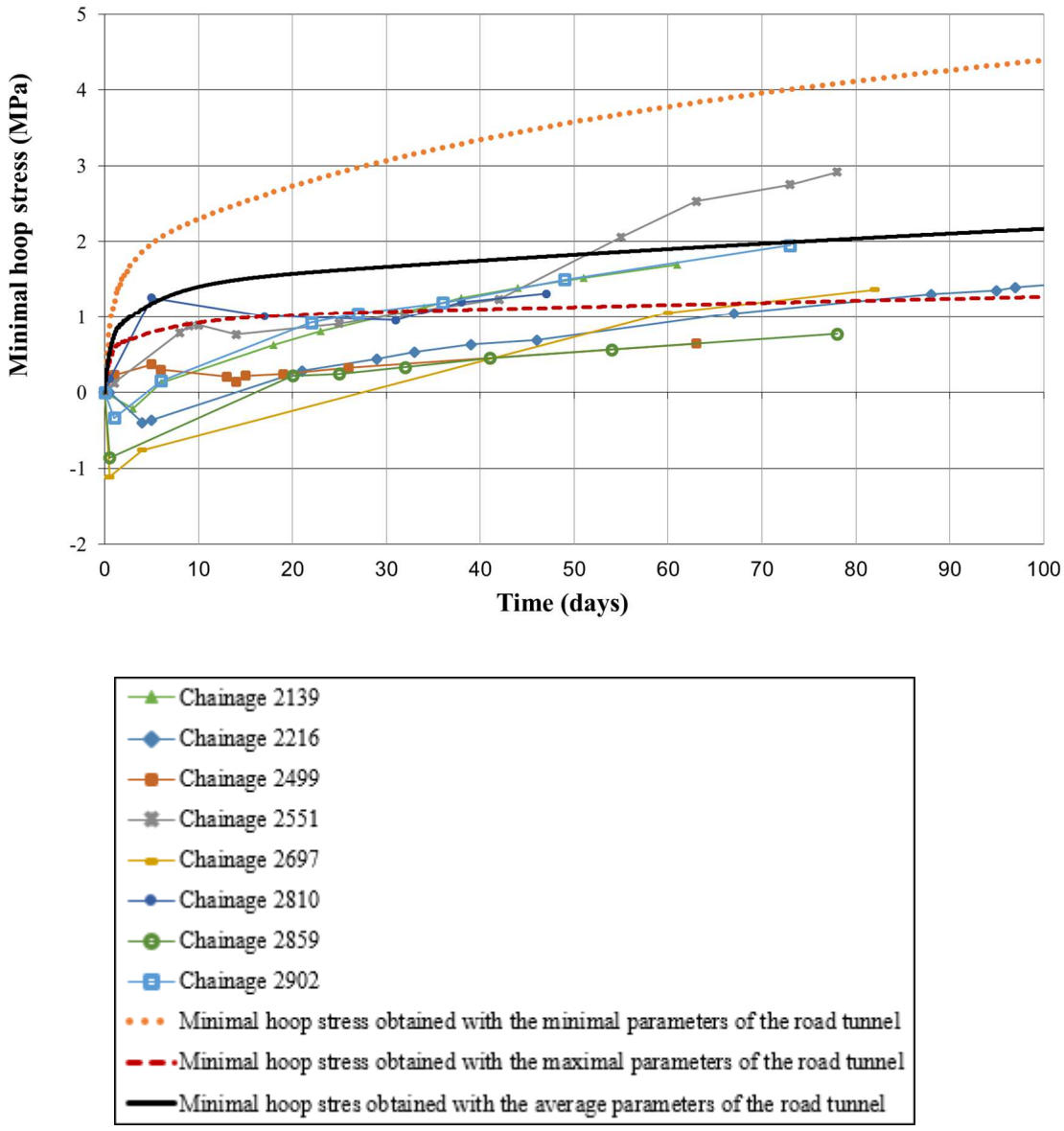

Fig. 8.6 Predicted envelope of minimal hoop stress in the safety gallery and retrieved minimal hoop stress from sections within zone A

Similarly, Fig. 8.6 shows the predicted envelope of the minimal hoop stresses in the lining. We observe that the minimal hoop stresses retrieved from the safety gallery are predicted with less accuracy than the retrieved maximal stresses. The numerical results tend to overestimate the minimal stresses and tensile stresses are not obtained.

Following the sign convention of FLAC^{3D}, compressions are taken negative, thus compressive stresses correspond to the minimal principal stresses as plotted in Fig 8.7. We can observe that the maximal compression is located at the invert as the mortar injected in the annular gap tends to lead to stress concentration in this area (see Fig. 8.7).

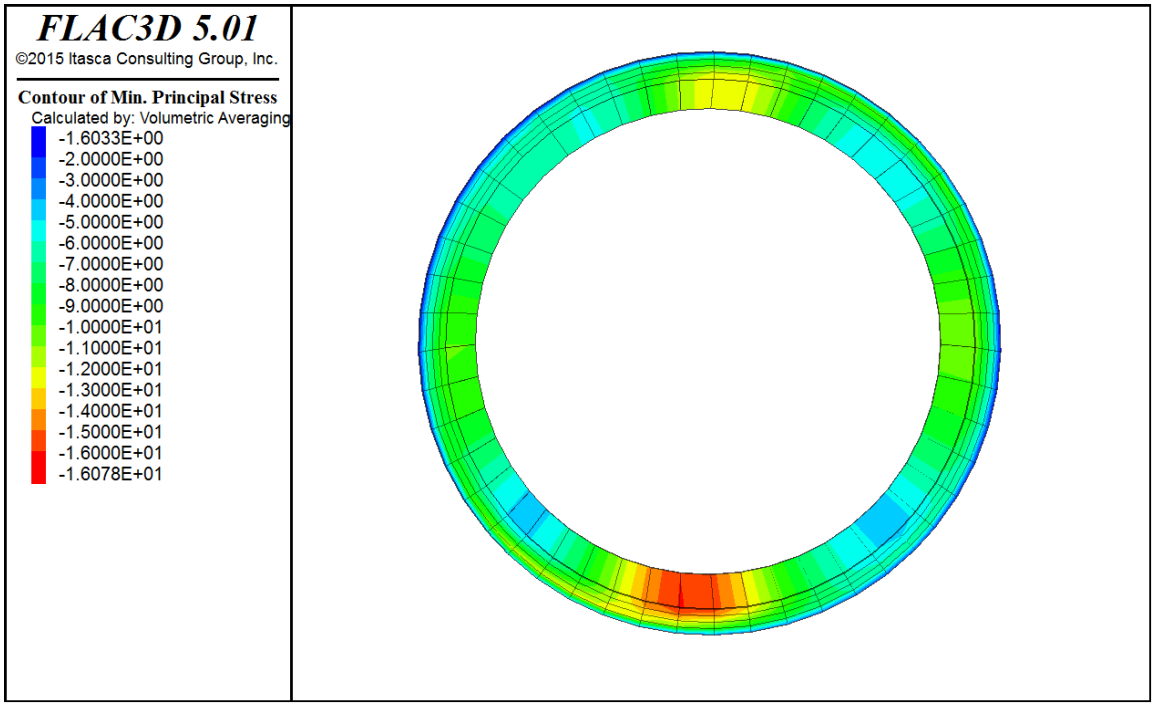

Fig. 8.7 Minimal principal stress (maximal compression) in the lining after 3 months (the constitutive parameters that give the larger efforts are assumed in the computation)

8.4 Long-term numerical prediction of the Fréjus safety gallery

The above numerical simulations show an accurate short-term prediction of the safety gallery response as a good approximation of field data has been achieved. However, the question arises concerning the long term predictive capacity of the numerical model as applied to the safety galley. Obviously no long term data are available at the moment, therefore only blind predictions can be performed. A numerical prediction of the average long-term behavior (40 years) of the Fréjus safety gallery has been carried out. For that, we consider the constitutive parameters of the model corresponding to the average behavior (see Fig. 8.5) as used for the short term predictions. For the segmental lining, we take a constant Young modulus of 12 GPa corresponding to the long term behavior of the concrete. The mechanical properties of the mortar and the gravel are kept unchanged. The numerical computations lead to a maximal compressive stress located at the invert of about 25 MPa in the lining after 40 years (see Fig. 8.8). This prediction looks reasonable and gives confidence to the predictive capability of the proposed approach.

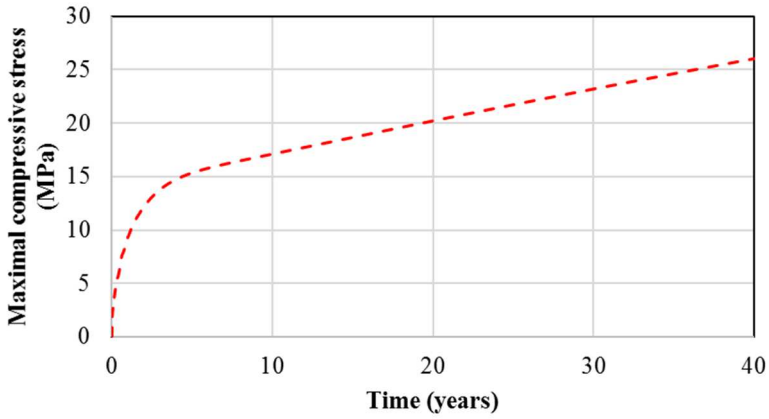

Fig. 8.8 Highest computed compressive stress as a function of time.

8.5 Effect of the backfilling on the efforts developed in the segmental lining

In the following, we explore the role of the backfilling on the efforts developed in the lining. For simplicity, a 2D "equivalent" plane strain model is proposed. As the unsupported span is 19.8 m, it is assumed that a deconfining rate of 100% has already taken place when the lining and the backfilling are installed. The 2D numerical simulation is carried out in two steps:

- Instantaneous excavation of the tunnel considering an instantaneous behavior of the ground (no time-dependent effect).
- Installation of the lining and the backfilling and activation of the time-dependent behavior of the ground in the numerical model.

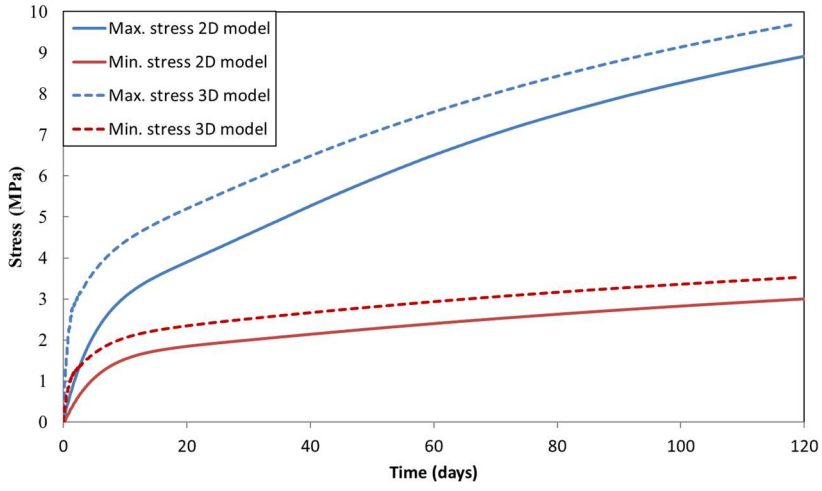

Fig. 8.9 Comparison of the evolution of the maximal and the minimal stresses in the lining obtained from a 3D model and a 2D plane-strain model

Fig. 8.9 shows the maximal and the minimal stresses in the lining obtained from the plane-strain and the 3D simulations (α = 0.65, c_j = 0.09 MPa, F = 10). The elements size of the mesh is the

same in both models. Both approaches show similar results. In Fig. 8.10 and 8.11 computed minimal principal stresses of both simulations are plotted. We can conclude that the 2D "equivalent" plane-strain model is acceptable as the stress state obtained from both computations is comparable.

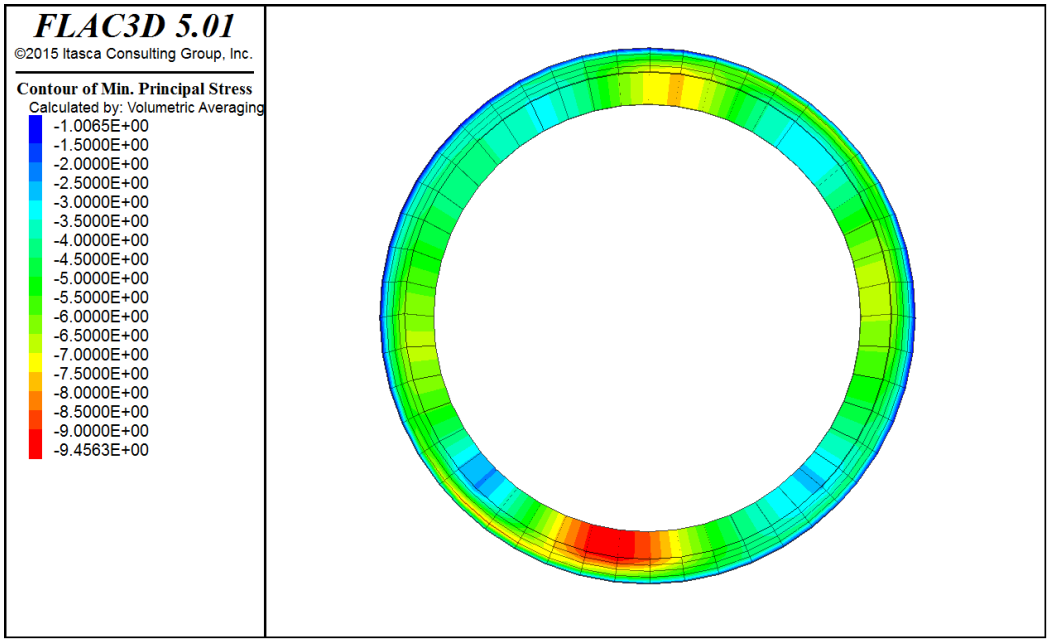

Fig. 8.10 2D plane-strain model: Minimal principal stress (maximal compression) four months after the lining installation

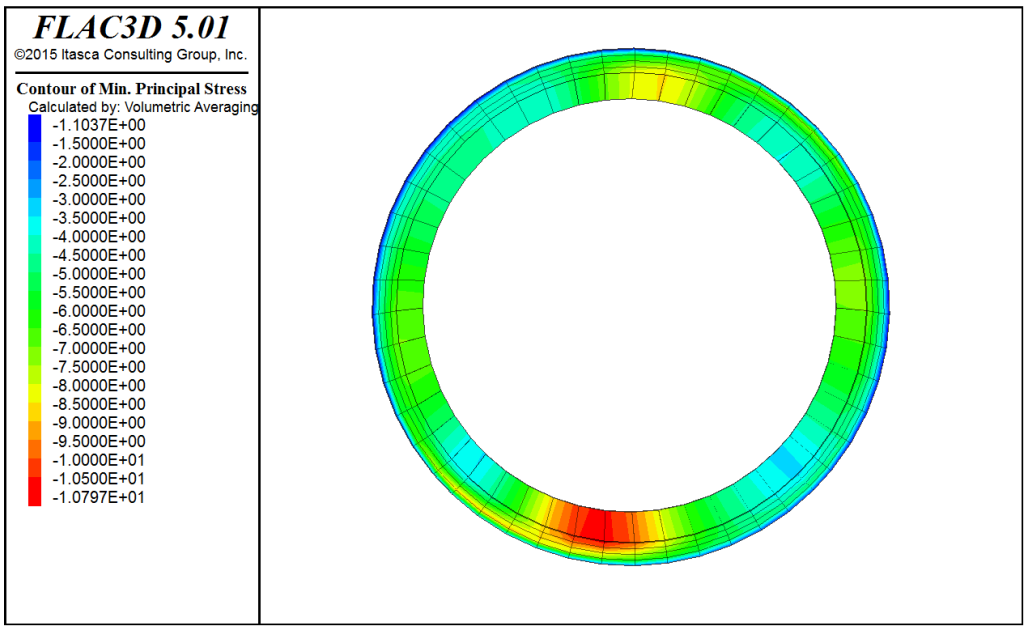

Fig. 8.11 3D model: Minimal principal stress (maximal compression) four months after the lining installation

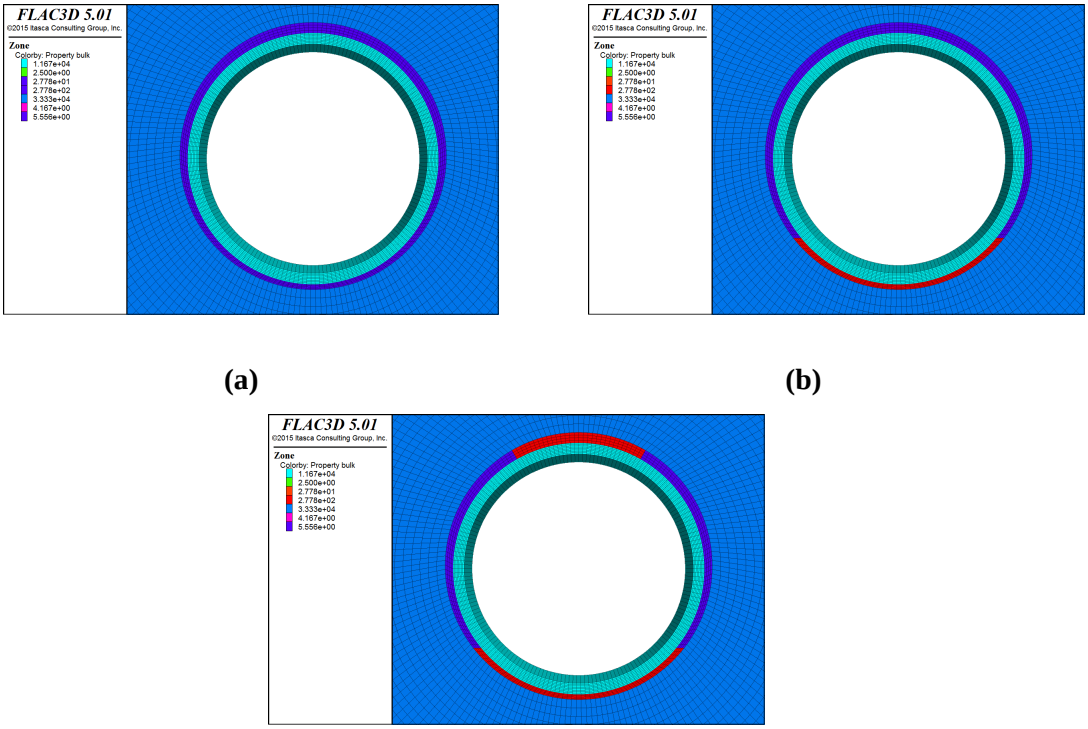

Fig. 8.12 Annular gap filled up with a homogenous backfilling material composed of gravel (gravel backfilling) **(a)**, annular gap filled up with mortar in the invert and with gravel in the rest (gravel + mortar backfilling) **(b)**, annular gap filled up with mortar in the invert and in the crown and with gravel in the rest ("sandwich" backfilling) **(c)**

In order to study the influence of the backfilling on the efforts in the lining three different configurations have been studied (Fig. 8.12): (i) annular gap filled up with a homogenous backfilling material composed of gravel (gravel backfilling), (ii) annular gap filled up with mortar in the invert and with gravel in the rest (gravel + mortar backfilling) and (iii) annular gap filled up with mortar in the invert and in the crown and with gravel in the rest ("sandwich" backfilling). An elastic response is assumed for the gravel and the mortar with a Young's modulus of 100 and 500 MPa respectively.

Each configuration has been studied under four different scenarios in order to assess the effect of anisotropic initial state and anisotropic behavior of the rock mass:

- Isotropic conditions. The stress state is isotropic ($K_0 = 1$) and the constitutive model is visco-elasto-plastic and isotropic with α = 0.65 and F = 10 (the joints are not activated within this scenario).
- Anisotropic constitutive model. The stress state is isotropic ($K_0 = 1$) and the constitutive model is visco-elasto-plastic anisotropic with α = 0.65, c_j = 0.09 MPa and F = 10.

- Anisotropic stress state. The stress state is anisotropic with K_0 of 1.4 and the constitutive model is visco-elasto-plastic and isotropic with α = 0.65 and F = 10 (the joints are not activated within this scenario).
- Anisotropic constitutive model and stress state. The stress state is anisotropic with K_0 of 1.4 and and the constitutive model is visco-elasto-plastic anisotropic with α = 0.65, c_j = 0.09 MPa and F = 10.

The efforts developed in the lining are studied for each configuration and each scenario (Fig 8.13).

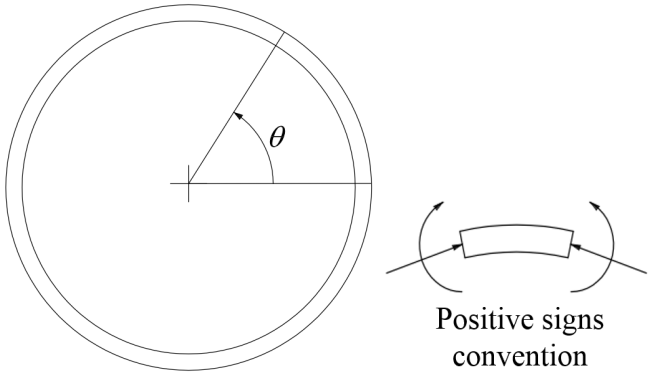

Fig. 8.13 Position and sign convention for the efforts developed in the lining

The configuration where the annular gap is only filled up with gravel (Fig. 8.11 (a)) is first studied (Fig. 8.14 and 8.15).

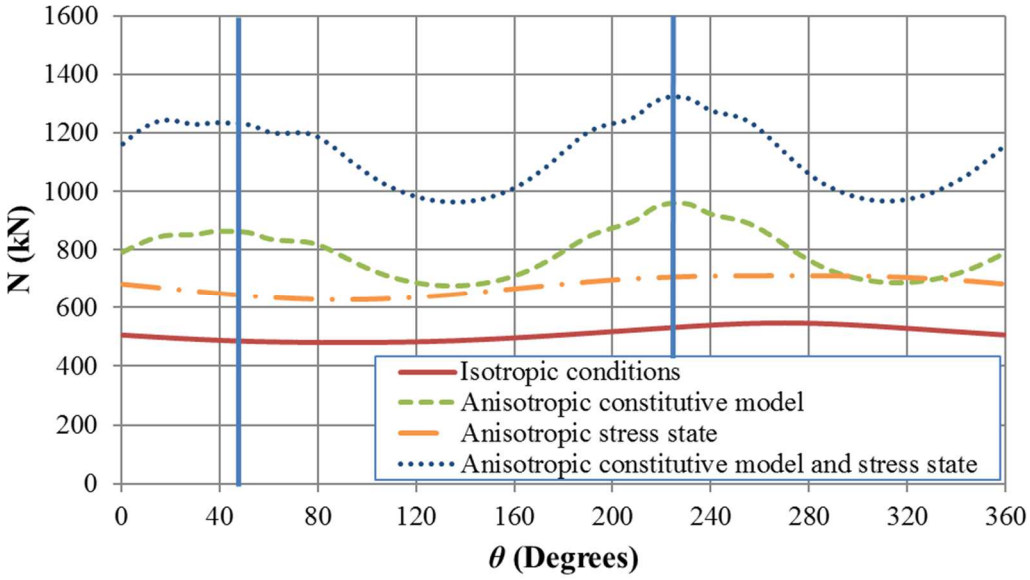

Fig. 8.14 Configuration with only gravel backfilling: Normal load developed in the lining in function of the position θ three months after the lining installation. Blue vertical lines indicate the points at the tunnel wall where larger convergences take place (when joints are active)

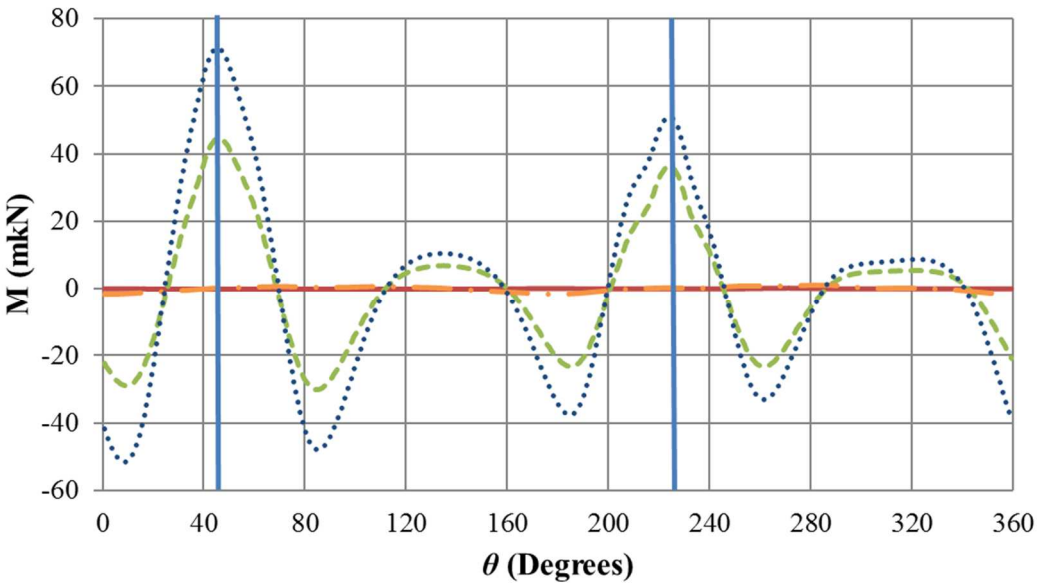

Fig. 8.15 Configuration with only gravel backfilling: Bending moments developed in the lining in function of the position θ three months after the lining installation. Blue vertical lines indicate the points at the tunnel wall where larger convergences take place (when joints are active)

The plots in Fig. 8.14 and Fig. 8.15 show that under isotropic conditions of the ground, bending moments developed in the lining are almost zero and normal efforts are almost constant. Small variations of the efforts are due to the small variations of the thickness of the annular gap because of the eccentricity of the lining (0.095 m) with respect to the TBM cutting head. When an anisotropic initial stress state is considered, normal efforts are increased everywhere in the lining. Furthermore, the bending moments are here again negligible because of the homogenization effect of the backfilling. However, the influence of an anisotropic constitutive behavior of the ground is more important. The presence of localized strong convergences at the tunnel wall induces an increase on the efforts everywhere in the lining. In particular, in those areas where the strongest convergences take place the strongest efforts are obtained. This effect is amplified when an anisotropic stress state is considered in the computations. It can be inferred from these results that when the joints are active, the performance of the backfilling is less than for an isotropic behavior of the ground.

Until chainage 1763, mortar was injected in the invert before the installation of the concrete rings. Fig. 8.16 and 8.17 show the computed distribution of the efforts in the lining for a “mortal + gravel” configuration. The effect of the mortar injected in the invert can be observed. The injected mortar concentrates normal loads in the lining. Furthermore, bending moments appear in the contact between mortar and gravel because of the differences in stiffness of both materials.

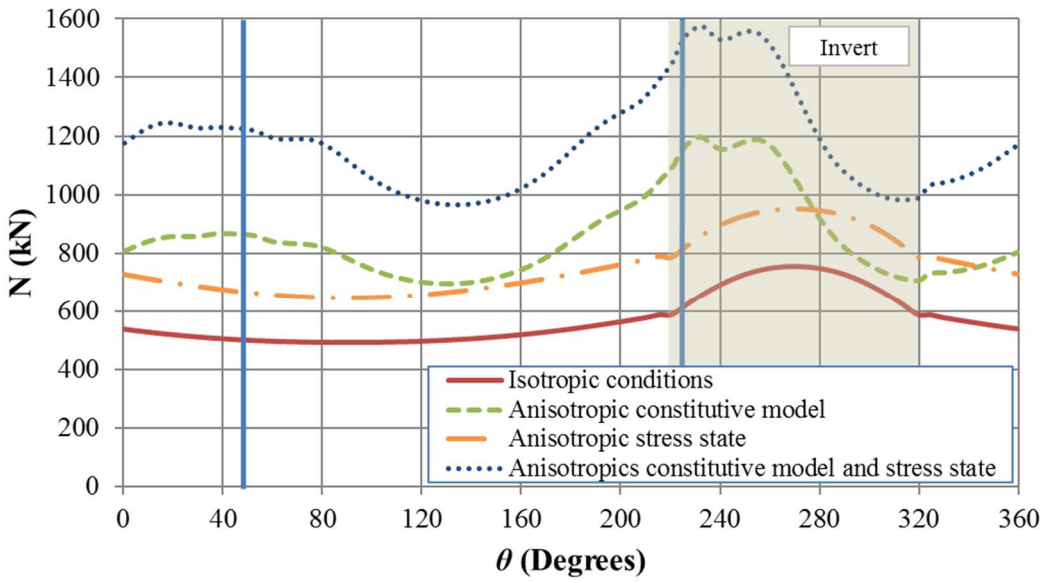

Fig. 8.16 Configuration with mortar + gravel backfilling: Normal loads developed in the lining in function of the position θ three months after the lining installation. Blue vertical lines indicate the points at the tunnel wall where larger convergences take place (if joints are active). Shaded areas in the graph indicate the zones where mortar was injected

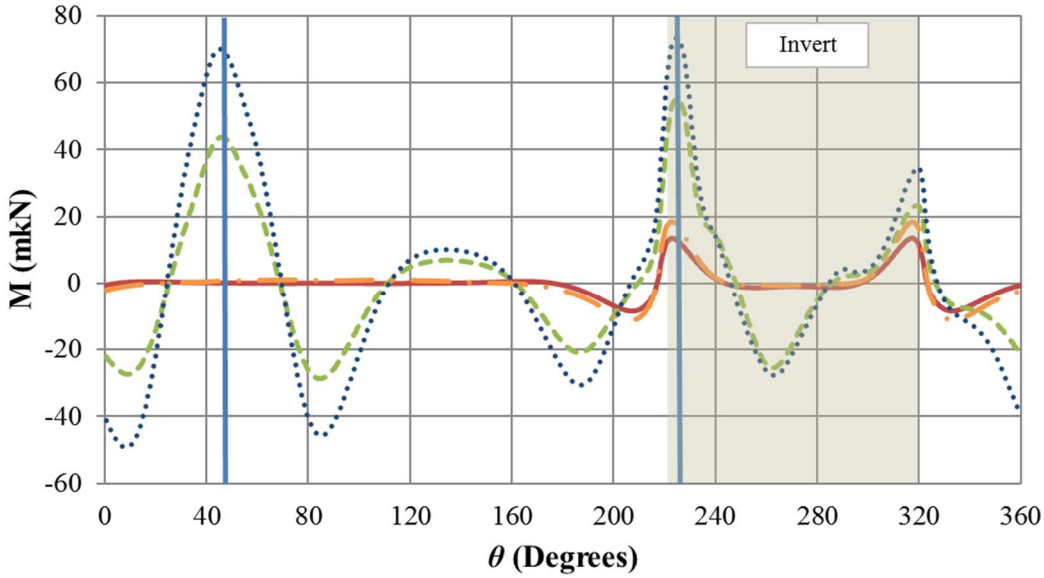

Fig. 8.17 Configuration with mortar + gravel backfilling: Bending moments developed in the lining in function of the position θ three months after the lining installation. Blue vertical lines indicate the points at the tunnel wall where larger convergences take place (if joints are active). Shaded areas in the graph indicate the zones where mortar was injected

With a “sandwich” type backfilling efforts are also increased in the crown (Fig. 8.18 and 8.19).

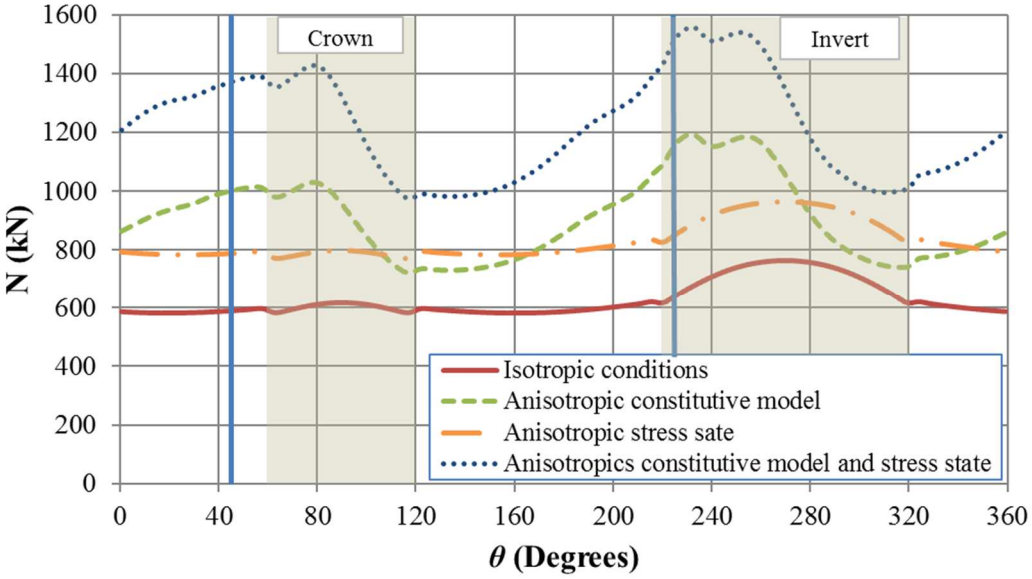

Fig. 8.18 Configuration with sandwich backfilling: Normal loads developed in the lining in function of the position θ three months after the lining installation. Blue vertical lines indicate the points at the tunnel wall where larger convergences take place (if joints are active). Shaded areas in the graph indicate the zones where mortar was injected

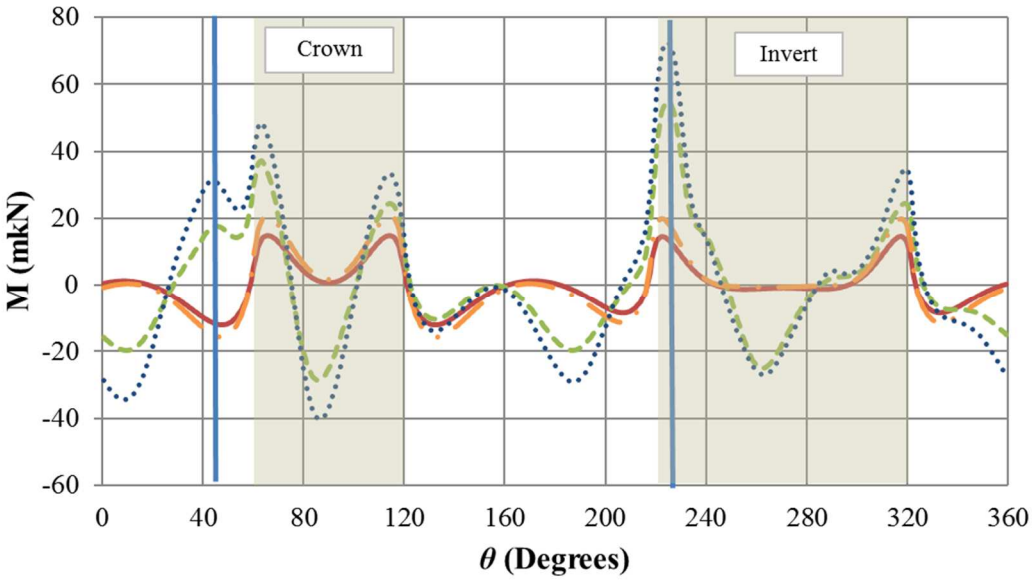

Fig. 8.19 Configuration with sandwich backfilling: Bending moments developed in the lining in function of the position θ (sandwich backfilling) three months after the lining installation. Blue vertical lines indicate the points at the tunnel wall where larger convergences take place (if joints are active). Shaded areas in the graph indicate the zones where mortar was injected

8.6 Conclusion

The Fréjus safety gallery response can be predicted by extrapolating the ground behavior identified from the study of the Fréjus road tunnel. It is observed that although instantaneous parameters can be assumed the same in both tunnels, the time-dependent constitutive parameters of the rock mass to be considered in the numerical model depend upon the excavation process. It is obtained that the shear modulus and the viscosity of the Kelvin element and the viscosity of the Maxwell element of the considered CVISC constitutive model have to be multiplied by a factor F=15 for the rock mass for TBM excavation (Fréjus safety gallery) as compared to drilling and blasting excavation process (Fréjus road tunnel). This can be attributed to the significant damage induced in the rock by blasting effects. Very good predictions of the maximal hoop stress are obtained when compared to the retrieved data. However, the minimal hoop stress is slightly overestimated.

Numerical computations have been pursued up to 40 years in an attempt to evaluate the predictive capacity of the model. For that, we consider a section of the safety gallery with model parameters corresponding to an average behavior. It is obtained that the maximal compressive stress reaches 25 MPa after 40 years. Of course, no field data are yet available for this long term response. However, one may consider that predicted stresses are in a reasonable range and that the limit strength of the lining might be reached in some sections.

The effect of the backfilling used in the safety gallery has been studied. It can be inferred that the backfilling homogenizes the stress state in the lining for isotropic behavior of the ground (even under anisotropic initial stress state). However, the performance of the backfilling is less for strong anisotropic behavior of the rock mass as strong convergences are concentrated within some areas at the tunnel wall. The injection of mortar in the invert and in the crown of the annular gap plays a major role in the stabilization of the concrete rings. However, it is observed that the discrepancy between the stiffness of the mortar and the stiffness of the gravel increases the efforts in the lining.

CONCLUSIONS AND PERSPECTIVES

1. Main findings and conclusions

The present work aimed at studying the behavior of tunnels excavated under squeezing conditions. Particular attention has been paid to the effect of the method of excavation on the response of the tunnel. For that, we have referred to the case study of the Fréjus road tunnel and of its safety gallery which are an example of two parallel tunnels excavated in such difficult conditions but with different methods. The Fréjus tunnel response which was excavated by drill and blast methods is compared to that of its safety gallery which was excavated with a TBM.

Applicability of the convergence-confinement method to full-face excavation of circular tunnels with stiff support installed near the face

In the present study, the ConVergence-ConFinement (CV-CF) methods have first been revisited. Their applicability in a pre-design stage of full-face circular tunnels with a stiff support system near the face has been studied. The CV-CF methods which are based on plane-strain assumptions are compared with numerical simulations. The numerical simulation is able to capture the 3D effects which take place close to the excavation face. It was conclude that the so called “implicit methods” (Nguyen-Minh & Guo or Vlachopoulos & Diederichs) in combination with any LDP expression (Panet, Corbetta or Vlachopoulos & Diederichs) give a reliable evaluation of the stress state at equilibrium in the support provided that the lining is relatively soft, and for for values of the stability number N ranging from 1 to 5. The evaluation of the radial convergence of the ground is good with any CV-CF approach. The accuracy of the equilibrium state prediction with the different methods decreases with increasing dilatancy angle.

Proposition of an empirical formula for the design of circular tunnels excavated in full section

A set of empirical formula have been proposed in order to predict the equilibrium state of circular tunnels excavated in full section. A large range of ground and lining properties have been covered with the empirical approach. The prediction of the stress state in the lining is obtained with an accuracy of 10% while the predicted displacement is obtained with an accuracy of around 20%.

Analysis of monitoring data of the Fréjus road tunnel

The Fréjus road tunnel was confronted to squeezing ground conditions during and well after its excavation which was performed by drill and blast methods. A survey campaign was carried out in the tunnel in order to monitor the convergences of the tunnel wall during the excavation works. The strongest convergence generally occurs along the direction defined by targets 2 and 4 which is quasi

perpendicular to the schistosity planes. A first analysis of the convergence data consisted in a robust fitting of the convergence measurements of Fréjus road tunnel by means of the semi-empirical law of Sulem et al. (1987). With this simple technique, ground convergences are well represented. Furthermore, this analysis has led to the identification of some "homogeneous" zones. These zones correspond to similar values of the instantaneous convergence $C_{\infty x}$ along direction 2-4. However, the rate of convergence does not seem to correlate to the magnitude of the convergences. The values of the characteristic time T of the convergence law are quite heterogeneous and range from 0.5 to 5 days.

Analysis of monitoring data of the Fréjus safety gallery

The Fréjus safety gallery runs in parallel to the road tunnel. In consequence, it encounters similar geotechnical conditions. During the excavation of the safety gallery carried out with a single shield TBM an important survey campaign took place. The collected monitoring data consisted in: convergence data at the inner face of the concrete ring, convergence data of the ground measured with hydraulic jacks through the TBM shield, monitoring data obtained from strain gauges embedded in the segmental lining of 49 sections which can provide information on the state of stress in the lining, cracks observations and other information obtained during the excavation such as the thrust force exerted by the TBM. From the analysis of these data it is concluded that the most reliable ones correspond to the ones retrieved from strain gauges.

A comparison between the two parallel tunnels has been carried out. There is a good agreement between the monitoring data of both tunnels. Those areas of the tunnel where strongest convergences are observed correspond to the zones of the gallery where a higher stress state was measured in the lining.

Numerical back-analysis of the Fréjus road tunnel

The instantaneous and the time-dependent behavior of the rock mass of the Fréjus road tunnel has been studied by means of a numerical back-analysis of the convergence measurements of the road tunnel. The constitutive model of the rock mass is visco-elasto-plastic with weakness planes (ubiquitous joints model) in the direction of the schistosity of the ground in order to account for its anisotropy. A calibration method has been developed in order to properly fit most of the sections in of one of the most complicated areas of the road tunnel. This method consists in the identification and on the back-analysis of the sections of the road tunnel showing the smallest and the larges convergences. The rest of the sections of the studied area can be fitted by adjusting the joints cohesion and a variability parameter which represents the magnitude of the convergences of the matrix. The limitations of the model in terms of anisotropy have been studied with this work as sections showing an anisotropy factor larger than 4 cannot be properly simulated.

Based on the extrapolation of the convergence law of Sulem et al. (1987) a prediction of the long-term convergences of the ground in an hypothetical unlined road tunnel has been carried out. These long-term convergences have been back-analyzed with the numerical model by using two set of parameters within the same numerical simulation: a first set of parameters used in order to back-analyze the short-term convergences and a second set of parameters used in the back-analysis of the long-term convergences. Finally, the behavior of the ground is used to simulate the road tunnel with its support system. Reasonable predictions of the stress state developed in the lining after 40 years have been obtained following this methodology.

Numerical back-analysis of the Fréjus safety gallery

An attempt to predict the response of the Fréjus safety gallery has been presented in this study. The behavior of the ground identified with the study of the road tunnel has been extrapolated to the parallel zones of the safety gallery. From the numerical results, we have concluded that although instantaneous parameters can be assumed the same in both tunnels, the time-dependent constitutive parameters of the rock mass to be considered in the numerical model depend upon the excavation process. In practice, the shear modulus and the viscosity of the Kelvin element and the viscosity of the Maxwell element need to be multiplied by a factor F=15 for the modelling of the TBM excavation (Fréjus safety gallery) as compared to drilling and blasting excavation process (Fréjus road tunnel). The reason of the existing of factor F stems from the fact that the damage induced in the rock by blasting effects is more important than the one induced by a mechanized excavation. The results of the prediction are very good in terms of the maximal hoop stress if compared to the retrieved field data (3 months of monitoring). However, the minimal hoop stress is slightly overestimated. With the same set of model parameters (except the consideration of a long term Young's modulus of the concrete of the lining), the computations are pursued up to 40 years. It is obtained that the proposed model leads to reasonable long term predictions which however cannot be confirmed in absence of long term field data.

A detailed study of the effect of the backfilling used in the safety gallery has also been proposed. For an isotropic behavior of the ground, the backfilling homogenizes the stress state in the lining (even if the initial stress state is anisotropic). However, if the rock mass exhibits a strongly anisotropic behavior the performance of the backfilling is less efficient as strong convergences are concentrated within some areas at the tunnel wall. The concrete rings need to be stabilized after their installation. For this reason, mortar is injected in the invert and in the crown of the annular gap. However, it is observed that the discrepancy between the stiffness of the mortar and the stiffness of the gravel increases the efforts in the lining.

2. Practical implications for the design

The study of the CV-CF methods has clarified their applicability to full face circular tunnels with stiff support near the face. It will allow the engineer to choose the most appropriate method for a preliminary stage of the design of a tunnel. If the parameters of the mechanical problem fall outside of the applicability domain, the proposed empirical formula can be used in order to obtain the equilibrium state between the ground and the support/lining.

The empirical law of Sulem et al. (1987) is a very powerful tool which can be used to accurately reproduce the convergences that take place at the tunnel wall. It can be used to determine homogeneous zones in a tunnel in terms of one or more parameters of the law. In the present work, the fitting law has also been used as a prediction tool in order to evaluate long-term convergences.

A simple methodology for the numerical back-analysis of a tunnel excavated by conventional methods (the Fréjus road tunnel) in squeezing ground has been proposed. The first step consists on the identification and the fitting of the sections showing an extreme behavior in terms of convergence data in the studied area. The response of these sections represents the envelope of convergences. The behavior of the rest of the sections will fall within the identified envelope. The rest of the sections can be fitted by adjusting a parameter related to the anisotropy of the section (the joints cohesion) and a parameter which is representative of the magnitude of the convergences. A similar approach could be applied to other projects of tunnels excavated in squeezing ground.

The constitutive model chosen for the numerical simulations of the Fréjus tunnel and of its safety gallery is quite simple and it is able to reproduce a visco-elasto-plastic and anisotropic behavior of the ground. However, it reaches its limits under strong anisotropic conditions. Furthermore, the presence of a constant dynamic viscosity of the Maxwell element η_M gives as a result a constant convergence rate at mid-term and at long-term. In practice, this parameter might be adjusted for reasonable long term predictions.

When survey galleries are excavated before the execution of a tunnel for the study of the ground properties, they are generally excavated with conventional techniques. These properties are in many cases directly used in the design of the main tunnel. However, the size effect and the technique of excavation play an important role in the mechanical response of the ground. If the main tunnel is excavated with a TBM, due attention should be paid to the extrapolation of the properties retrieved from the survey gallery as the damage state of ground might be significantly different.

From the numerical study of the backfilling, it can be assessed that the injection of mortar in the annular gap of a tunnel excavated with a TBM should be carefully studied. Hard points can be created in the backfilling which could punctually favor stress concentration in the lining.

3. Suggestions for future research

Preliminary design methods

The study of the CV-CF methods falls within the framework of an instantaneous behavior of the ground. The consideration of the time-dependent and anisotropy effects would be the next step in this research. The differed effects could be considered by progressively degrading the mechanical parameters of the ground as proposed by Tran Manh et al (2016) or by means of visco-plastic rheological models.

The proposed empirical formula in order to predict the equilibrium state of circular tunnels excavated in full section have considered an unsupported length equal to the tunnel diameter (the normalized parameter d^*has been fixed to 1). It would be interesting to extend the formulation having this parameter as a variable. More generally, other constitutive models (such as Hoek and Brown failure criterion) could be considered to enrich the empirical approach. The empirical formula could be enhanced with an equation for the convergence that takes place between the tunnel face and the shield tail.

Numerical developments

Concerning the time-dependent and anisotropic behavior of the ground, in the proposed visco-elasto-plastic anisotropic model, the anisotropy of the rock mass is taken into account by considering weakness planes in a isotropic matrix. Extension of the model to an anisotropic matrix will permit to describe stronger anisotropic effects as observed in some sections of the Fréjus tunnel. Furthermore, introducing non-linear parameters for the Maxwell and the Kelvin elements will permit to describe decreasing creep rates in the long-term. One possibility would be that these parameters evolve with the cumulated deviatoric strain. Another type of constitutive models based on time-dependent degradation of the rock mass properties could be further developed. This approach has been initiated in the paper of Tran Manh et al. (2016) and presently pursued in another PhD work devoted to the Lyon-Turin base tunnel. Furthermore, it would be useful to relate the mechanical parameters of the visco-elasto-plastic anisotropic numerical model and the parameters of the convergence law. For that, one could pursue the development of empirical relationships (Tran Manh et al., 2016)

REFERENCES

AFTES (2002) Recommandations pour l'emploi de la méthode convergence-confinement. Tunnels et Ouvrages Souterrains 170:79-89 (in French)

ASTM (1991) In-situ compressive stress within solid unit masonry estimated using flat-jack measurements, ASTM Standard C 1196-91

Aydan, Ö., Akagi, T., & Kawamoto, T. (1993). The squeezing potential of rocks around tunnels; theory and prediction. Rock mechanics and rock engineering, 26(2):137-163

Aydan, Ö., Akagi, T., & Kawamoto, T. (1996). The squeezing potential of rock around tunnels: theory and prediction with examples taken from Japan. Rock mechanics and rock engineering, 29(3):125-143

Barla, G., & Rossi, P. P. (1983). Stress measurements in tunnel linings. ISMES.

Barla G (1995) Squeezing rocks in tunnels. ISRM News journal, 44-49

Barla, G. (2001) Tunnelling under squeezing rock conditions. Euro-summer-School in Tunnel Mechanics, Innsbruck 169-268

Barla G, Bonini M, Debernardi, D (2007). Modelling of tunnels in squeezing rock. ECCOMAS Thematic Conference on Computational Methods. Tunnelling (EURO:TUN 2007). Vienna, Austria, August 27-29

Barla G, Bonini M, Debernardi D (2008) Time Dependent Deformations in Squeezing Tunnels. 12th International Conference of International Association for Computer Methods and Advances in Geomechanics (IACMAG). Goa,India

Barla G, Bonini M, Debernardi D (2010) Time Dependent Deformations in Squeezing Tunnels. International Journal of Geoengineering Case Histories 2(1):40–65

Barla G. Debernardi, D, Sterpi D (2011) Time-dependent modeling of tunnels in squeezing conditions. International Journal of Geomechanics ASCE, (December) 697–710

Barla G, Barla M., Debernardi D, Bonini M (2014) Guidelines for TBM tunnelling in squeezing conditions – a case study. Géotechnique Letters, 4(April-June), 83–87

Barla G (2016) Full-face excavation of large tunnels in difficult conditions. Journal of Rock Mechanics and Geotechnical Engineering, 8(3):294–303

Barton, N., Lien, R., & Lunde, J. (1974). Engineering classification of rock masses for the design of tunnel support. Rock mechanics, 6(4):189-236

Beau J R, Cabanius J, Courtecuisse G, Fourmaintraux D, Gesta P, Levy M, ... & Vouille G (1980) Tunnel du Fréjus: les mesures géotechniques effectuées sur le chantier français et leur application pour la détermination et l'adaptation du soutènement provisoire. Revue Française de Géotechnique 12:57-82 (in French)

Bergmeister K (2007) Brenner base tunnel: link between Munich and Verona. Tunnel 1:9-20

Bernaud D, Rousset G (1992) La « nouvelle méthode implicite » pour l'étude du dimensionnement des tunnels. Revue française de Géotechnique 60:5-26 (in French)

Bernaud D, Benamar I, Rousset G (1994) La « nouvelle méthode implicite » pour le calcul des tunnels dans les milieux élastoplastiques et viscoplastiques. Revue française de Géotechnique,

68:3-19 (in French)

Bieniawski, Z. T. (1973). Engineering classification of jointed rock masses. Civil Engineer in South Africa, 15(12)

Bieniawski, Z. T. (1989). Engineering rock mass classifications: a complete manual for engineers and geologists in mining, civil, and petroleum engineering. John Wiley & Sons.

Billaux, D., & Cundall, P. (1993). Simulation des géomatériaux par la méthode des éléments Lagrangiens. Revue française de Géotechnique, (63):9-21

Boidy E (2002) Modélisation numérique du comportement différé des cavités souterraines (Doctoral dissertation, Université Joseph-Fourier-Grenoble I).

Bonini M, Barla G (2012) The Saint Martin La Porte access adit (Lyon-Turin Base Tunnel) revisited. Tunnelling and Underground Space Technology Incorporating Trenchless Technology Research 30:38–54

Cantieni L, Anagnostou G (2009) The effect of the stress path on squeezing behavior in tunneling. Rock mechanics and rock engineering 42(2):289-318

Cantieni L, Anagnostou G, Hug R (2011) Interpretation of core extrusion measurements when tunnelling through squeezing ground. Rock mechanics and rock engineering, 44(6):641

Cartney SA (1977) The Ubiquitous Joint Method. Cavern Design at Dinorwic Power Station. Tunnels & Tunneling 9:54-57

Corbetta F, Bernaud D, Nguyen-Minh D (1991) Contribution à la méthode convergence-confinement par le principe de la similitude. Revue française de géotechnique, 54:5-11 (in French)

Dalgıç S (2002). Tunneling in squeezing rock, the Bolu tunnel, Anatolian Motorway, Turkey. Engineering Geology, 67(1–2):73–96

Deere, D. (1988). The rock quality designation (RQD) index in practice. In Rock classification systems for engineering purposes. ASTM International

De Labriolle GC (2017) Amélioration des méthodes analytiques basées sur des concepts, simples pour le dimensionnement des tunnels superficiels et profonds en sol meuble. Revue Française de Géotechnique 151:2 (in French)

De la Fuente M, Sulem J, Taherzadeh R, Subrin D (2017) Traitement et rétro-analyse des auscultations réalisées dans le tunnel routier du Fréjus et sa galerie de sécurité lors de leurs constructions respectives. Congrès International AFTES 2017, Paris 155 (in French)

De la Fuente M, Tahezadeh R, Sulem J, Subrin D (2018) Analysis and comparison of the measurements of Fréjus road tunnel and of its safety gallery. Eurock symposium 2018, Saint Petersburg v2 1143-1148

Einstein HH (1989) Design and analysis of underground structures in swelling and squeezing rocks. Underground Structures Design and Instrumentation Developments in Geotechnical Engineering, 202– 262

Eisenstein, Z, Branco P (1991) Convergence-Confinement method in shallow tunnels. Tunnelling and underground space technology, 6(3):343-346

Eurocode 2 (2005) Design of concrete structures

Flügge W (1960) Stresses in shells. (Springer-Verlag, New York), Google scholar 449

Gioda, G (1982) On the non-linear 'squeezing'effects around circular tunnels. International Journal for Numerical and Analytical Methods in Geomechanics, 6(1):21-46

Goel RK, Jethwa JL and Paithakan AG (1995) Tunnelling through the young Himalayas – a case history of the Maneri-Uttarkashi power tunnel. Engineering Geology., 39(1-2):31-44.

Gonzalez-Nicieza C, Alvarez-Vigil AE, Menendez-Diaz A, Gonzalez-Palacio C (2008) Influence of the depth and shape of a tunnel in the application of the convergence–confinement method. Tunnelling and Underground Space Technology 21(1):25–37

Grimstad, E, Barton N (1993) Updating of the Q-system for NMT. Proceedings of the International Symposium on Sprayed Concrete. Modern Use of Wet Mix Sprayed Concrete for Underground Support, Fagernes. Norwegian Concrete Association, Oslo

Grimstad, E., Kankes, K., Bhasin, R., Magnussen, A. W., & Kaynia, A. (2002). Rock mass quality Q used in designing reinforced ribs of sprayed concrete and energy absorption. Report, Norwegian Geotechnical Institute

Guayacán-Carrillo LM, Sulem J, Seyedi, DM, Ghabezloo S, Noiret A, Armand G (2016) Analysis of Long-Term Anisotropic Convergence in Drifts Excavated in Callovo-Oxfordian Claystone. Rock Mechanics and Rock Engineering 49(1):97–114

Hanafy EA., & Emery JJ (1980, May). Advancing face simulation of tunnel excavation and lining. Placement. In Underground Rock Engineering, 13th Canadian Rock Mechanics Symposium 119-125

Hasanpour, R. (2014). Advance numerical simulation of tunneling by using a double shield TBM. Computers and Geotechnics, 57:37–52

Hasanpour, R., Rostami, J., & Ünver, B. (2014). 3D finite difference model for simulation of double shield TBM tunneling in squeezing grounds. Tunnelling and Underground Space Technology, 40:109–126

Hasanpour R, Rostami J, Barla G (2015). Impact of Advance Rate on Entrapment Risk of a Double-Shielded TBM in Squeezing Ground. Rock Mechanics and Rock Engineering 48(3):1115–1130.

Hoek E, Brown ET (1980) Empirical strength criterion for rock masses. Journal of Geotechnical and Geoenvironmental Engineering, ASCE 106 (GT9) 1013-1035

Hoek, E. (1994). Strength of rock and rock masses. ISRM News Journal, 2(2), 4-16.

Hoek, E., Marinos, P., & Benissi, M. (1998). Applicability of the Geological Strength Index (GSI) classification for very weak and sheared rock masses. The case of the Athens Schist Formation. Bulletin of Engineering Geology and the Environment 57(2):151-160

Hoek E, Marinos P (2000) Predicting tunnel squeezing problems in weak heterogeneous rock masses. Tunnels and Tunnelling International, 45-51: part one; 33-36: part two

Hoek E. (2001). Big tunnels in bad rock. Journal of Geotechnical and Geoenvironmental Engineering, 127(9)726-740

Hoek, E., Carranza-Torres, C., & Corkum, B. (2002). Hoek-Brown failure criterion-2002 edition. Proceedings of NARMS-Tac, 1:267-273

Hoek, E., (2007), Practical rock engineering, RocScience

Hoek, E., & Guevara, R. (2009) Overcoming squeezing in the Yacambú-Quibor tunnel, Venezuela. Rock Mechanics and Rock Engineering, 42(2):389-418

ITASCA (2011) Fast Lagrangian analysis of continua (FLAC3D), Minnesota: Itasca Consulting Group, Inc

Jethwa JL, Singh B (1984) Estimation of ultimate rock pressure for tunnel linings under squeezing rock conditions – a new approach. Design and Performance of Underground Excavations, ISRM Symposium, Cambridge, E.T. Brown and J.A.Hudson eds., 231-238

Jethwa JL, Dhar BB (1996) Tunnelling under Squeezing Ground Condition. Proc. Recent Advances in Tunnelling Technology, New Delhi, 209–214

Kazakidis VN, Diederichs MS (1993) Tehnical Note: Understanding Jointed Rock Mass Behavior Using a Ubiquitous Joint Approach. International Journal of Rock Mechanics and Mining Science 163-172

Kovári K, Amstad C, Koppel H (1979) New developments in the instrumentation of underground openings. In: Proceedings of the 4th Rapid Excavation and Tunnelling Conference, Atlanta, USA 817-837

Kovari, K (1986). Rock deformation problems when using full-facing cutting equipment in rock, Part 2. Tunnel, 4(86):289-298

Kovári, K. (1995). The two base tunnels of the Alptransit project: Lötschberg and Gotthard. In Weltneuheiten im Tunnelbau= Worldwide Innovations in Tunnelling= Innovations mondiale dans la Construction de Tunnel: Vorträge World Tunnel Congress/STUVA-TAGUNG'95 in Stuttgart 36:23-29.

Kovari, K. (1998) Tunnelling in squeezing rock. Tunnel, 5:12-31

Lee SW, Jung JW, Nam SW, Lee IM (2007). The influence of seepage forces on ground reaction curve of circular opening. Tunnelling and Underground Space Technology, 22(1):28-38.

Levy M, Courtecuisse G, Barral JP (1981). Les travaux du tunnel routier du Fréjus. Annales de l'ITBTP, 400 (TRAV PUBLICS-19) (in French)

Li G, Li H, Kato H, Mizuta Y (2003) Application of ubiquitous joint model in numerical modeling of Hilltop Mines in Japan. Chines Journal of Rock Mechanics and Engineering 22(6):951–956

Lunardi, P. (1980). APPLICATION DE LA MECANIQUE DES ROCHES AUX TUNNELS AUTOROUTIERS-EXEMPLE DES TUNNELS DU FREJUS (COTE D'ITALIE) ET DU GRAN SASSO-1ERE PARTIE. REV FR GEOTECH, (12) (in French)

Lunardi, P., Bindi, R., & Focaracci, A. (1993, May). Technical and financial planning of underground works: the ADECO-RS method. In VI Forum Europeo di Ingegneria Economica-Università Bocconi-Milano (pp. 13-14).

Maiolino, S. (2006). Fonction de charge générale en géomécanique: application aux travaux souterrains (Doctoral dissertation, Ecole Polytechnique X)

Marinos V, Fortsakis P, Prountzopoulos G (2011) Estimation of geotechnical properties and classification of geotechnical behaviour in tunnelling for flysch rock masses. In: Anagnostopoulos A, Pachakis M, Tsatsanifos C, editors. Proceedings of the 15th European Conference on Soil Mechanics and Geotechnical Engineering (Vol. 1); Athens, Greece 435-40

Marinos V (2014). Tunnel behaviour and support associated with the weak rock masses of flysch. Journal of Rock Mechanics and Geotechnical Engineering 6(3):227-239

Mezger, F., Anagnostou, G., & Ziegler, H. J. (2013). The excavation-induced convergences in the Sedrun section of the Gotthard Base Tunnel. Tunnelling and underground space technology, 38, 447-463.

Muirwood AM (1972) Tunnels for road and motorways. Q. J. Eng. Geol. 5:119 120

Nakano, R. (1979) Geotechnical properties of mudstone of neogene tertiary in Japan. International Symposium of Rock Mechanics, Oaxaca, 1:75-92

NGI (Norwegian Geotechnical Institute) 2015. Using the Q-system

Nguyen-Minh D, Guo C (1996) Recent progress in convergence-confinement method. Eurock'96, Barla (ed.), Turin 855-860

Nguyen XS (2018) Evaluation des performances d'un tunnelier. Rapport de stage de fin d'études de l'Ecole des Mines de Nancy.

Oreste, P (2009) The Convergence-Confinement Method: Roles and Limits in Modern Geomechanical Tunnel Design. American Journal of Applied Sciences 6(4):757–771

O'Rourke TD (1984) Guidelines for tunnel lining design. ASCE

Panet M, Guellec P (1974) Contribution à l'étude du soutènement d'un tunnel à l'arrière du front de taille. Progrès en mécanique des roches comptes rendus du 3eme congrès de la société internationale de mécanique des roches, Denver (2) (in French)

Panet M, Guenot A (1983) Analysis of convergence behind the face of a tunnel. Tunnelling 82, proceeding of the 3rd international symposium, Brighton 197-204

Panet M (1995) Le calcul des tunnels par la méthode convergence-confinement, Presses de l'Ecole Nationale des ponts et chaussées, Paris (in French)

Panet M (1996) Two case histories of tunnels through squeezing rocks. Rock mechanics and rock engineering, 29(3):155-164

Pellet F (2009). Contact between a tunnel lining and a damage-susceptible viscoplastic medium. Comput Model Eng Sci 52(3):279-295

Plana D, López C, Cornelles J. Muñoz P. (2004) Numerical Analysis of a Tunnel in an Anisotropy Rock Mass. Envalira Tunnel (Principality of Andorra). Engineering Geology for Infrastructure Planning in Europe. Springer Berlin Heidelberg 153-161

Ramoni M, Anagnostou G (2006) On the feasibility of TBM drives in squeezing ground. Tunnelling and Underground Space Technology, 21(3):262-262

Ramoni M., Anagnostou G (2008) TBM drives in squeezing ground-Shield-Rock interaction. Building underground for the future; AFTES International Congress Monaco, Montecarlo, 163-172; Edition specifique Limonest

Ramoni M, Anagnostou G, (2010) Thrust force requirements for TBMs in squeezing ground. Tunnelling and Underground Space Technology 25(4):433–455

Ramoni M, Anagnostou G, (2011a) The Interaction Between Shield, Ground and Tunnel Support in TBM Tunnelling Through Squeezing Ground. Rock Mechanics Rock Engineering 44:37-61

Ramoni M, Lavdas N, Anagnostou G (2011b) Squeezing loading of segmental linings and the effect of backfilling. Tunneling and Underground Space technology 26(6):692-717

Richard P, Pogu F, Augereau M. (2006). Tunnel de base du Lötschberg: 28 km d'excavation pour le lot de Mitholz. Travaux, 834:26-31.

Russo G, Repetto L, Piraud J, Laviguerie R (2009) Back-analysis of the extreme squeezing conditions in the exploratory adit to the Lyon-Turin base tunnel, (May) 9–14

Schubert W, Schubert P (1993) Tunnels in squeezing rock: Failure phenomena and counteractions. Assessment and prevention of failure phenomena in rock engineering. International Symposium Instabul 479-484

Schürch R, Anagnostou, G (2012) The applicability of the ground response curve to tunnelling problems that violate rotational symmetry. Rock mechanics and Rock Engineering 45(1):1-10

Singh B, Jethwa JL, Dube AK, Singh B (1992) Correlation between observed support pressure and rock mass quality. Tunnelling and Underground Space Technology, 7:59- 74

Sing B, and Goel RK (1999) Rock mass classification: a practical approach in Civil Engineering. Elsevier Science Ltd. U.K.

SITAF (1982) Traforo autostradale del Fréjus (in Italian)

SteinerW (1996). Tunnelling in squeezing rocks: case histories. Rock Mechanics and Rock Engineering, 29(4):211-246

Steiner P, Yeatman R (2009, January) New instruments improve site characterization with time based measurements. In ISRM Regional Symposium-EUROCK 2009. International Society for Rock Mechanics

Sharifzadeh M, Tarifard A., Moridi, MA (2013) Time-dependent behavior of tunnel lining in weak rock mass based on displacement back analysis method. Tunnelling and Underground Space Technology, 38:348-356

Sulem J. (1983) Comportement différé des tunnels profonds. PhD Thesis, Ecole Nationale des Ponts et Chaussées, [cité p. 71, 74, 163, 166]

Sulem J, Panet M, & Guenot A (1987a) An analytical solution for time-dependent displacements in a circular tunnel. International journal of rock mechanics and mining sciences & geomechanics abstracts, Pergamon, 24(3):155-164

Sulem J, Panet M., Guenot A (1987b).Closure Analysis in Deep Tunnels. International journal of rock mechanics and mining sciences & geomechanics abstracts 24(3): 145-154

Sulem J (1994) Analytical methods for the study of tunnel deformation during excavation. Barla G (ed) Proceedings of the 5th ciclo di conferenze di Mecanica e Ingegneria delle Rocce, Politecnico di Torino, 3.1-3.17

Sulem J. (2013) Tunnel du Fréjus: Mesures géotechniques et interprétation, Manuel de Mécanique des Roches Tome IV, chap. 7, Presse des Mines.

Terzaghi K (1946) Rock defects and loads on tunnel supports.

Tran Manh, H. (2014). Comportement des tunnels en terrain poussant. Thèse de doctorat de l'Université Paris Est.

Tran-Manh H, Sulem J, Subrin D, & Billaux D (2015a) Anisotropic Time-Dependent Modeling of Tunnel Excavation in Squeezing Ground. Rock Mechanics and Rock Engineering 48(6):2301–2317

Tran-Manh, H, Sulem, J, Subrin, D (2015b) A Closed-Form Solution for Tunnels with Arbitrary Cross Section Excavated in Elastic Anisotropic Ground. Rock Mechanics and Rock Engineering, 48(1):277–288

Tran-Manh, H, Sulem, J, Subrin, D (2016) Progressive degradation of rock properties and time dependent behavior of deep tunnels. Acta Geotecnica 11(3)693-711

Vinnac A. (2012). Rétro-analyse du creusement au tunnelier de la galerie de sécurité du tunnel routier du Fréjus. Mémoire de mastère spécialisé 'Tunnels et Ouvrages souterrains', ENTPE (in French).

Vlachopoulos N, Diederichs MS (2009) Improved longitudinal displacement profiles for convergence confinement analysis of deep tunnels. Rock Mechanics and Rock Engineering 42(2):131-146

Vlachopoulos N, Diederichs MS (2014) Appropriate uses and practical limitations of 2D numerical analysis of tunnels and tunnel support response. Geotechnical and Geological Engineering 32(2):469-488

Vu TM, Sulem J, Subrin D, Monin N, Lascols J (2013) Anisotropic Closure in Squeezing Rocks: The Example of Saint-Martin-la-Porte Access Gallery. Rock Mechanics and Rock Engineering 46(2):231–246

Vydrová, L. Č. (2015). comparison of tunneling methods NATM and ADECO-RS.

Wang TT, Huang TH (2009) A constitutive model for the deformation of a rock mass containing sets of ubiquitous joints. International Journal of Rock Mechanics and Mining Sciences 46(3):521–530

Wang TT, Huang TH (2013) Anisotropic Deformation of a Circular Tunnel Excavated in a Rock Mass Containing Sets of Ubiquitous Joints: Theory Analysis and Numerical Modeling. Rock Mechanics and Rock Engineering 47(2):643–657

Wong H, Subrin D, Dias D (2006) Convergence confinement analysis of a bolt-supported tunnel using the homogenization method. Canadian geotechnical journal 43(5):462-483.

Zhao K, Janutolo M, Barla G (2012) A completely 3D model for the simulation of mechanized tunnel excavation. Rock Mech Rock Eng 45(4):475–497

Zhao K, Bonini M, Debernardi D, Janutolo M, Barla G, Chen G (2015) Computational modelling of the mechanised excavation of deep tunnels in weak rock. Computers and Geotechnics 66:158-171

APPENDIX

APPENDIX A - Total set of results of the comparison of $\sigma_{max}{}^{*}$ between the different approaches

In an attempt to assess the applicability of the CV-CF methods to tunnels excavated with a double shield TBM some numerical simulations have been carried out by fixing the value of the parameter d^{*} to 2. The results are summarized in Fig. A1. and Fig. A2. It is inferred from the results that a classical CV-CF method in combination with the LDP of Panet provides an equilibrium state which is in agreement with the numerical simulations if $E^{*} > 0.25$. The effect of the stiffness of the lining on the GRC is less than in the case of single shield tunneling. The implicit method of Guo & Minh combined with an LDP of Panet provides also reasonable results except for N=5 where the implicit method reaches its limits (N=5 and d^{*}=2).

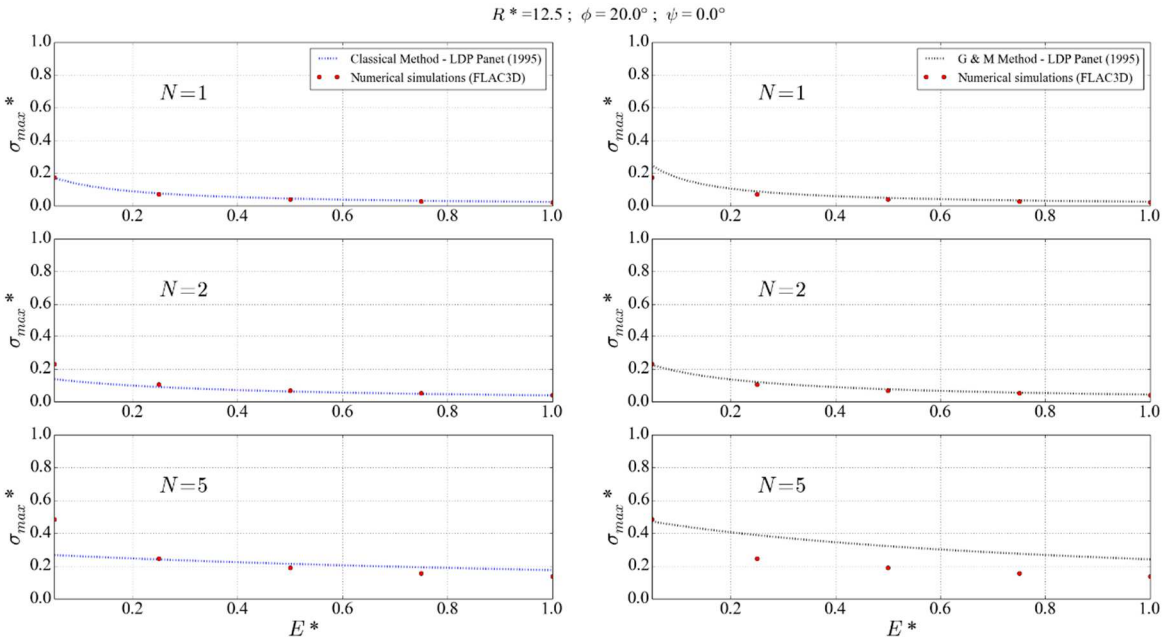

Fig. A1. Comparison of $\sigma_{max}{}^{*}$ between the different approaches when d^{*}=2, R^{*}=12.5 and ϕ=20° for incompressible plasticity (ψ = 0). Classical method on the left column and implicit method of Nguyen-Minh & Guo on the right column

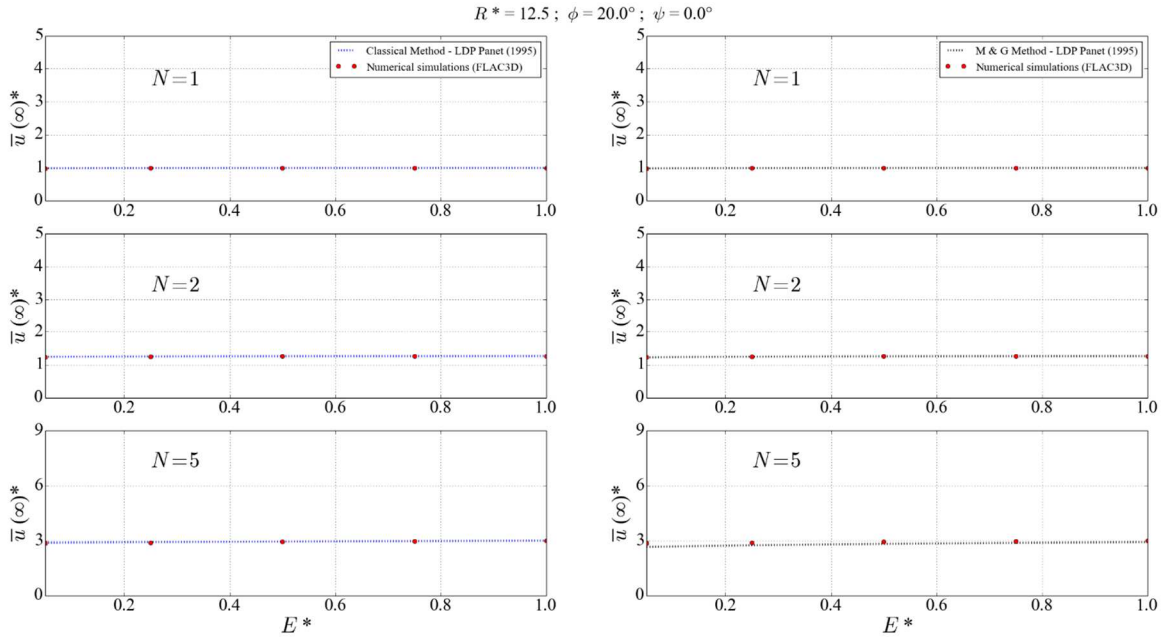

Fig. A2. Comparison of $\bar{u}(\infty)^*$ between the different approaches when d^*=2, R^*=12.5 and ϕ=25° for incompressible plasticity (ψ = 0). Classical method on the left column and implicit method of Nguyen-Minh & Guo on the right column

APPENDIX B - Total set of results of the comparison of $\sigma_{max}{}^{*}$ between the different approaches

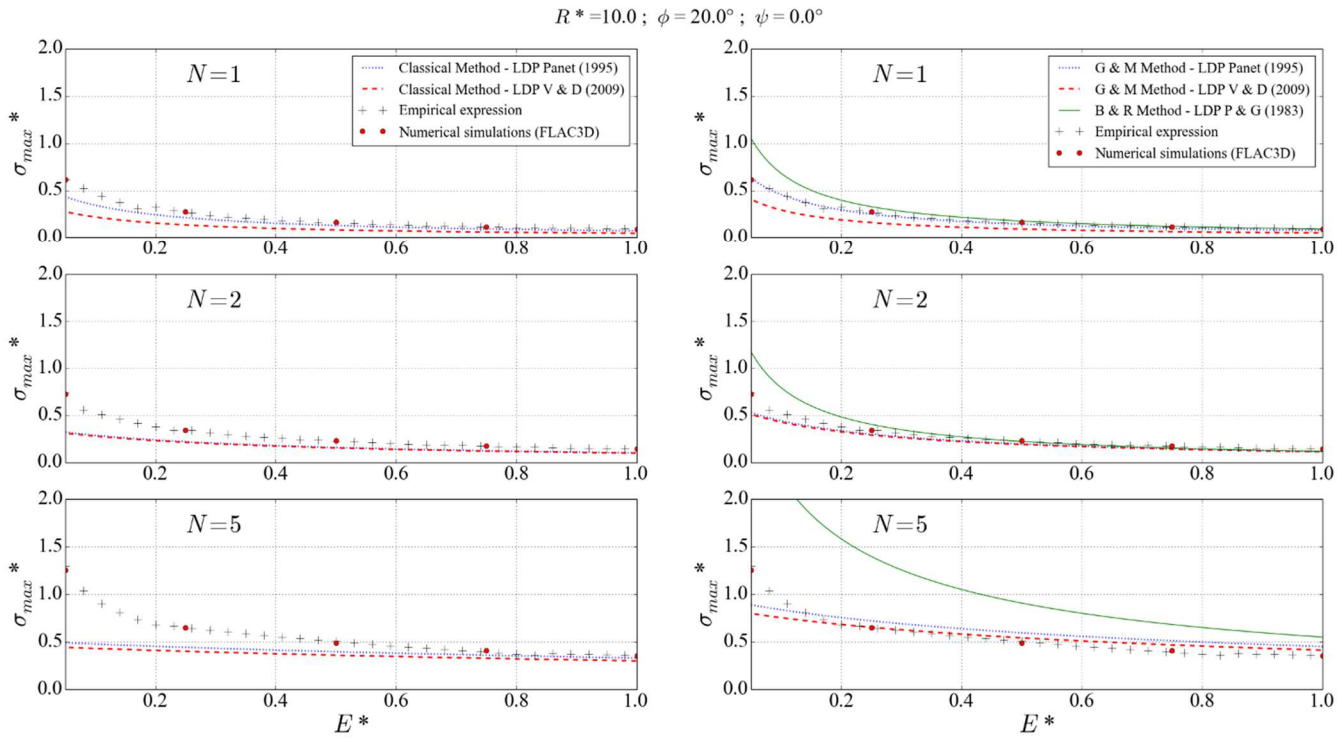

Comparison of $\sigma_{max}{}^{*}$ between the different approaches when R^{*}=10 and ϕ=20° for incompressible plasticity (ψ = 0). Classical methods on the left column and implicit methods on the right column

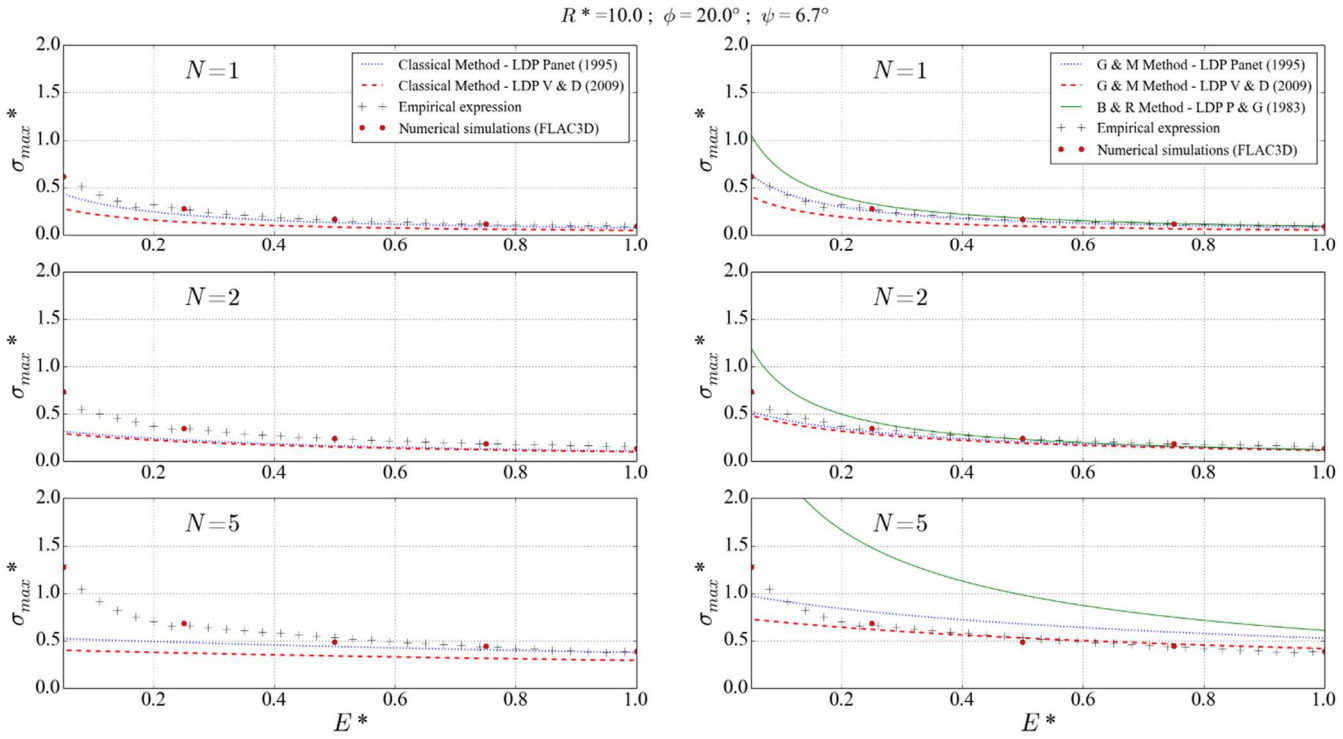

Comparison of $\sigma_{max}{}^{*}$ between the different approaches when R^{*}=10 and ϕ=20° for non-associate plasticity (ψ = ϕ/3). Classical methods on the left column and implicit methods on the right column

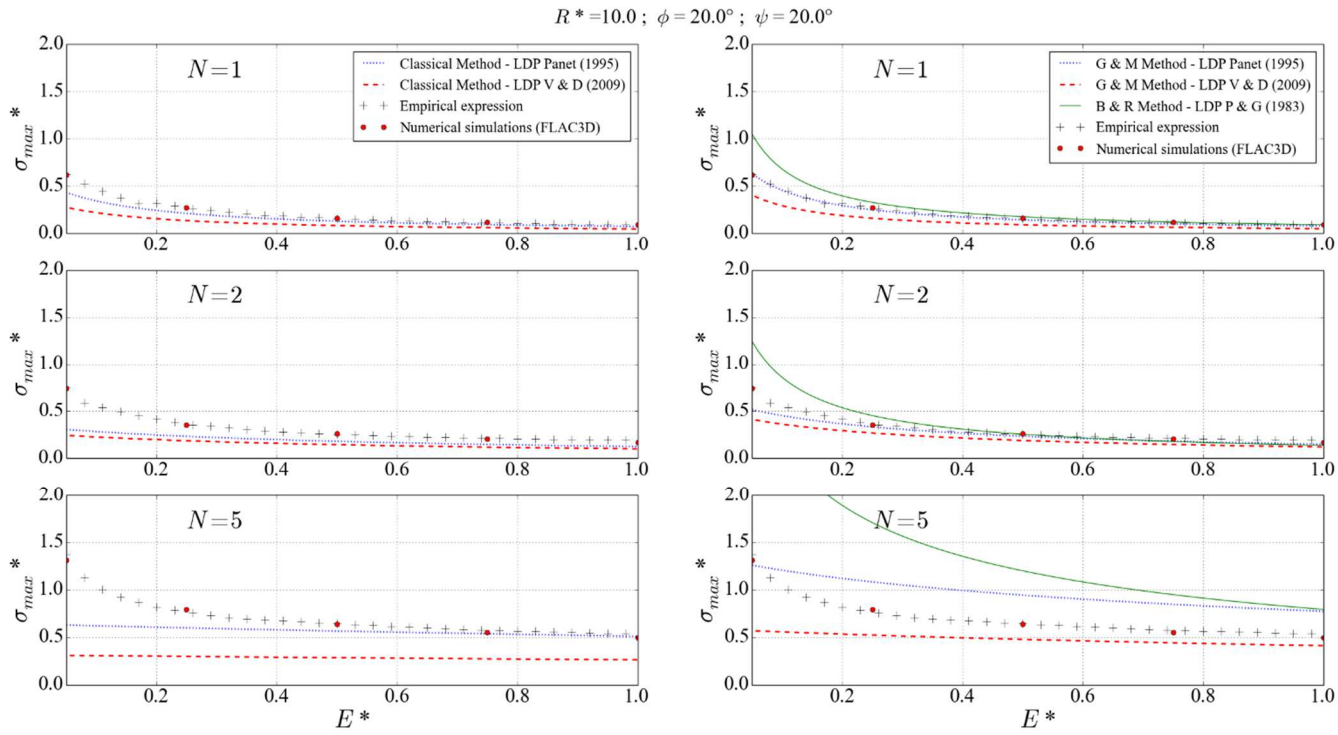

Comparison of $\sigma_{max}{}^{*}$ between the different approaches when R^{*}=10 and ϕ=20° for associate plasticity (ψ = ϕ). Classical methods on the left column and implicit methods on the right column

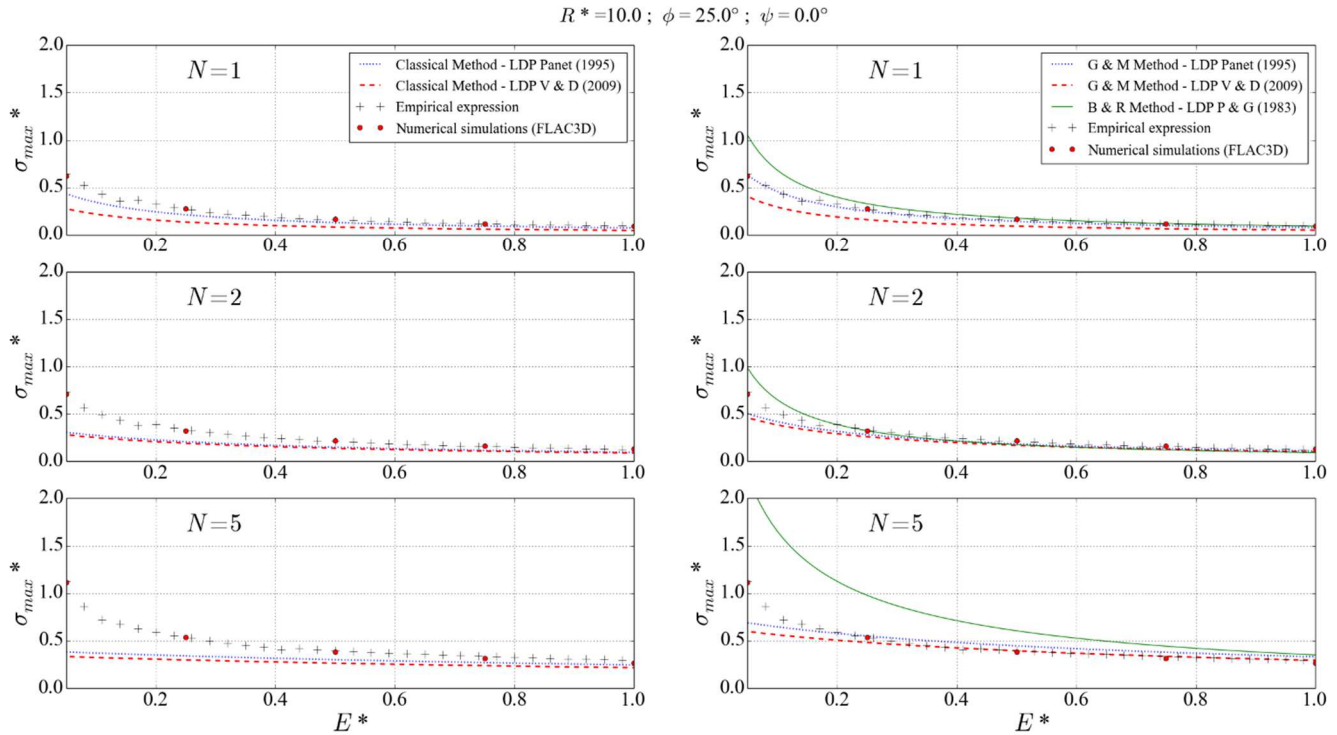

Comparison of $\sigma_{max}{}^{*}$ between the different approaches when R^{*}=10 and ϕ=25° for incompressible plasticity (ψ = 0). Classical methods on the left column and implicit methods on the right column

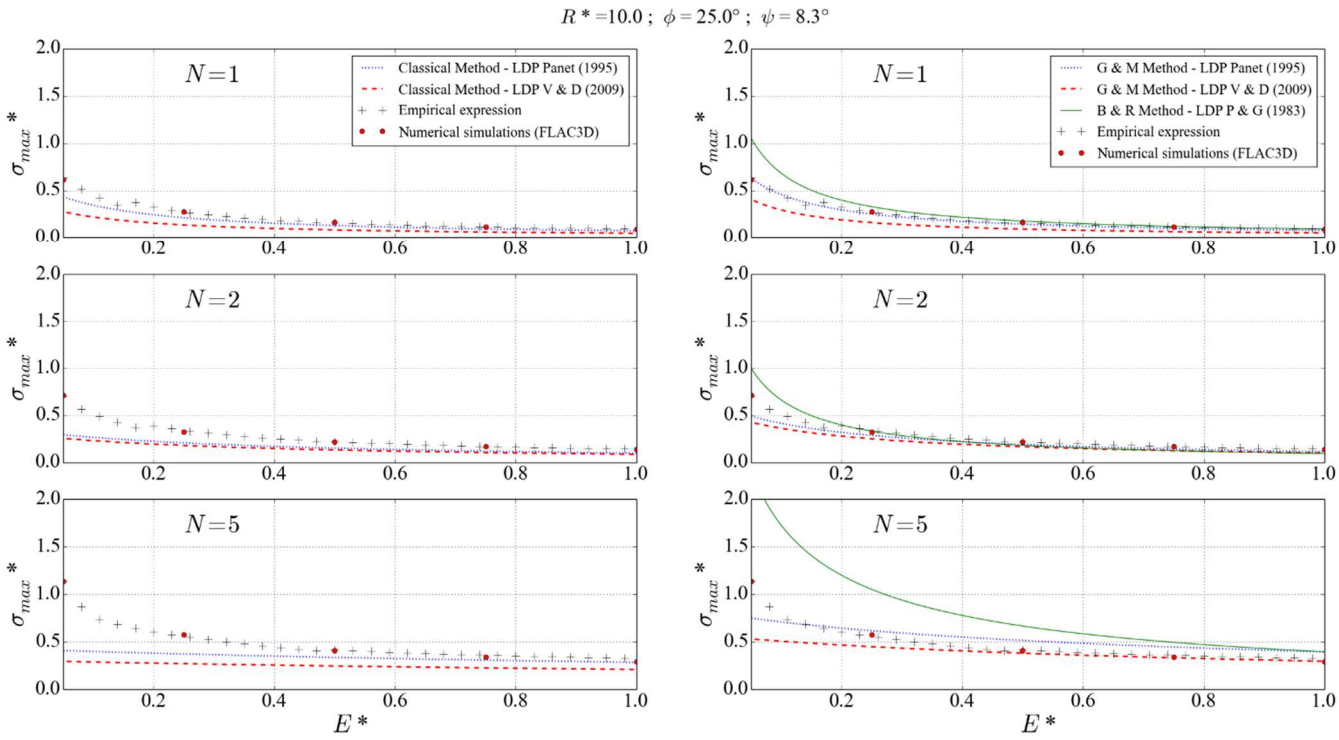

Comparison of $\sigma_{max}{}^{*}$ between the different approaches when R^{*}=10 and ϕ=25° for non-associate plasticity (ψ = ϕ/3). Classical methods on the left column and implicit methods on the right column

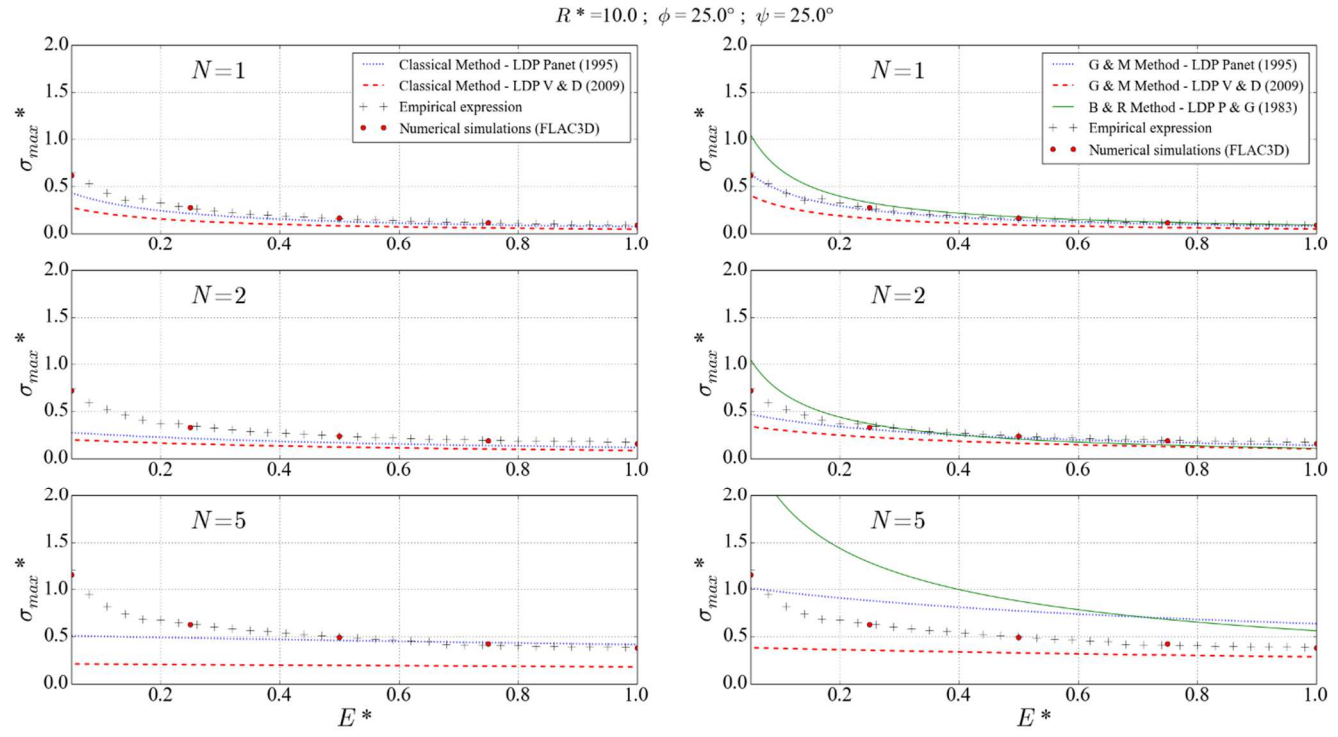

Comparison of $\sigma_{max}{}^{*}$ between the different approaches when R^{*}=10 and ϕ=25° for associate plasticity (ψ = ϕ). Classical methods on the left column and implicit methods on the right column

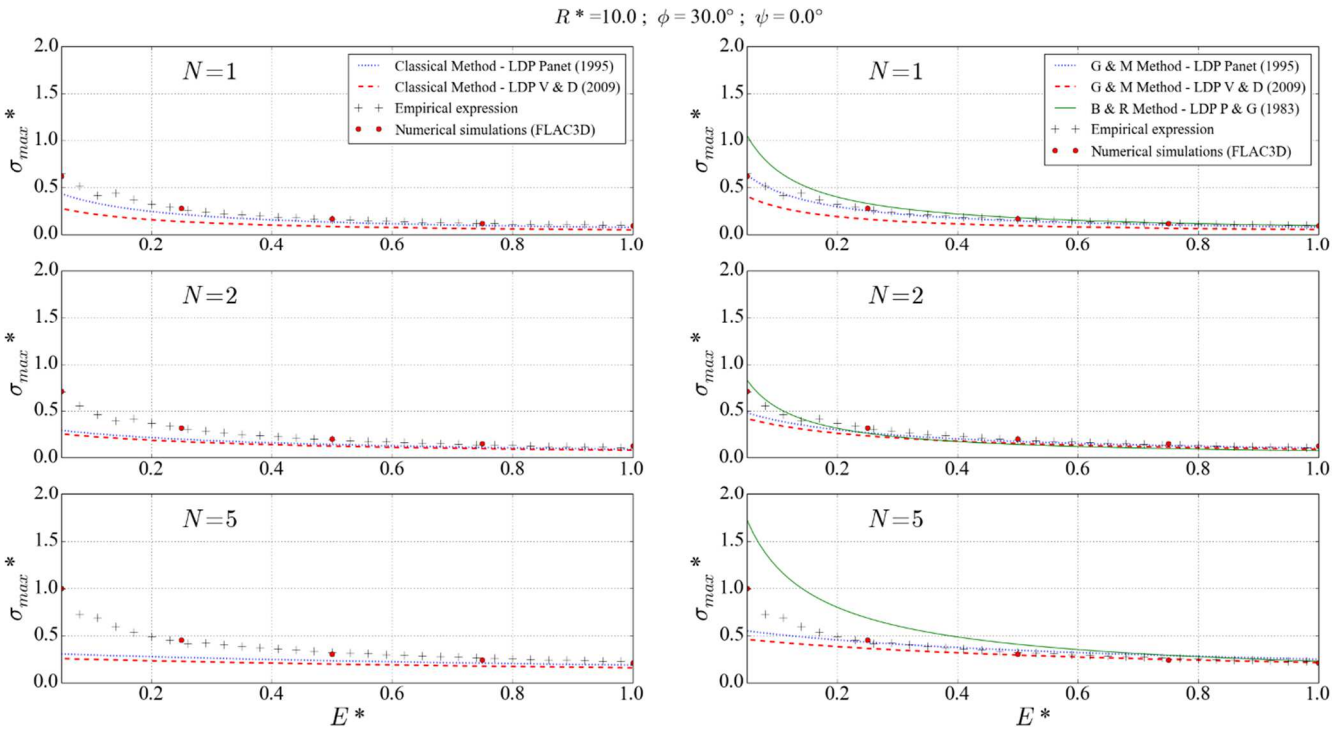

Comparison of $\sigma_{max}{}^{*}$ between the different approaches when R^{*}=10 and ϕ=30° for incompressible plasticity (ψ = 0). Classical methods on the left column and implicit methods on the right column

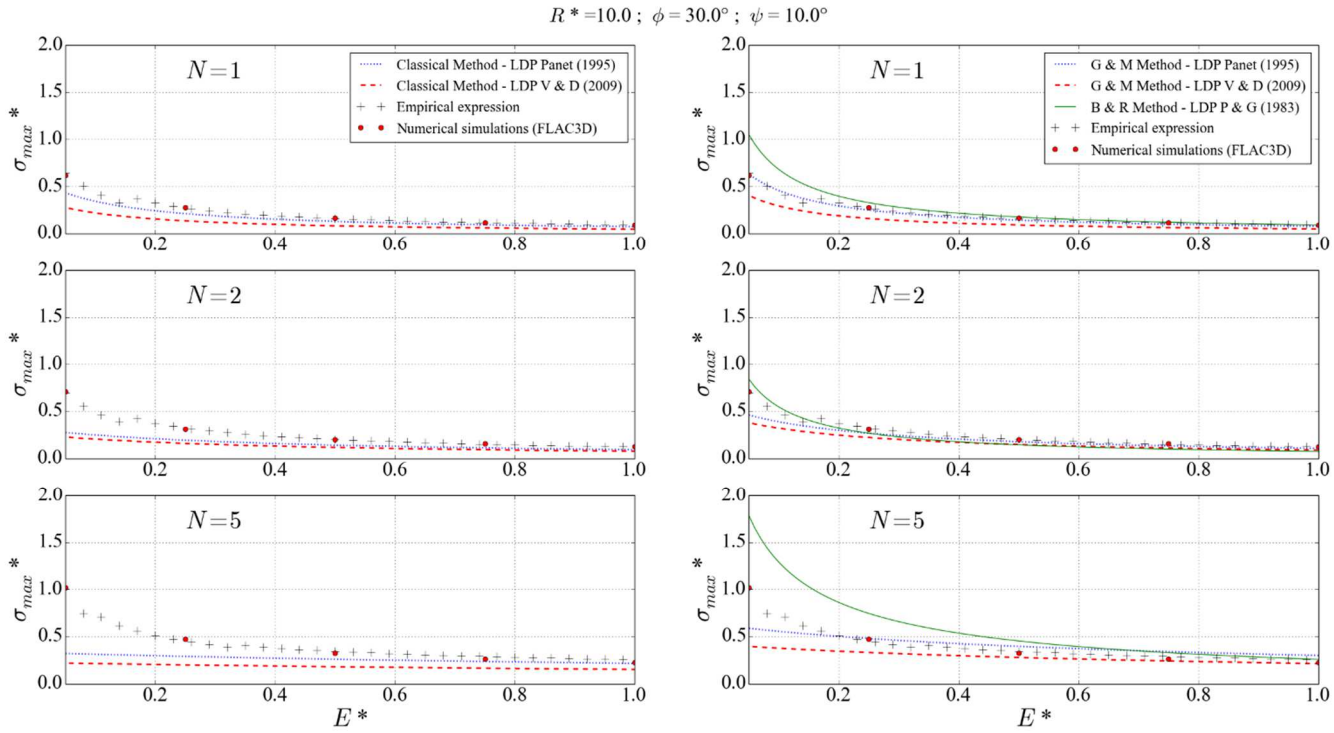

Comparison of $\sigma_{max}{}^{*}$ between the different approaches when R^{*}=10 and ϕ=30° for non-associate plasticity (ψ = ϕ/3). Classical methods on the left column and implicit methods on the right column

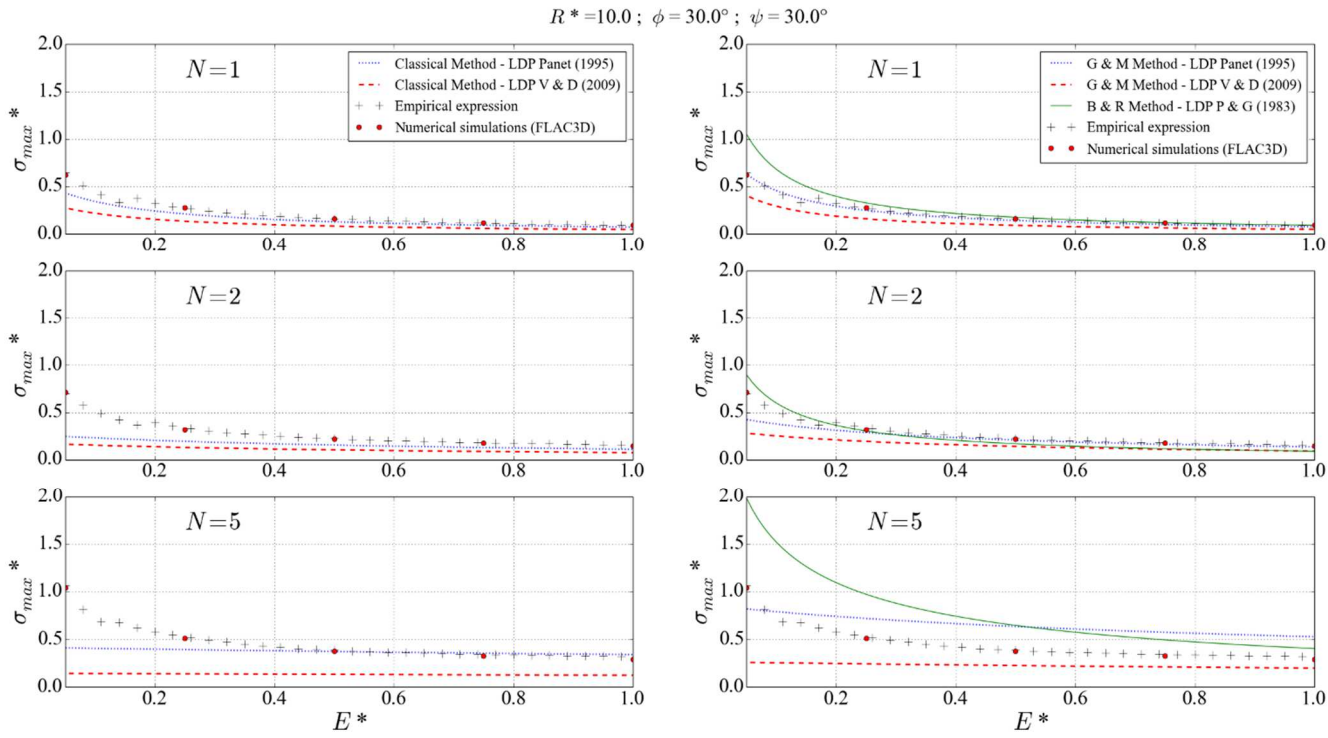

Comparison of $\sigma_{max}{}^{*}$ between the different approaches when R^{*}=10 and ϕ=30° for associate plasticity (ψ = ϕ). Classical methods on the left column and implicit methods on the right column

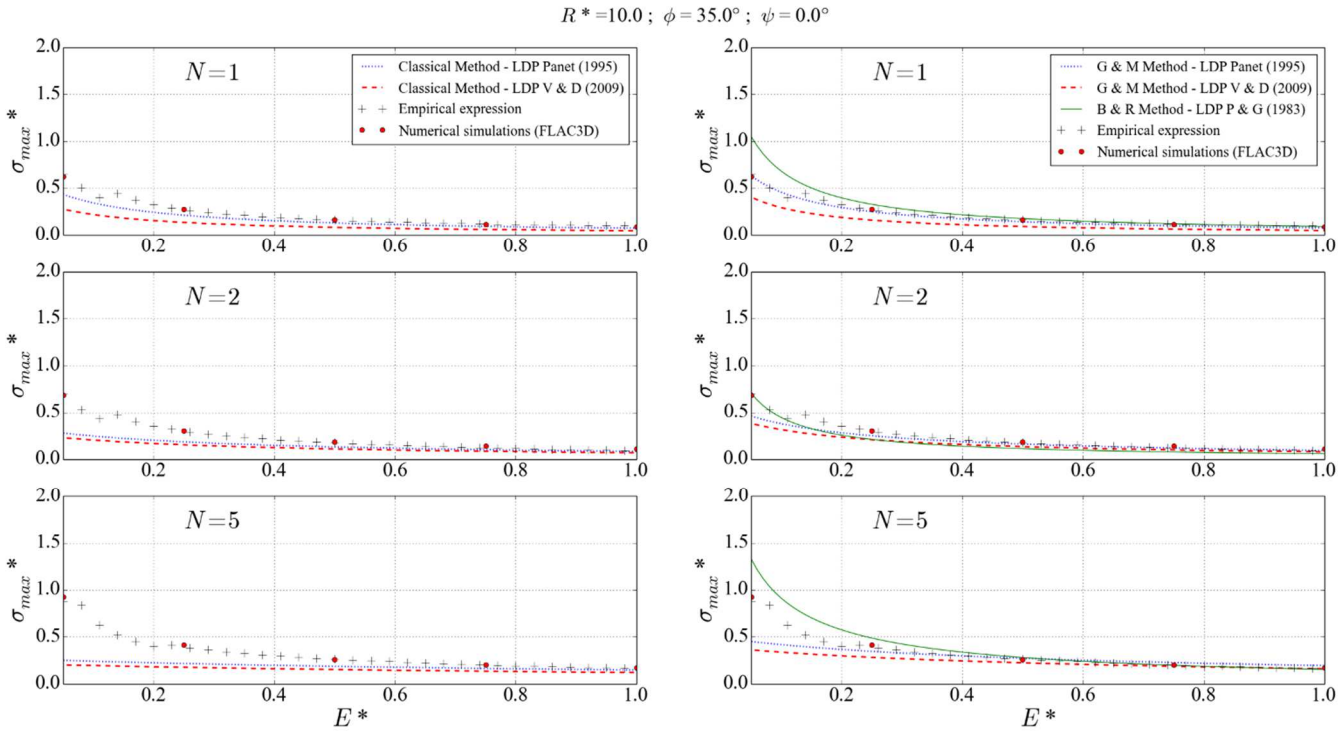

Comparison of $\sigma_{max}{}^{*}$ between the different approaches when R^{*}=10 and ϕ=35° for incompressible plasticity (ψ = 0). Classical methods on the left column and implicit methods on the right column

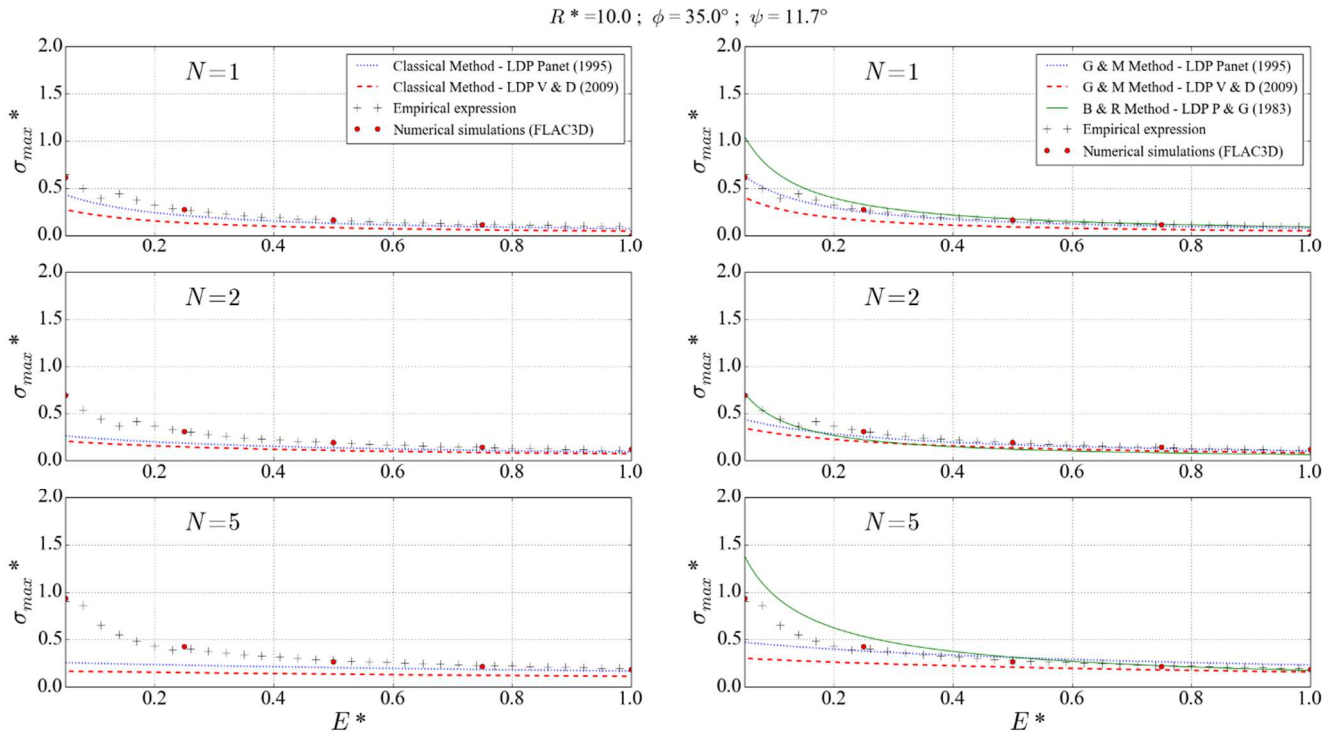

Comparison of $\sigma_{max}{}^{*}$ between the different approaches when R^{*}=10 and ϕ=35° for non-associate plasticity (ψ = ϕ/3). Classical methods on the left column and implicit methods on the right column

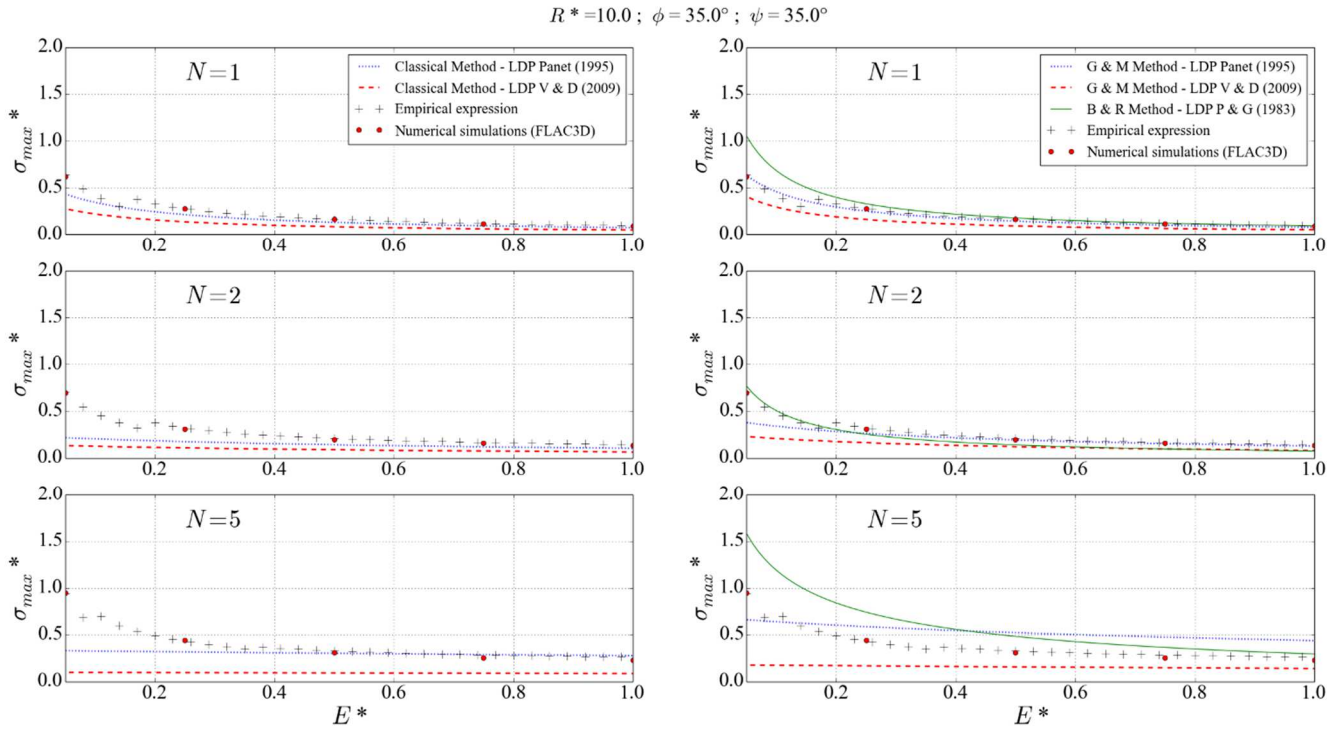

Comparison of $\sigma_{max}{}^{*}$ between the different approaches when R^{*}=10 and ϕ=35° for associate plasticity (ψ = ϕ). Classical methods on the left column and implicit methods on the right column

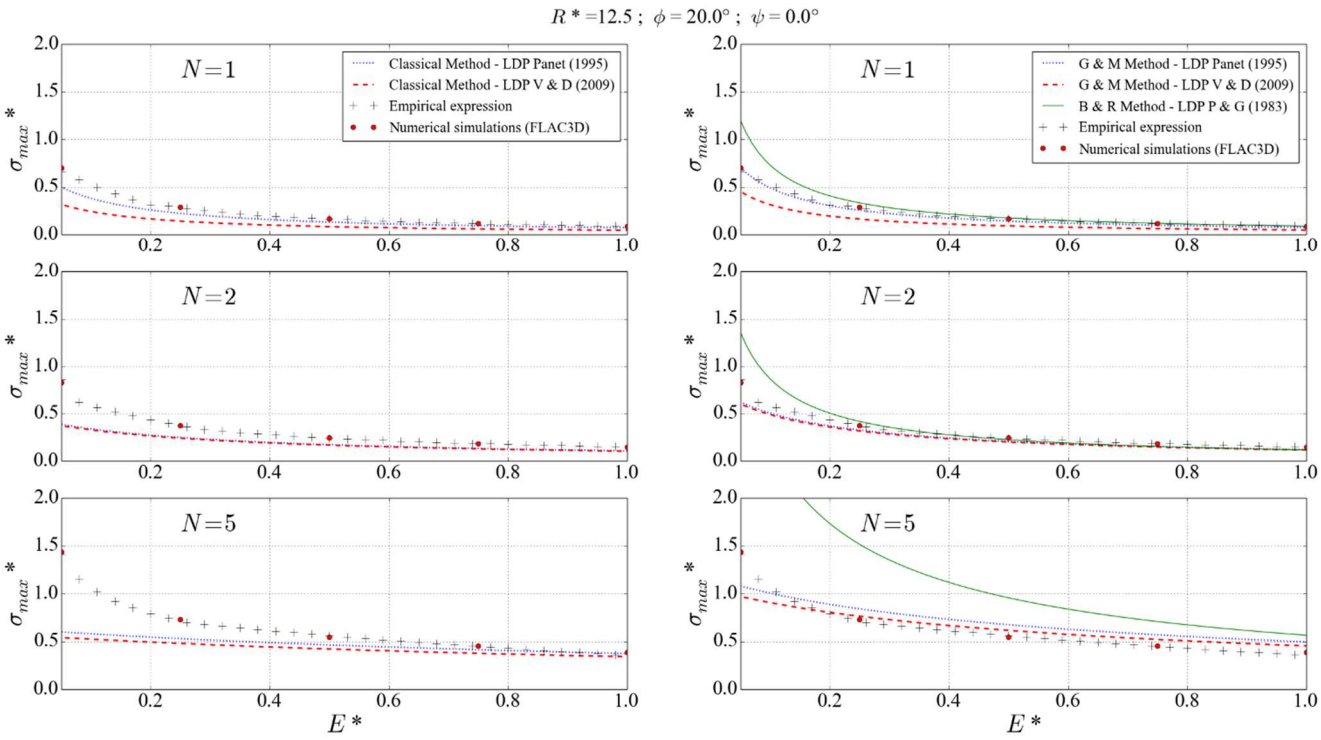

Comparison of $\sigma_{max}{}^{*}$ between the different approaches when R^{*}=12.5 and ϕ=20° for incompressible plasticity (ψ = 0). Classical methods on the left column and implicit methods on the right column

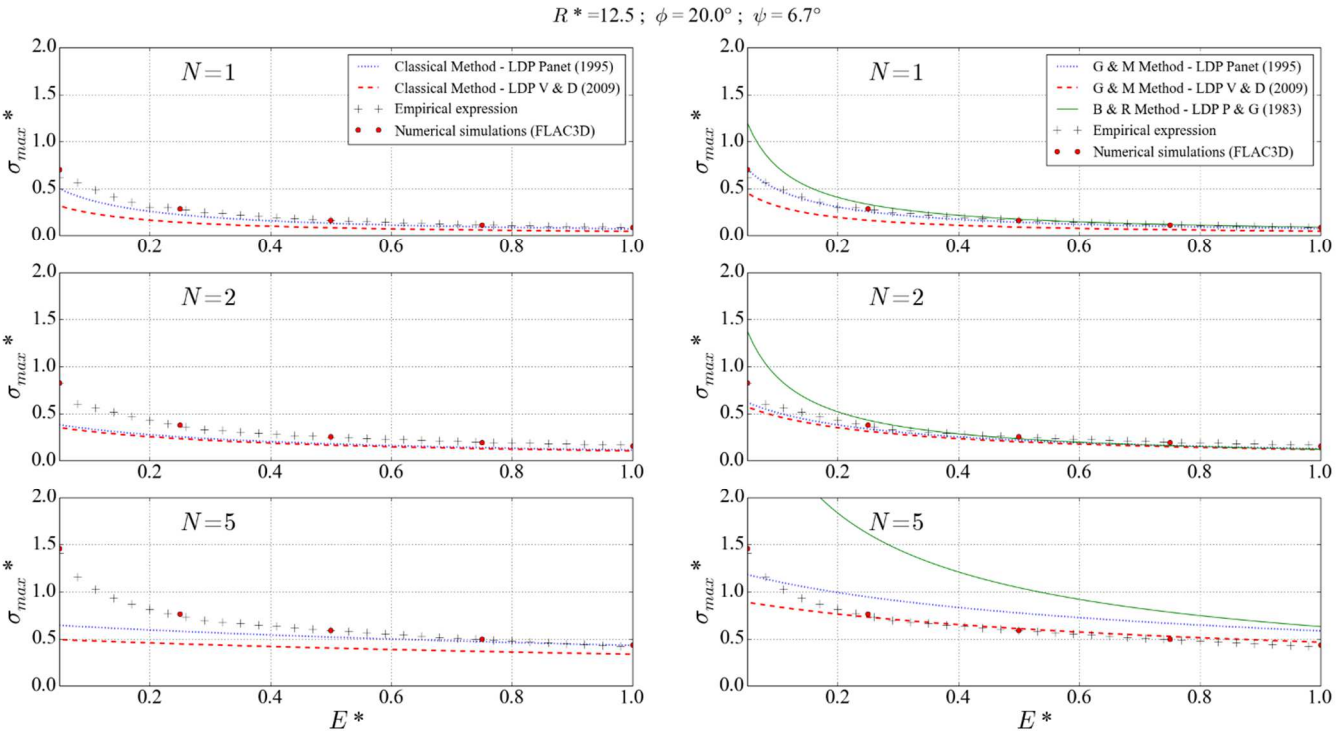

Comparison of $\sigma_{max}{}^{*}$ between the different approaches when R^{*}=12.5 and ϕ=20° for non-associate plasticity (ψ = ϕ/3). Classical methods on the left column and implicit methods on the right column

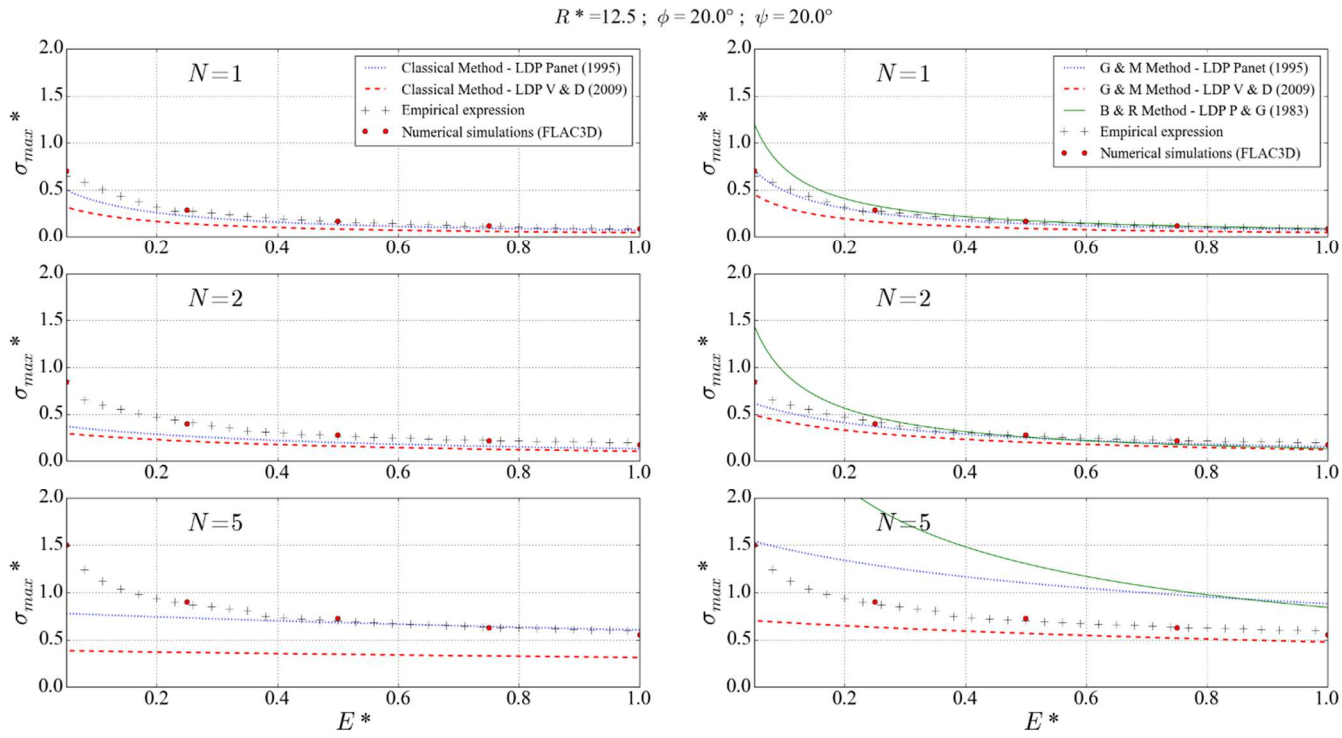

Comparison of $\sigma_{max}{}^{*}$ between the different approaches when R^{*}=12.5 and ϕ=20° for associate plasticity (ψ = ϕ). Classical methods on the left column and implicit methods on the right column

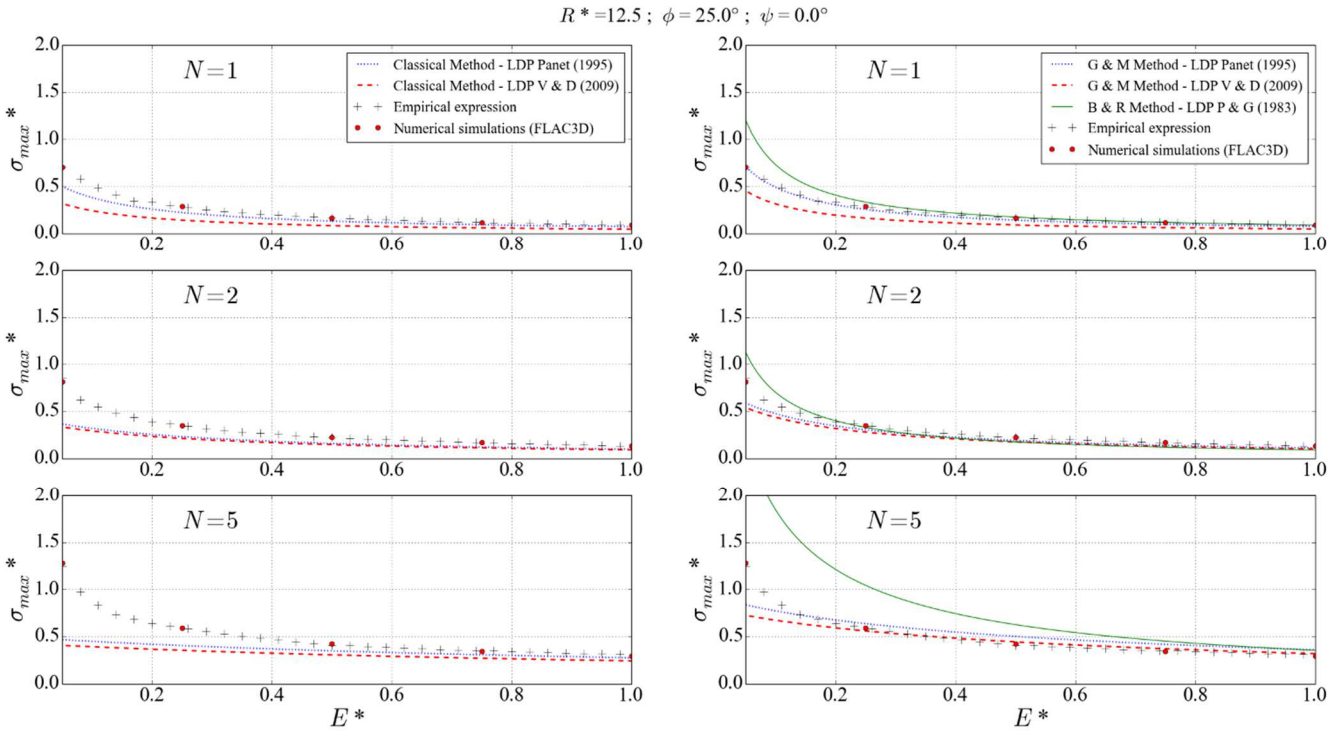

Comparison of $\sigma_{max}{}^{*}$ between the different approaches when R^{*}=12.5 and ϕ=25° for incompressible plasticity (ψ = 0). Classical methods on the left column and implicit methods on the right column

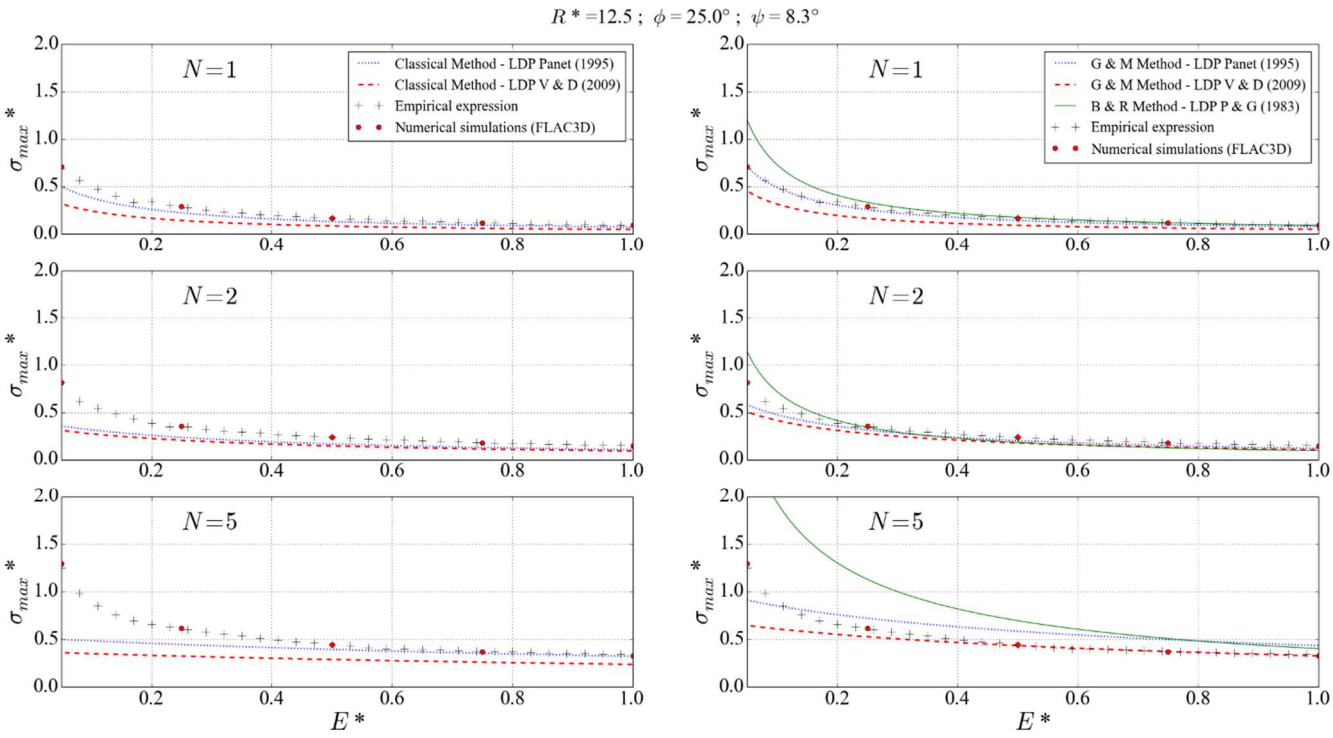

Comparison of $\sigma_{max}{}^{*}$ between the different approaches when R^{*}=12.5 and ϕ=25° for non-associate plasticity (ψ = ϕ/3). Classical methods on the left column and implicit methods on the right column

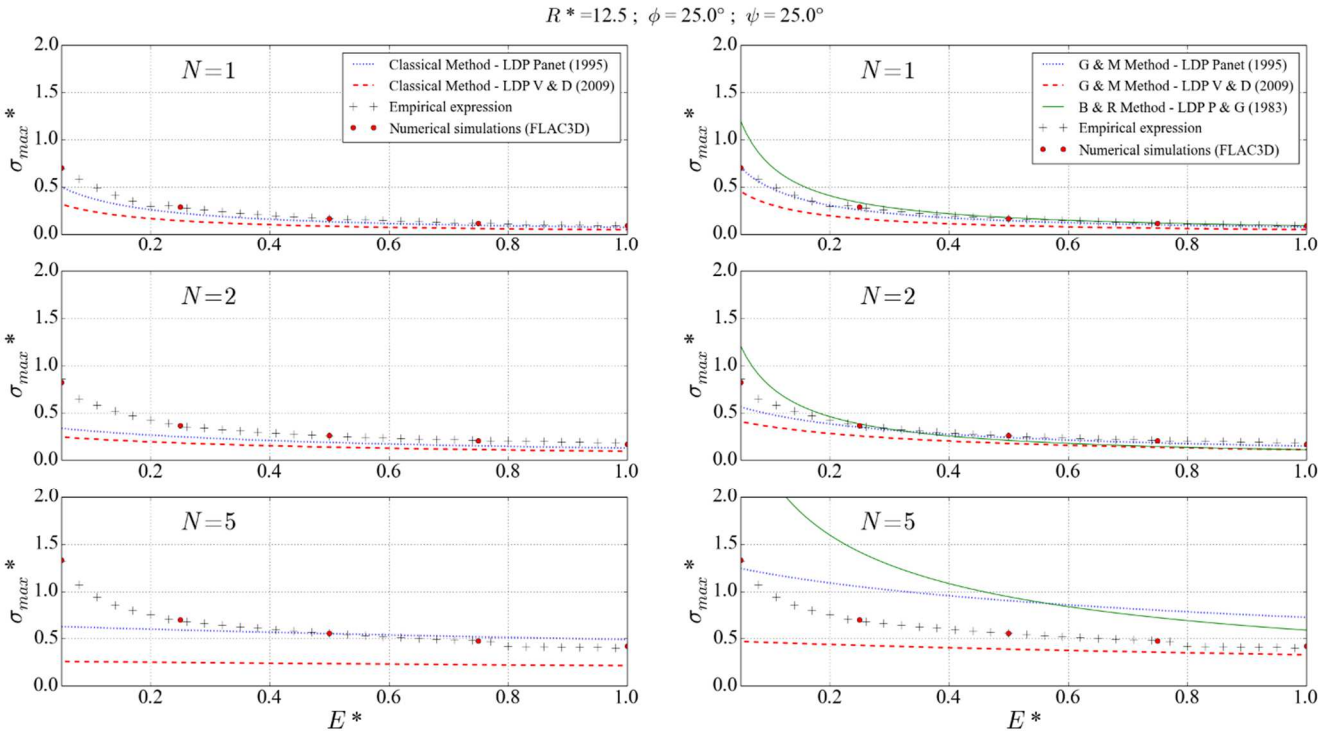

Comparison of $\sigma_{max}{}^{*}$ between the different approaches when R^{*}=12.5 and ϕ=25° for associate plasticity (ψ = ϕ). Classical methods on the left column and implicit methods on the right column

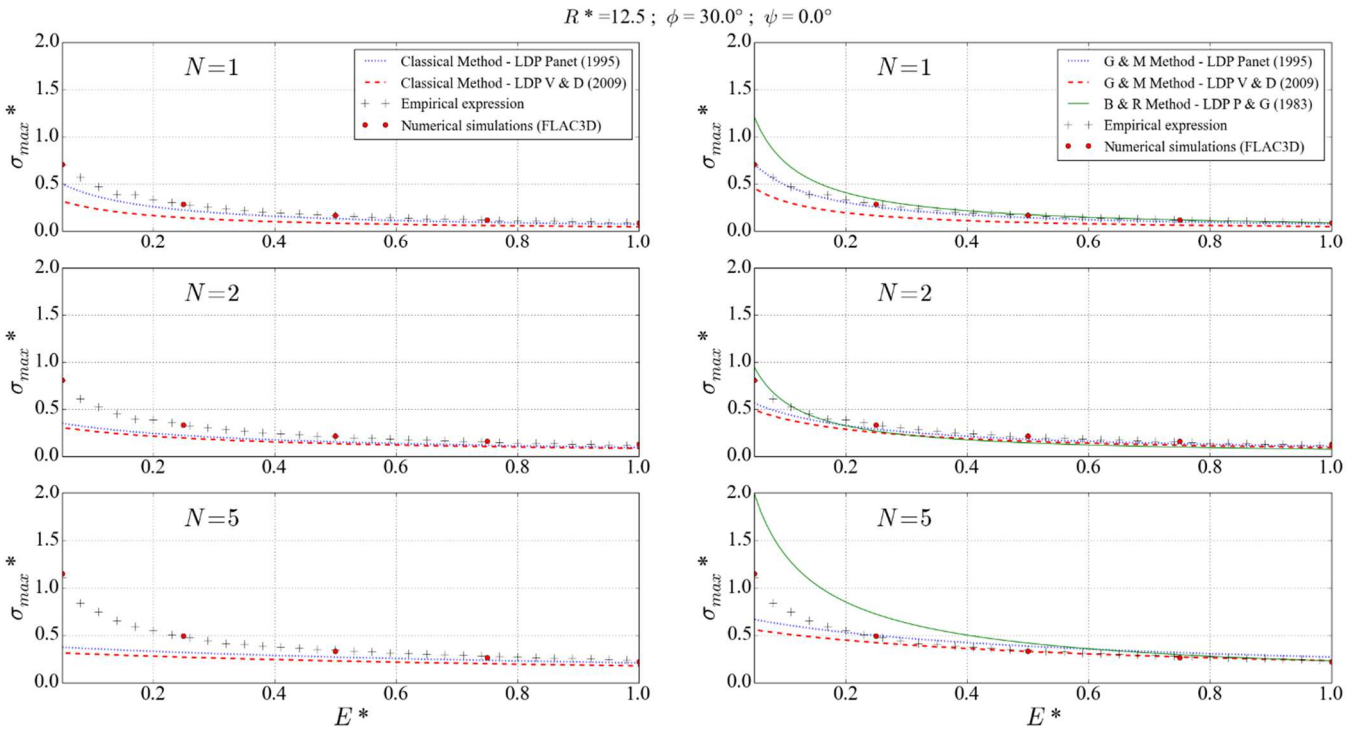

Comparison of $\sigma_{max}{}^{*}$ between the different approaches when R^{*}=12.5 and ϕ=30° for incompressible plasticity (ψ = 0). Classical methods on the left column and implicit methods on the right column

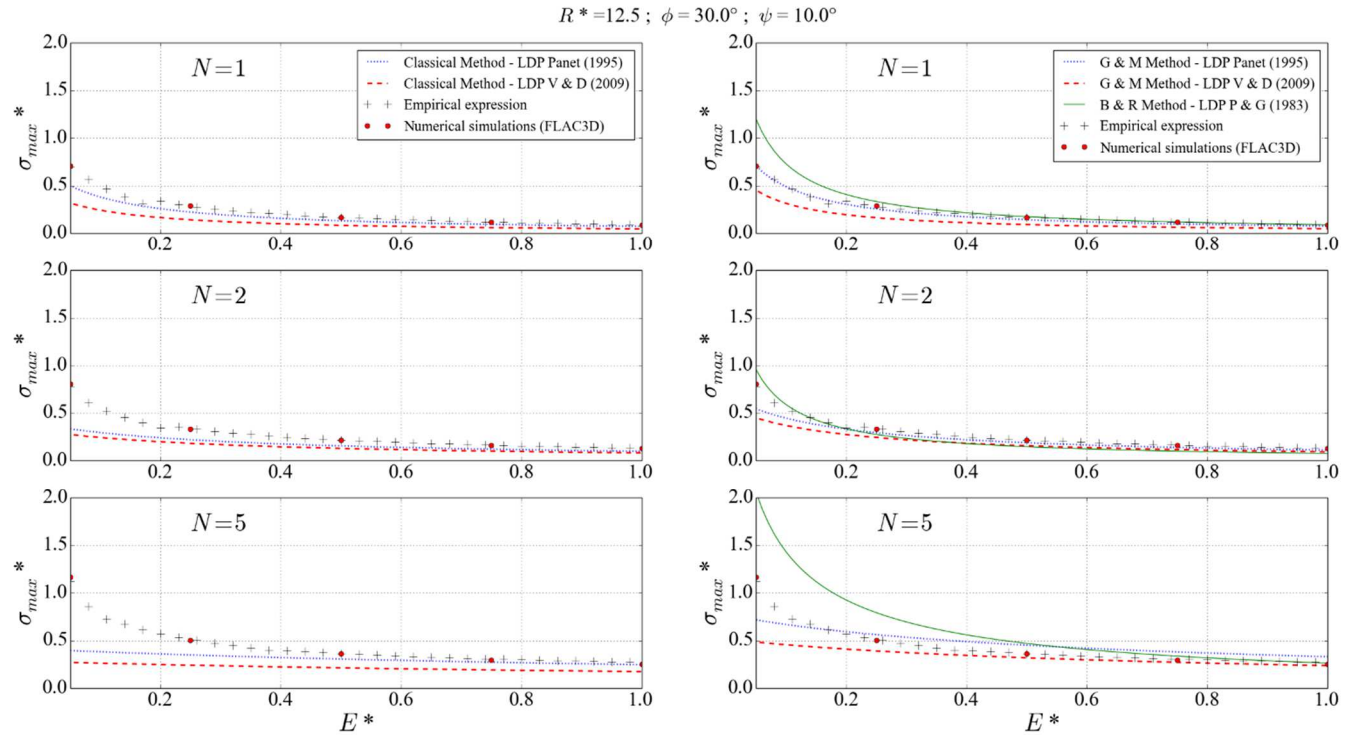

Comparison of $\sigma_{max}{}^{*}$ between the different approaches when R^{*}=12.5 and ϕ=30° for non-associate plasticity (ψ = ϕ/3). Classical methods on the left column and implicit methods on the right column

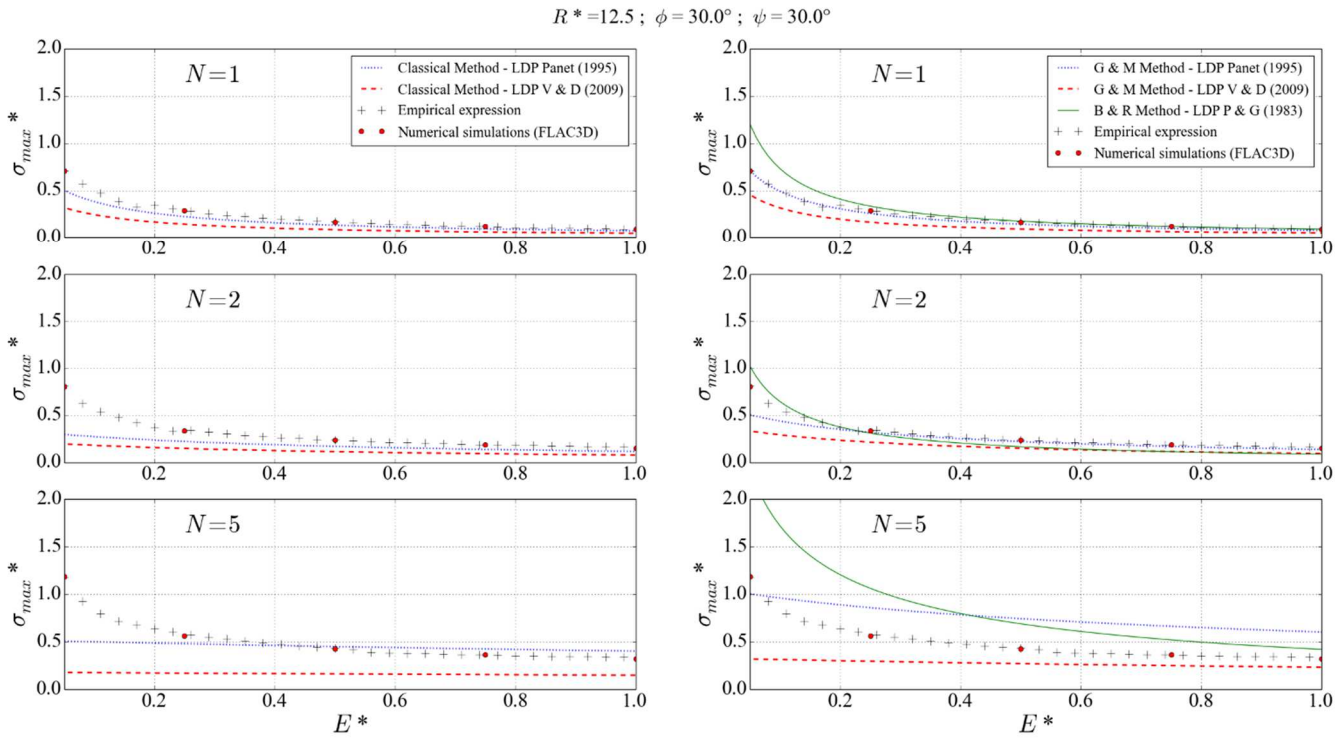

Comparison of $\sigma_{max}{}^{*}$ between the different approaches when R^{*}=12.5 and ϕ=30° for associate plasticity (ψ = ϕ). Classical methods on the left column and implicit methods on the right column

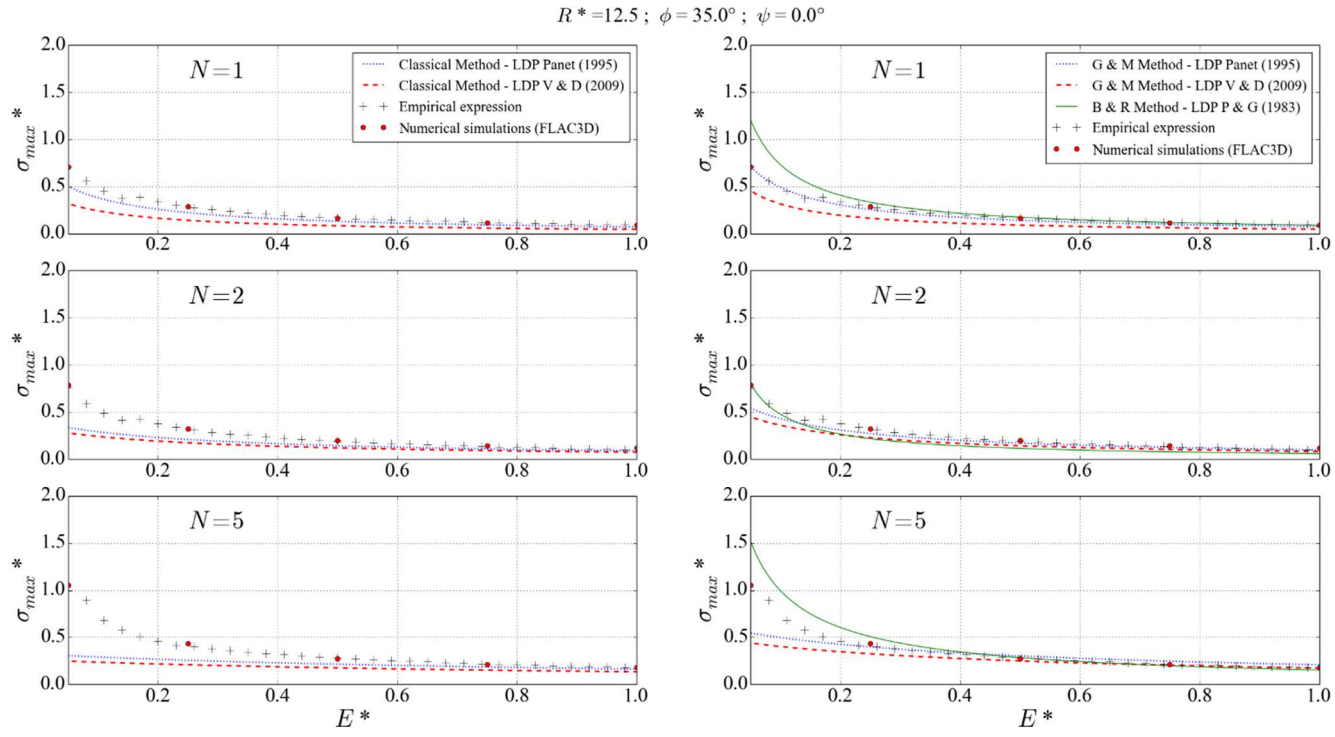

Comparison of $\sigma_{max}{}^{*}$ between the different approaches when R^{*}=12.5 and ϕ=35° for incompressible plasticity (ψ = 0). Classical methods on the left column and implicit methods on the right column

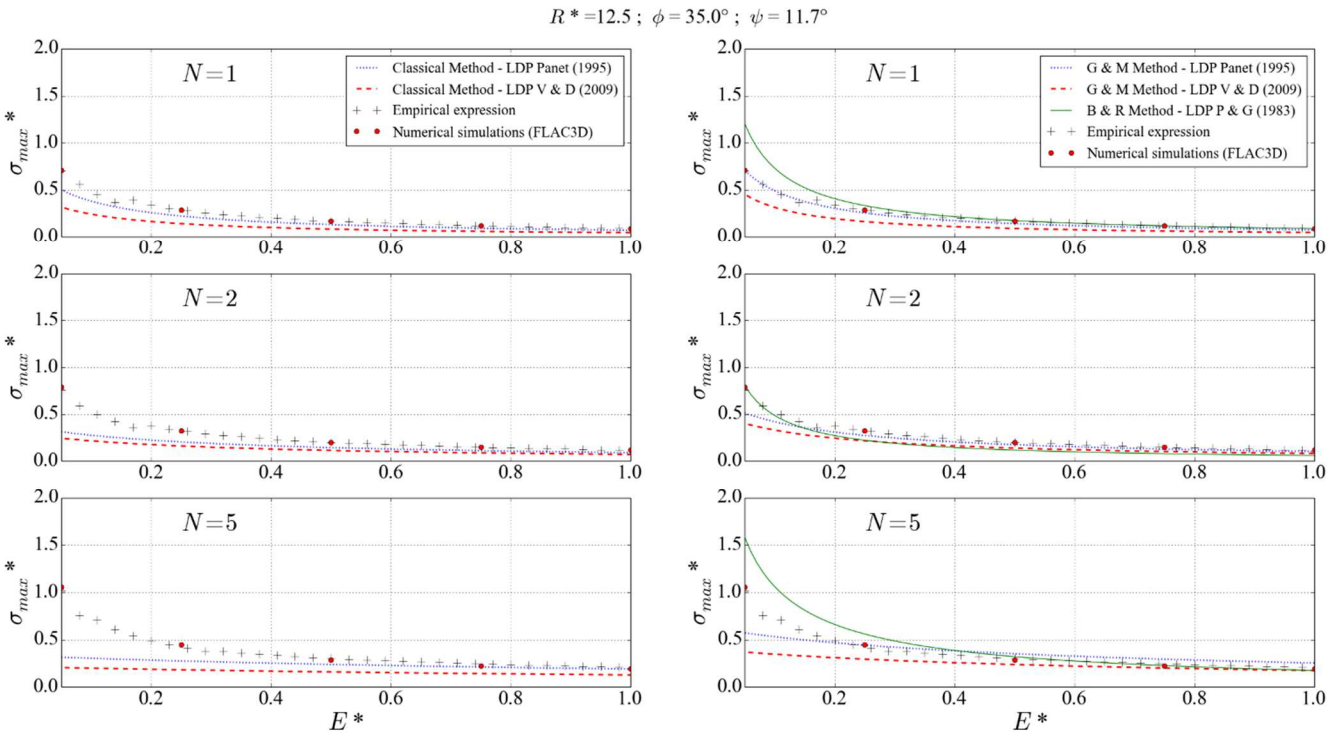

Comparison of $\sigma_{max}{}^{*}$ between the different approaches when R^{*}=12.5 and ϕ=35° for non-associate plasticity (ψ = ϕ/3). Classical methods on the left column and implicit methods on the right column

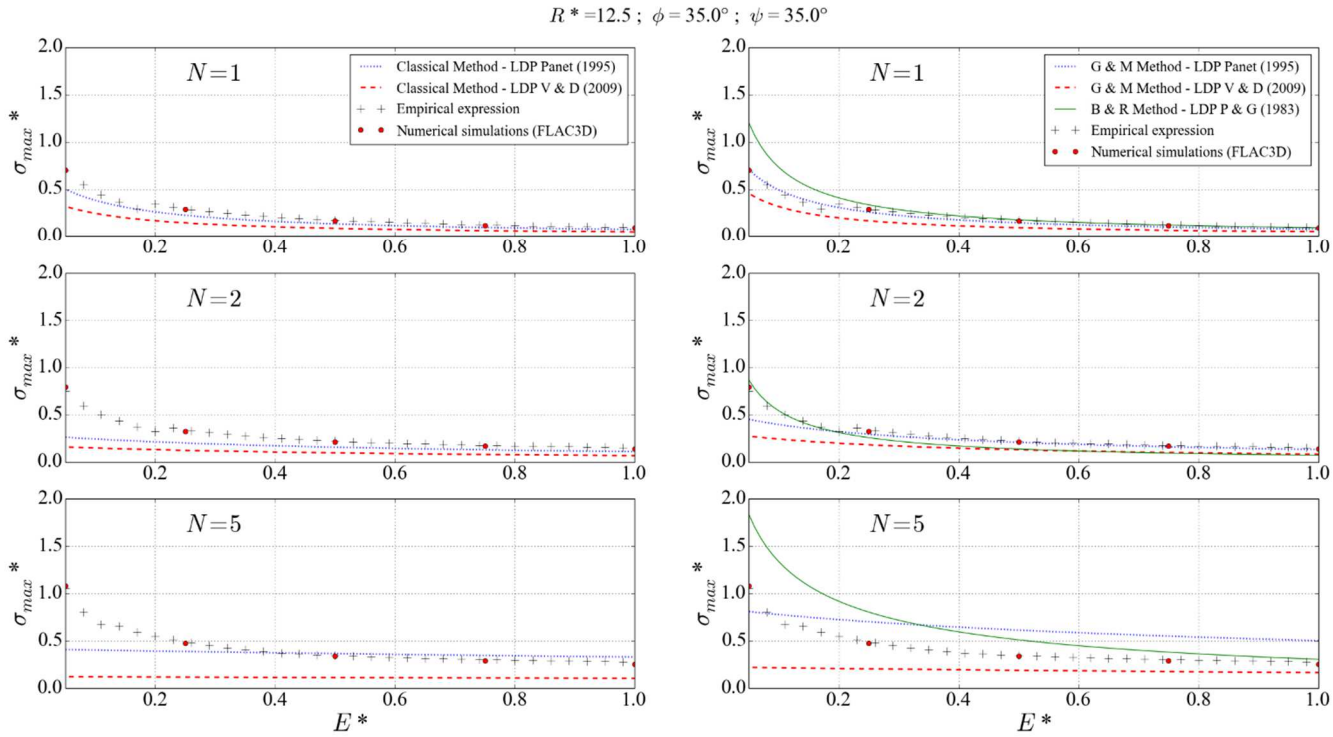

Comparison of $\sigma_{max}{}^{*}$ between the different approaches when R^{*}=12.5 and ϕ=35° for associate plasticity (ψ = ϕ). Classical methods on the left column and implicit methods on the right column

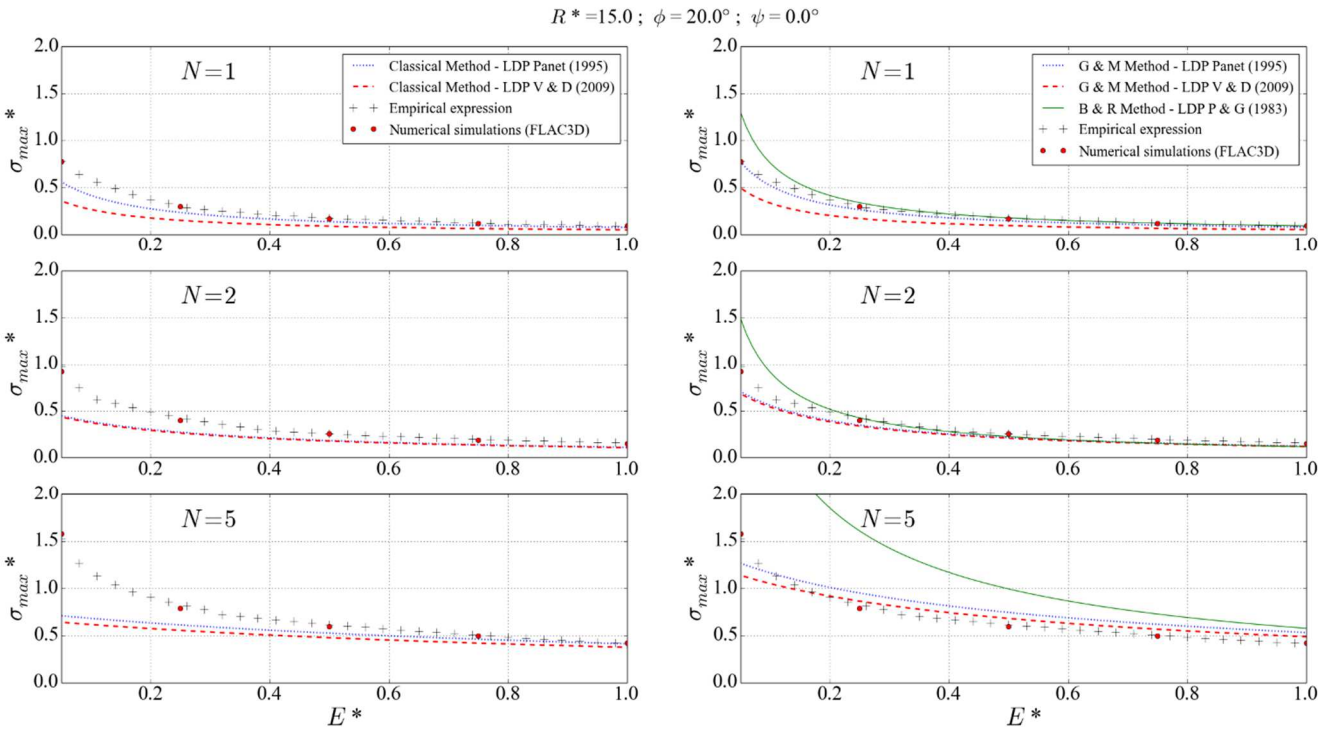

Comparison of $\sigma_{max}{}^{*}$ between the different approaches when R^{*}=15 and ϕ=20° for incompressible plasticity (ψ = 0). Classical methods on the left column and implicit methods on the right column

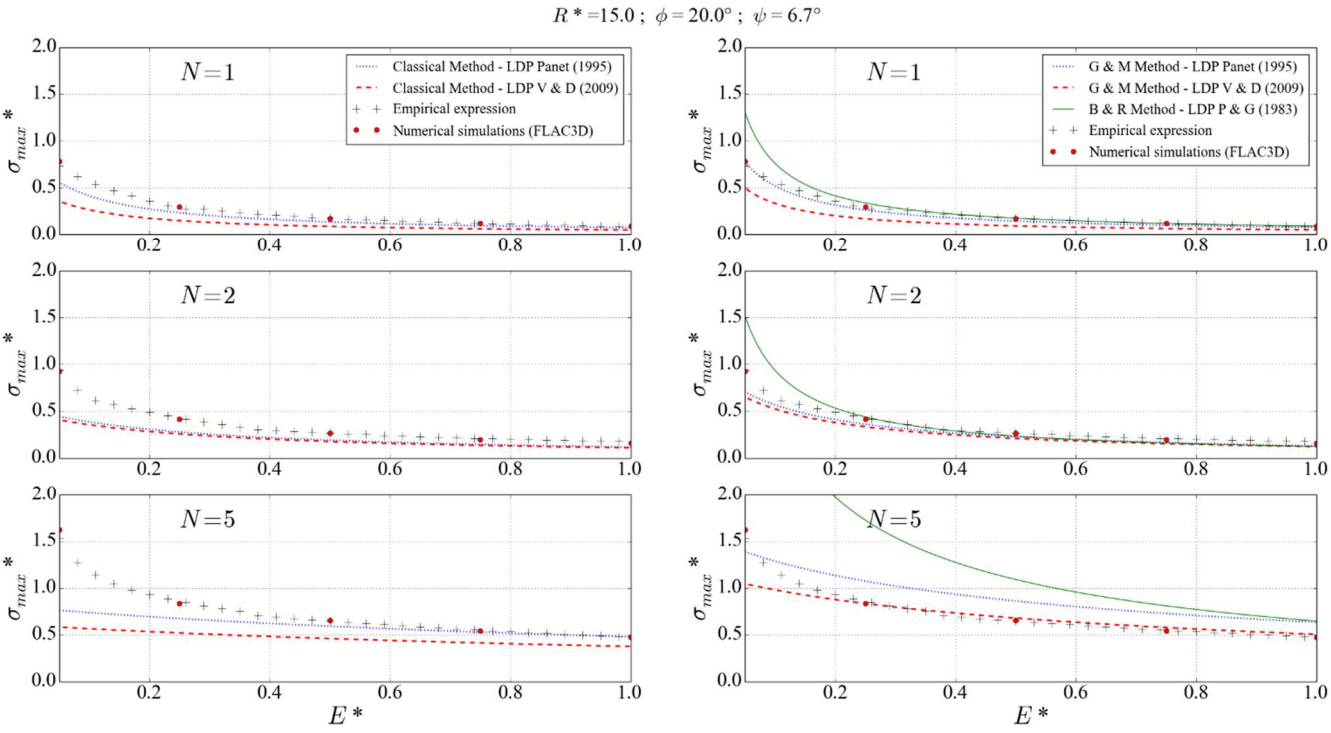

Comparison of $\sigma_{max}{}^{*}$ between the different approaches when R^{*}=15 and ϕ=20° for non-associate plasticity (ψ = ϕ/3). Classical methods on the left column and implicit methods on the right column

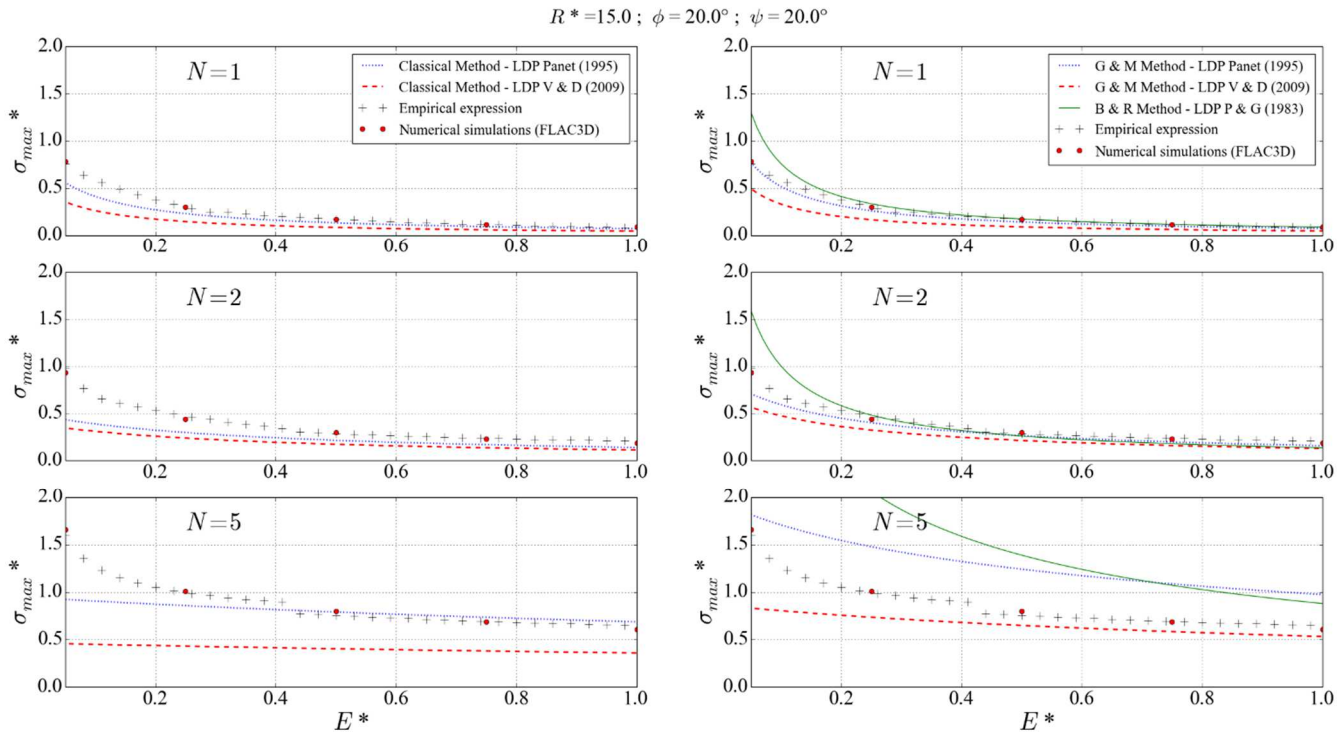

Comparison of $\sigma_{max}{}^{*}$ between the different approaches when R^{*}=15 and ϕ=20° for associate plasticity (ψ = ϕ). Classical methods on the left column and implicit methods on the right column

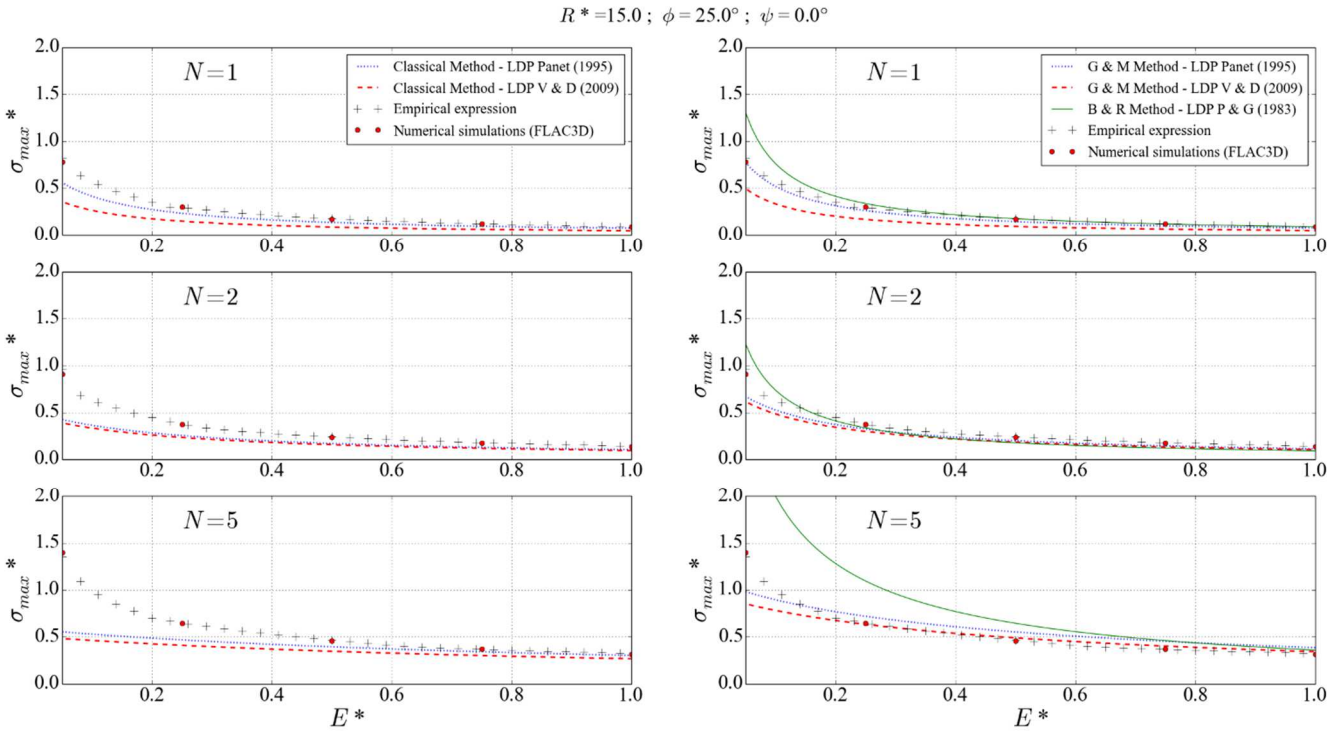

Comparison of $\sigma_{max}{}^{*}$ between the different approaches when R^{*}=15 and ϕ=25° for incompressible plasticity (ψ = 0). Classical methods on the left column and implicit methods on the right column

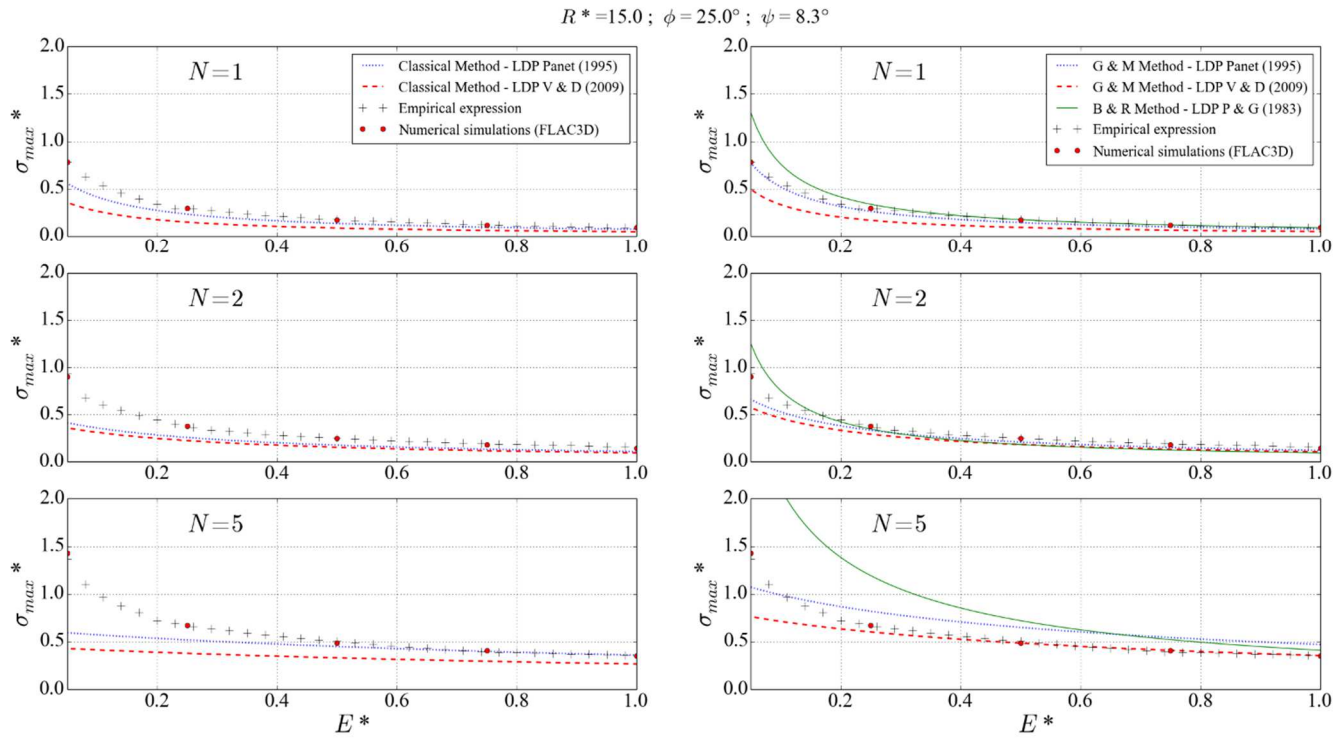

Comparison of $\sigma_{max}{}^{*}$ between the different approaches when R^{*}=15 and ϕ=25° for non-associate plasticity (ψ = ϕ/3). Classical methods on the left column and implicit methods on the right column

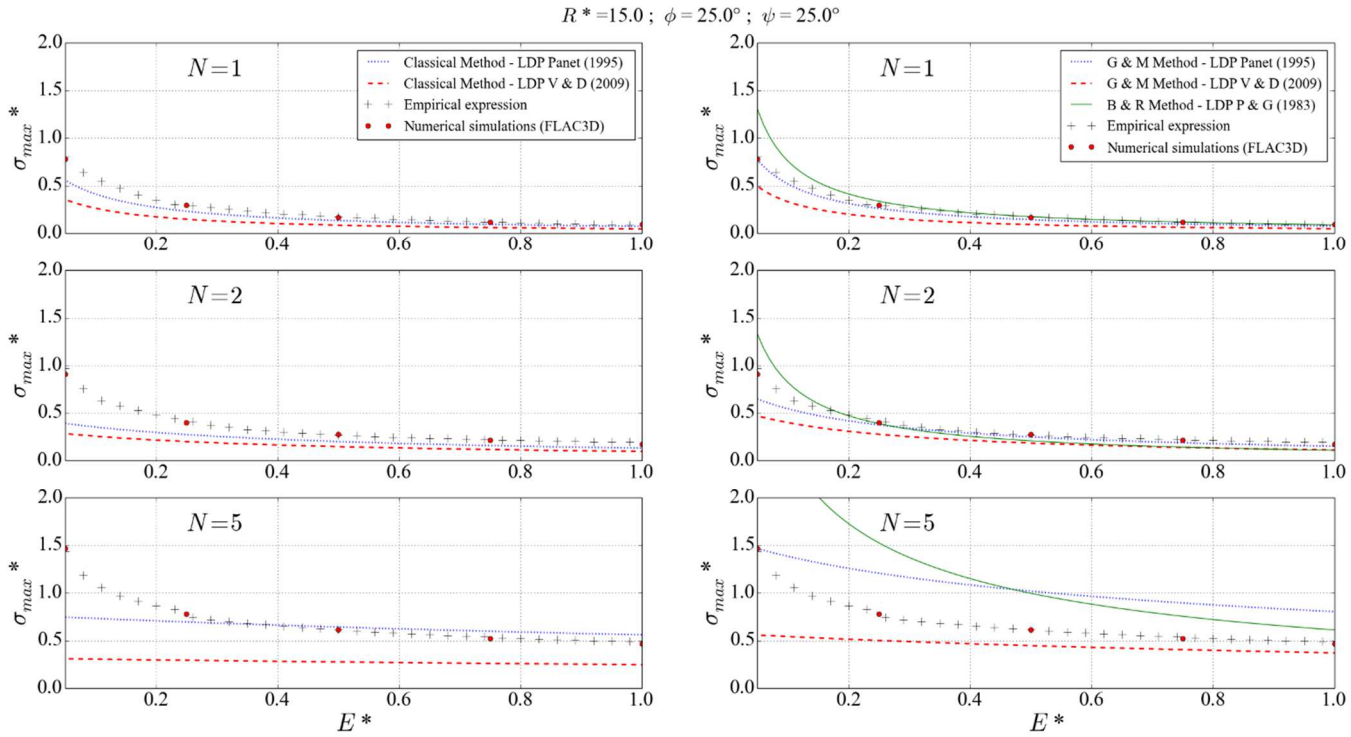

Comparison of $\sigma_{max}{}^{*}$ between the different approaches when R^{*}=15 and ϕ=25° for associate plasticity (ψ = ϕ). Classical methods on the left column and implicit methods on the right column

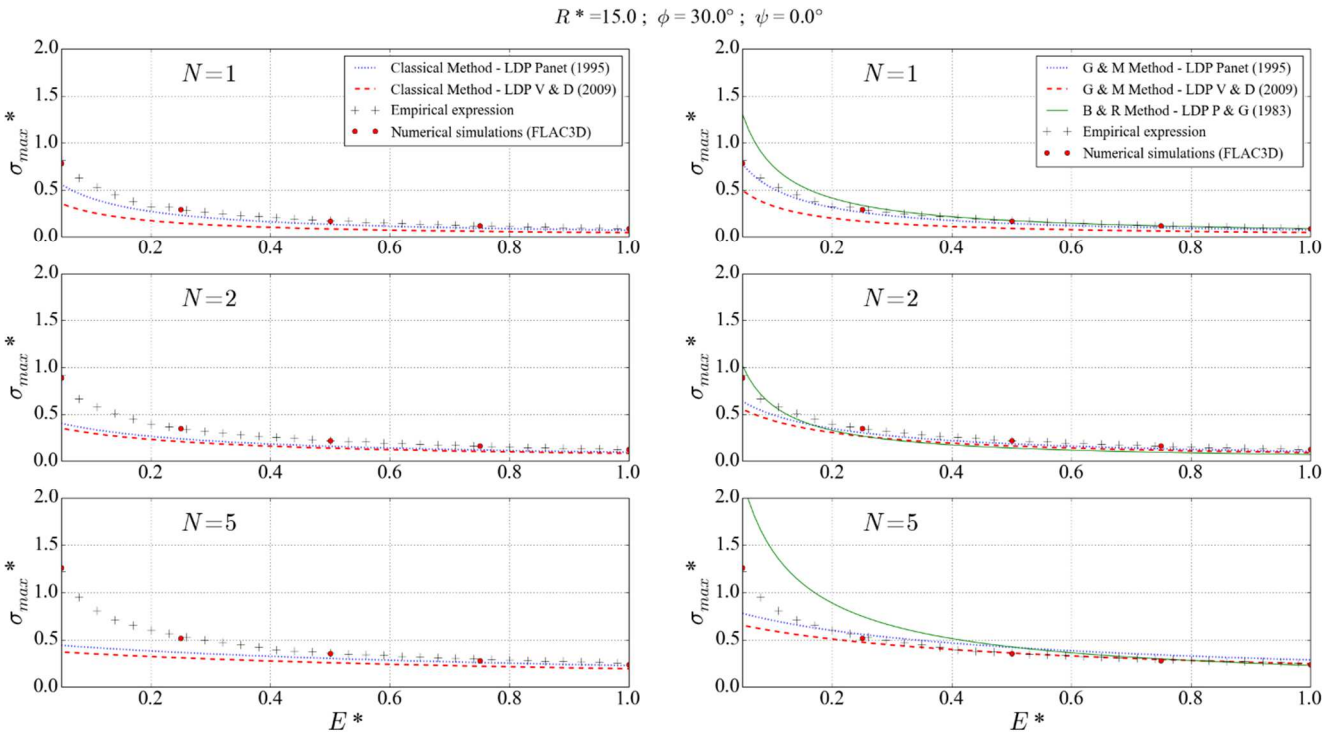

Comparison of $\sigma_{max}{}^{*}$ between the different approaches when R^{*}=15 and ϕ=30° for incompressible plasticity (ψ = 0). Classical methods on the left column and implicit methods on the right column

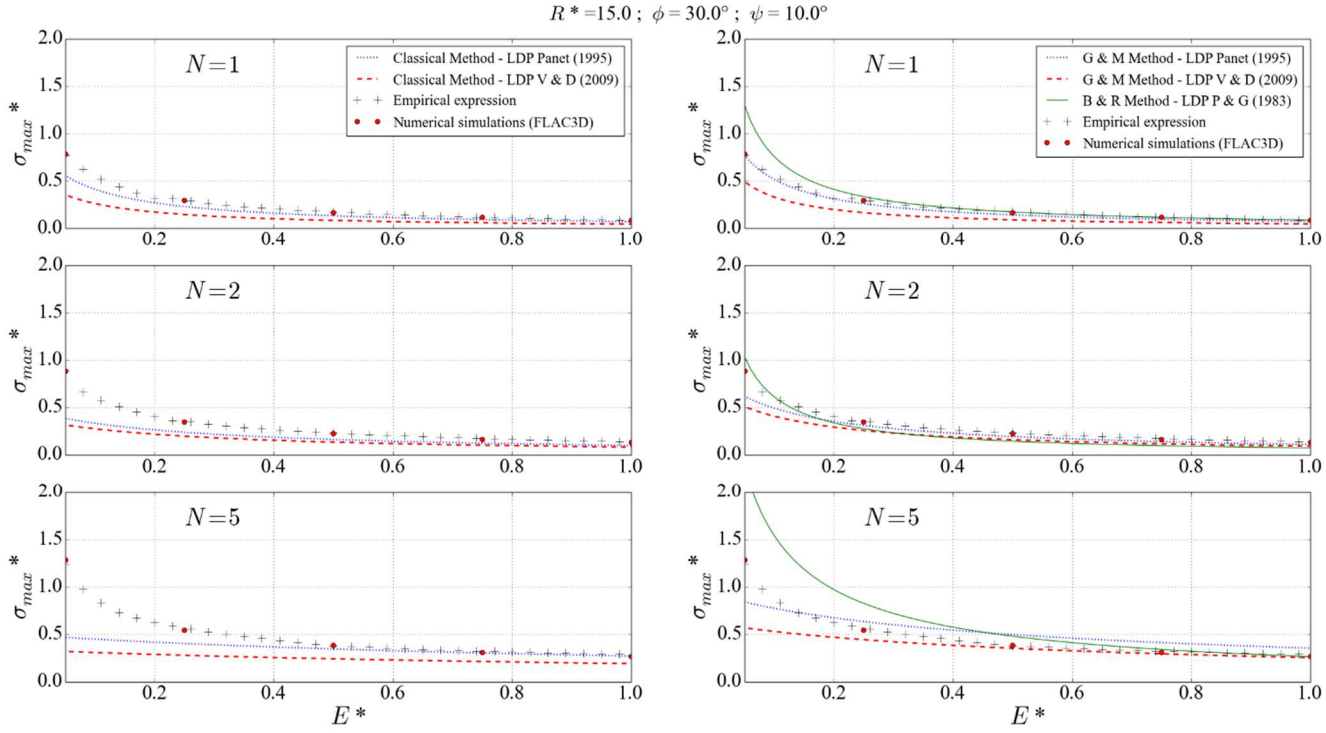

Comparison of $\sigma_{max}{}^{*}$ between the different approaches when R^{*}=15 and ϕ=30° for non-associate plasticity (ψ = ϕ/3). Classical methods on the left column and implicit methods on the right column

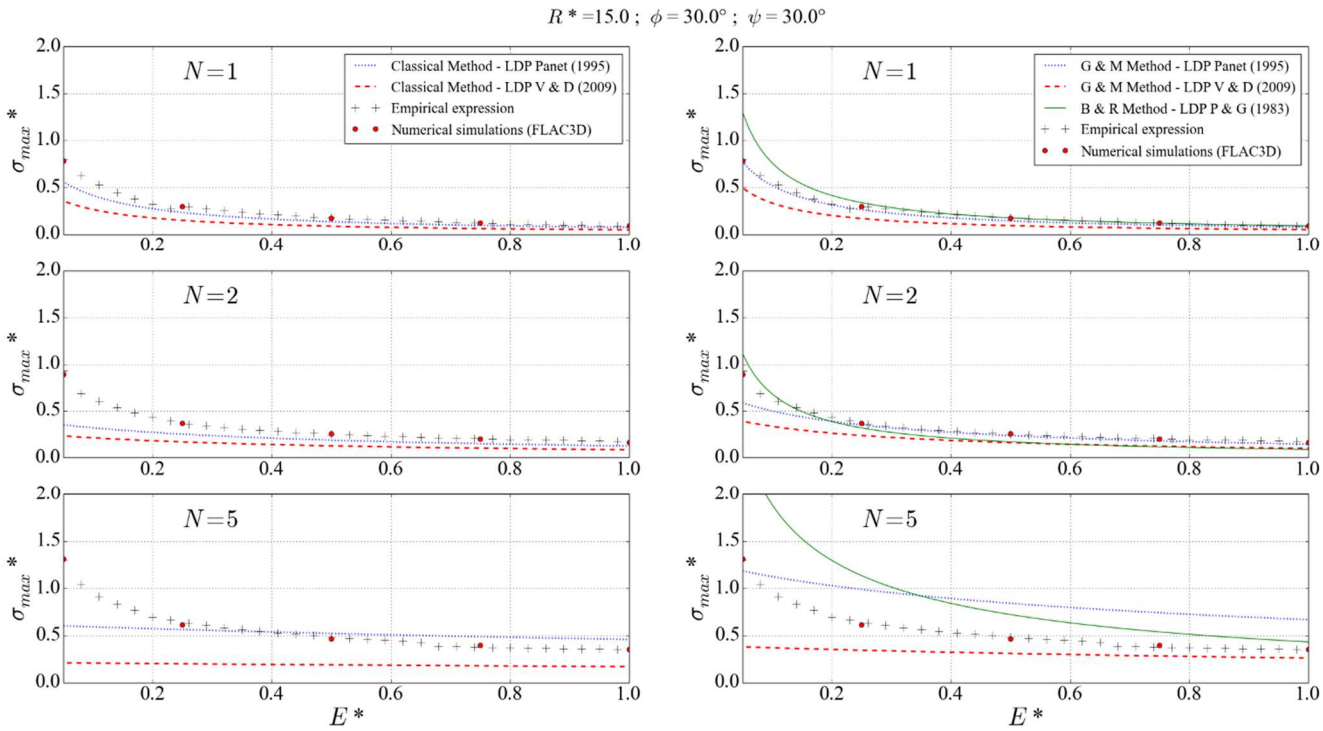

Comparison of σ_{max}^{*} between the different approaches when R^{*}=15 and ϕ=30° for associate plasticity (ψ = ϕ). Classical methods on the left column and implicit methods on the right column

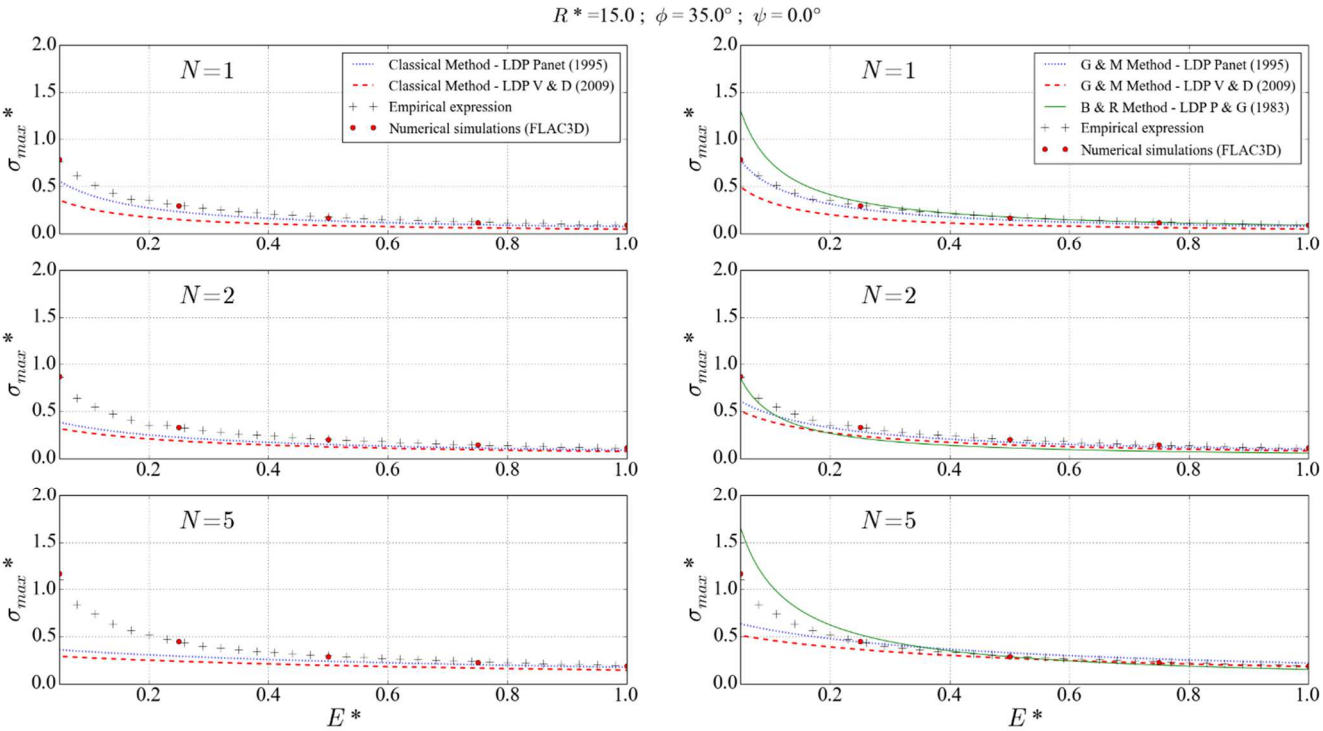

Comparison of σ_{max}^{*} between the different approaches when R^{*}=15 and ϕ=35° for incompressible plasticity (ψ = 0). Classical methods on the left column and implicit methods on the right column

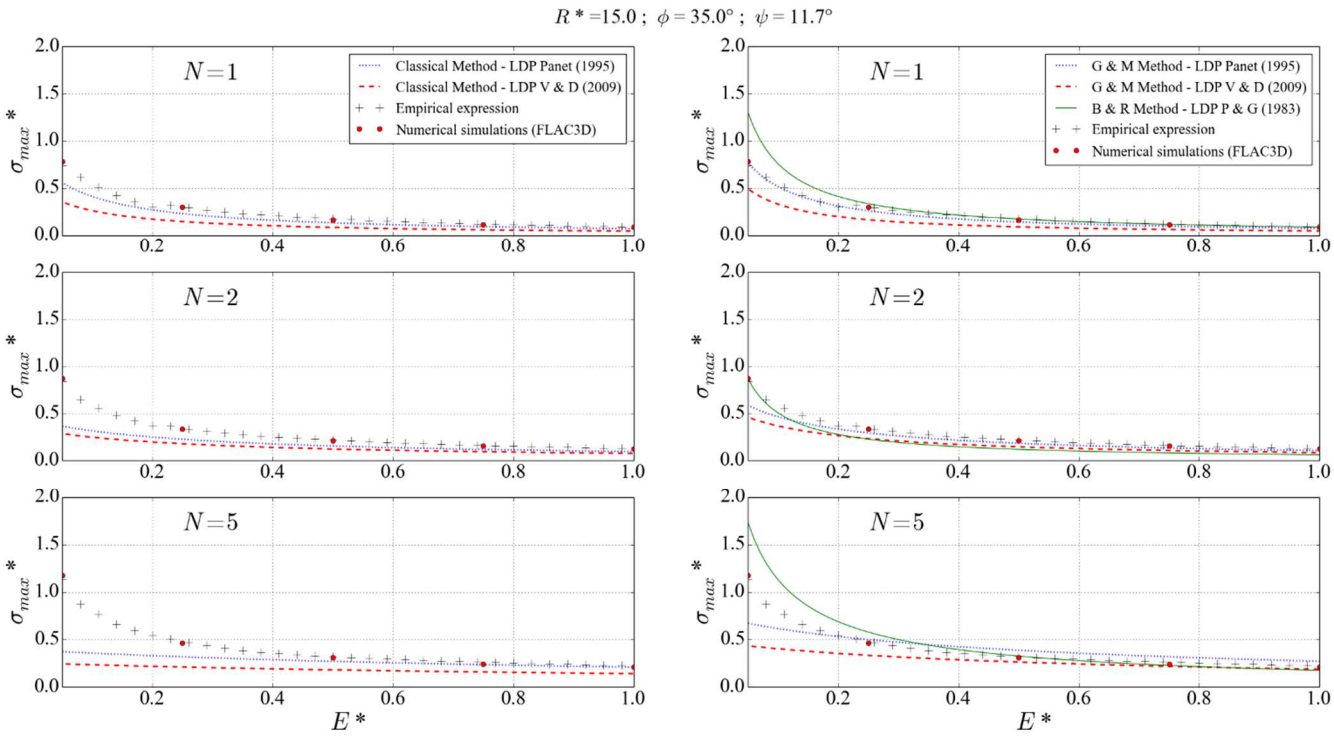

Comparison of $\sigma_{max}{}^{*}$ between the different approaches when R^{*}=15 and ϕ=35° for non-associate plasticity (ψ = ϕ/3). Classical methods on the left column and implicit methods on the right column

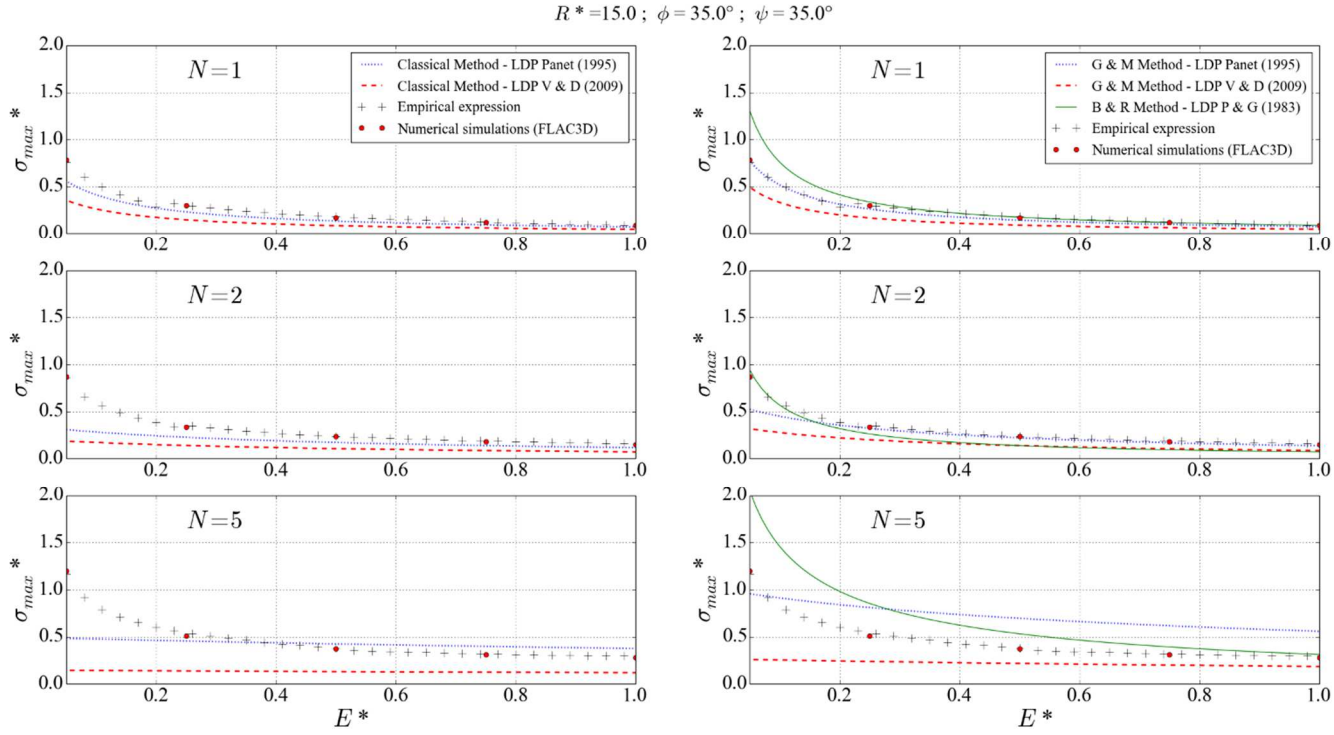

Comparison of $\sigma_{max}{}^{*}$ between the different approaches when R^{*}=15 and ϕ=35° for associate plasticity (ψ = ϕ). Classical methods on the left column and implicit methods on the right column

APPENDIX C - Total set of results of the comparison of $\overline{\boldsymbol{u}}(\infty)^*$ between the different approaches

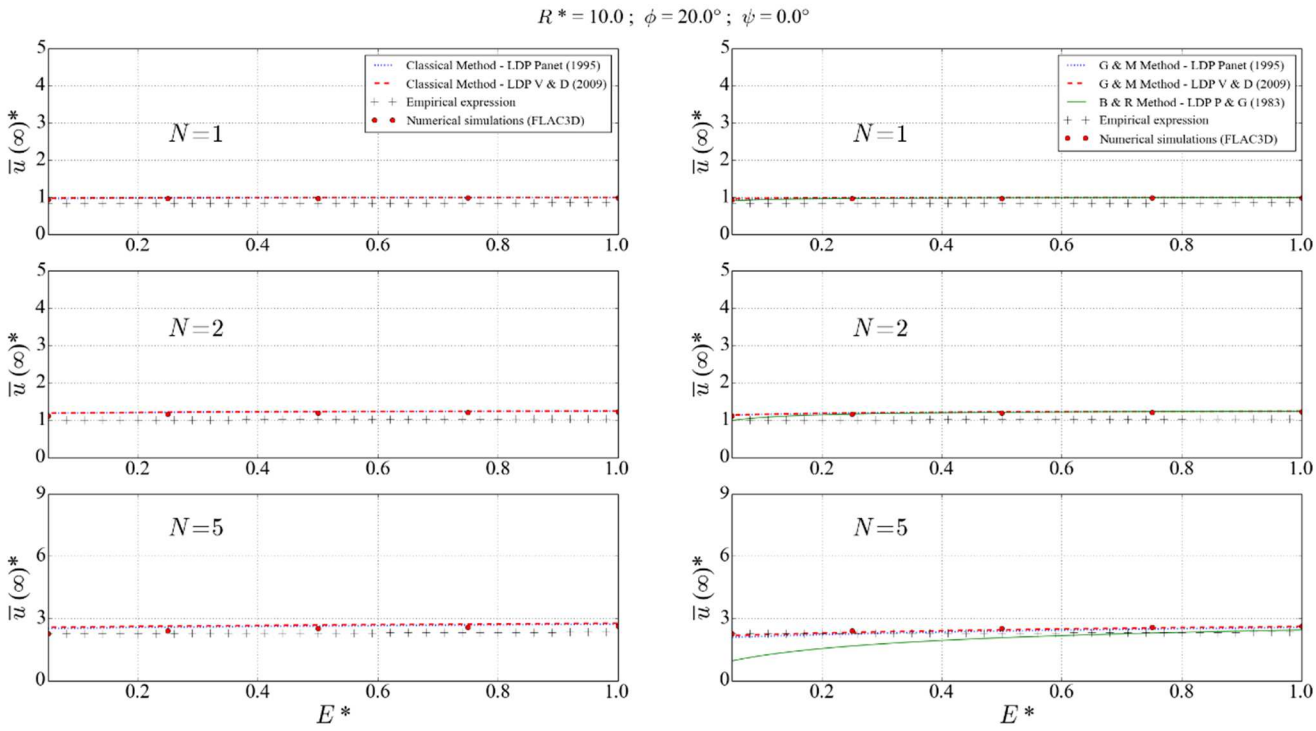

Comparison of $\bar{u}(\infty)^*$ between the different approaches when R^*=10 and ϕ=20° for incompressible plasticity (ψ = 0). Classical methods on the left column and implicit methods on the right column

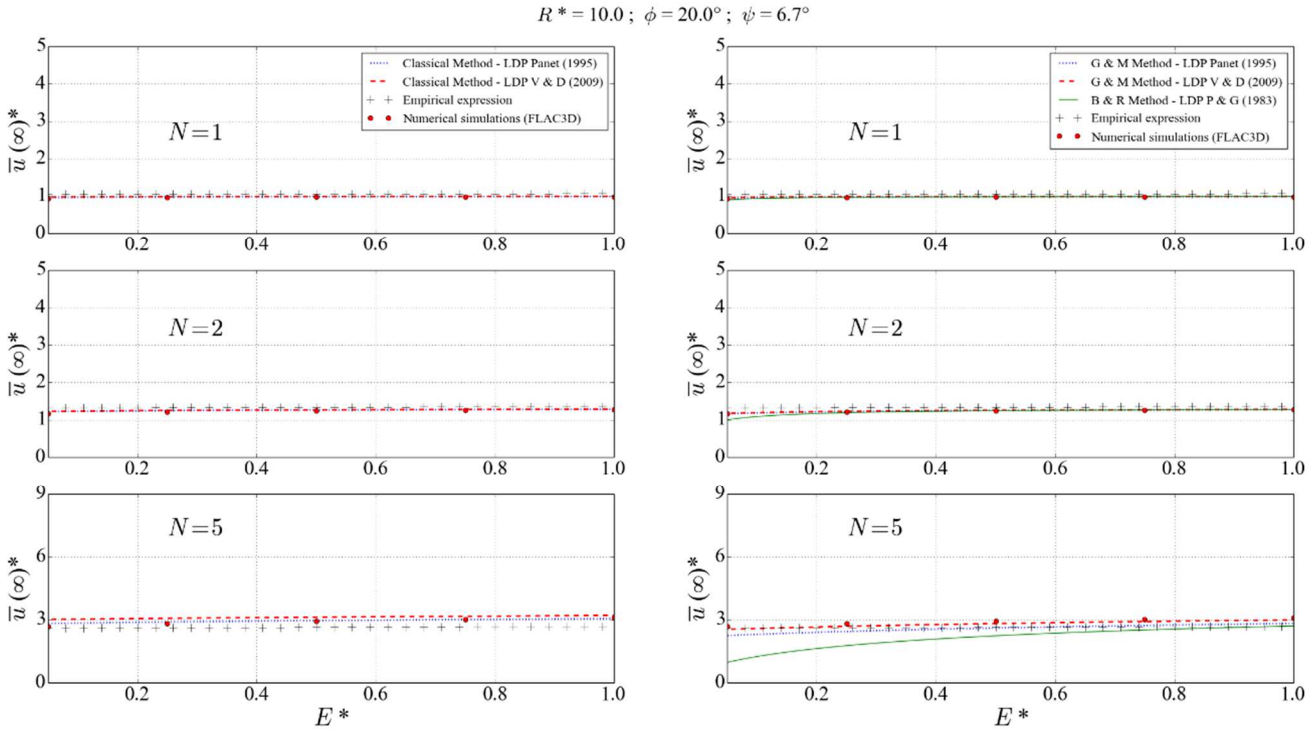

Comparison of $\bar{u}(\infty)^*$ between the different approaches when R^*=10 and ϕ=20° for non-associate plasticity (ψ = ϕ/3). Classical methods on the left column and implicit methods on the right column

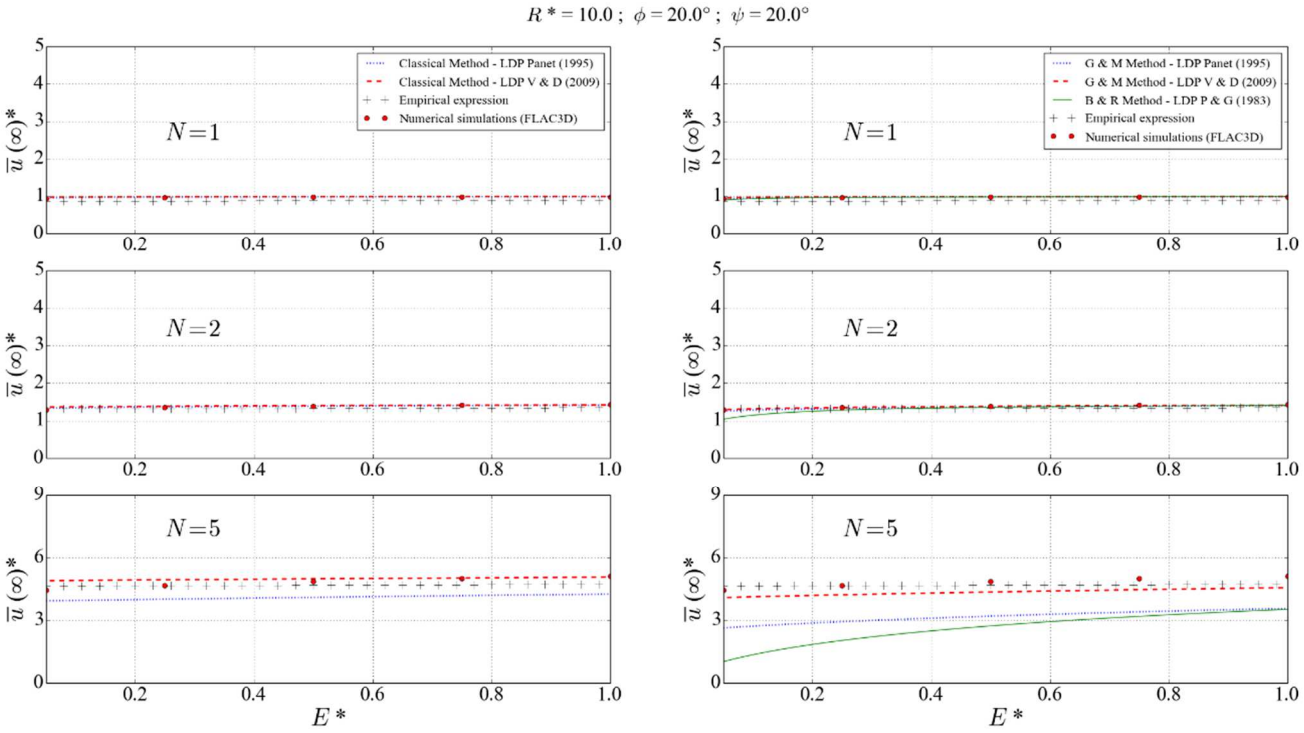

Comparison of $\bar{u}(\infty)^*$ between the different approaches when R^*=10 and ϕ=20° for associate plasticity (ψ = ϕ). Classical methods on the left column and implicit methods on the right column

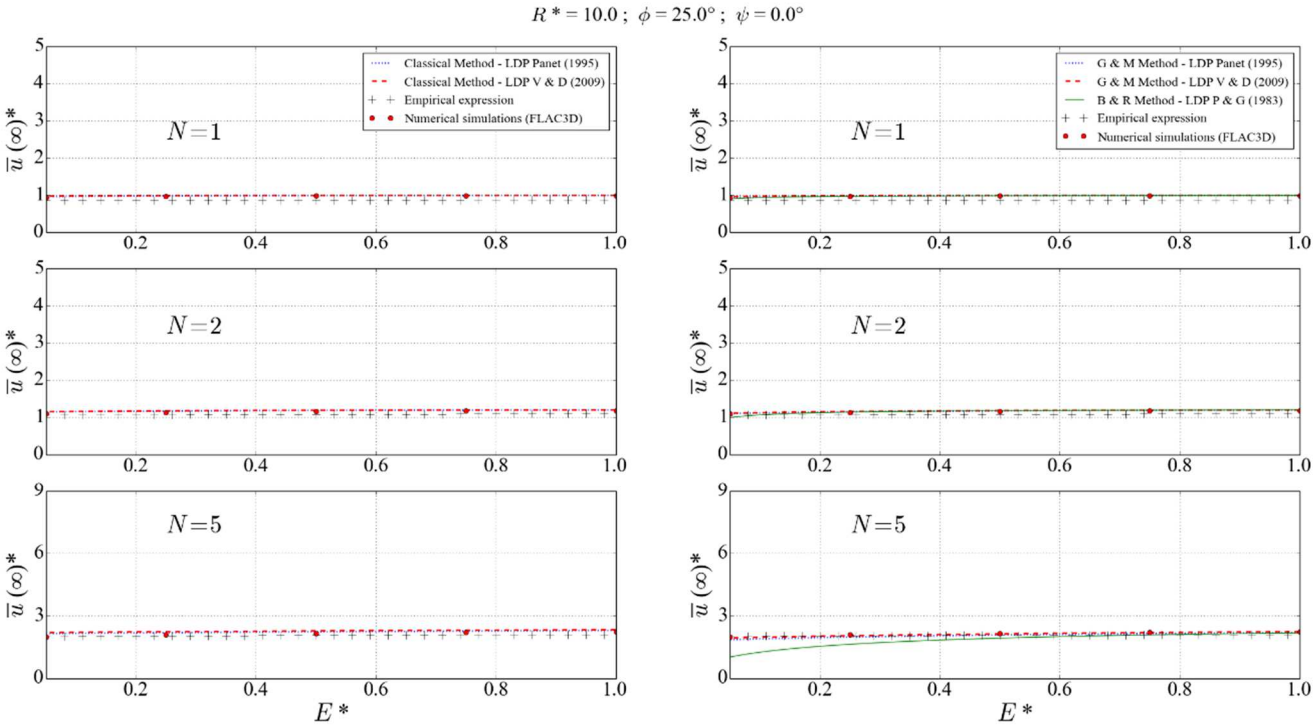

Comparison of $\bar{u}(\infty)^*$ between the different approaches when R^*=10 and ϕ=25° for incompressible plasticity (ψ = 0). Classical methods on the left column and implicit methods on the right column

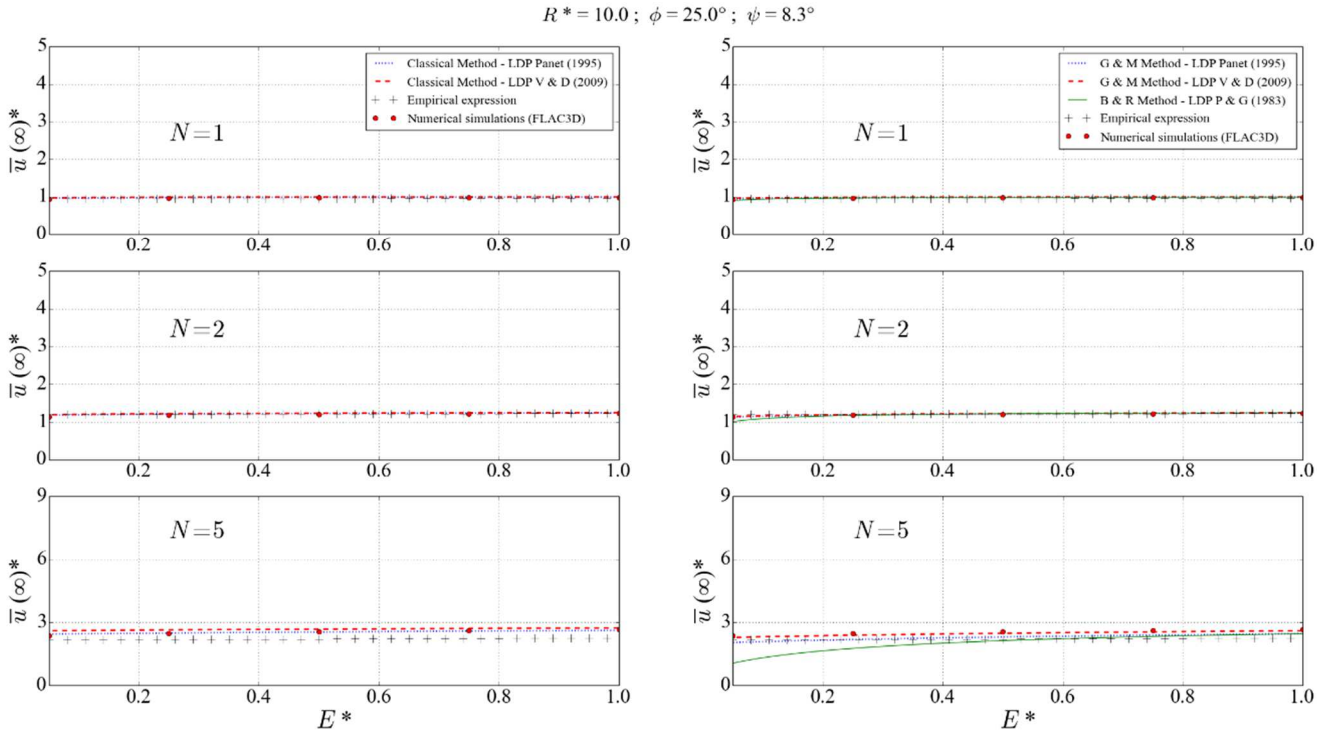

Comparison of $\bar{u}(\infty)^*$ between the different approaches when R^*=10 and ϕ=25° for non-associate plasticity (ψ = ϕ/3). Classical methods on the left column and implicit methods on the right column

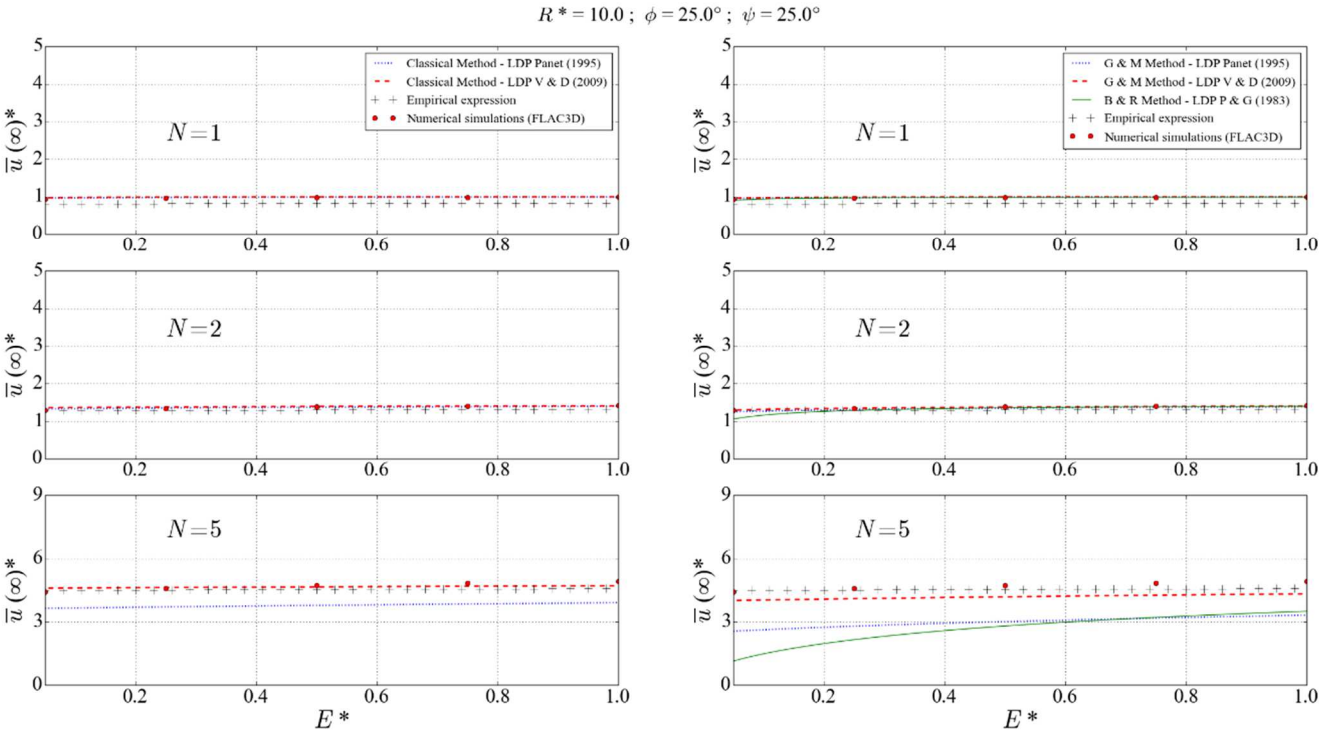

Comparison of $\bar{u}(\infty)^*$ between the different approaches when R^*=10 and ϕ=25° for associate plasticity (ψ = ϕ). Classical methods on the left column and implicit methods on the right column

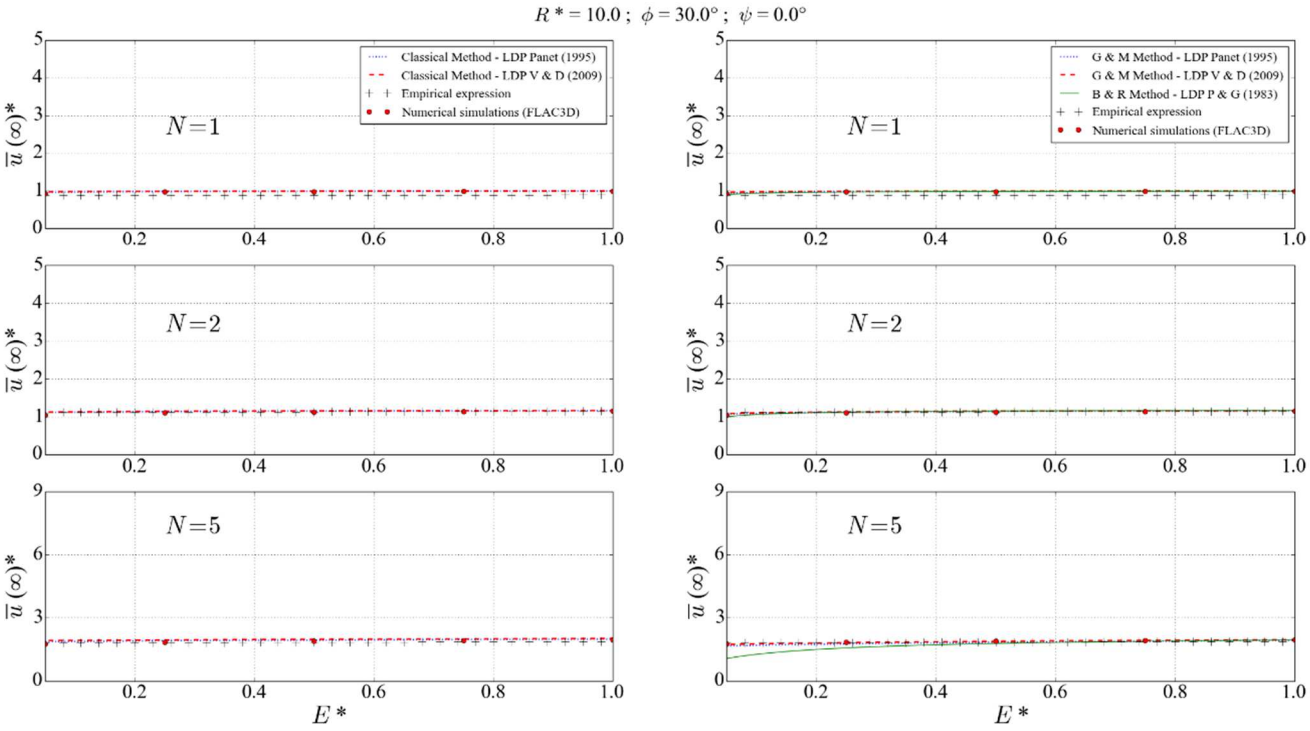

Comparison of $\bar{u}(\infty)^*$ between the different approaches when R^*=10 and ϕ=30° for incompressible plasticity (ψ = 0). Classical methods on the left column and implicit methods on the right column

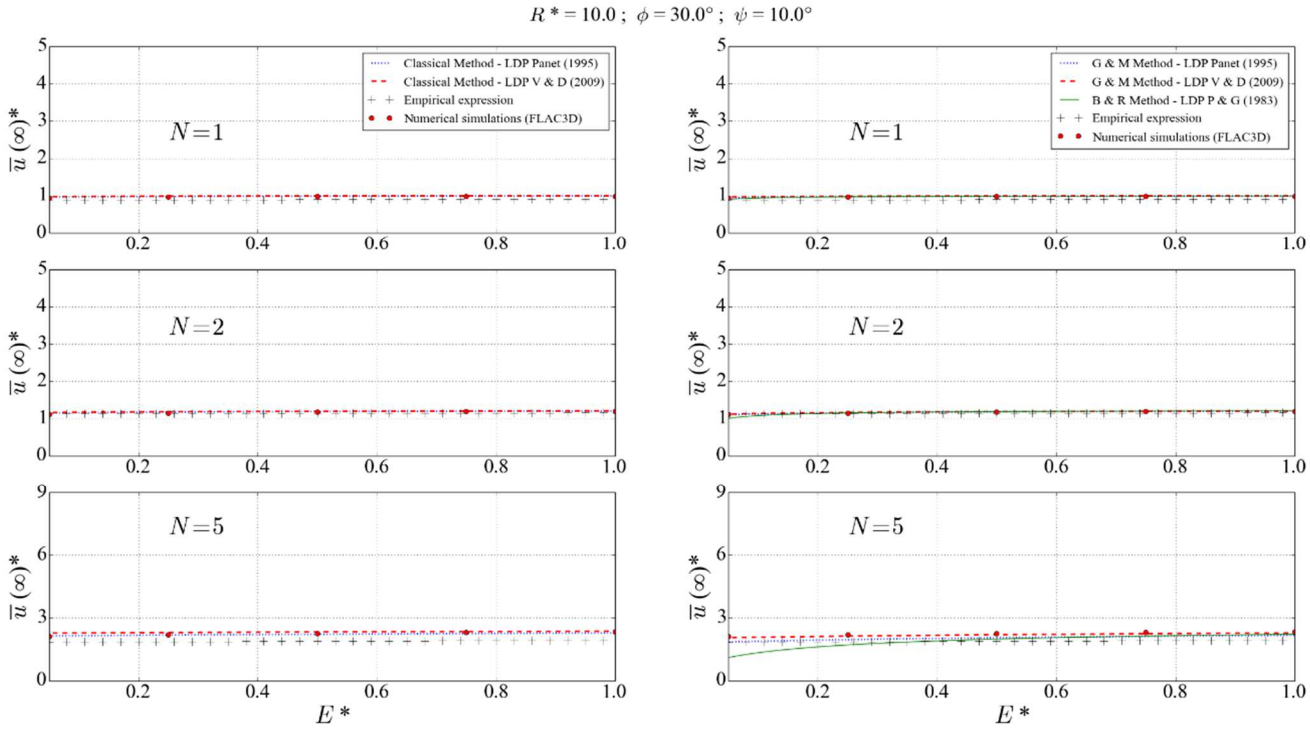

Comparison of $\bar{u}(\infty)^*$ between the different approaches when R^*=10 and ϕ=30° for non-associate plasticity (ψ = ϕ/3). Classical methods on the left column and implicit methods on the right column

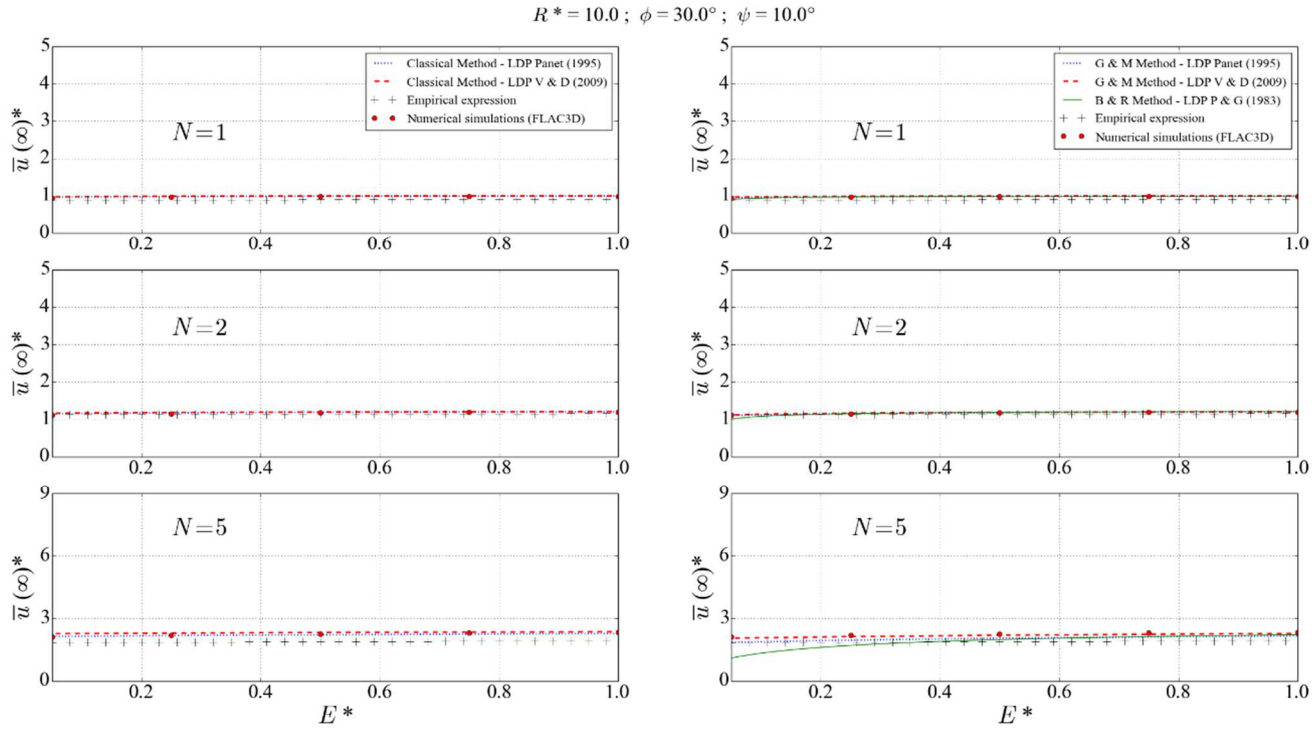

Comparison of $\bar{u}(\infty)^*$ between the different approaches when R^*=10 and ϕ=30° for associate plasticity (ψ = ϕ). Classical methods on the left column and implicit methods on the right column

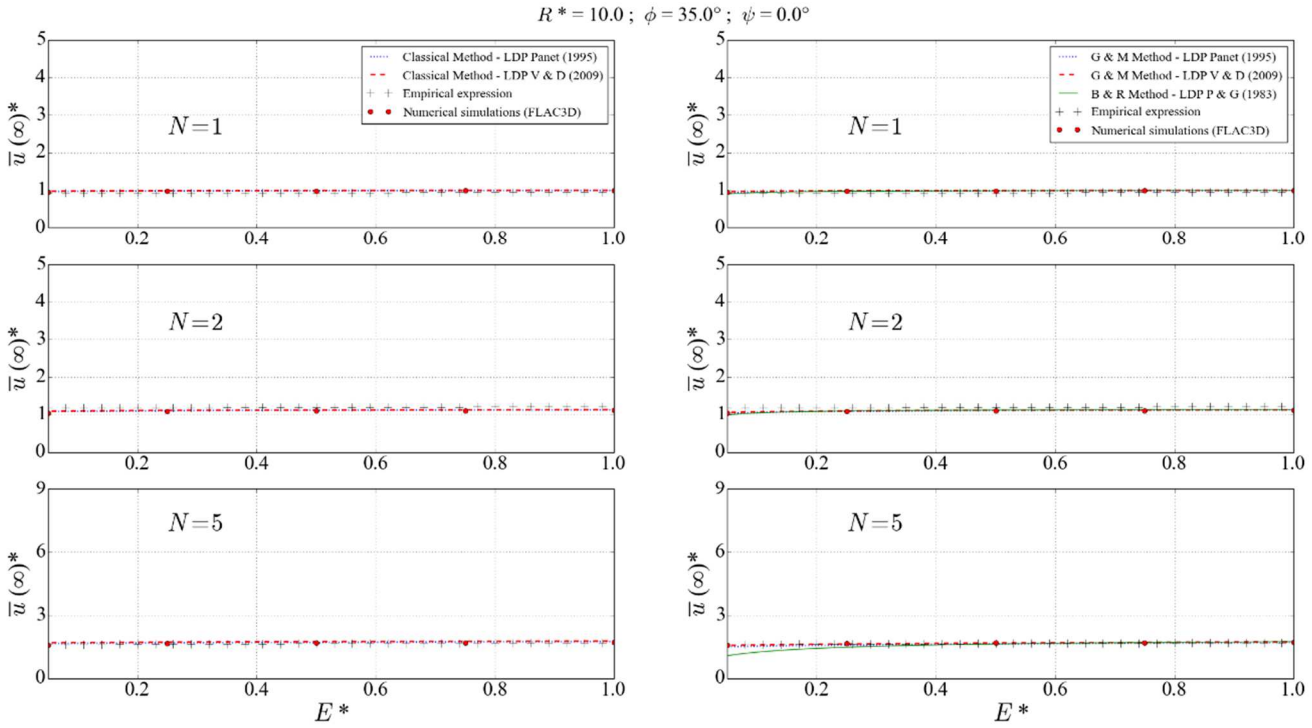

Comparison of $\bar{u}(\infty)^*$ between the different approaches when R^*=10 and ϕ=35° for incompressible plasticity (ψ = 0). Classical methods on the left column and implicit methods on the right column

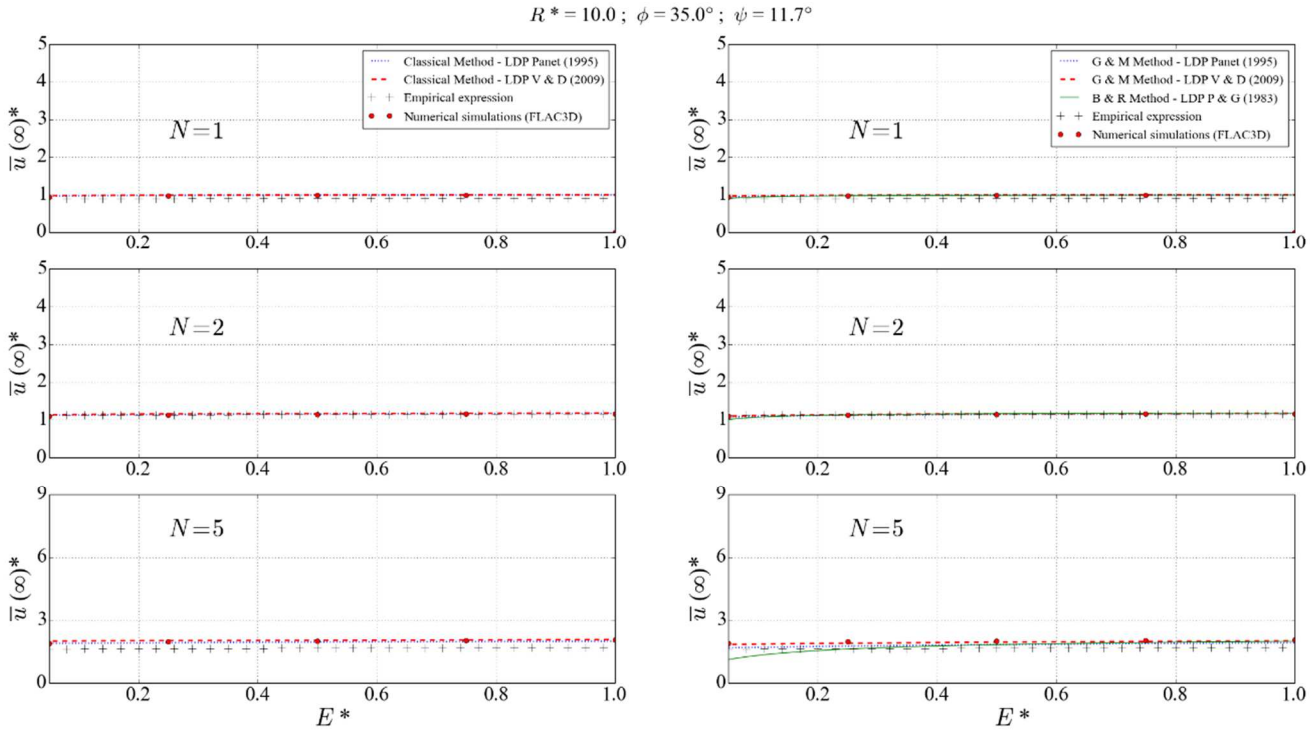

Comparison of $\bar{u}(\infty)^*$ between the different approaches when R^*=10 and ϕ=35° for non-associate plasticity (ψ = ϕ/3). Classical methods on the left column and implicit methods on the right column

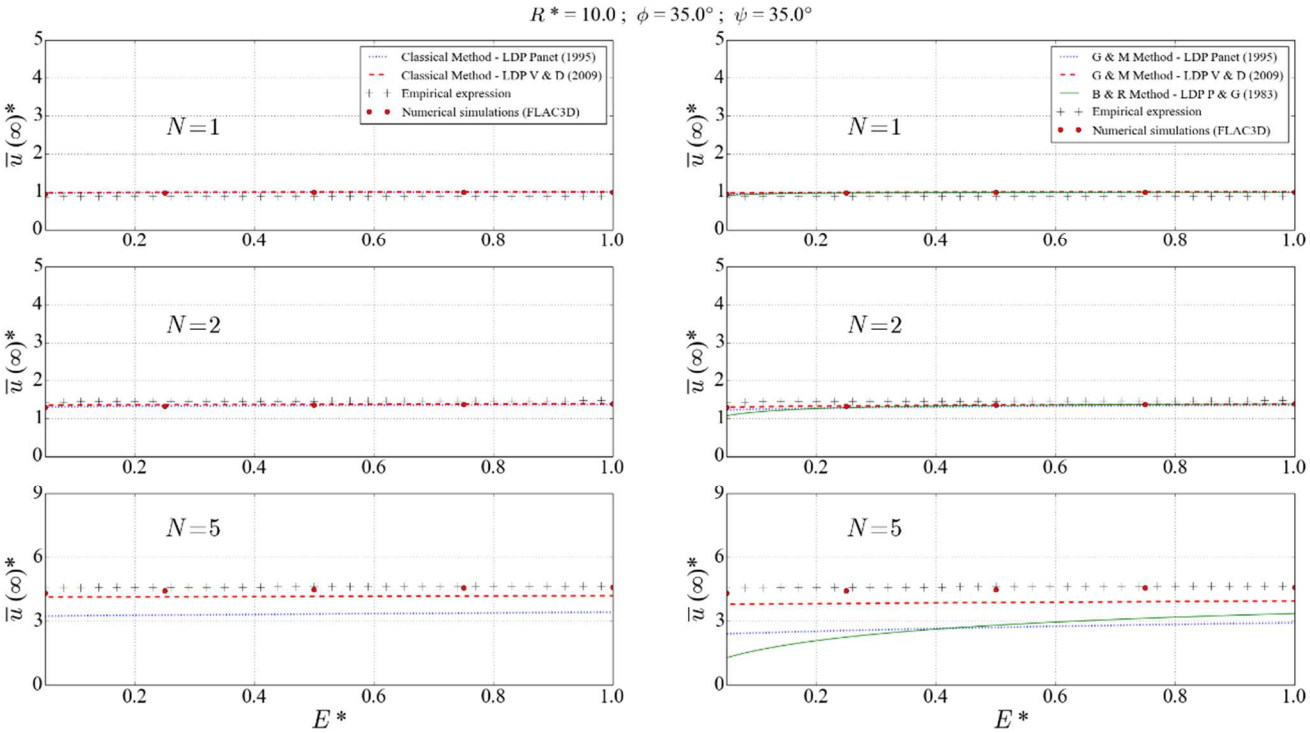

Comparison of $\bar{u}(\infty)^*$ between the different approaches when R^*=10 and ϕ=35° for associate plasticity (ψ = ϕ). Classical methods on the left column and implicit methods on the right column

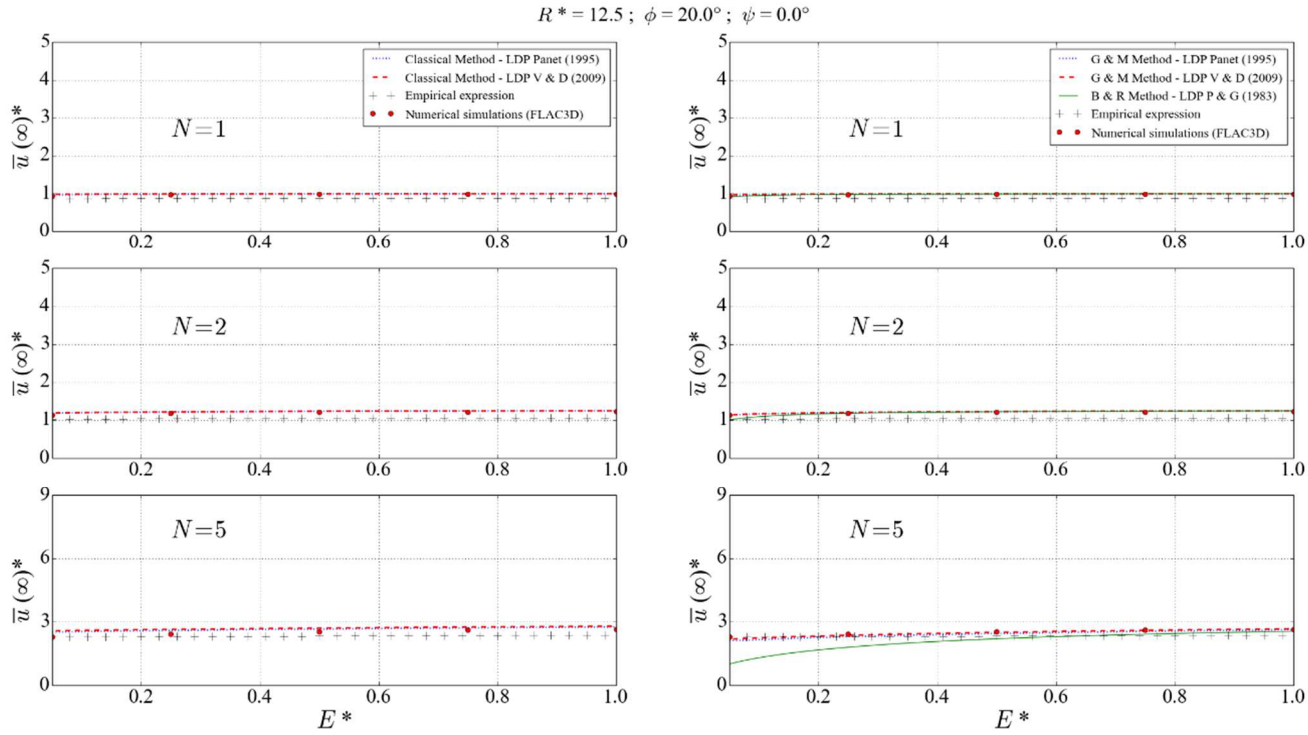

Comparison of $\bar{u}(\infty)^*$ between the different approaches when R^*=12.5 and ϕ=20° for incompressible plasticity (ψ = 0). Classical methods on the left column and implicit methods on the right column

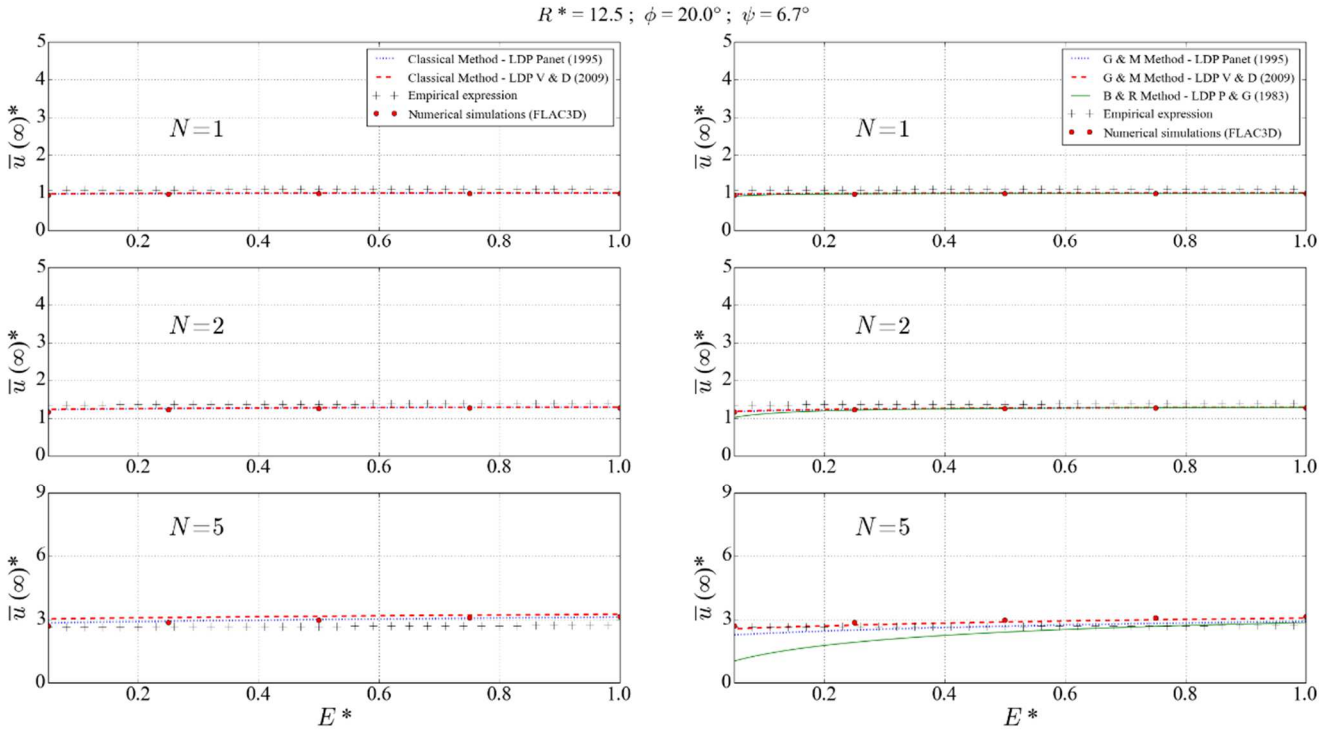

Comparison of $\bar{u}(\infty)^*$ between the different approaches when R^*=12.5 and ϕ=20° for non-associate plasticity (ψ = ϕ/3). Classical methods on the left column and implicit methods on the right column

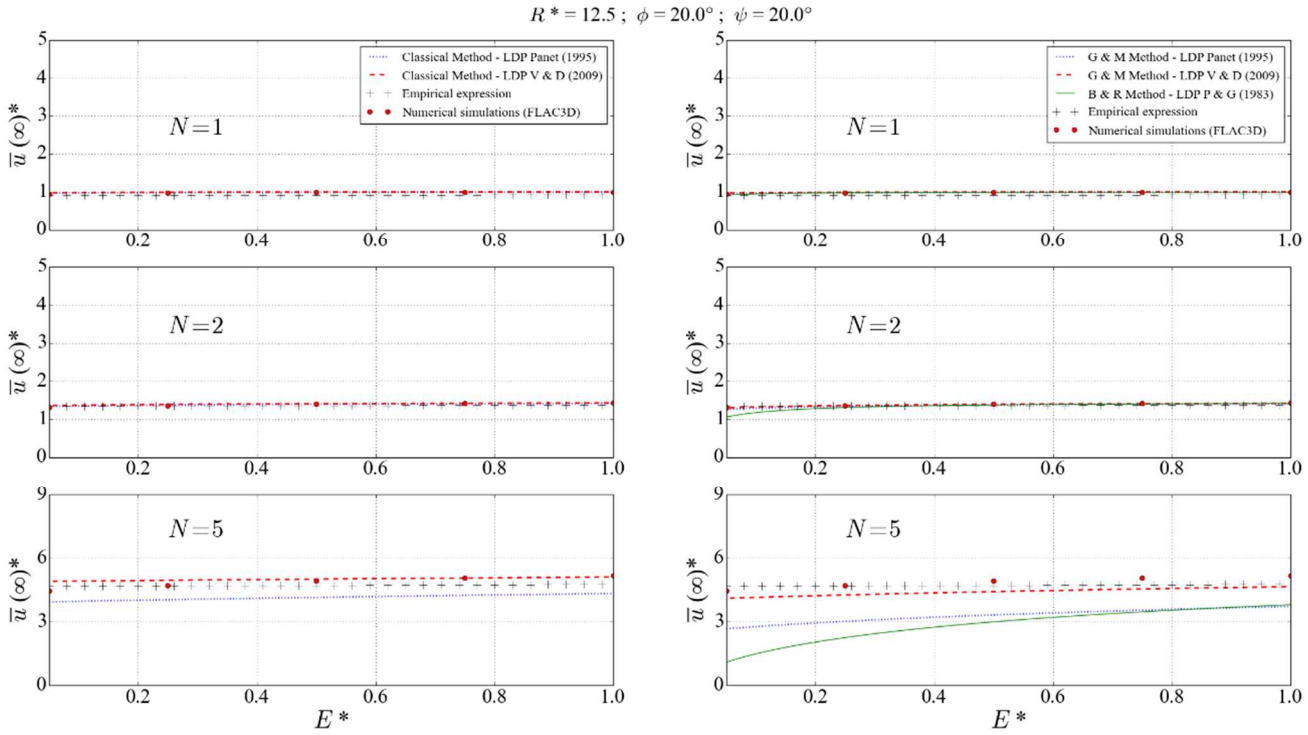

Comparison of $\bar{u}(\infty)^*$ between the different approaches when R^*=12.5 and ϕ=20° for associate plasticity (ψ = ϕ). Classical methods on the left column and implicit methods on the right column

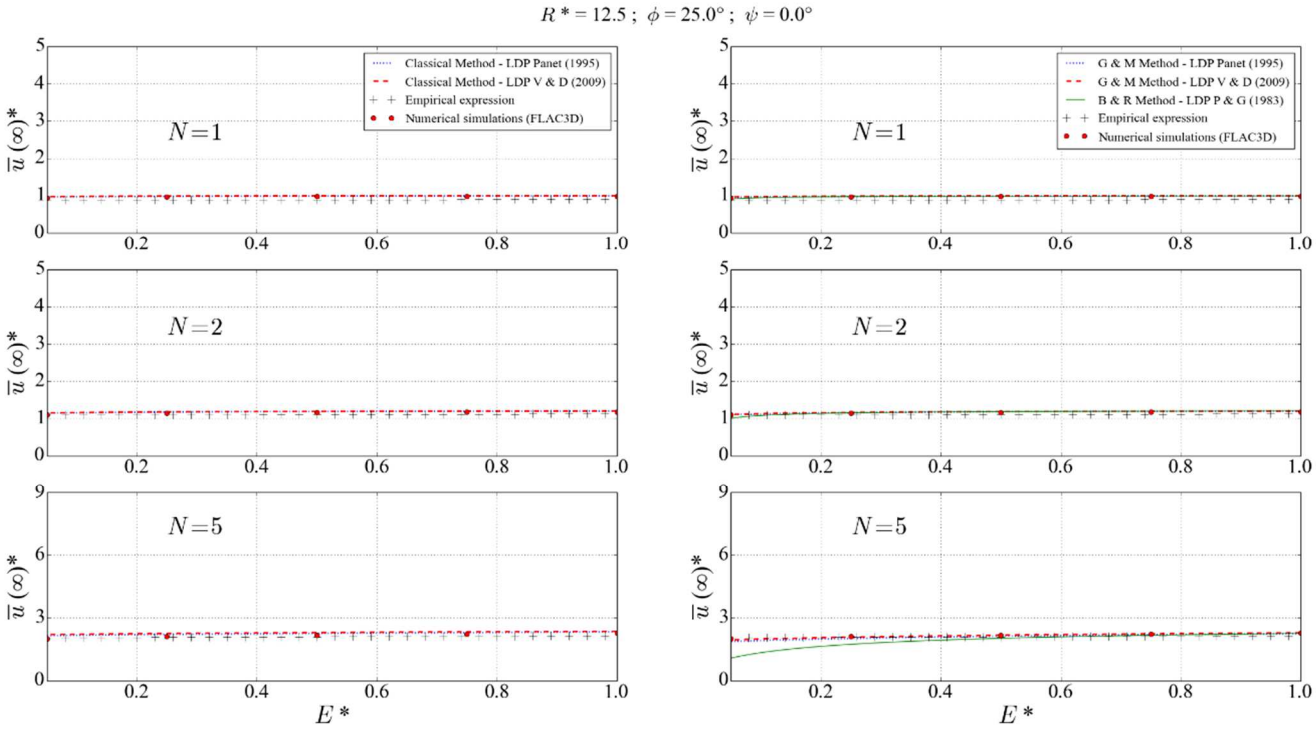

Comparison of $\bar{u}(\infty)^*$ between the different approaches when R^*=12.5 and ϕ=25° for incompressible plasticity (ψ = 0). Classical methods on the left column and implicit methods on the right column

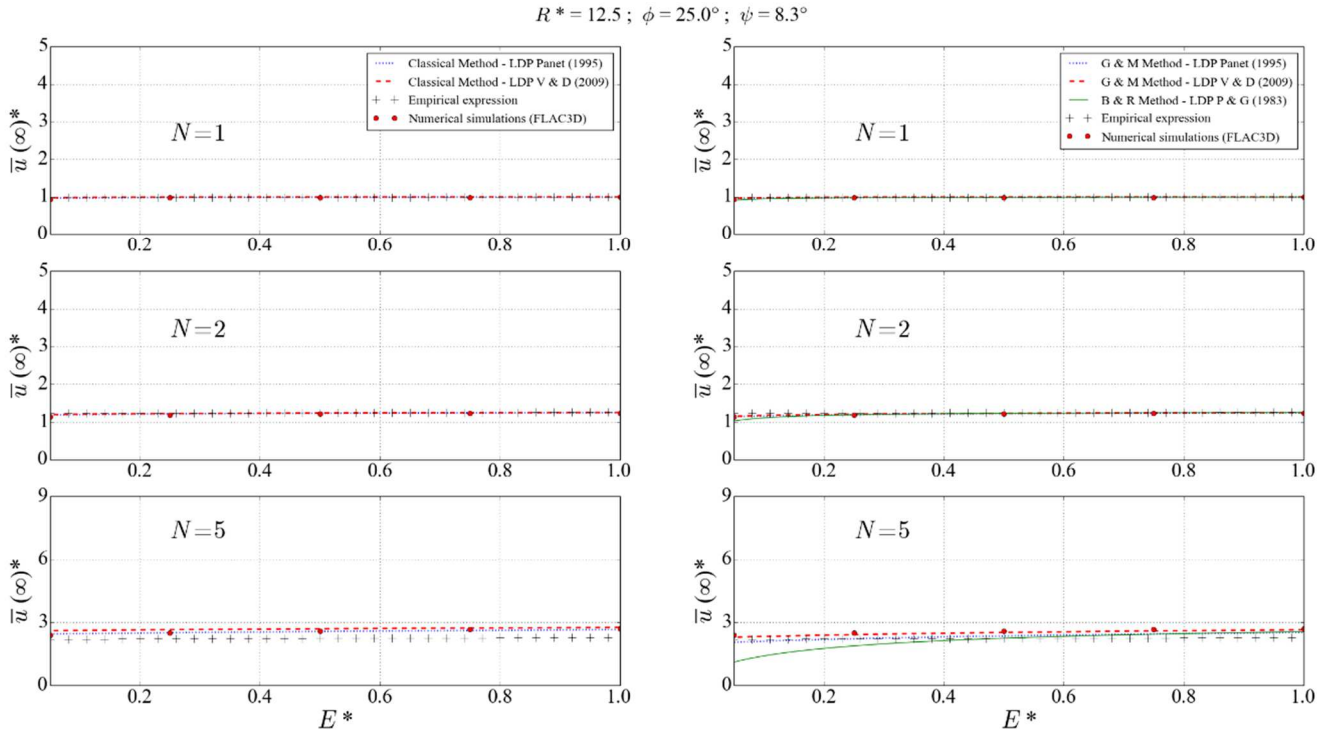

Comparison of $\bar{u}(\infty)^*$ between the different approaches when R^*=12.5 and ϕ=25° for non-associate plasticity (ψ = ϕ/3). Classical methods on the left column and implicit methods on the right column

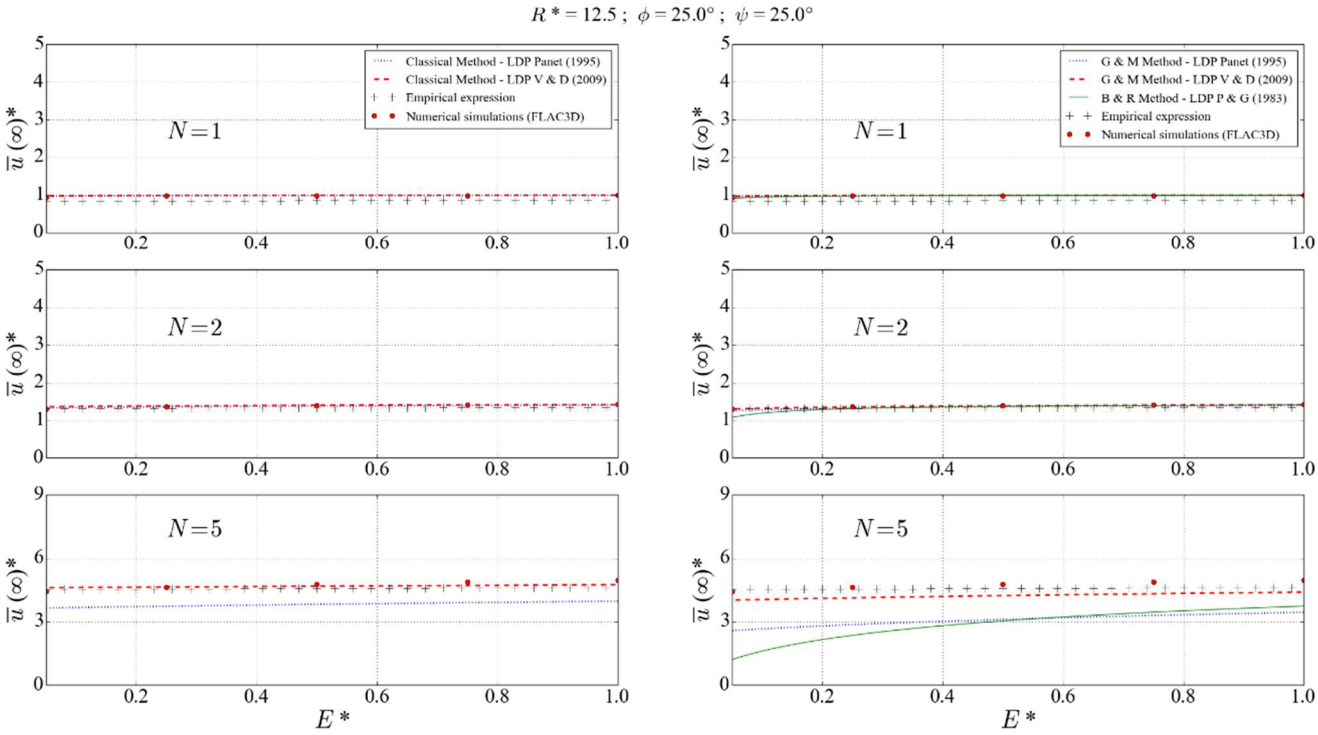

Comparison of $\bar{u}(\infty)^*$ between the different approaches when R^*=12.5 and ϕ=25° for associate plasticity (ψ = ϕ). Classical methods on the left column and implicit methods on the right column

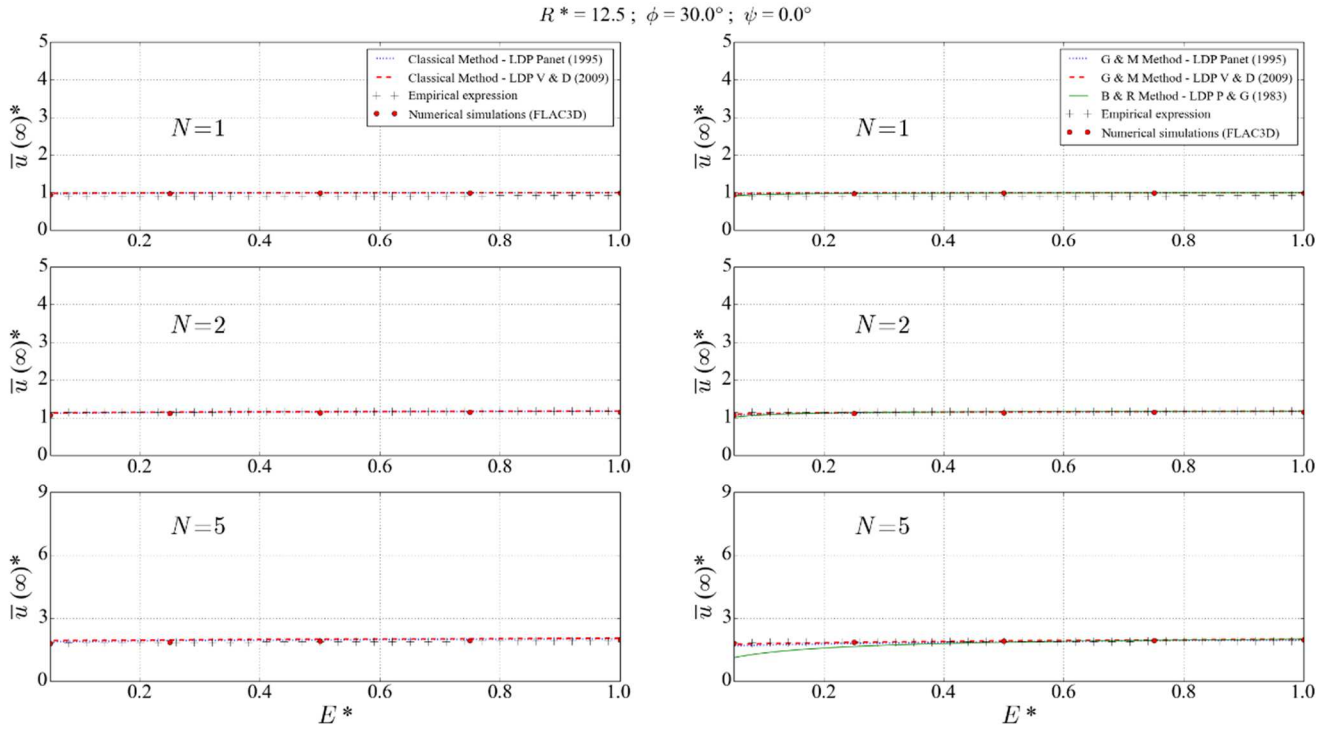

Comparison of $\bar{u}(\infty)^*$ between the different approaches when R^*=12.5 and ϕ=30° for incompressible plasticity (ψ = 0). Classical methods on the left column and implicit methods on the right column

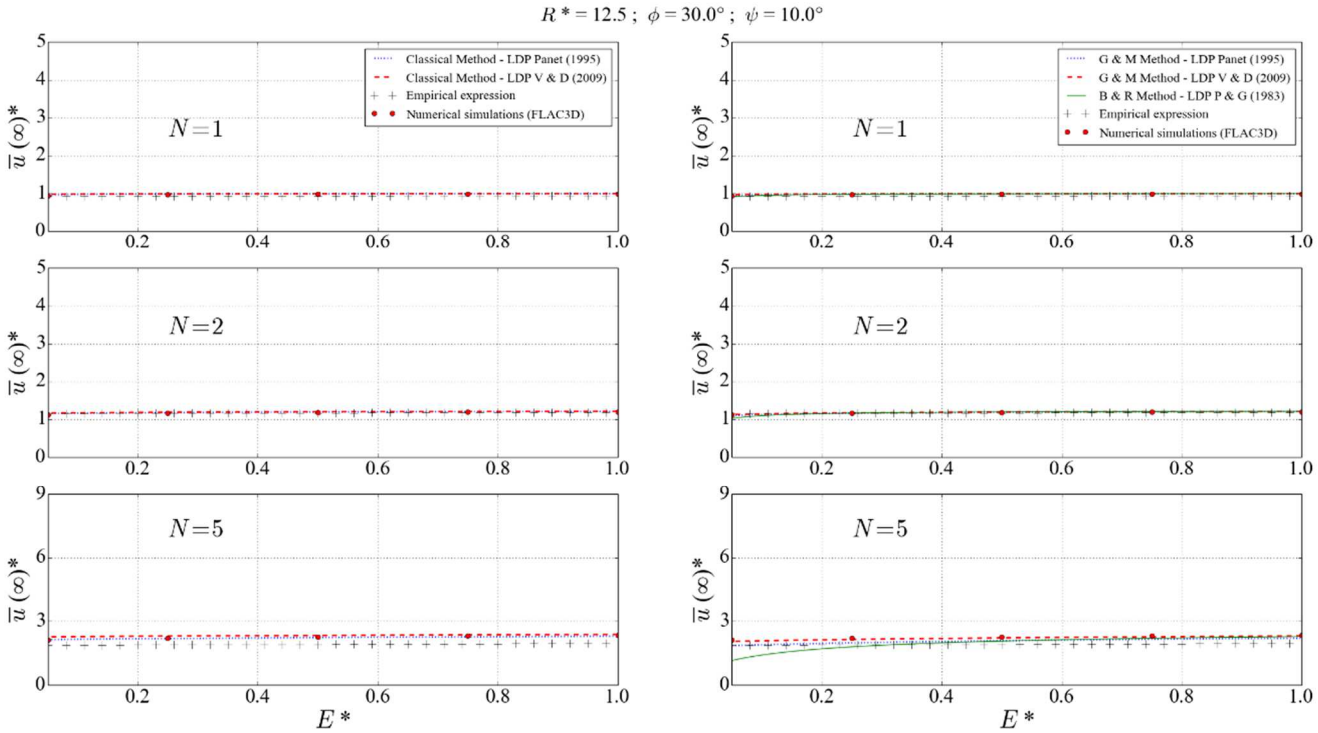

Comparison of $\bar{u}(\infty)^*$ between the different approaches when R^*=12.5 and ϕ=30° for non-associate plasticity (ψ = ϕ/3). Classical methods on the left column and implicit methods on the right column

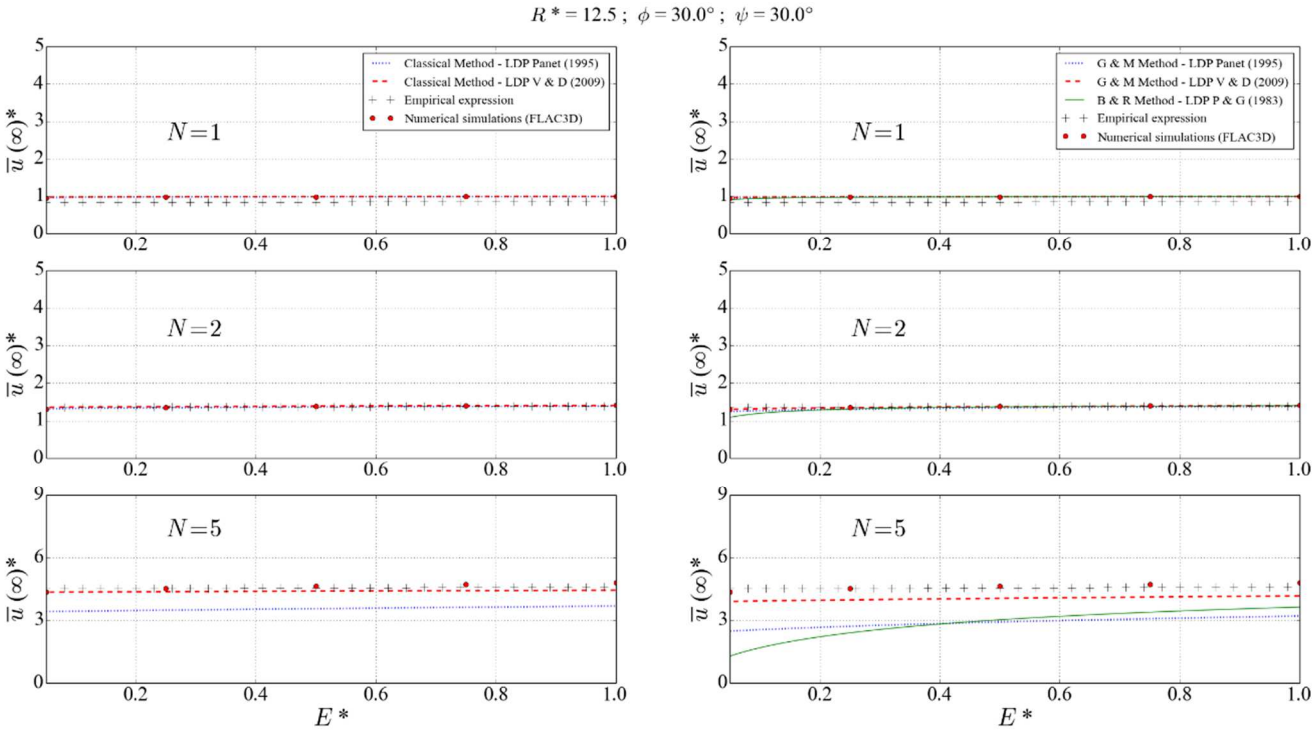

Comparison of $\bar{u}(\infty)^*$ between the different approaches when R^*=12.5 and ϕ=30° for associate plasticity (ψ = ϕ). Classical methods on the left column and implicit methods on the right column

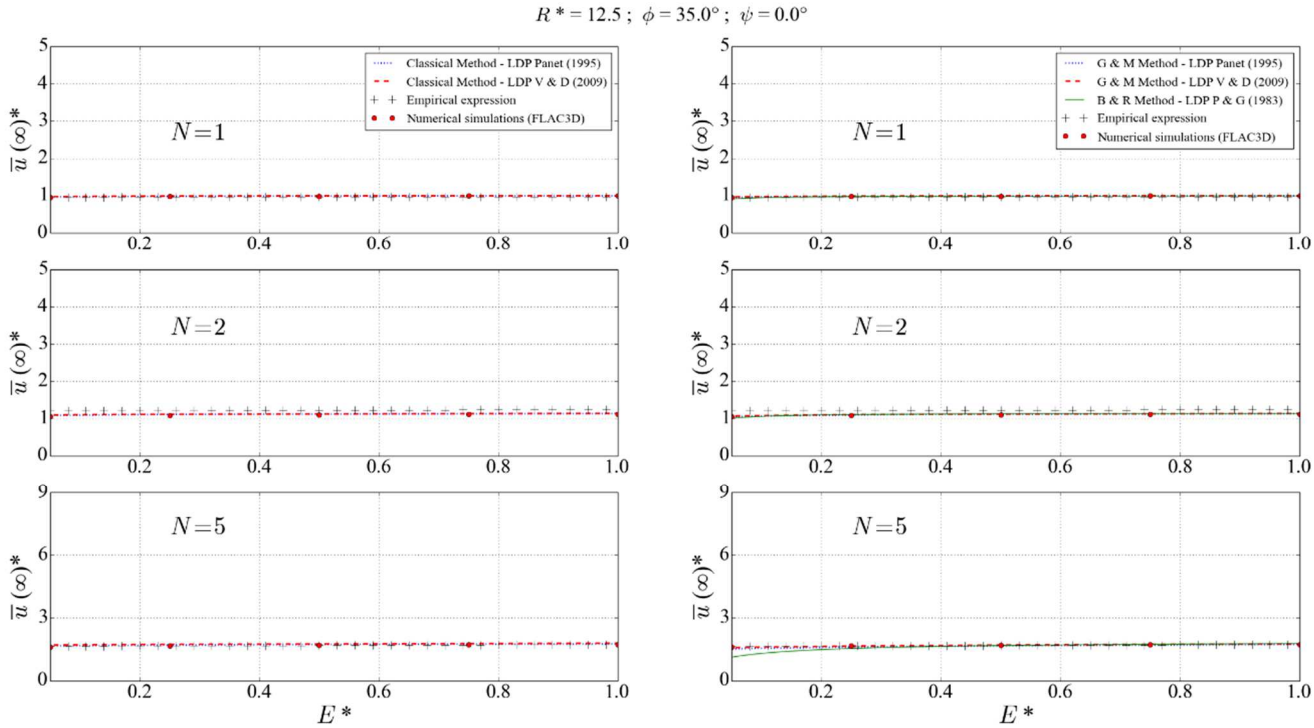

Comparison of $\bar{u}(\infty)^*$ between the different approaches when R^*=12.5 and ϕ=35° for incompressible plasticity (ψ = 0). Classical methods on the left column and implicit methods on the right column

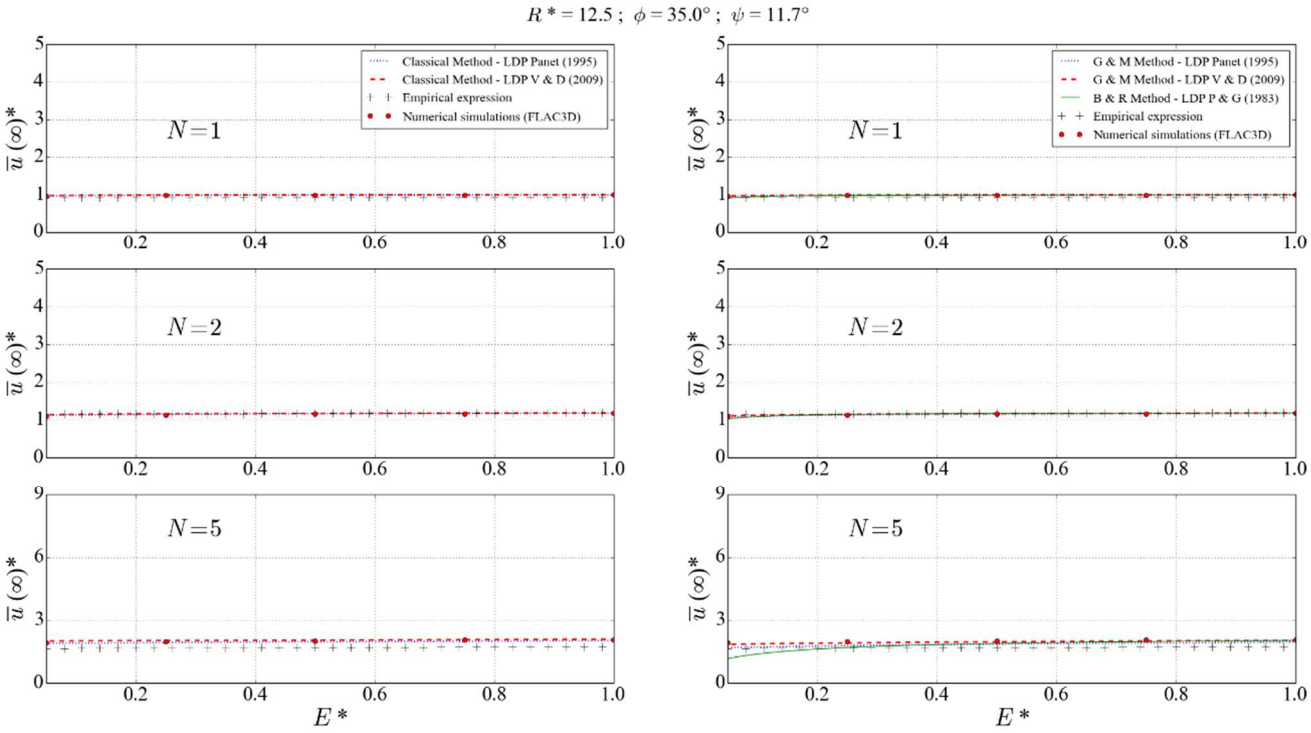

Comparison of $\bar{u}(\infty)^*$ between the different approaches when R^*=12.5 and ϕ=35° for non-associate plasticity (ψ = ϕ/3). Classical methods on the left column and implicit methods on the right column

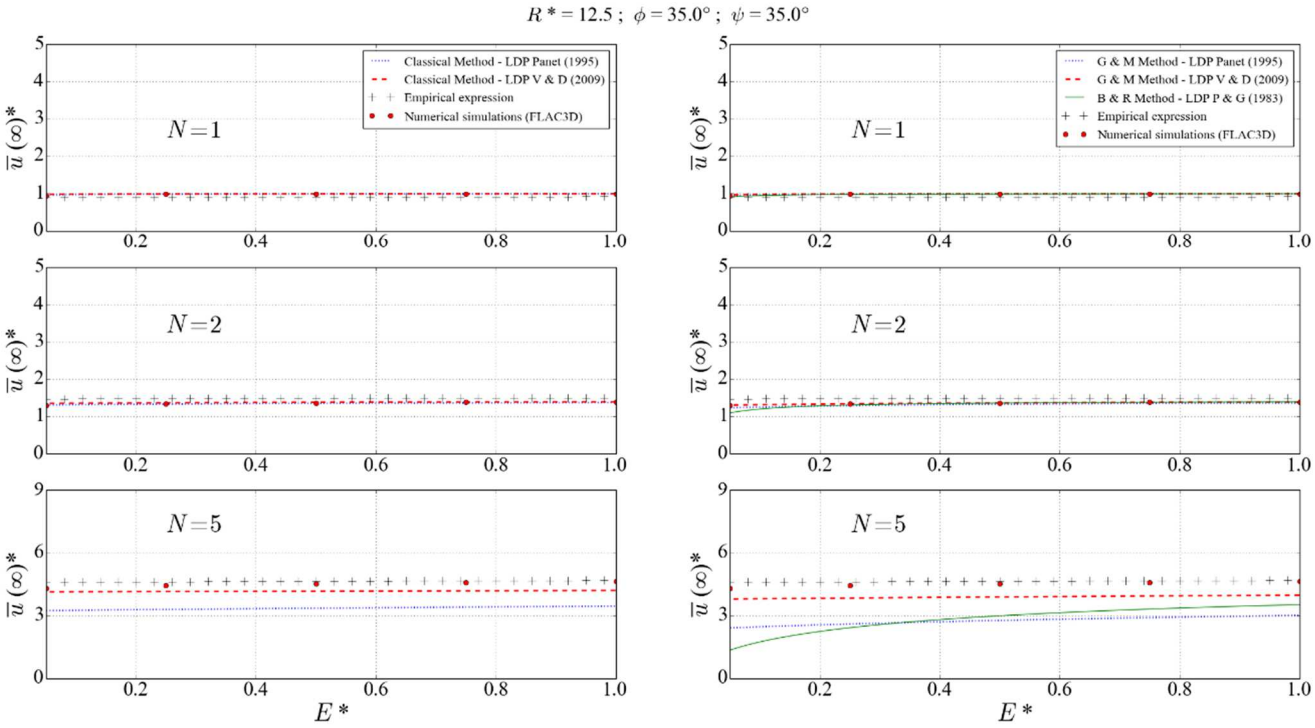

Comparison of $\bar{u}(\infty)^*$ between the different approaches when R^*=12.5 and ϕ=35° for associate plasticity (ψ = ϕ). Classical methods on the left column and implicit methods on the right column

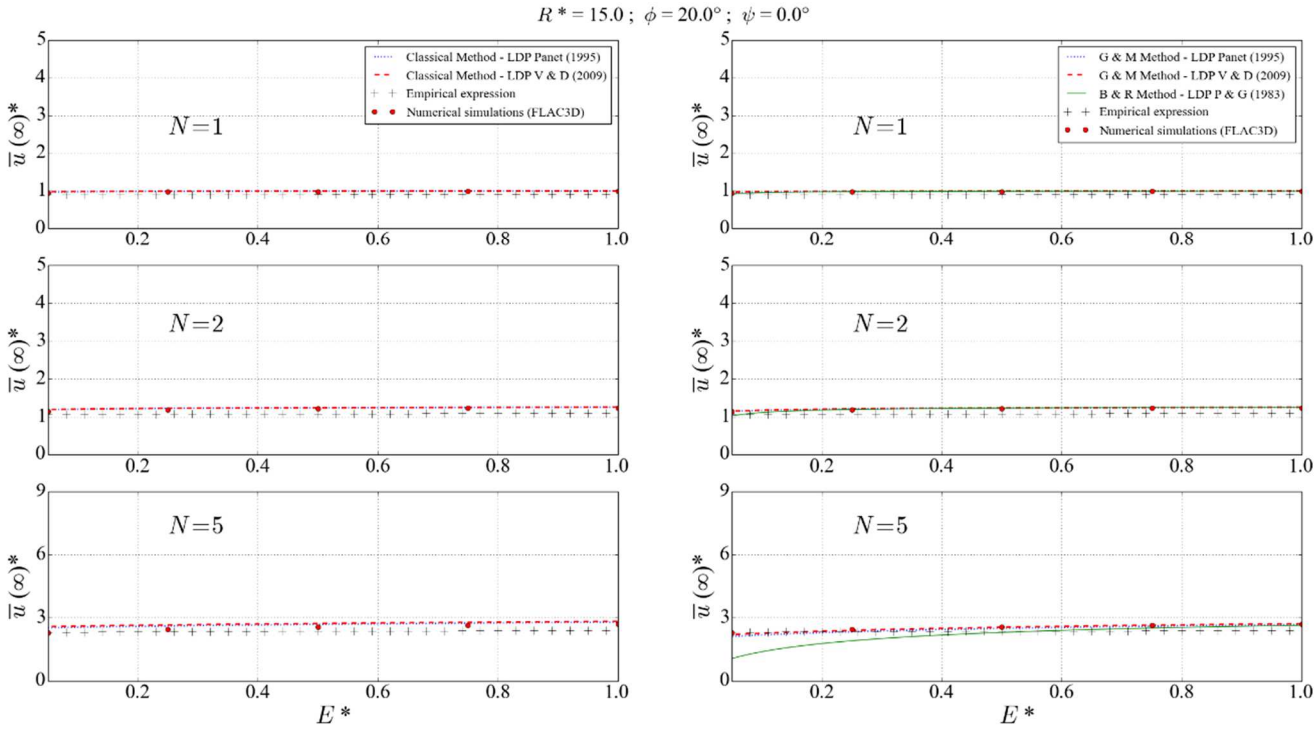

Comparison of $\bar{u}(\infty)^*$ between the different approaches when R^*=15 and ϕ=20° for incompressible plasticity (ψ = 0). Classical methods on the left column and implicit methods on the right column

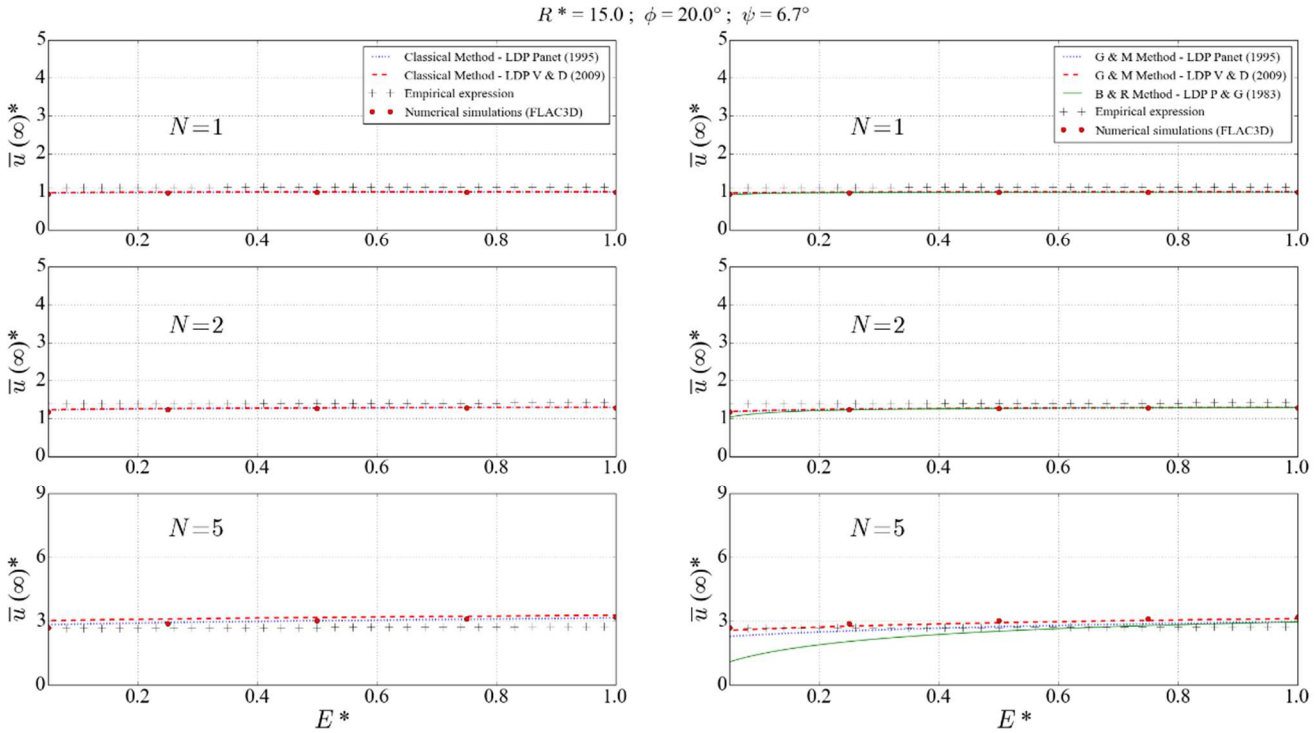

Comparison of $\bar{u}(\infty)^*$ between the different approaches when R^*=15 and ϕ=20° for non-associate plasticity (ψ = ϕ/3). Classical methods on the left column and implicit methods on the right column

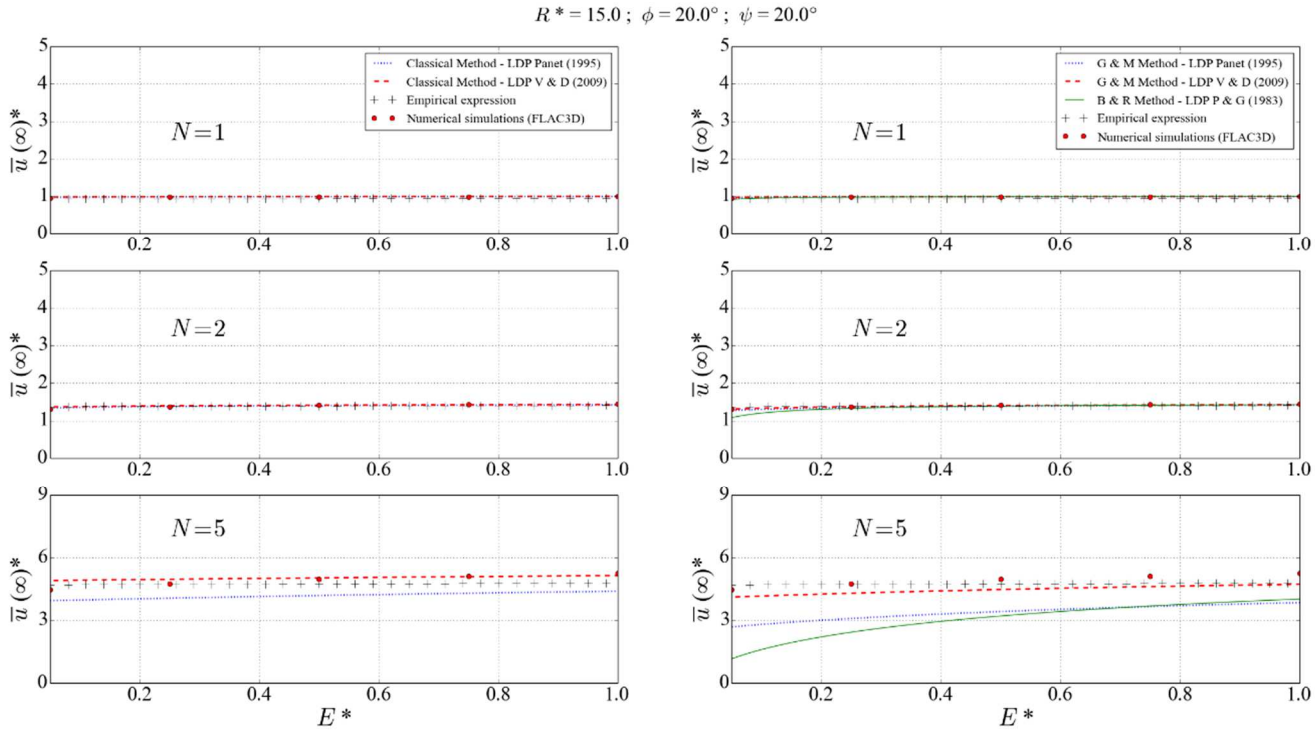

Comparison of $\bar{u}(\infty)^*$ between the different approaches when R^*=15 and ϕ=20° for associate plasticity (ψ = ϕ). Classical methods on the left column and implicit methods on the right column

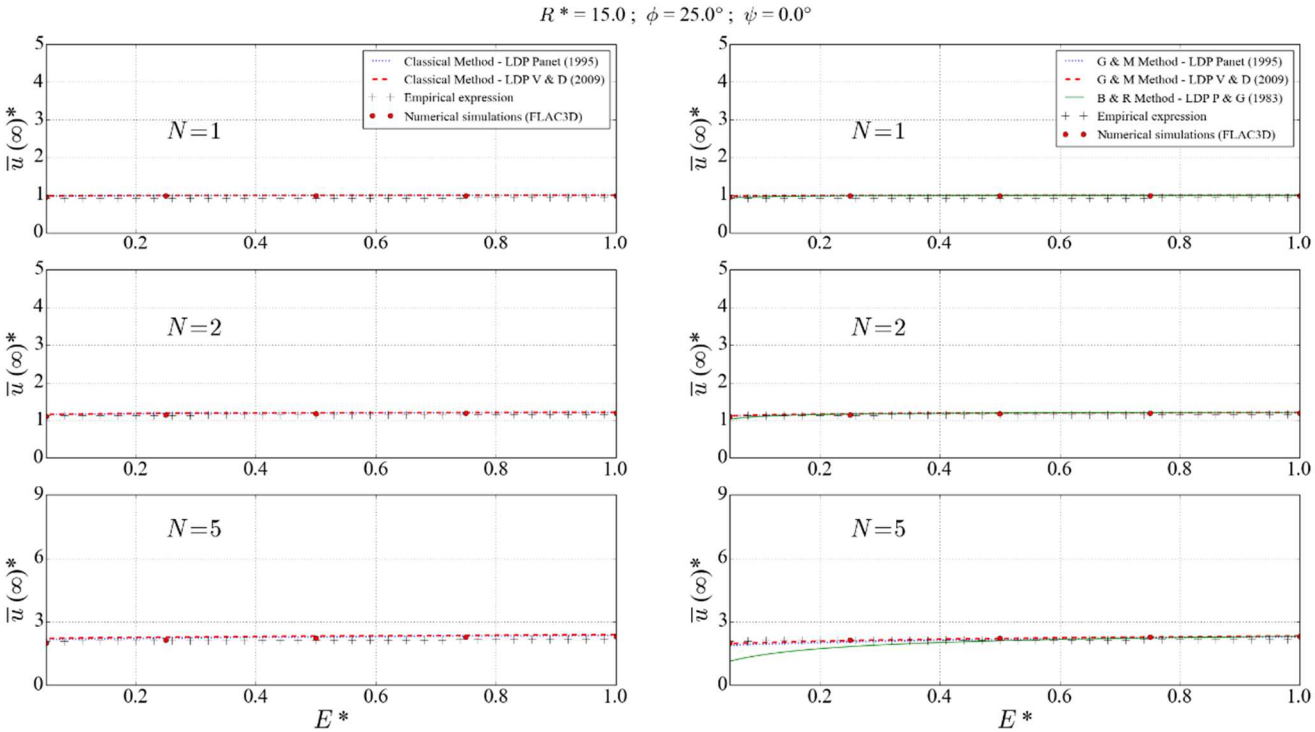

Comparison of $\bar{u}(\infty)^*$ between the different approaches when R^*=15 and ϕ=25° for incompressible plasticity (ψ = 0). Classical methods on the left column and implicit methods on the right column

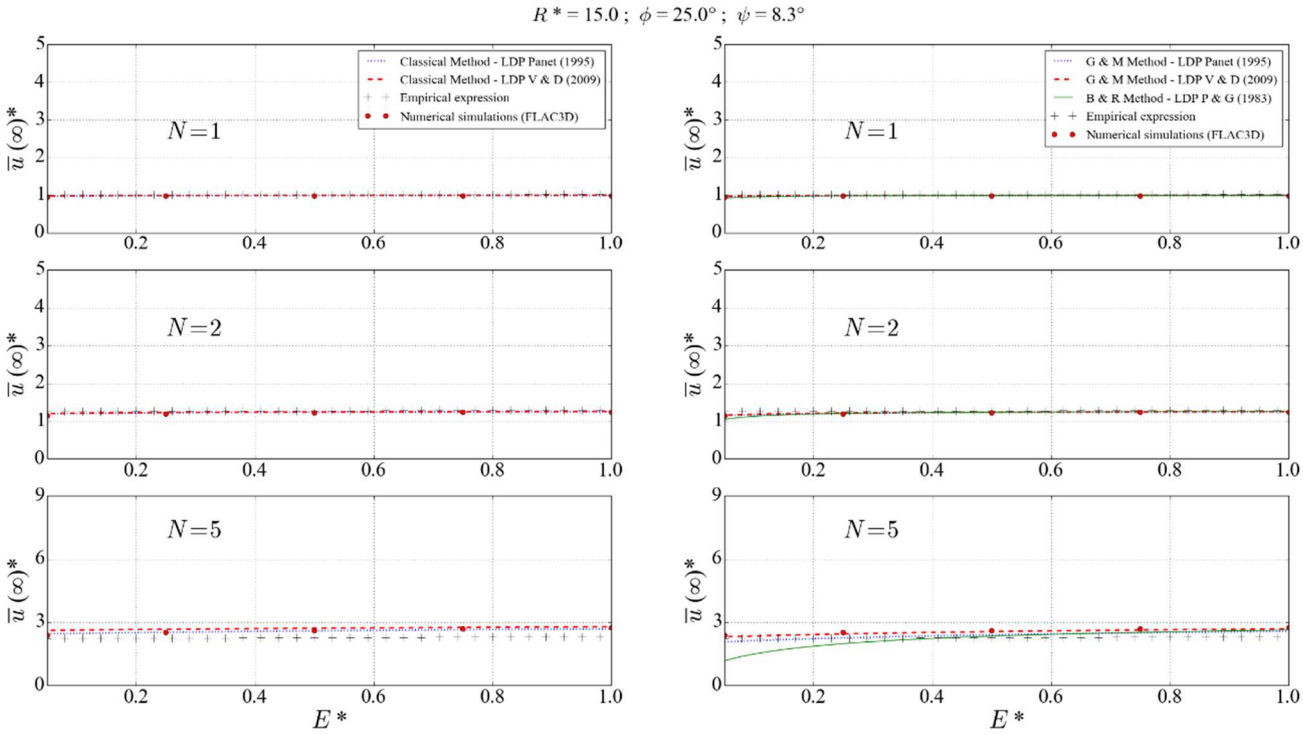

Comparison of $\bar{u}(\infty)^*$ between the different approaches when R^*=15 and ϕ=25° for non-associate plasticity (ψ = ϕ/3). Classical methods on the left column and implicit methods on the right column

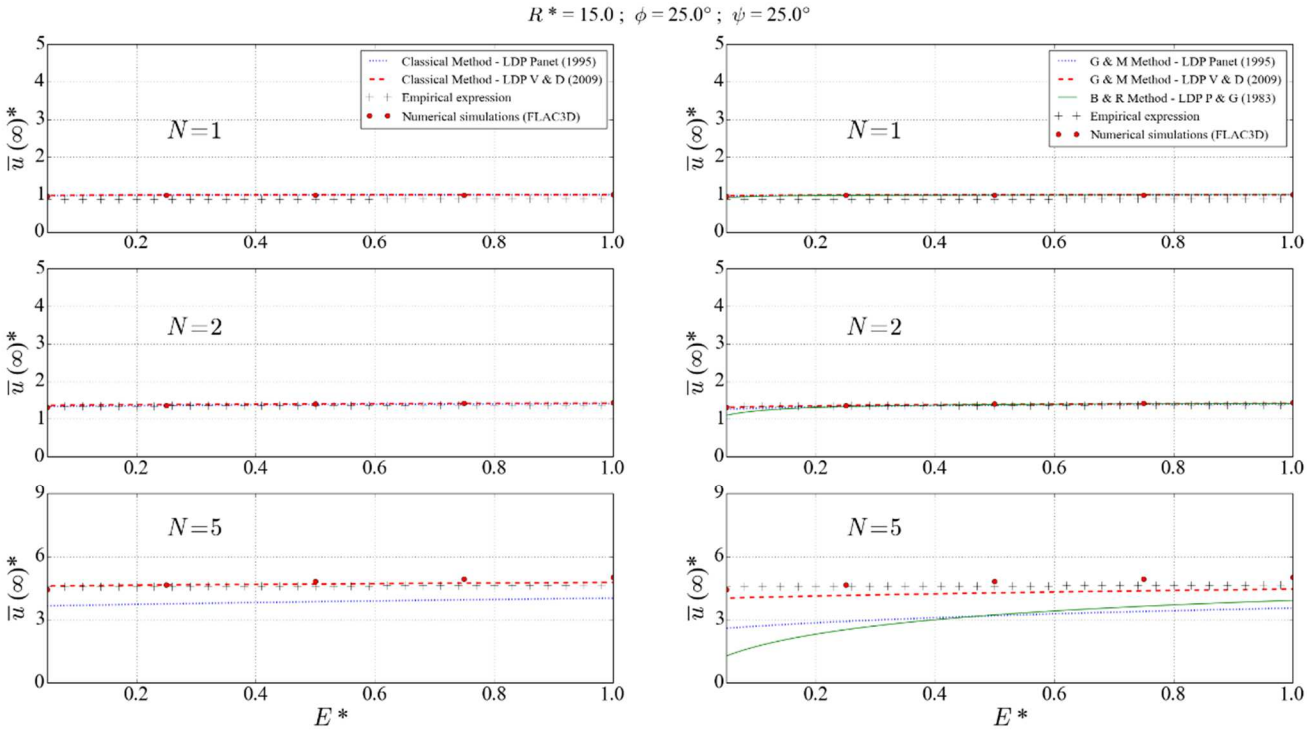

Comparison of $\bar{u}(\infty)^*$ between the different approaches when R^*=15 and ϕ=25° for associate plasticity (ψ = ϕ). Classical methods on the left column and implicit methods on the right column

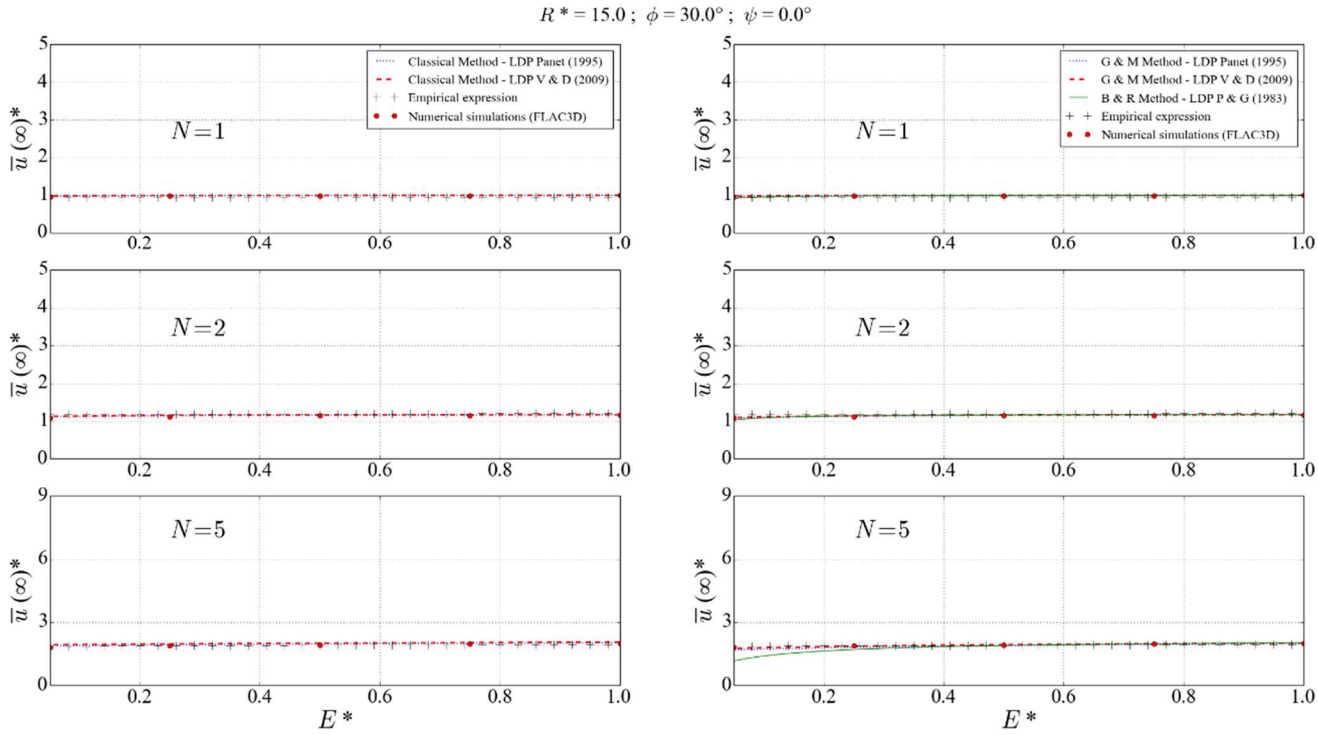

Comparison of $\bar{u}(\infty)^*$ between the different approaches when R^*=15 and ϕ=30° for incompressible plasticity (ψ = 0). Classical methods on the left column and implicit methods on the right column

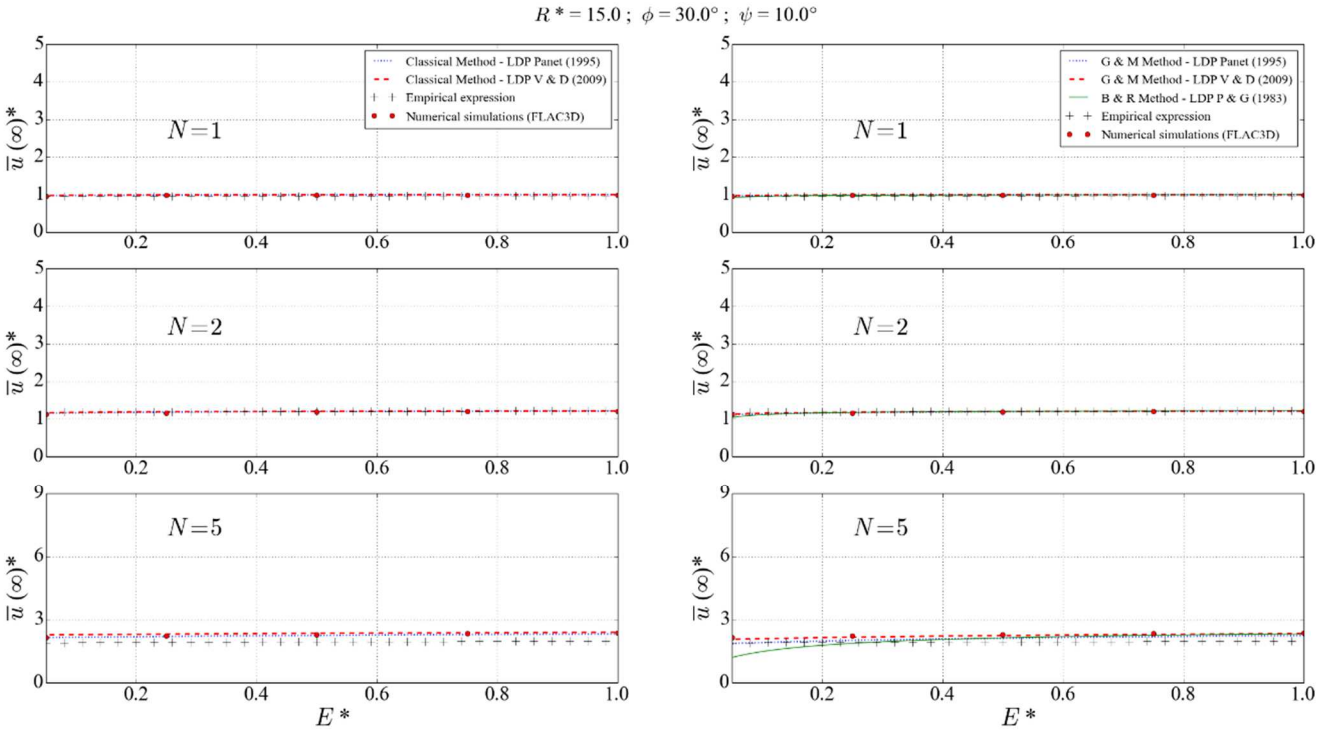

Comparison of $\bar{u}(\infty)^*$ between the different approaches when R^*=15 and ϕ=30° for non-associate plasticity (ψ = ϕ/3). Classical methods on the left column and implicit methods on the right column

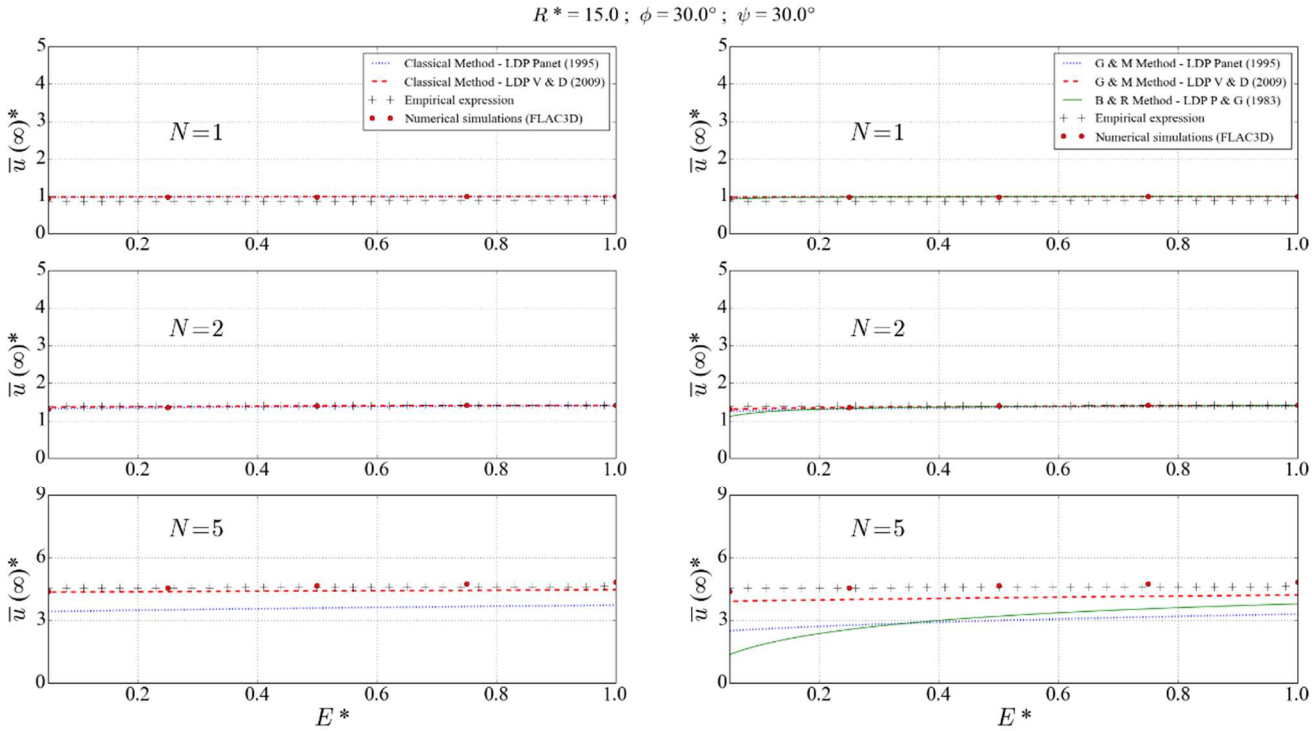

Comparison of $\bar{u}(\infty)^*$ between the different approaches when R^*=15 and ϕ=30° for associate plasticity (ψ = ϕ). Classical methods on the left column and implicit methods on the right column

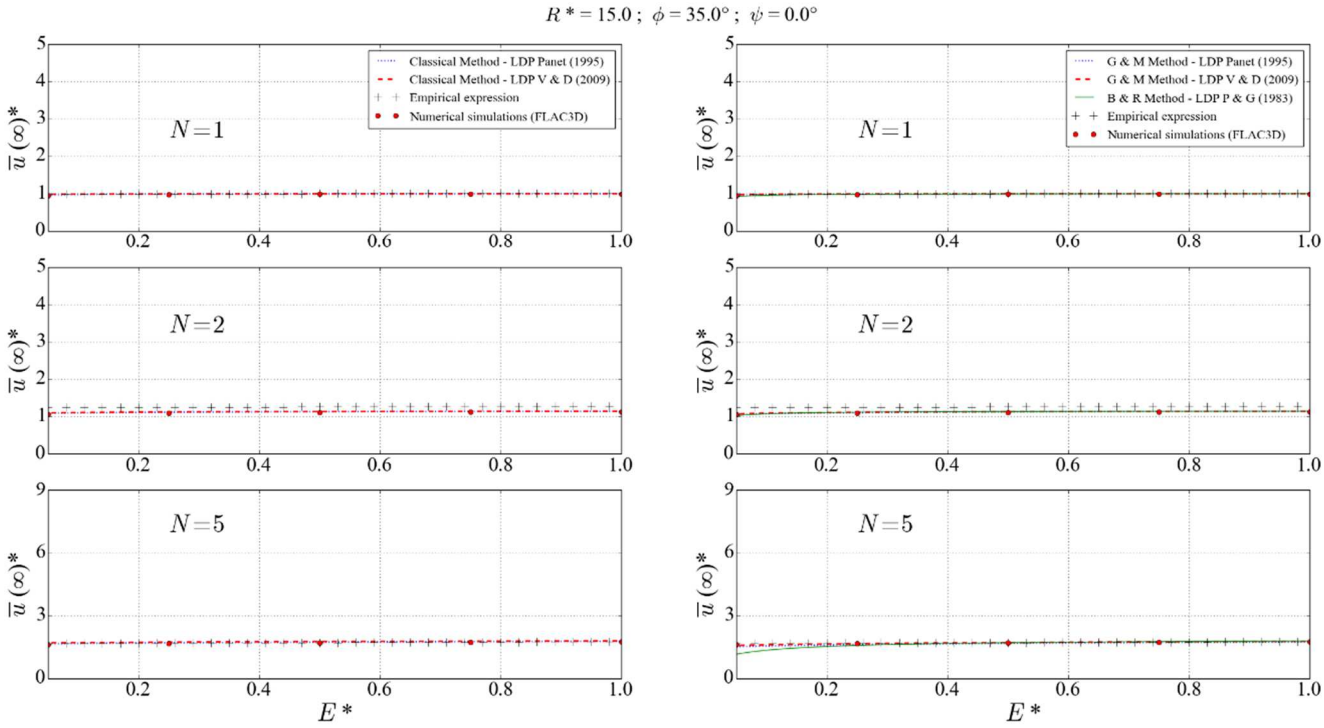

Comparison of $\bar{u}(\infty)^*$ between the different approaches when R^*=15 and ϕ=35° for incompressible plasticity (ψ = 0). Classical methods on the left column and implicit methods on the right column

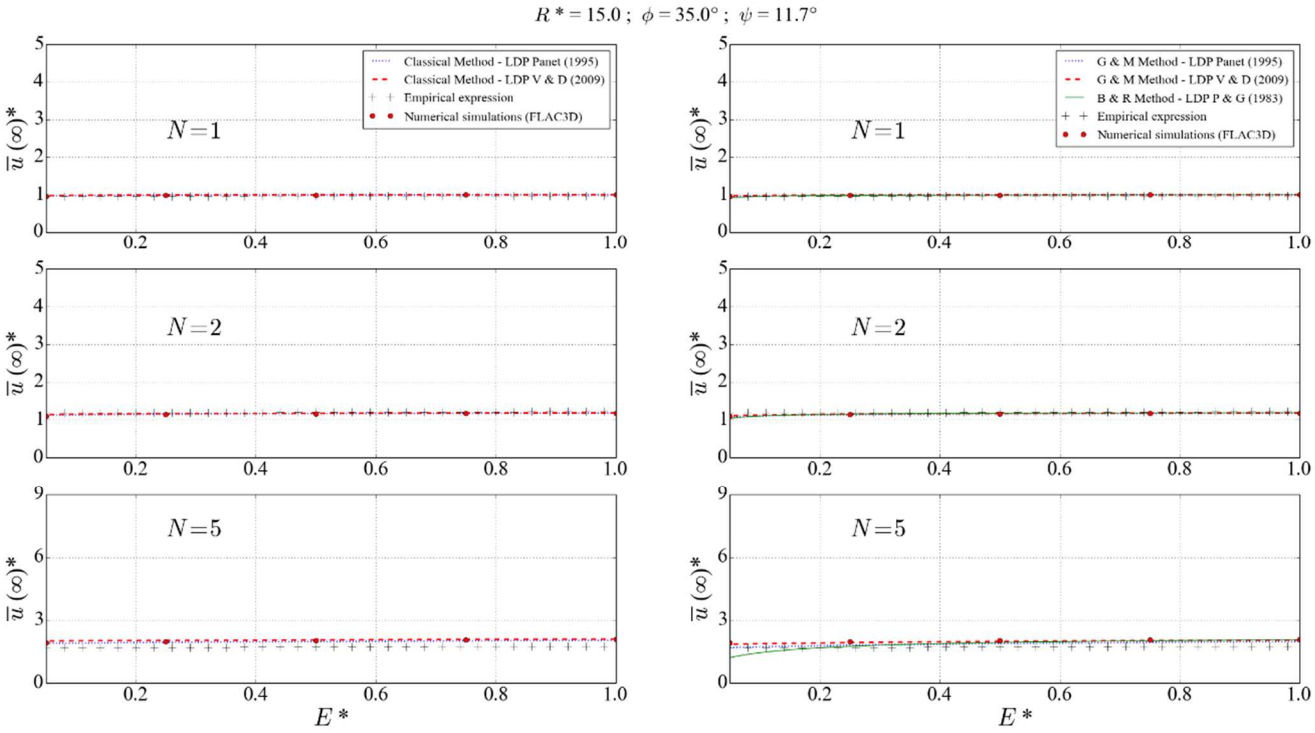

Comparison of $\bar{u}(\infty)^*$ between the different approaches when R^*=15 and ϕ=35° for non-associate plasticity (ψ = ϕ/3). Classical methods on the left column and implicit methods on the right column

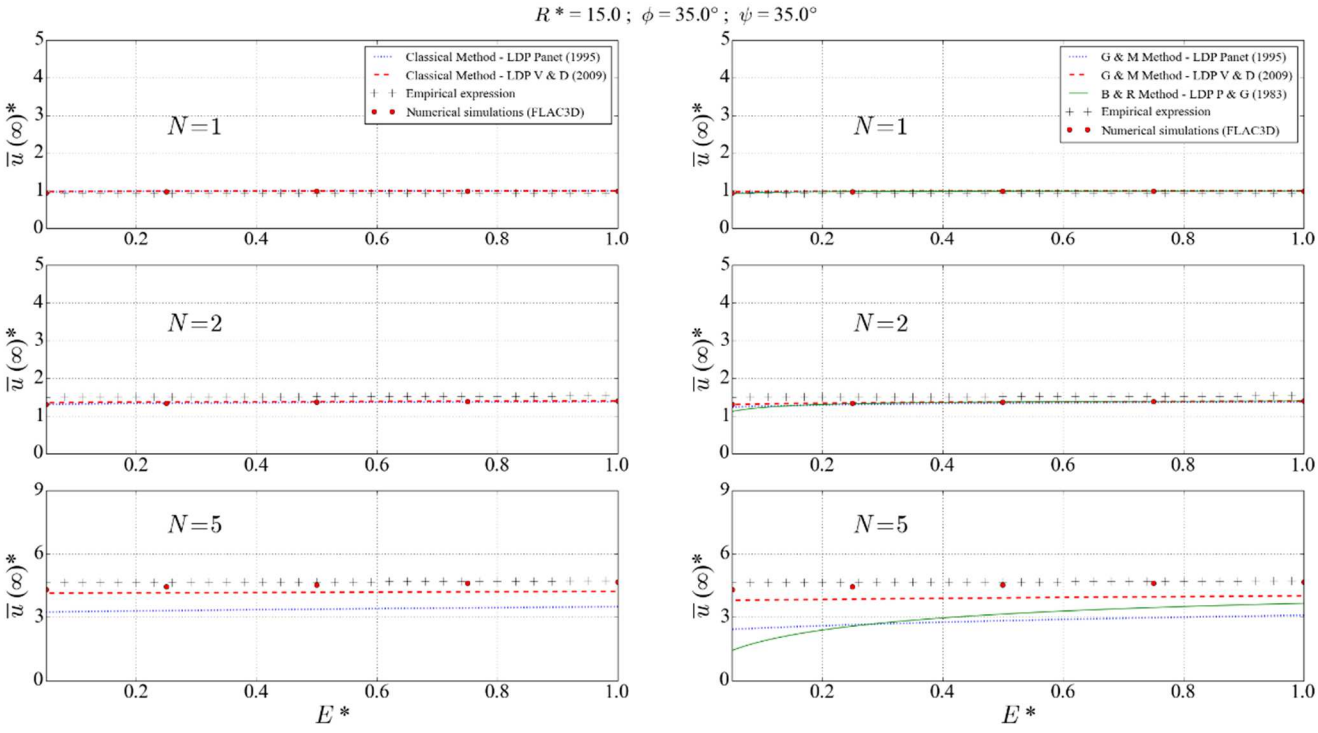

Comparison of $\bar{u}(\infty)^*$ between the different approaches when R^*=15 and ϕ=35° for associate plasticity (ψ = ϕ). Classical methods on the left column and implicit methods on the right column

APPENDIX D - Back analysis of convergence data of sections within zone A (from chainage 1905 to chainage 2723)

Section 8 (Chainage 1905)

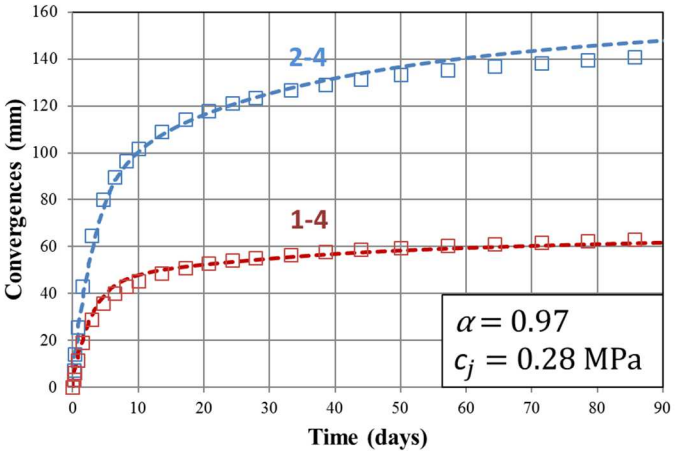

Section 13 (Chainage 1998)

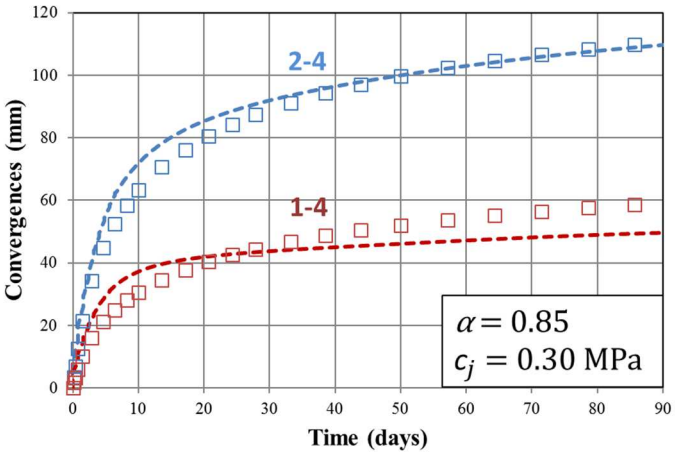

Section 14 (Chainage 2018)

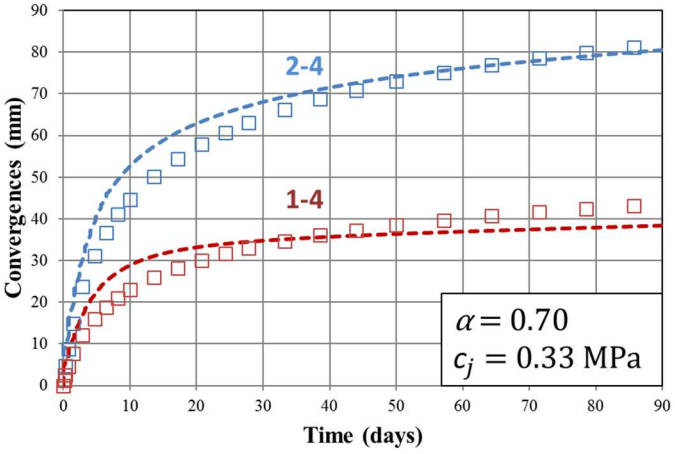

Section 16 (Chainage 2063)

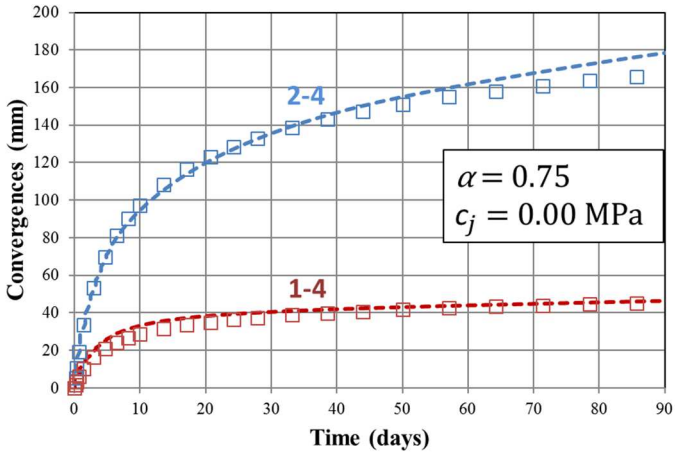

Section 18 (Chainage 2136)

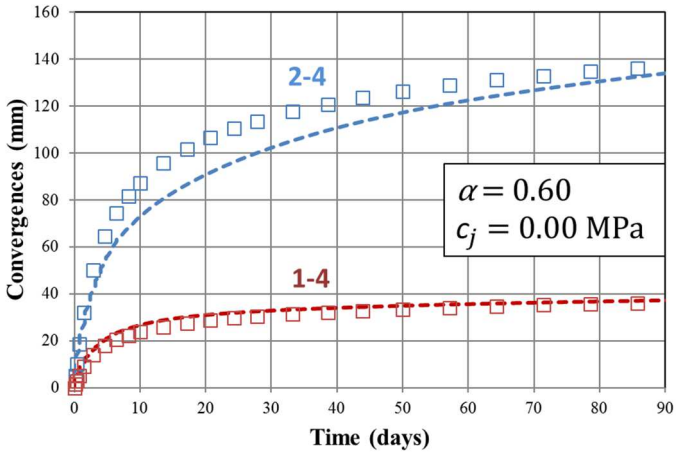

Section 25 (Chainage 2289)

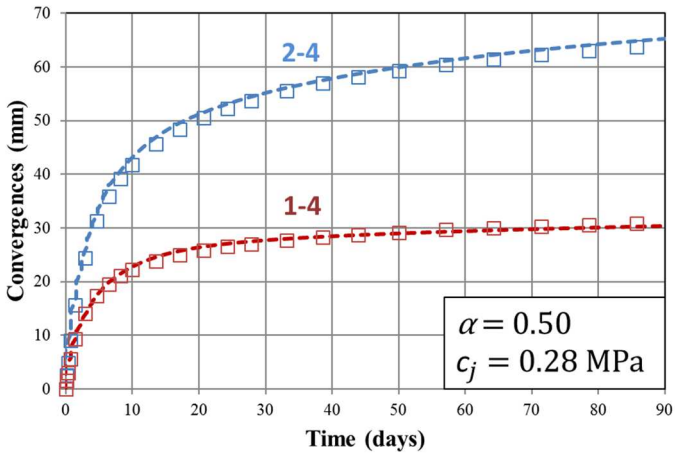

Back analysis of convergence data of sections within zone A (from chainage 1905 to chainage 2723)

Section 26 (Chainage 2292.5)

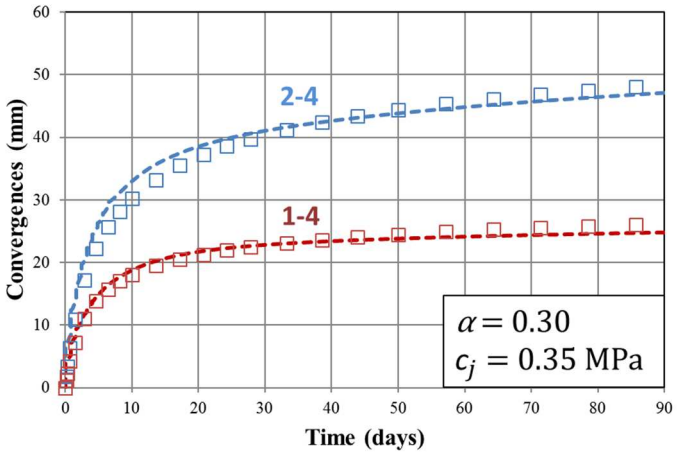

Section 28 (Chainage 2296)

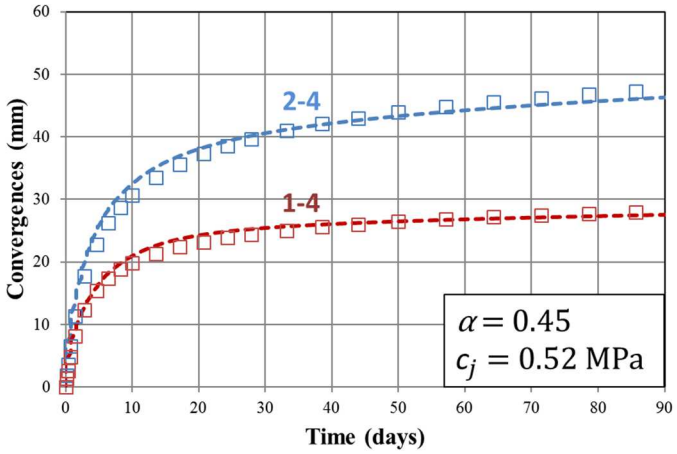

Section 30 (Chainage 2341)

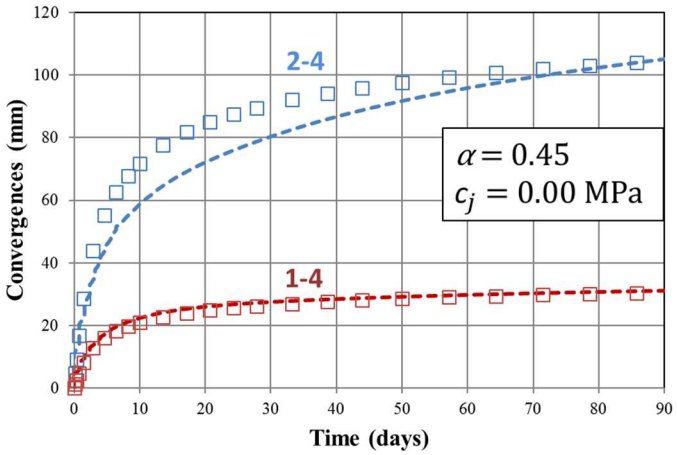

Back analysis of convergence data of sections within zone A (from chainage 1905 to chainage 2723)

Section 36 (Chainage 2509)

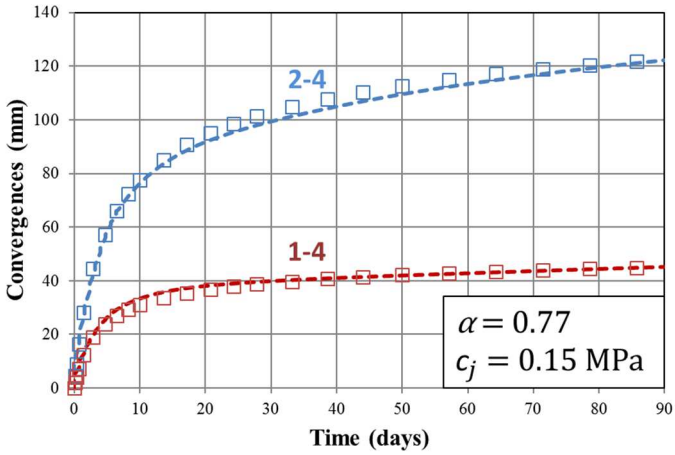

Section 37 (Chainage 2531)

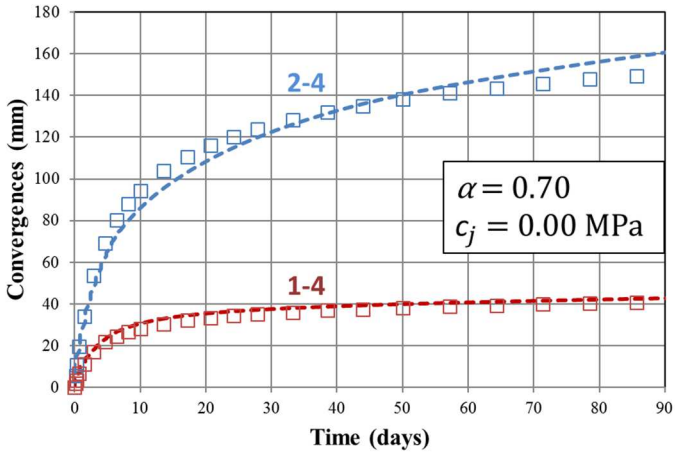

Section 41 (Chainage 2626)

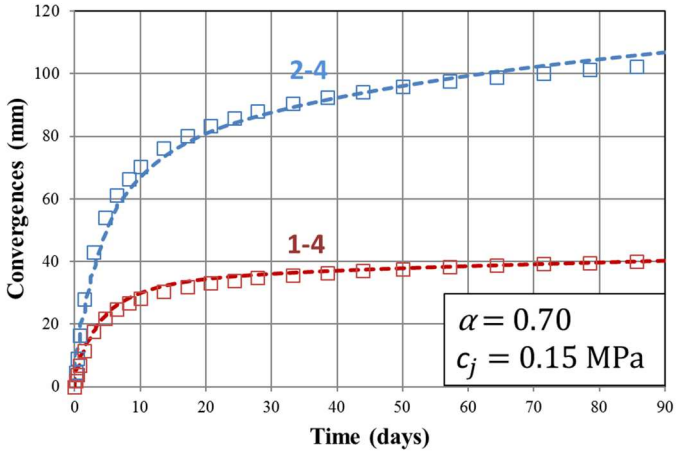

Back analysis of convergence data of sections within zone A (from chainage 1905 to chainage 2723)

Section 43 (Chainage 2682)

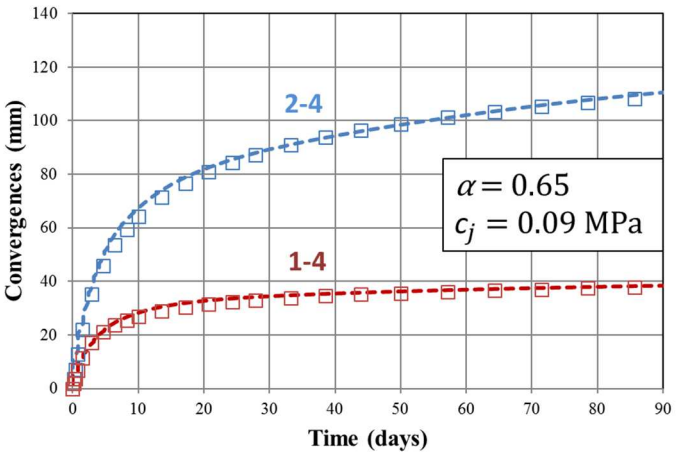

Section 44 (Chainage 2723)

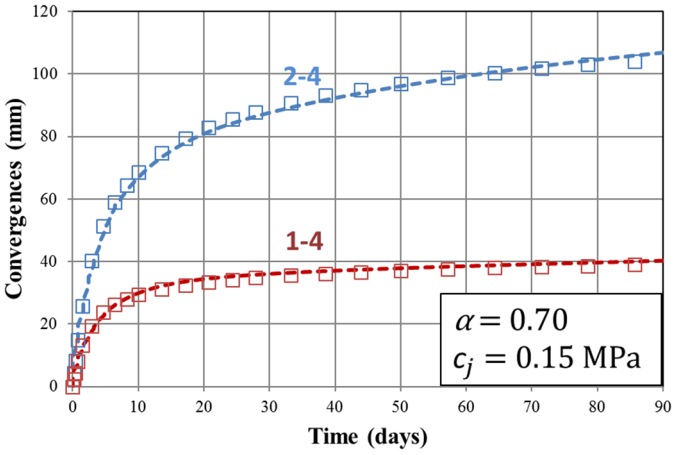

Back analysis of convergence data of sections within zone A (from chainage 1905 to chainage 2723)